Dissertation
submitted to the
Combined Faculties of the Natural Sciences and Mathematics
of the Ruperto-Carola-University of Heidelberg, Germany
for the degree of
Doctor of Natural Sciences

Put forward by
Johannes Ludwig
born in: Schweinfurt, Germany
Oral examination: 28th April, 2014

A Survey of Dwarfs and Tidal Debris around Nearby Massive Galaxies
–
Deep Imaging with Medium-Sized Telescopes

Referees: Prof. Dr. E. K. Grebel
Prof. Dr. J. Heidt

ABSTRACT

A Survey of Dwarfs and Tidal Debris around Nearby Massive Galaxies

—

Deep Imaging with Medium-Sized Telescopes

The goal of this thesis was to search for interaction signatures among massive galaxies and to quantify the properties of their satellites. We performed deep wide-field imaging on nearby massive spiral galaxies in a distance range of 8 to 35 Mpc. The spirals cover a variety of morphologies and are located in environments of different densities and richness. We studied the surroundings of 47 massive galaxies. 29 targets were studied in detail. For all of them, we were able to detect dwarf companions. In total we found 55 mostly new candidate dwarf galaxies (CDG), on average about two CDGs per target. Based on their structural parameters and colors, we classified the majority of the CDGs as dwarf spheroidal galaxies, but also dwarf elliptical and dwarf irregular galaxies are included in the sample. The satellites' observed surface brightness in the B-band falls in the range $22 \lesssim \mu_B \lesssim 26$ mag arcsec^{-2}, the colors vary from $0.8 \lesssim (B-R)_0 \lesssim 1.5$ mag, and the measured range of luminosities is $-8 \lesssim M_{B,0} \lesssim -17$. The number of CDGs observed is quantitatively in agreement with the expected number compared to the Milky Way or M31 within our sensitivity limits. Furthermore, about 54% of our host galaxies show signs of tidal interactions. These range from prominent tidal tails, plumes and clouds to thin and faint stellar streams. 35% of the massive galaxies exhibit signs of tidal tails or bridges, 11% show plumes or clouds, and only 8% show stellar streams. We discuss possible progenitors of these features based on their colors.

ZUSAMMENFASSUNG

Zwerggalaxien in der Umgebung von Spiralgalaxien und deren Wechselwirkungen

Ziel dieser Dissertation ist die Suche nach Wechselwirkungssignaturen um massereiche Galaxien und die Quantifizierung der Eigenschaften ihrer Satellitengalaxien. Zu diesem Zweck nahmen wir tiefe Weitfeldabbildungen naher massereicher Spiralgalaxien auf, die einen Entfernungsbereich von 8 bis 35 Mpc überdecken. Die Spiralgalaxien zeigen eine Reihe unterschiedlicher Morphologien und befinden sich in Umgebungen unterschiedlicher Dichte. Wir untersuchten die Umgebungen von 47 massereichen Galaxien. 29 unserer Zielobjekte wurden im Detail untersucht. Bei allen konnten wir Zwergbegleiter entdecken. Insgesamt fanden wir 55 überwiegend neu entdeckte Zwerggalaxienkandidaten; im Schnitt folglich zwei pro massereicher Galaxie. Anhand ihrer Struktur- und Farbeigenschaften identifizierten wir die meisten Zwerggalaxienkandidaten als sphäroidale Zwerggalaxien, aber auch elliptische und irreguläre Zwerggalaxien wurden gefunden. Die Flächenhelligkeiten unserer Satelliten liegen im B-Band im Bereich von $22 \lesssim \mu_B \lesssim 26$ mag arcsec^{-2}, die Farben reichen von $0.8 \lesssim (B-R)_0 \lesssim 1.5$ mag, und die absoluten B-Bandhelligkeiten decken einen Bereich von $-8 \lesssim M_{B,0} \lesssim -17$ mag ab. Die Anzahl der beobachteten Zwerggalaxienkandidaten stimmt quantitativ mit der Zahl überein, welche man angesichts der Satelliten der Milchstraße oder M31 innerhalb unserer Empfindlichkeitsgrenzen erwarten würde. Darüber hinaus zeigen etwa 54% unserer massereichen Galaxien Anzeichen für Wechselwirkungen. Diese erstrecken sich von prominenten Gezeitenschweifen bis hin zu dünnen lichtschwachen Gezeitenströmen. 35% unserer massereichen Galaxien zeigen Gezeitenschweife oder Brückenstrukturen, 11% klumpige oder wolkenartige Störungen und etwa 8% leuchtschwache Gezeitenströme. Wir diskutieren anhand der gemessenen Farben, welche Galaxien diese Strukturen verursacht haben könnten.

Für meine Familie,
ihr seid für mich das Wichtigste
und eine ständige Inspiration für neue Ideen.

Contents

1

INTRODUCTION

The different morphology of galaxies is fascinating Astronomers since the start of extragalactic observations. The most important step in classifying galaxies is the Hubble sequence, which describes massive galaxies. Later on the observation of dwarf galaxies extended the picture of known galaxy types, making the previous known Hubble classification scheme incomplete. Many new observations of different kinds of dwarf galaxies demonstrate that these come with a unforeseen diversity. Now scientists try to put all these different type of galaxies into a schematic picture of galaxy evolution.

In this introduction we will summarize the current models of galaxy evolution and describe the evolution of galaxies in groups. We will discuss the morphology of dwarf galaxies found in groups and their basic properties. The second main topic of this Thesis is tidal debris, the observed types and properties will be illustrated in the final sections of this chapter.

1.1 GALAXY EVOLUTION

Galaxy evolution describes the life of galaxies from the first stages after the big bang to evolved systems which can be observed at redshifts z~ 0. The most common and established description on how galaxies assemble and evolve is the hierarchical growth of galaxy structure , which will be explained in section 1.1.1.

1.1.1 HIERARCHICAL GALAXY EVOLUTION

The theory of galaxy formation and evolution which describes the mass assembly of galaxies suggests that galaxies progressively grow via minor and major mergers (e.g., White & Frenk 1991). In order to test this model of galaxy formation against observations it is necessary to connect the cosmological density perturbations with the understanding of many different astrophysical processes like gas cooling, feedback, formation of stars, the evolution of stellar populations as well as the merging process of galaxies (Cole et al. 2000). Steinmetz & Navarro (2002) demonstrate that the Hubble sequence traces the accretion history of galaxies in the scenario of hierarchical structure formation, where disks form by a smooth deposition of cool gas in the central region of dark matter halos, mergers shape discs to spheroidal systems and bars are produced by tides from satellite galaxies. Observations of galaxy clusters and their distribution agree with the predictions of hierarchical growth. Interestingly, the largest fraction of baryonic matter is not found in these high density regions, but corresponds to filamentary structures and galaxy groups. For example, in the nearby universe about 85% of all galaxies are found either in galaxy groups or in the field (Tully 1987; Karachentsev 2005).

1.2 THE GROUP ENVIRONMENT

Galaxy groups come in a variety of structures, ranging from loose groups to very compact fossil groups. They have usually by definition less than 50 galaxies with $L \gtrsim L_\star \sim 2 \times 10^{10} L_\odot$ and have masses smaller than $\sim 10^{14} M_\odot$ (Sparke & Gallagher 2007). The fraction of mass which is located in stars increases with decreasing group size, therefore most of the stellar mass can be found in Local-Group-sized systems (Eke et al. 2005). Additionally, many groups show extended HI features like streams which are mostly connected to late-type spiral galaxies, but can also be associated with early type galaxies (Haynes 1981). HI surveys often help to find low-surface-brightness dwarf companions, which are usually classified as dwarf irregular galaxies (Lo & Sargent 1979).

The evolution of galaxies in groups can be affected by several processes which shape the galaxy observed properties:

1. **Dynamical friction** describes the effect when a massive body is moving through lighter particles, e.g. when a satellite galaxy is moving through the halo of its parent galaxy. Gravitational forces accelerate the lighter particles and they achieve momentum and kinetic energy when the satellite is moving through a “sea” of stars and dark matter. Energy and momentum conservation cause a slow down, which is called dynamical friction. The satellite is decelerated on its orbit and is spiraling to the central halo.

   Colpi et al. (1999) note that on the first orbit tidal stripping can remove about 60% of the mass and thus increases the orbital decay time. Satellites with low, surface mass density are disrupted on the same timescale as the decay time of their rigid counterparts, while satellites with small cores are able to survive in the halo over a time which is of the order of the Hubble time, e.g. dwarf spheroidal galaxies such as Sgr A or Fornax have undergone already stripping and their sinking times are larger than 10 Gyr (Colpi et al. 1999).

   Dynamical friction leads to galaxy mergers in dark matter halos mergers and is responsible for the stellar mass, the color of the observed galaxies and their morphology (Boylan-Kolchin et al. 2008).

2. **Ram pressure stripping** happens when the galaxy gaseous component (cold atomic/molecular gas and hot extended component) interacts with a wind caused by the galaxy motion relative to the intracluster medium (McCarthy et al. 2008). The efficiency of ram pressure stripping is function of the heliocentric velocity, the mass of the host galaxy, the mass of the satellite and the density of the intracluster medium. (Bekki 2009)

3. **Galaxy mergers** play an important role in the assembly of galaxies, and they preferentially occur in galaxy groups. Merging galaxies will be explained in detail in section 1.4

Other effects like harassment or tidal truncation are more often observed in rich groups and galaxy clusters.

1.3 DWARF GALAXIES IN GALAXY GROUPS

The largest fraction of galaxies in groups consists of dwarf galaxies. Many different types of dwarf galaxies can be found there, which will be described in the following sections.

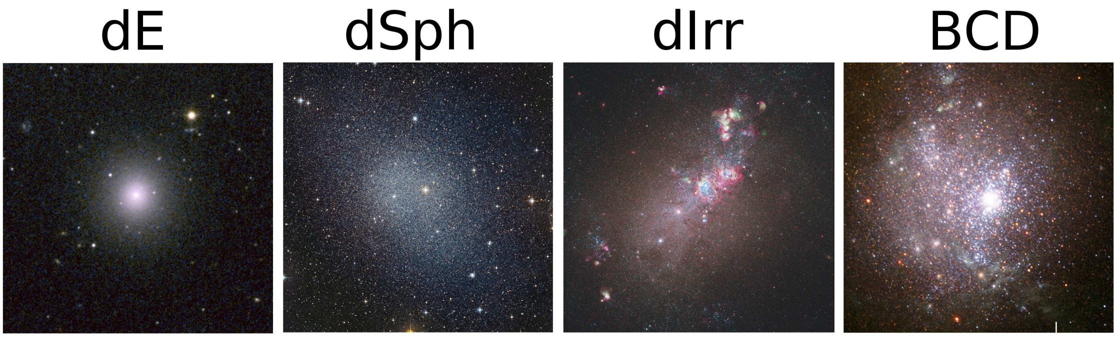

Figure 1.1: Overview of different types of dwarf galaxies studied in our work. The single images are taken from http://hubblesite.org/ and http://nasa.gov. On the left a dE of the Perseus cluster can be seen, then the dSph Fornax and the dIrr NGC 4214 is shown. On the right hand side is the BCD NGC 1705.

Dwarf galaxies are low mass objects and have much lower luminosities compared to massive galaxies. By definition all galaxies with $M_V \gtrsim -18$ are classified as dwarf galaxies. In order to find a classification scheme for dwarf galaxies, for instance Sandage & Binggeli (1984) tried to apply the Hubble sequence. In the scheme of Sandage & Binggeli (1984) early type dwarf galaxies (dE and dSphs) are the counterparts of elliptical galaxies, and late-type dwarf galaxies (dIrr) and blue compact dwarf galaxies (BCD) correspond to spiral and irregular galaxies. Detailed studies of dwarf galaxies show that it is not proper to use the same classification system as for massive galaxies, since, for instance, disc structures can be observed in dEs (Lisker et al. 2006) and many dEs exhibit significant rotation (van der Marel 1994; Simien & Prugniel 2002). van den Bergh (1977) tried to classify dwarf galaxies among active dwarfs with intergalactic HII regions, less active dwarfs and inactive dwarfs with no gas and which do not show any star formation. In reality dwarf galaxies show a continuous distribution over these types. When comparing dwarf and giant galaxies, van den Bergh (1977) noted that the fraction of spiral galaxies at $M_V \sim -16$ is similar to the fraction of irregular galaxies, while at $M_V \sim -20$ spirals outnumber irregulars. This suggests that dwarf galaxies differ significantly from giant, massive galaxies.

In the group environment and around massive spiral galaxies the following dwarf galaxy types can be observed.

1.3.1 DWARF ELLIPTICAL GALAXIES

Dwarf elliptical galaxies (dE) are one of the most common galaxy type in the local universe (Binggeli et al. 1988), especially in cluster environments like the Virgo cluster (e.g. Lisker et al. 2008). Also around massive spirals like the close-by M31 it is not uncommon to find dEs (e.g. NGC 147, NGC 185, NGC 205). These elliptical systems have a luminosity range of $-17 \lesssim M_V \lesssim -14$ mag and can show a central nucleus.

1.3.2 DWARF SPHEROIDAL GALAXIES

Diffuse and low surface brightness systems are called dwarf spheroidal galaxies (dSph), they are fainter versions of dEs (Sparke & Gallagher 2007). They do not show any recent star formation and are the faintest systems among dwarf galaxies. By definition dSphs are fainter than $M_V \gtrsim -14$. They are usually found close to massive galaxies and show typical properties like surface brightnesses $\mu_V \gtrsim 22$ mag arcsec^{-2}, masses of about $10^7 M_\odot$ and have no substantial rotation (Grebel 2001).

1.3.3 DWARF IRREGULAR GALAXIES

Dwarf irregular galaxies (dIrr) appear very unstructured and optically irregular. DIrrs are very gas rich and show a clumpy distribution of their HI, which can be more extended than their older stellar component; together with surface brightnesses of $\mu_V \gtrsim 23$ mag arcsec^{-2}, total masses of $\sim 10^{10} M_\odot$ and M$_{HI} \lesssim 10^9 M_\odot$ these are the typical properties of this galaxy type (Grebel 2001). These metal poor system are characterized by a discontinuous star formation history with short bursts rather than constant star formation (Tolstoy 2000). Rotation can be tendentially found in the more massive systems. The different dwarf galaxy types cannot be distinguished clearly, rather there is a continuum between the different types. van Zee et al. (2004) for instance suggest that rotationally supported dEs could be stripped dIrrs while they are falling into the Virgo cluster. The most well known dIrr galaxy is the Small Magellanic Cloud, which is located at a distance of about ~ 60kpc and can be observed by eye on the southern hemisphere.

1.3.4 BLUE COMPACT DWARF GALAXIES

Blue compact dwarf galaxies (BCD) include HII galaxies and can be described as blue and amorphous. Their structure is mostly caused by centrally located gas, stars and starbursts (Grebel 2001). BCDs therefore often show different components, an exponential component in the outskirts with the older stellar population, a plateau at intermediate radii and in the center a Gaussian component, the origin of the last two components is caused by the ongoing starburst (Papaderos et al. 1996). Papaderos et al. (1996) also report that color profiles get redder with increasing radius.

Typical properties of BCDs are total masses M=10^8 – 10^{10} M$_\odot$, M$_{HI} \leq 10^9 M_\odot$, colors (B-R)=0.7 mag, an absolute B-band magnitude M$_B$ =-16.1 mag. Usually an evolved stellar population is needed to describe their observed properties (only the most metal-poor BCDs can be explained by only a young star burst) (Gil de Paz et al. 2003).

1.3.5 ULTRA COMPACT DWARF GALAXIES

Ultra compact dwarf galaxies (UCD) are the smallest dwarf galaxies which are observed, their luminosities range from M$_B$ ~ -10 to -14 mag and their structure is similar to globular clusters. This relatively new type was first observed in the Fornax cluster; Drinkwater et al. (2004) suggested that UCDs are stripped nucleated dEs with B-R colors ranging from 0.4 to 1.6 mag. BCDs are usually observed in galaxy clusters. As we have no spectroscopic data nor enough resolution, this type was not studied in our survey.

1.3.6 TIDAL DWARF GALAXIES

Merging galaxies also show an additional type of dwarf galaxies, which are tidal dwarf galaxies (TDG) and are usually formed in tidal tails. The formation process of this galaxy type can be studied in numerical simulations, a local collapse of gas in a tidal tail can trigger the formation of new stars; this way a tidal dwarf galaxy is formed (Wetzstein et al. 2007). Observations of interacting systems show several candidates for this galaxy type (e.g. Duc et al. 2000; Hibbard et al. 2001; Weilbacher et al. 2000; Makarova et al. 2002). Because they are not associated with dark matter, TDGs are expected to be unstable systems due to their dissolution into the parent galaxy.

1.4 TIDAL DEBRIS

Tidal debris of galaxies includes a huge variety of different features which can be observed; shells, plumes, bridges and tidal tails to very prominent streams ranging far beyond the galactic halo. The origin and the processes which form such structures are still a matter of debate. NGC 5907 and its faint tidal features are often used as prime example for minor mergers (Martínez-Delgado et al. 2008), with typical mass ratios less than 1:3. On the contrary numerical simulations show that these features can also be produced by major mergers; for NGC 5907 a 3:1 merger is needed in order to explain the shape of its tidal debris (Wang et al. 2012). This controversy is also supported by the fact that the nucleus of the accreted satellite is often missed from the observations. During a major merger the two galactic nuclei are expected to sink quickly to the center of the merger, whereas in a minor merger the nucleus of the accreted satellite should follow the orbit of the rest of the satellite, and thus be visible in the tidal debris in the early phases of the merger. A key tool in order to distinguish between major and minor mergers is the star formation rate of the merging galaxies, as during a major merger the star formation is by a factor of two more efficient than in minor mergers or in non-interacting galaxies (Lambas et al. 2012).

Close galaxy pairs can be used to study the merger rate of galaxies, e.g. Xu et al. (2004) find that 2% of all galaxies are in the phase of a major merger. Interestingly the rate of major mergers is strongly redshift dependent – $\sim (1+z)^2$ – whereas the minor merger rate is not a strong function of redshift with a merger rate 3 times higher at $z \sim 0.7$ (Lotz et al. 2011) than the major merger rate.

Tidal tails in gas rich mergers can show recent star formation in the form of young star clusters. Around the NGC 2782 merger system these clusters show a blue color range (Knierman et al. 2013). Wehner et al. (2006) also found blue colors for the tidal debris structures around NGC 3310.

1.4.1 TIDAL STREAMS

A special feature of tidal debris are the tidal streams, which show thin and confined trail of a disrupted satellite. Ultra-faint imaging of nearby galaxies revealed many faint streams in the outskirts of galaxies (e.g. Schweizer & Seitzer 1988; Malin & Hadley 1999; Martínez-Delgado et al. 2010; Mouhcine et al. 2010, 2011; Mouhcine & Ibata 2009) and also on larger scales these are observed for instance around the interacting M81 group (e.g., Yun et al. 1994; Makarova et al. 2002).

These faint structures are often used as tracers of accretion events for the hierarchical galaxy formation model. Features like the Monoceros tidal stream which is close to the galactic plane of the MW disk or similar structures around M31 suggest that minor mergers are influencing the formation of spiral discs at large radii (Martínez-Delgado et al. 2009).

Tidal streams are very difficult to observe as they are faint and dissolve rapidly after the onset of the accretion. Numerical simulations of the accretion process demonstrate that after 1 gigayear the dissolution of the faint features causes the surface brightness of these objects to decrease by about two magnitudes (Johnston et al. 2001). Thus these features are only observable with ultra deep imaging, Mouhcine et al. (2010) demonstrate that observed streams can also be resolved into single stars with $i \approx 26.8 - 27.0$ mag.

2

SURVEY

The main part of this thesis consists of the survey which will be introduced in this chapter. The motivation of the survey and the properties of the selected targets will be illustrated and the used facilities will be introduced in the next sections.

2.1 GIANT GALAXIES, DWARFS AND DEBRIS SURVEY (GGADDS)

The thesis concentrates on galaxy groups in the nearby universe within a distance range of $\sim$ 8 to $\sim$ 35 Mpc. The main goal is to detect dwarf galaxy candidates and possible tidal features in order to constrain their properties as a function of the environment, and to explore whether links exist between these two aspects of the surroundings of giant galaxies. We currently use deep imaging with small to medium-size optical telescopes (0.9 m to 4 m-class) to support photometric and structural studies, later to be complemented with spectroscopy.

The targets of this survey were selected using the Nearby Galaxies Catalog (NGB, Tully & Fisher 1988). In order to detect faint substructure of galaxies only galaxies with a high inclination angle were selected, otherwise the distinction between spiral arms and tidal debris could have caused problems.

The selected dominant group galaxies have an absolute magnitude range from $M_B = -19$ to -23 mag and are located in environments with densities varying from 0.08 to 1.6 galaxies Mpc^{-3}.

The distance range of the targets is motivated by the choice of telescopes: at 10 – 35 Mpc, the instrument field of view of commonly used wide-field imagers ($\sim 36' \times 36'$ to $59' \times 59'$) covers an area of typically (175×175) kpc^2 to (611×611) kpc^2, while the instrument sensitivity allows us to reach a limiting surface brightness of 27 mag arcsec^{-2} in the g-band as well as in the B-band. For comparison, numerical simulations by Johnston et al. (2008) show that tidal streams due to accretion events should be detectable at this surface brightness for minor mergers that occurred in the last Gyr. Minor mergers have baryonic mass ratios $\leq 1:4$ for $M_{satellite}/M_{primary}$ (Lotz et al. 2011).

The limit in observational depth guarantees that most of the candidate dwarf galaxies (CDG) that are comparable in luminosity to the bright Local Group (LG) dwarf galaxies should be detected by the observations. The available field of view implies that only close-by companions can be detected and the resolution of the instrument sets a size limit on the capability of resolving small dwarf galaxies. In conclusion, the comparatively low available resolution is responsible for only the most extended dwarf companions to be identified as CDG.

2.2 USED TELESCOPES AND DETECTORS

We used three different telescopes for the GGADDS survey. In the northern hemisphere the WIYN 0.9m (the WIYN consortium consists of the University of Wisconsin, Indiana University, Yale University, and the National Optical Astronomy Observatory – NOAO) and the Mayall 4m telescope at Kitt Peak National Observatory (KPNO) were available for data acquisition. In the southern hemisphere we complemented the survey with the 2.2m telescope on La Silla, which is operated by the European Southern Observatory (ESO).

The survey consists of 6 observation runs. It was started with two runs at the 0.9 m telescope at KPNO in order to test the feasibility of the project. In a total number of 11 nights 12 galaxies were imaged. The first run was from October 14th to 19th 2009, the second from March 8th to 12th 2010. The 4m Mayall telescope at KPNO was used from December 9th to 12th 2010. In 4 nights 8 galaxies were studied.

The project was granted observing time at La Silla 3 times. The ESO/MPG 2.2 m telescope in combination with WFI was used from November 6th to 10th 2010, from September 25th to 30th 2011 and from May 14th to 17th 2012. During 15 nights around 27 galaxies were imaged (25 galaxies were matched by the full observing schedule).

The Mosaic[1] camera (on the WIYN 0.9m and Mayall 4m) offers SDSS filters[2]. The *g*- and *r*-band filters were selected as the sensitivity of the detector peaks at the central wavelength of these filters[3]. The same reason motivated the filter selection for the observing runs with Wide Field Imager (WFI): The B and R band filters provide the best sensitivity[4]. As the main aim of the survey was the detection of faint substructures of galaxies, the choice of filters was driven only by the instrument sensitivity. The available luminance filters were not considered for the following reasons. Reflections are problematic for wide-field image cameras (WFIC). But as reflections depend on wavelength, and since the telescope construction materials have different light reflecting properties, the selection of suitable wavelength ranges was one way to distinguish real from artificial features. Some observations confirm that reflections are much more pronounced in the SDSS g-band and in the B-band, therefore the criteria of wavelength depend reflections worked out for several targets. In order to study the stellar populations and the nature of faint tidal debris one color is the minimum information required. A second color would have been extremely helpful for this as well, but long integration times of about 1.5 hour per target and filter and the low sensitivity in the other available filters would have resulted in an inefficient use of telescope time.

2.3 OVERVIEW OF THE SELECTED TARGETS

The most critical step in statistical studies is the sample selection. In order to study the abundance of faint tidal debris and the luminosity function of spiral galaxies at the faint end several criteria were the basis of the selection process, concentrating on the properties of the nearby universe. Unfortunately it is nearly impossible to avoid selection biases with the small number of studied targets, nevertheless it was ensured that the observed 44 galaxies cover a range in environmental density, distance and morphology. The properties of the sample will be described in the following list:

---

[1] Basic information about the instrument can be found via http://www.noao.edu/kpno/mosaic/

[2] These filters are similar to the ones used by the Sloan Digital Sky Survey (SDSS), the advantage of these filters is that the SDSS can be used for the photometric calibration later on.

[3] In the manual of Mosaic the quantum efficiency of the CCDs was compared to the central wavelength of the filters, more details can be found at http://www.noao.edu/kpno/mosaic/manual/

[4] The response of the detector as a function of the wavelength and the transmission curves of the filters can be found in the instrument manual which is available at http://www.eso.org/sci/facilities/lasilla/instruments/wfi/doc/2P2-MAN-ESO-90100-0001.pdf

1. One aim of the survey is to study the influence of the environment where the galaxies are located. In Fig. 2.1 an overview of the densities of the observed targets is given (all values were taken from Tully & Fisher 1988). The densities are expressed as the average number of galaxies with $B_T \leq -16$ in a 1 Mpc size box. Tully & Fisher (1988) calculated the local density on a three-dimensional grid with 0.5 Mpc spacings and using a Gaussian smoothing function.

   Most of the studied galaxies have local densities ranging from 0.06 to 0.22 galaxies Mpc^{-3}. The reason for this selection in density is that most of the nearby galaxies which were in the observable distance range show these densities and mostly only in direction to the Virgo cluster higher densities can be observed. Limited observing time during the observability of the targets at an environment with a high density also limited the number substantially.

2. The distance range was given by the field of view and the resolution. Most of the studied galaxies are located at about 20 Mpc, ensuring a field of view (at 20 Mpc about 200 kpc) where still most of the expected dwarf galaxies around spirals should be found and a reasonable angular resolution to resolve dwarf companions is available.

3. In order to study the role of dwarf galaxies in the evolution of galaxies, late-type galaxies of different types were selected. Elliptical galaxies were mostly excluded as they would need to be studied in a different aspect.

4. We favored galaxies with hints of tidal debris and possible CDG. These were chosen in order to test the feasibility of our project, for instance to measure the surface brightness limits and to have targets where our results can be compared to.

It was aimed to take into account all these properties during the selection process, but also the criteria presented in section 2.1 played a key role. We have a strong bias in our target selection, because we selected preferentially visibly interacting galaxies, but still we tried to use targets with as much as varying properties as possible.

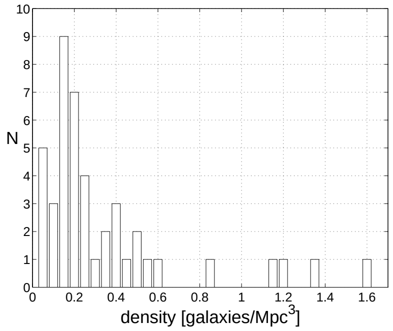

Figure 2.1: The environmental properties of the targets

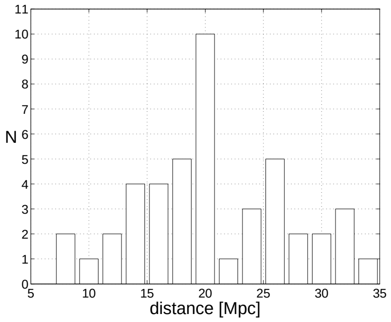

Figure 2.2: The distance range of the observed galaxies

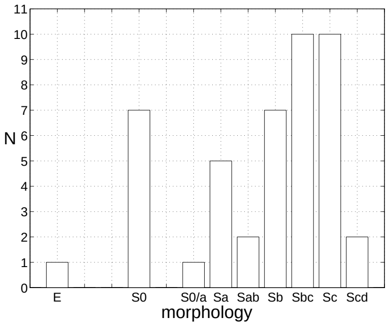

Figure 2.3: Overview of the morphology of the different targets

2.3.1 SKY COVERAGE

The local volume with a radius of 50 Mpc contains around 2300 galaxies with a luminosity brighter than $B_T \lesssim -16$. Figure 2.4 shows a projection of the galaxies in the nearby universe taken from Tully & Fisher (1988). In order to highlight how the selected targets are distributed, we plot these as red dots. It can be seen that all targets are very well distributed over the whole sky, except for areas of high foreground extinction in the Galactic disk, this way it was aimed to exclude any observational bias. As this survey is concentrating on galaxies in groups, high density environments like the Virgo cluster were not studied.

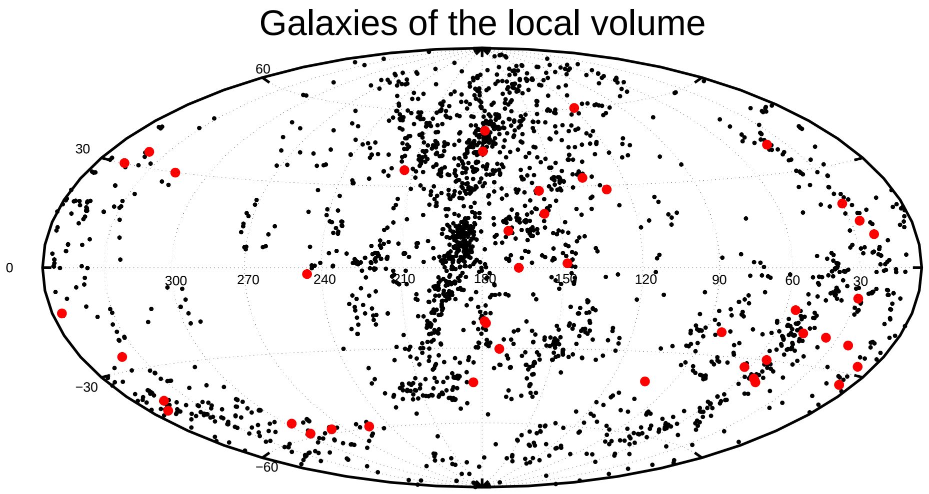

Figure 2.4: An overview of all galaxies in the nearby universe that are more luminous than $B_T \lesssim -16$ (black dots). The observed targets were plotted as red dots.

3

REDUCTION OF WIDE-FIELD MULTI-CCD DATA

In modern astronomical imaging techniques detectors often consist of multiple CCDs. The reduction of the raw data needs many different steps, which we will describe in the following sectors. Three different instruments were used: MOSAIC 1.0 and 1.1 on the WIYN 0.9m telescope, MOSAIC 1.1 on the Mayall 4m telescope (both telescopes are located at KPNO) and WFI on the 2.2m telescope at the ESO La Silla. In total we collected about 1 TB of raw data, which needed to be processed.

The properties of the different detectors and the different steps of the data reduction will be explained in this chapter. For basic reductions we used IRAF[1]. In order to understand the necessary reduction steps the manual of the NOAO Deep Wide-Field Survey MOSAIC Data Reductions[2] was followed and modified the default parameters in the recommended routines in order to improve the final reduced images.

In the following the properties of the used detectors will be described together with a detailed explanation of all necessary reduction steps.

3.1 MULTI-CCD IMAGERS

For technical reasons the sizes of single CCDs are still limited. The main criterion is that these detectors must be very homogeneous up to a certain value, in order to optimize the calibration of the data. In favor of covering a larger region of the focal plane, and thus to increase the field of view of the instrument a modern imaging detector consists of several CCDs. The MOSAIC and WFI cameras have a total number of 8 CCDs (see Figure 3.1). Each CCD consists of 2048 × 4096 pixels. In total we get a 8192 × 8192 pixel detector and mosaiced images with a total size of 67.1 Megapixels.

This type of imager thus increases the field of view covered by the observations ranging from 34' × 33' (WFI on the 2.2m) to 59' × 59' (MOSAIC on the WIYN 0.9m). In Table 3.1 the most important data of the used detectors are listed.

In order to make an effective use of telescope time the read-out time is an important factor. The old-style MOSAIC 1.0 detector take 2.5 minutes for each read-out, which increased the resulting overheads between the observations. Modern detectors like MOSAIC 1.1 and WFI have improved electronic devices and the resulting read-out times are as short as 40 seconds.

---

[1] IRAF is distributed by the National Optical Astronomy Observatory, which is operated by the Association of Universities for Research in Astronomy, Inc., under cooperative agreement with the National Science Foundation.

[2] The manual can be found at http://www.noao.edu/noao/noaodeep/ReductionOpt/frames.html

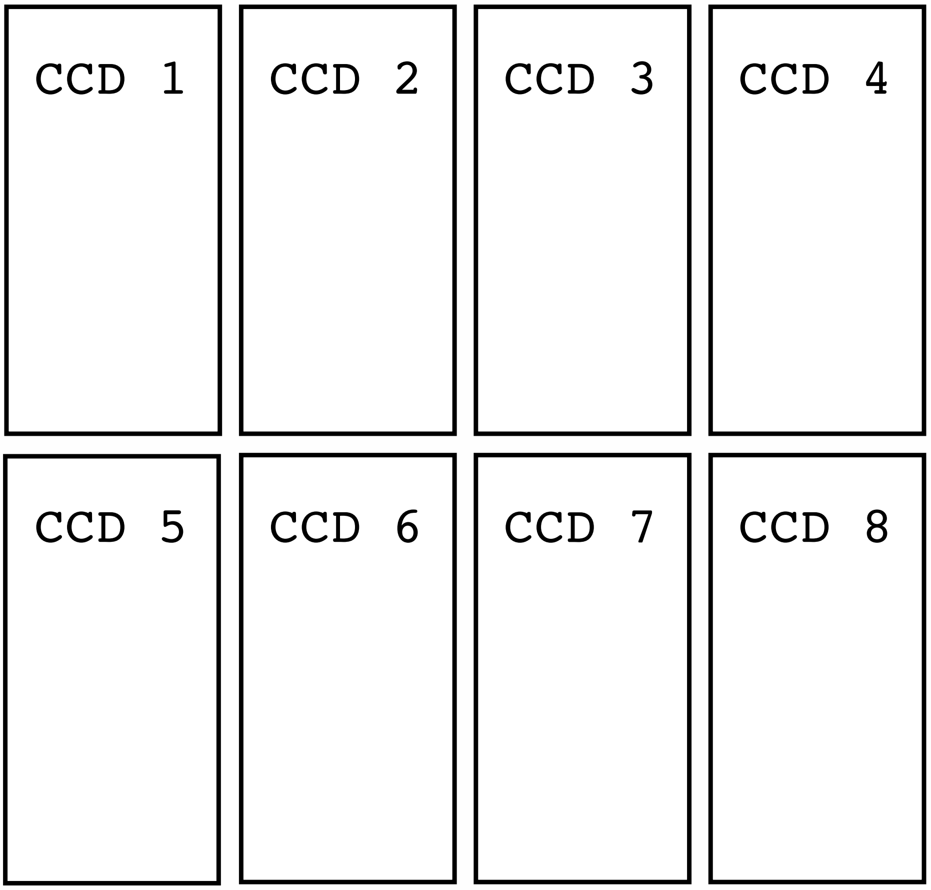

Figure 3.1: The structure of the used Multi-CCD imagers. The CCD names are just examples. Each CCD has a size of 2048 × 4096 pixel with a pixel size of 15 μm. The gap sizes between CCDs amounts to 80 pixels (Mosaic 1.1, similar for the other detectors).

The use of multiple CCDs brings also side-effects, which have to be taken into account. These include:

1. The construction of a multiple CCD imager does not allow to align the CCDs with a gap-less design, therefore we will always have gaps of a few mm between each CCD. The first drawback is that for gap-free observations a minimum of 5 dithering pointings are necessary. Furthermore also the data reduction includes many more steps, as in the final image the gaps have to be removed.

2. The gaps between the CCDs can cause reflections onto the detection area, which is problematic for ultra faint imaging.

3. The optical design of telescopes causes that only at the center the maximum amount of light reaches the detector. Moving from the center to the edges, not all light rays are reflected onto the detection area, as the convolution of the mirrors is preventing that all light rays from the outer regions are falling onto it.

4. Nearby bright stars can cause problems like reflections, therefore only observations are recommended where no bright stars are inside or close to the covering field of view.

5. The use of eight CCDs with a final image size of 67 Megapixel produces very large files. Every single calibration and science image is about 256 Mb. In total we collected about 1TB for all runs. The processing of such data amounts is time intensive and needs modern computer hardware.

Table 3.1: Properties of the used Detectors

Name	Field of view	Pixel scale
MOSAIC 1.0/1.1 - 4m	36’ × 36’	0.26”/pixel
MOSAIC 1.0/1.1 - 0.9m	59’ × 59’	0.43”/pixel
WFI on 2.2m	34’ × 33’	0.238”/pixel

6. The calibration of multi-CCD detectors is one of the most critical steps in the reduction. Every CCD has its own properties, both in terms of sensitivity as well as in efficiency. Apart from that also pixel defects can vary from single pixels to larger areas of several rows, which causes further necessary corrections.

There are important advantages when using multi-CCD detectors, which make it worth to use these types of detector:

1. The biggest advantage is that the field of view observable with a single exposure can be extended by a large factor. This enables a completely different class of observations.

2. The size of the detector allows one to use a bigger area of the optical plane of telescopes. Therefore astronomers can use the potential of modern telescopes much better.

3. The telescopes can be used much more efficiently, as for wide-field observations much less observational time is needed. Especially aspects like the seeing and transparency conditions remain much more similar when data are acquired. In particular for extremely deep imaging the calibration and the flatness of the images is improved.

Besides the numerous disadvantages of these detectors the improved observational conditions when using multi-CCD imagers make it worthwhile to find a workaround for the problems caused by the instantaneous use of different CCDs at a given time. In the following sections we describe our reduction techniques and the methods we used to correct for the problems which have been discussed so far.

3.2 GAIN AND READ-OUT NOISE

The gain translates (for more details see Howell 2006) the amount of charge that was collected in each pixel to an Analog-to-Digital Unit (ADU). For the WFI we used the gain values given in the WFI manual. They scatter around 2 (e^-/ADU) depending on the different CCDs. The corresponding gain values for the MOSAIC imagers are already stored in the image headers and are initially taken from the IRAF database `msdb`.

During the read-out process of the device an additional electronic noise is added to the signal in every pixel – the so called read-out noise. The conversion from electrons to ADUs is responsible for this type of noise and during the readout process spurious electrons will be added to the original signal. The exposure time does not influence this noise source and therefore it is possible to study this effect with bias frames.

3.3 BIAS

The effects of the electronic read out process of CCDs can be investigated with bias frames. The detector characteristics are analyzed to measure the noise of each single pixel. This noise is varying from pixel to pixel, so the aim is to study the influence of the electronics on the imaging data.

In order to correct for the proposed pixel variations the detector is read out without opening the shutter of the camera (i.e., no light falls onto the detector) and with an exposure time of zero seconds (hereafter, zero frame). Usually 10 zero frames are taken for each night, which were later on combined

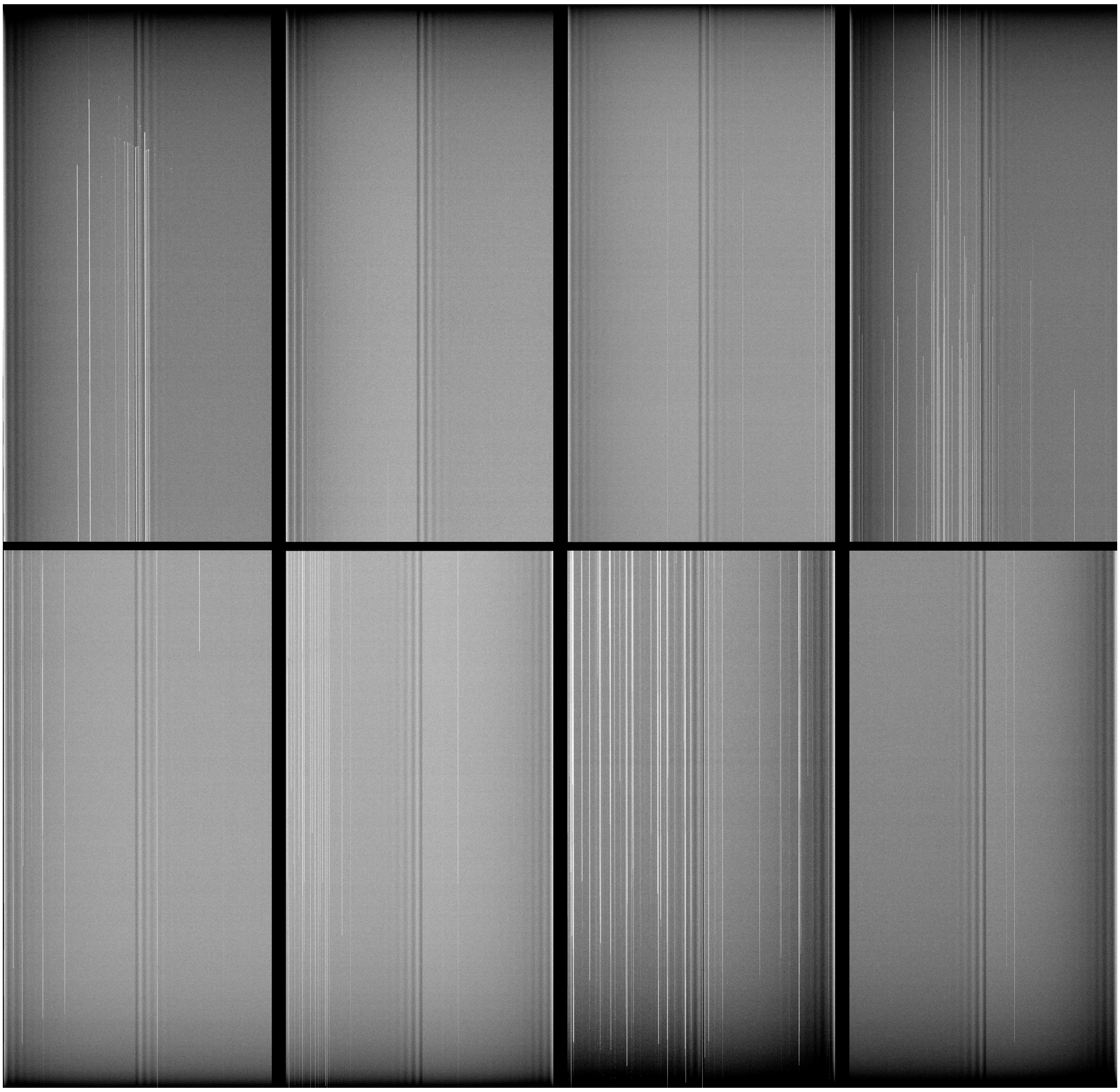

Figure 3.2: One of the master zero frames which was processed out of 10 single zero frames.

by using a median function into a master zero frame. An example can be seen in Figure 3.2. This master bias frame shows the noise produced by the read out process (and bad columns), the master bias frame is subtracted from all calibration and science images.

3.4 FLAT-FIELD CORRECTIONS

When an extended target perfectly uniform in brightness illuminates a CCD across its full area (this is the definition of a “flat-field”), the output of the image detector will not be flat and show variations due to different reasons like quantum efficiency variations, dust on the optics or vignetting (McLean 2008).

These properties are also changing with the used filter system, so for every used filter an individual correction is necessary. It is usually recommended that at least about 10 flat-field frames are used and then combined to study this effect (Martinez & Klotz 1998). The flat-field correction is necessary for several reasons that will be explained in the following.

Every pixel on the CCD has its own characteristics and therefore pixel-to-pixel variations in sensitivity are visible, which are caused mainly by different quantum efficiencies. Responsible for these differences is the production of the CCD itself as well as microscopic dust particles which are located on the optical elements or directly on the CCD. This is causing then optical attenuation (see McLean 2008, for more details).

In order to produce master flats we corrected each flat-field image for bias, before combining them to a master flat these needed to be normalized to the same mean value. In the next step these were median combined to a master flat and normalized to have a mean value of one. Finally the science frames are divided by the master flat for the correction for pixel-to-pixel sensitivity variations. In the following the used flat-fielding techniques are described and the differences between each method are explained.

3.4.1 DOME-FLAT

The first correction for the previously discussed effects can be done during daytime.

A white screen, which is usually illuminated by several halogen lamps is used for the acquisition of dome-flats. Small scale variations are best corrected this way, as the signal is strong (high S/N) and can be reproduced as many times as desired. As the illumination of the white screen is not completely homogeneous, it is recommended to use different other techniques like twilight- or super-flats (which will be explained in the next sections) in order to correct for these effects.

Usually five to ten dome-flats were taken per night for every filter. After correction for the bias we combined them into a master dome-flat using the median of all images and normalized the master dome-flat by its median value. An example can be seen in Figure 3.3. In this image one can recognize very easily the vignetting by the telescope which causes less illumination at the edges of the detector as well as some pixel defects like bad columns and dust grains which are on the filters or on the CCD entrance window.

3.4.2 TWILIGHT-FLAT

In order to have a more homogeneous surface the so-called twilight-flats can be used. These are taken during twilight with the telescope pointing to a clear sky at regions without bright stars and near zenith. Due to the fact that the twilight is very uniform with respect to brightness fluctuations these flats can be used to correct for pixel-to-pixel sensitivity variations when light enters the telescope in the same way as during a science acquisition.

The production of usable twilight-flats is more difficult than for dome-flats, as the sky brightness is changing rapidly in time. In order to ensure that the count levels are in the linear regime of the CCD the integration time needs to be changed for every single calibration file. At KPNO the exposure time of the twilight-flats has to be adjusted always by the observer, therefore count levels were not stable and we had to find our own model to keep the counts in a constant range. However, at La Silla ESO provides an automatic tool for the calculation of the integration time in order to get always similar count statistics. Once calibrated with one observation, the system gives the integration time for a given observing time and for each filter, scaled to the desired count level.

Usually the calibration plan contained four to five twilight flats for each filter, avoiding to point the telescope towards regions with bright stars, as these start to be visible at the end of the twilight.

The twilight flats were corrected for bias and master dome-flat. These were later on normalized by their median value in order to derive a master twilight flat.

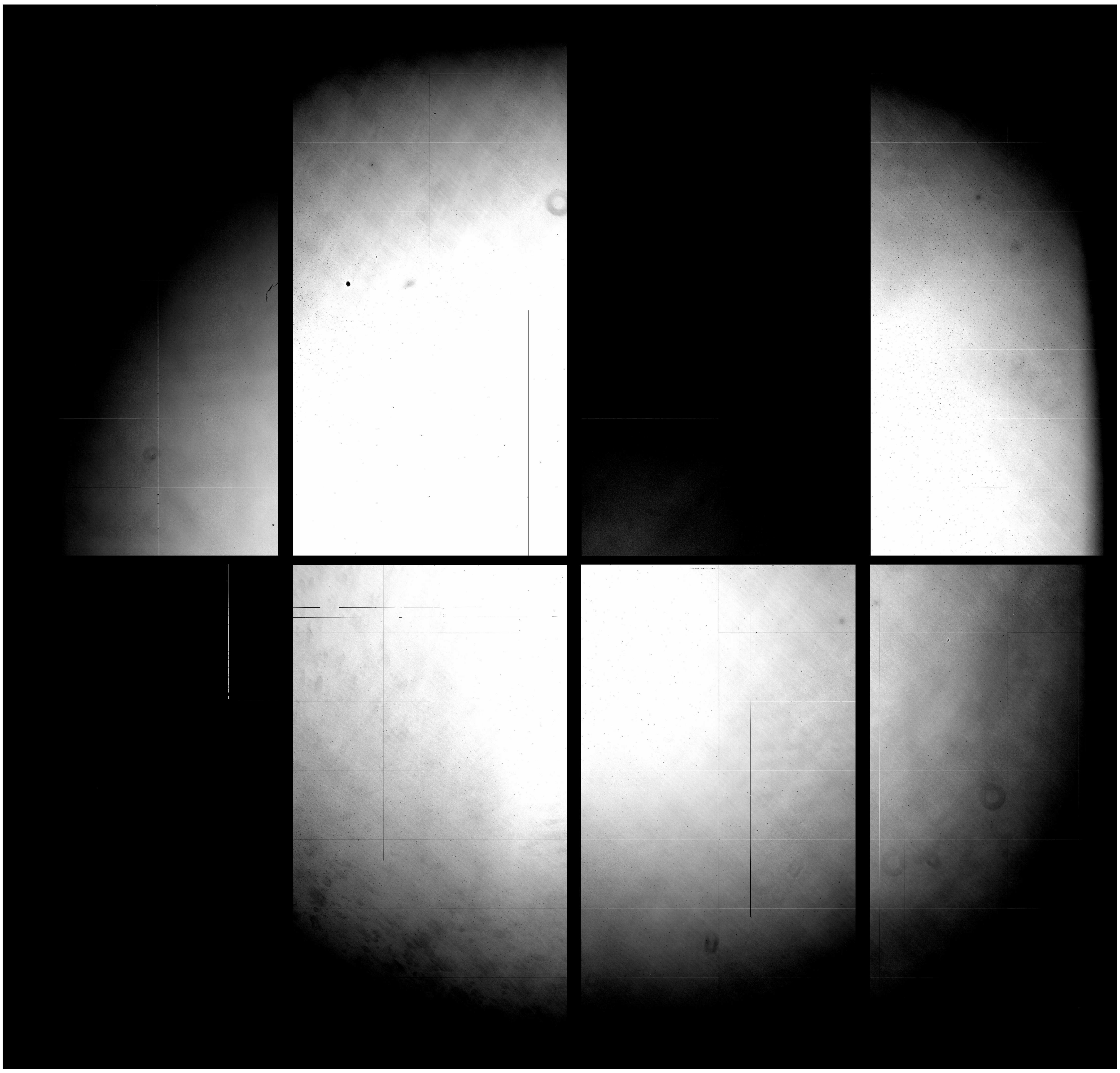

Figure 3.3: One of the master dome-flat frames which was processed out of 10 single dome-flat images in the B-band.

3.4.3 SUPER-FLAT - ULTIMATE STUDY OF THE CCD UNIFORMITY

The best way to correct for the flat-field, which we have described before, is the so called super-flat which is built from the science images themselves. At first it is necessary to mask the objects in the images, the IRAF tool `objmasks` can be used for masking stars and galaxies in the science frames. Afterwards a sky subtraction is performed on every image. Finally all the images that were observed with a particular filter are combined by using the median of the corresponding images. One example can be seen in Figure 3.4. For the other used filters a super-flat frame is produced in the same way.

Before a super-flat is used in order to flatten the science images it must be corrected for the dome-flat as well. Two different kind of variations are reduced this way. Firstly, small scale variations are removed by the dome flat, as there are large signal to noise values for this kind of flat. But the illumination of the imaged screen is not perfect. The lamps often do not illuminate the screen homogeneously and the screen itself is not uniform, therefore the produced flat correction is not perfect and large scale variations

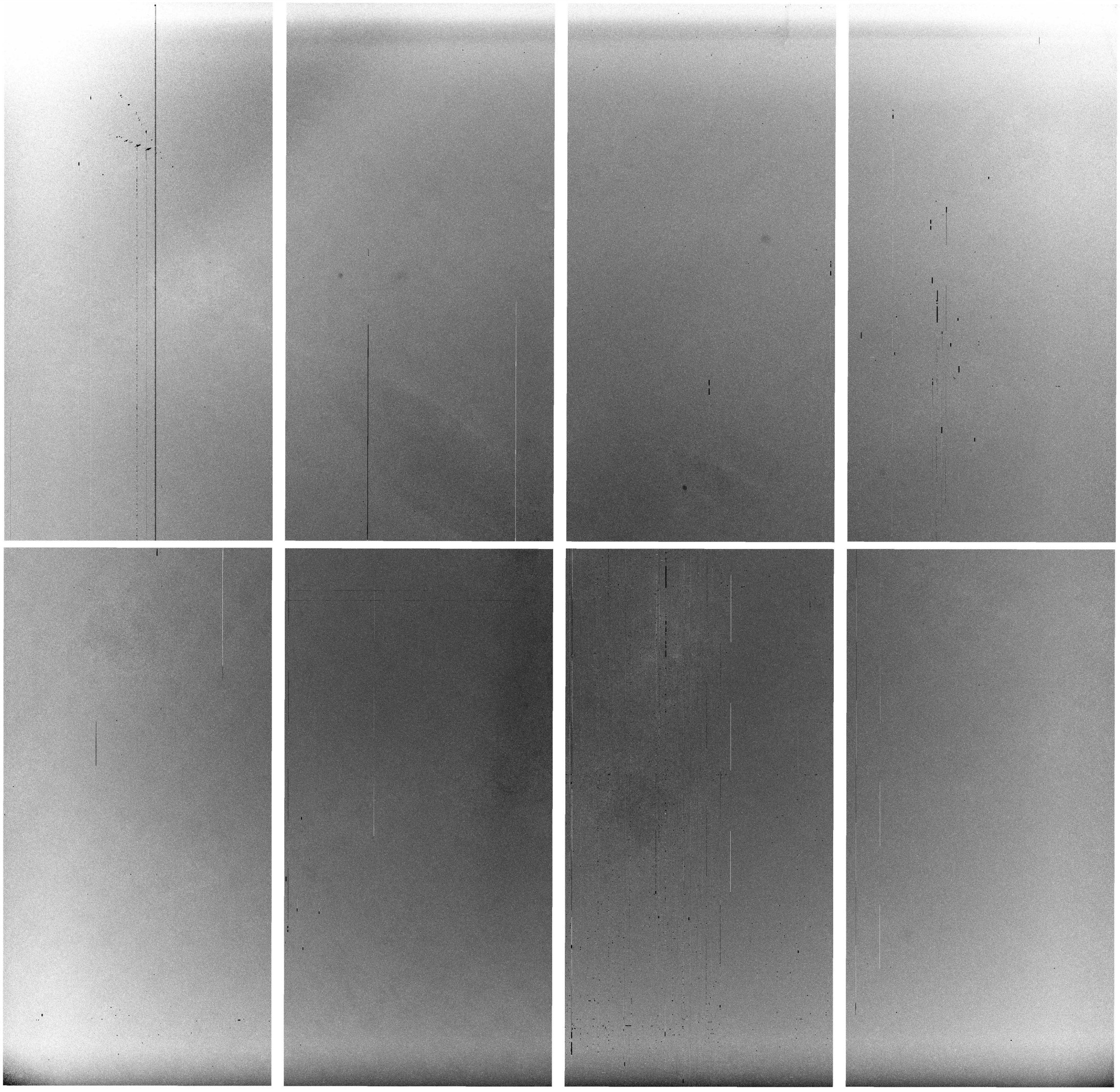

Figure 3.4: One of the used super-flat frames which was processed out of all science images in one filter band (here B-band).

are still visible. In combination with the dome-flat which removes the small scale variations therefore secondly the super-flat removes the large scale variations due to how light from an infinite distance enters the telescope (Chromey 2010).

The great advantage of the super-flat is that it is derived directly from the actual night sky. The dark sky is the best known flat-field image. Across limited areas on the sky which are comparable to the size of the detector the variations in sky brightness are extremely small. The only difficulty is to successfully remove the objects in the images. If this is done carefully one obtains a very useful correction for the large scale variations of the detector.

3.4.4 COMPARISON OF DOME, TWILIGHT AND SUPER-FLAT CORRECTIONS

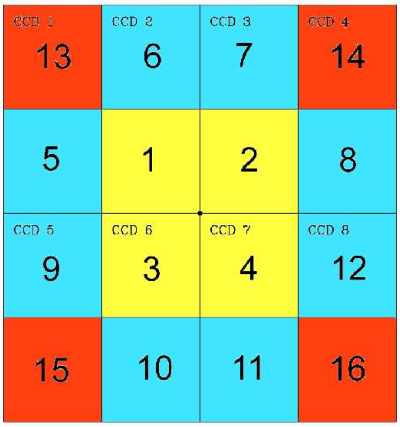

CCD 1 13	CCD 2 6	CCD 3 7	CCD 4 14
5	1	2	8
CCD 5 9	CCD 6 3	CCD 7 4	CCD 8 12
15	10	11	16

Figure 3.5: Overview of the used areas, the inner parts are labeled in yellow, blue shows the outer parts and red marks the corner areas.

flatfield technique	inner	outer	corner parts
dome-flat	0.0232	0.067	0.081
dome-flat & twilight-flat	0.0194	0.018	0.024
dome-flat & super-flat	0.0082	0.015	0.020

The average flat-field variation values of the background (calculated with equation 3.1) of all images of one target in SDSS r-band filter are listed in this table. They represent the accuracy of the correction for flat-field. The values for the inner, outer and corner parts from different flat-fielding techniques are compared to each other.

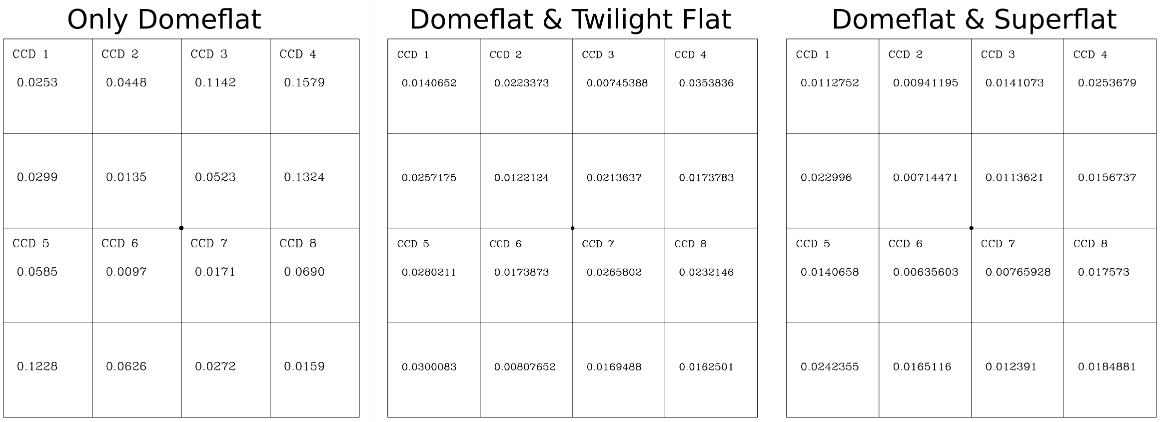

Only Domeflat

CCD 1 0.0253	CCD 2 0.0448	CCD 3 0.1142	CCD 4 0.1579
0.0299	0.0135	0.0523	0.1324
CCD 5 0.0585	CCD 6 0.0097	CCD 7 0.0171	CCD 8 0.0690
0.1228	0.0626	0.0272	0.0159

Domeflat & Twilight Flat

CCD 1 0.0140652	CCD 2 0.0223373	CCD 3 0.00745388	CCD 4 0.0353836
0.0257175	0.0122124	0.0213637	0.0173783
CCD 5 0.0280211	CCD 6 0.0173873	CCD 7 0.0265802	CCD 8 0.0232146
0.0300083	0.00807652	0.0169488	0.0162501

Domeflat & Superflat

CCD 1 0.0112752	CCD 2 0.00941195	CCD 3 0.0141073	CCD 4 0.0253679
0.022996	0.00714471	0.0113621	0.0156737
CCD 5 0.0140658	CCD 6 0.00635603	CCD 7 0.00765928	CCD 8 0.017573
0.0242355	0.0165116	0.012391	0.0184881

Figure 3.6: Comparison of the flat-field accuracy (see equation 3.1) in the different regions of the detector, on the left hand side the results can be seen when the science frame was corrected by only the dome-flat, in the middle the dome-flat was used in combination with the twilight-flat, and on the right hand side the dome-flat was applied together with the super flat.

For one observed target a flat-field test was performed. For testing the flat field properties the complete mosaic image of one science frame, which consists of 8 single CCD images, was divided into 16 areas, as it can be seen in Figure 3.5.

Parts 1 to 4 are the inner parts, 5 to 12 the outer parts and 14 to 16 the corner parts. For calculating the flat-field error, the mode of the whole image (i.e. background) is calculated and is therefore referred to as the global mode. Then the local mode is calculated for each individual CCD sub-area and afterwards the flat-field error is calculated via:

$$flat-field\ accuracy\ =\ (global\ mode\ -\ local\ mode)\ /\ global\ mode \tag{3.1}$$

Assuming that the intrinsic background is homogeneous and uniform across all images, its variations are thus due to a non perfect correction for flat-field. The flat-field accuracy was computed on the same observed science frame corrected with the different master flat-fields described above. The results can be seen in Figure 3.6.

The results show clearly that the correction for dome-flat and the super-flat is the best option as it provides the best accuracy. For the central parts the flat-field accuracy decreases from 2.32% when only the dome-flat was used to 1.94% when a twilight-flat is used as well. Finally the super flat reaches an accuracy of 0.82%, thus improving the flatness of the images by a factor of 3. Due to these results for every night super-flats were produced.

Therefore, during the observations, the main and extended galaxy was always placed on a different CCD in each exposure in order to later construct a usable super-flat. If it was not possible to create a satisfying super-flat for one of the nights, because not enough science frames were observed, the super-flat of the night before was used in the data reduction.

3.5 HEADER EDITING

The header contains all informations regarding the image like the date, the exposure time, the used filter, the observational conditions like temperature, the reduction steps which are added later on and so on. The header is stored separately from the pixel values as a text file. In each multi image file (MEF) every CCD image has its own header. The header information is very helpful during the data reduction process, as keywords like the used filter or the gain as well as the saturation limit enable scripts to go through the data without further input from outside.

When using data from the MOSAIC camera IRAF is able to read out the stored keywords instantaneously. Unfortunately it is not that easy for the WFI data, as the ESO HIERARCH structure cannot be read by IRAF. The IRAF esowfi package written by Frank Valdez was used for the translation of the header. The package needed to be updated with new keywords, which have changed in the WFI headers.

Additionally some more header editing was needed. We added the values for the CCD gain and read-out-noise to every sub-header. We also translated the world coordinate system (WCS) keywords from their original sexagesimal format to decimal values using the command `%h\n`.

3.6 BAD PIXEL MASKS

The physical condition of the different CCDs of one detector can be very different and also their lifetime is limited. One will always find defects like hot or cold pixels on CCDs. With time the numbers of pixels which are not working will increase. Pixels that are not working are usually producing long stripes (bad columns), which is due to the line-wise reading out sequence of CCDs. One example can be seen in Fig 3.7. We used bias corrected dome-flats in order to identify bad pixels which we then registered in proper bad-pixel masks (BPM).

The IRAF function imreplace can be used to replace pixel values with a selection criterion. All regular pixels in a flat-field frame will be in a certain range of counts. In this way it is possible to identify hot pixels due to their unusually high counts. All regular pixels will therefore be set to zero in the BPM and the deviant pixels to 1. Later on this mask can be used to extrapolate over the bad pixels using IRAF/fixpix for this correction.

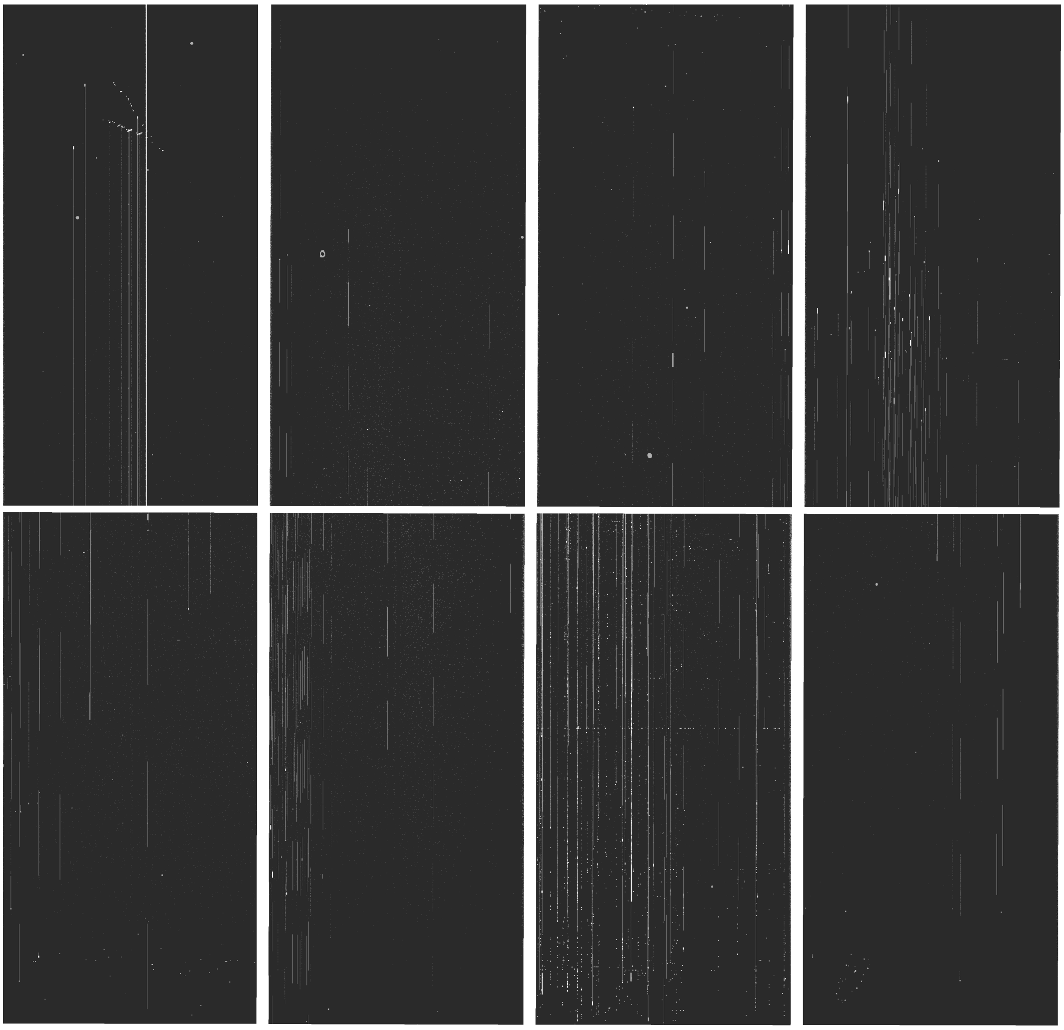

Figure 3.7: The master BPM for one night; a significant number of bad columns and hot pixels can be identified in in every single CCD image as white points or white stripes.

The BPM only removes defects intrinsic to the used CCDs. Additionally, bright sources like stars, galaxies or trails of satellites or meteors can produce bleeding trails on the images. During the reduction process these can be added to the initially created BPM using ccdproc and instruct the routine ccdproc that BPM are produced. For this step it is necessary to define values when bleeding is expected and at which length a bleeding trail is defined. One example of such an BPM can be seen in Figure 3.8. During the reduction process the science images are corrected with these masks as well.

3.7 WCS SOLUTION

The world coordinate system (WCS) of an astronomical image assigns a pair of celestial coordinates (Right Ascension, RA and Declination, DEC) to every pixel. The field of view is quite large for WFIC and given that we performed several ditherings per object, it is necessary to find a WCS solution for every single image in order to combine all individual observations to a final single image. For the further reductions this is one of the most critical steps.

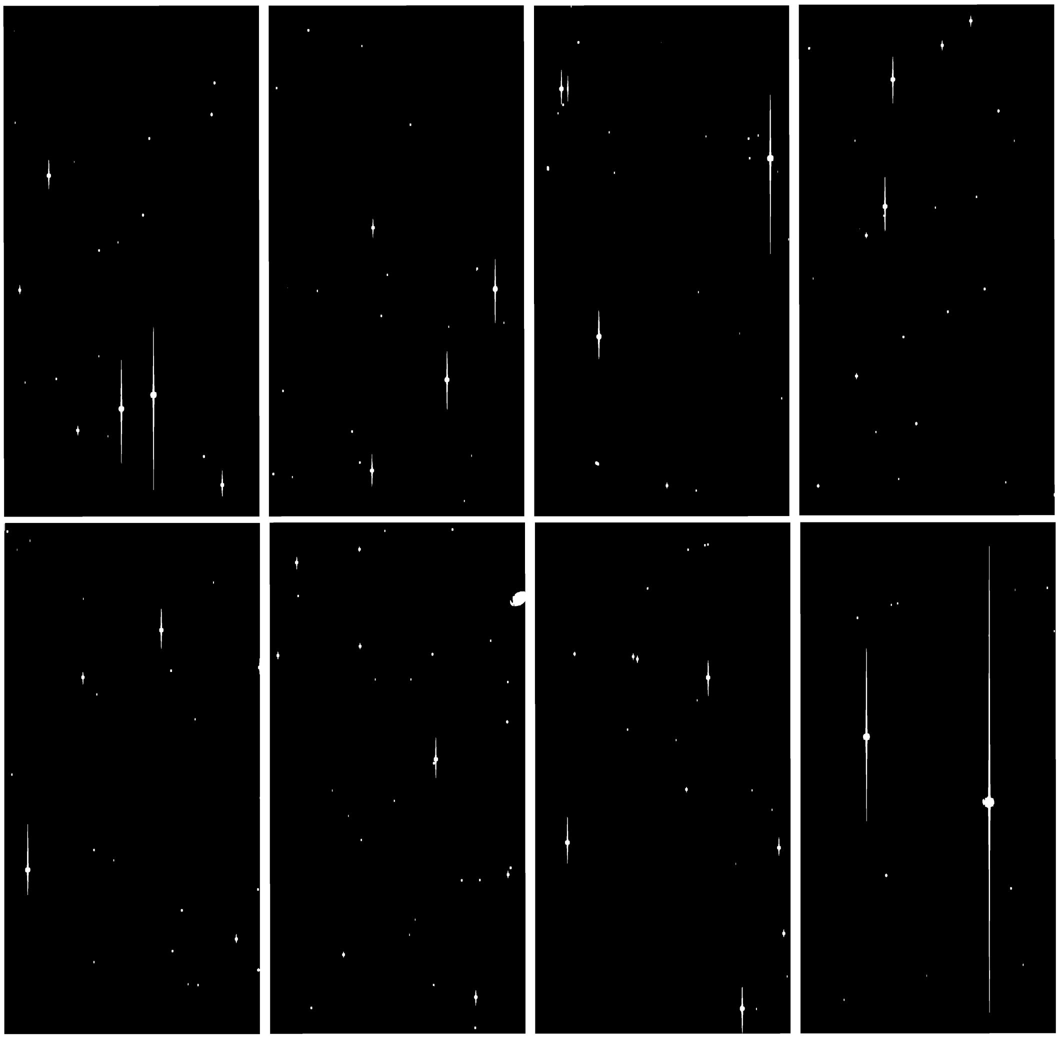

Figure 3.8: A BPM for one science image; bleeding trails and overexposed regions can be seen in every single CCD image.

At first the images are processed with the IRAF tool `mscsetwcs`, which translates the stored coordinate positions (RA/DEC) with a standard solution into a first WCS for the entire mosaic image (containing all different CCDs). The RA and DEC values of the center of the field of view and the pixel scale are stored in the header. Afterwards `msccmatch` can be used to fit a new WCS solution to the entire image. A catalog of stars which are overlapping with the image is needed for a successful fit. The fitting is performed by `geomap`. We measured typical RMS values of about $0.2''$ (0.5 to 0.8 pixel) after a few runs with `msccmatch` in order to increase the accuracy of the fitted WCS solution. Such an accuracy also depends on the used star catalog.

3.7.1 STAR CATALOGS

Numerous star catalogs are available for the creation of a WCS solution for images, which provide accurate astrometric data. The USNO-A2 (Monet D., et al 1998) star catalog is the standard setting when using IRAF. The change to the USNO-B1 catalog (Monet et al. 2003) improved the RMS of the fit of the WCS solution of our images from 0.5 to 0.2″. The routine mscgetcat can be used to download the coordinates of the catalog stars within a specified magnitude and field of view range. The coordinates of the field of view center in each images are taken from the image header.

3.7.2 DEPROJECTING IMAGES

Astronomical imaging maps the celestial sphere onto a flat detector. In order to combine different observations to a final image the individual mosaic images needed to be deprojected onto the same spatial grid. The tool mscimage can be used to deproject images with using a reference center. We set one single CCD which was overlapping with the studied galaxy as reference image. In this way the 8 single CCDs frames can be combined into a mosaic and this is done for each observation of a given galaxy.

3.8 ATMOSPHERIC EXTINCTION

Ground based observations are affected by light having to pass through the atmosphere.

When light is going through the different atmosphere layers, it is absorbed and scattered. Hayes & Latham (1975) state that there are three forms of attenuation: Molecular absorption, Rayleigh scattering by molecules and aerosol scattering. The airmass X during the observation, which depends on the zenith angle z (zenith distance) via $X = sec(z)$, is directly connected to the length of the lightpath through the atmosphere.

The intensity of the light which is falling on our detector, I, is a function $I = I_0 e^{-k^* X}$ of the amount of light coming from the source I_0, the Airmass X and the extinction coefficient k which depends on wavelength. The conversion from intensity to magnitudes m (measured) and m_0 (native signal before the atmosphere), respectively, gives $m = m_0 + kX$. Using the measured counts on the CCD with $m = -2.5 log(counts)$ we obtain

$$counts(m_0) = counts(m) 10^{0.4kX} \rightarrow D_{airmass} = 10^{0.4kX} \tag{3.2}$$

This provides the correction factor $D_{airmass}$ by which the counts were multiplied. Technically the airmass values could be read out from the header with hselect and then automatically processed.

The values for the extinction coefficient were taken from the observatory manuals in correspondence with the central wavelength of the used filter[3]. We note that this procedure assumes that the atmospheric extinction coefficients are constant with time and for instance neglects variations due to differing amounts of aerosols or dust.

The other influencing effect is the blurring of the light sources caused by the atmosphere, which is called seeing. For the used telescopes correction methods like adaptive optics were not available, therefore the removal of this effect was not possible. The typical measured seeing varied from 1.1″ to 1.7″ for KPNO and from 0.7″ to 1.1″ for La Silla. As the observed targets are well extended, the seeing is not a severe problem for the subsequent analysis of the data.

3.9 SKY BACKGROUND

The sky is not completely transparent, as the atmosphere diffuses the incoming light depending on its wavelength, this diffuse light is usually referred to as background. After all the corrections which have been presented above were applied, the background correction was performed. The IRAF tool imstat can

---

[3] For La Silla these can be found at http://www.ls.eso.org/lasilla/Telescopes/2p2/D1p5M/misc/Extinction.html and for KPNO the extinction coefficients are stored in the IRAF directory onedstds in the file kpnoextinct.dat.

be used to measure the statistics of the counts in every image. The median of the entire mosaic image was allocated as the background of the sky. This value was subtracted from every image, but this was only a global correction. The wide field of view which our detectors provided shows that the background is not uniform and homogeneous. Therefore, for a detailed analysis of the observed targets and their substructures also an additional local background was examined.

3.10 TRANSPARENCY

The transparency of the sky is not constant, especially when thin clouds or cirrus are overlapping with the observed region. Photometric conditions feature nearly transparent sky, but this was not the case during our observation runs. Therefore we had to correct for changing transparency during different single observations of the same object. The flux of a bright star near the observed galaxy was measured in every single image. The image with the highest count number was set as reference image with the best transparency conditions and the other images were scaled so to reach the same count levels. The corrections between different observations varied from 0.5 to 15 %.

3.11 STACKING OF IMAGES

The last step of the data reduction is combining the single mosaics of each galaxy to a final stack. The single observations needed to be prepared for the stacking, as during the reduction of the images the pixels in the CCD gaps turned out not to be zero as in the raw data. Due to the background correction these pixels have highly negative values and can be identified easily. Before the stacking is done the gap regions were assigned null counts using `imreplace`. All single mosaics in the same filter were aligned on the basis of their WCS solution and added up using `imcombine`. Because of the CCD gaps and the dithering technique, pixels in the gaps and at the edges of the field of view of the detector were not exposed the same number of times, i.e. their total exposure time is lower than the total exposure time of the pixels covered by a target. In order to take this difference into account, we built a total exposure time frame by which we normalized the stacked mosaic of a given target.

The single mosaic of that target is used for creating such a mask, using `imreplace` to set the gaps pixels to 0 and the rest to 1. Later on, these were aligned on the basis of their WCS and added up with `imcombine`. By using this method every pixel is assigned the number of how often it was exposed. Finally, the stacked image was divided by the mask and scaled to the same exposure time. The gaps are still visible in the final image as the signal-to-noise (S/N) is different there, this can be improved by a higher number of dithering steps. The choice of how many dithering steps to perform was limited by the time needed to read out the 8 CCDs.

3.12 DITHERING PATTERN

The dithering pattern of our observations were selected in order to only fill the gaps caused by the detector design with several CCDs (see Figure 3.1), and in order to have deep observations across the whole field of view. Therefore the dithering strategy included that the movements are minimized in their length. The dithering pattern is visualized in Figure 3.9, the detector was moved by distances corresponding the gap sizes. At first the studied galaxy is moved onto one of the central CCDs, with keeping the distance to the horizontal gap (see Figure 3.1) minimal and without placing any gap onto the studied target. After this larger offset we dithered around in five steps corresponding to the gap size. During these five steps the detector was moved around for every single observation of the galaxy in a way that the region, where vertical and horizontal gaps are overlapping, does not coincide with another gap in one of the other dithering steps. This was important to limit the number and areas with lower exposure time.

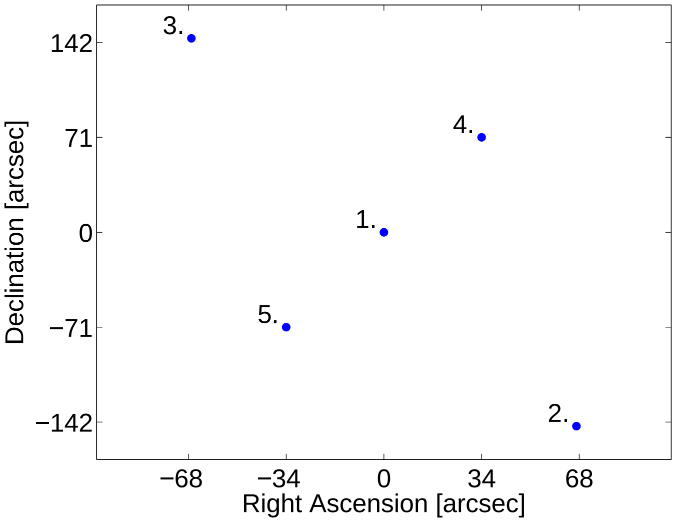

Figure 3.9: The dithering pattern for each target, the steps are chosen in order to fill the gaps. The blue dots mark the center of the field of view.

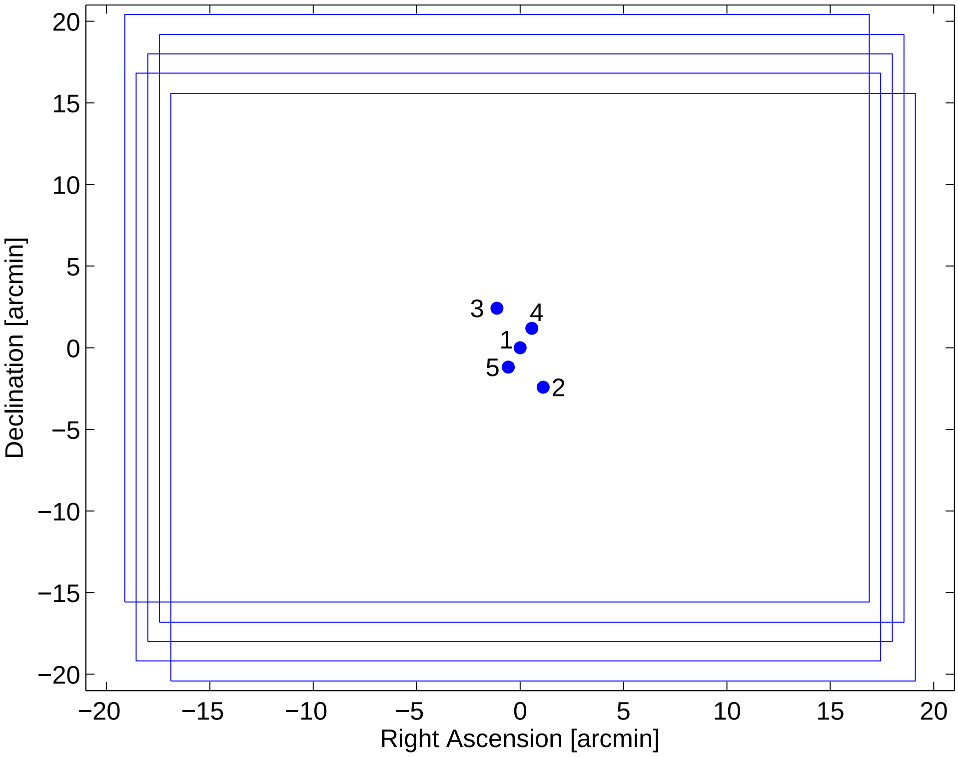

Figure 3.10: The field of view of dithering pattern. The blue dots mark the center of the field of view and the rectangle shows the corresponding field of view of each single step.

4

BASIC CALIBRATION AND ANALYSIS

In this chapter all the used image analysis tools and methods are described. Most of the data analysis can already be found in Ludwig et al. (2012). In astronomical image analysis a huge variety of tools are available. The standard tools which are necessary for optical image data analysis in Astronomy are available through IRAF[1]. But for many tasks we supplemented the used methods with other available more specialized tools. The description of these techniques are explained in the next paragraphs.

4.1 PHOTOMETRIC CALIBRATION

For the scientific analysis of imaging data it is necessary to convert the measured photons which are available as ADUs to the flux emitted by the sources. The observations were performed in two filter systems: MOSAIC provided the SDSS filter system (SDSS *g*- and *r*-band were used). Out of the available broadband filters of WFI the B- and R-band filters were selected. Two different methods were implemented for the photometric calibration, which will be explained in the following sections.

4.1.1 STETSON STANDARD STAR FIELDS

The photometric calibration of any imager and filter system relies on standard star fields. Therefore Stetson/Landolt standard star fields (Stetson 2000; Landolt 1983) were observed in the beginning, in the middle and at the end of each night. A number of three to five ditherings for every used filter were performed in a way that the same star is always lying on a different CCD. These calibration observations were processed in the same way as the science images. Later on, the positions of the standard stars in each observed image were translated into their (RA/DEC) coordinates using the WCS of their images with rd2xy. In this way it was possible to examine the flux of each standard star[2] in our images. We used the daophot tool phot that provides the flux (total counts of a star) inside a given aperture, also corrected for the local background as measured in an annulus around the aperture. The measured count rate C and the calibration magnitudes $m_{\mathrm{Stetson/Landolt}}$ in the same filter give the zeropoint ZP for the transformation of counts into magnitudes:

---

[1] IRAF is distributed by the National Optical Astronomy Observatory, which is operated by the Association of Universities for Research in Astronomy, Inc., under cooperative agreement with the National Science Foundation.

[2] A full list of all Stetson/Landolt star fields with magnitudes in different filters and positions can be found via http://www3.cadc-ccda.hia-iha.nrc-cnrc.gc.ca/community/STETSON/standards/

$$ZP = m_{Stetson/Landolt} + 2.5 log(C/exposure\ time) \tag{4.1}$$

In order to get reliable values we did a magnitude cut on both ends. Stars with bright magnitudes were not used as the number of counts might have exceeded the linear regime of the CCD or the star might already have been saturated. The cut at the low end is due to low S/N ratios for faint stars as at this point the RMS variations of the measured flux produce a large scatter. The measured zeropoints have standard deviations ranging from 0.04 to 0.09 mag.

Most of the observing nights were not photometric, therefore only the images of standard star fields acquired under acceptable conditions were employed for the photometric calibration. It is clear that this is limiting the calculated photometry so that the magnitudes and colors measured for our targets have to be considered with some caution.

4.1.2 THE SDSS AS CALIBRATION TOOL

For those observed targets which are in overlap with the SDSS we can derive a more precise photometric calibration in our survey. Only galaxies that are observed in the SDSS *g*- and *r*-band can be calibrated with this technique. Stars that are in common with the SDSS and the target field can be used to measure the zeropoints in the same way as before. The magnitudes of the stars are taken from the SDSS and their count rates are measured in the final processed science image. A magnitude cut is performed on both ends as well, and stars in proximity to bright sources, stars that are not observed in all dithered images as well as double stars are removed. A more precise solution can be obtained with this technique as different photometric conditions are not affecting our measurements too much. The better photometric conditions of the SDSS improve the calibration as the same field is observed near-simultaneously in contrast to standard star fields, which are often at completely different positions on the sky and are observed by us during different times. The errors of the calibration when using the SDSS are usually about ~ 0.05 mag. It needs to be kept in mind, though, that using the SDSS in this way implies the use of tertiary standards. Had our nights been perfectly photometric, the regular standard star technique would have been the method of choice for best results.

4.2 GALACTIC FOREGROUND EXTINCTION

We used the extinction maps of Schlegel et al. (1998) and the extinction law of Cardelli et al. (1989) with $R_V = 3.1$ to calculate the Galactic foreground extinction towards our targets and at the central wavelength of the SDSS *g*- and *r*-bands (R_V is the ratio of total to selective extinction in the *V*-band). Likewise, the extinction was calculated also for the used B and R filters on WFI. All the magnitudes and surface brightnesses derived in this work are given already corrected for Galactic foreground extinction as will later be indicated by the subscript “0”.

4.3 PHOTOMETRY OF DWARF GALAXIES

In order to analyze the candidate dwarf galaxies (CDG) stamp images were produced with the CDG in the center, and sizes between 200 to 400 pixels depending on the size of the candidate. This has two advantages; first the images are much smaller and can be handled this way much easier and secondly it is possible to measure the local background and the rms fluctuations precisely in the region where the CDG is located.

The image analysis tool SExtractor (Bertin & Arnouts 1996) is used to measure different properties of the CDG. The background and its RMS are calculated directly, furthermore the isophotal flux up to a signal 3 times above the background (if the target is too faint up to 1 σ above the background) is calculated and the corresponding magnitude and error are given in the output catalog. The most useful advantage of SExtractor is that other sources are modeled and removed from the original target. In addition, SExtractor provides also the coordinates of the galaxy center and the galaxy ellipticity.

In order to measure the color of every CDG the isophotal magnitudes can not be used, as the S/N is varying in different filters and the areas do not match each other. Therefore the IRAF tool ellipse is run on the CDG.

Ellipses are fitted to the intensity distribution using IRAF. We assumed the center and ellipticity derived by SExtractor and kept them fixed, while we left the position angle (PA) as a free parameter. We overplotted the isophotes on the CDG image with isoimap in order to check their ellipticity and PA values. We adjusted the PA value upon visual inspection and used it for a second run of ellipse. The measured flux inside of the ellipses with intensities of 3 sigma above the background is used to calculate the color. It was ensured that in both filters the same area is covered for the color measurement.

4.4 ANALYSIS OF FAINT DEBRIS REGIONS

In our survey several examples of faint debris regions around massive spiral galaxies were found. One of the main aims was to study the nature of these features. The observed color in these regions can be taken as a rough tracer for the stellar populations in the faint outskirts of galaxies.

The observed tidal debris regions are very extended, thus these are contaminated by foreground stars and background objects. In order to measure the color and the surface brightness, empty regions without back- or foreground targets were selected visually and later on we measured their mean, mode, median and the RMS with imstat there. We chose the median to compute surface brightness (SB) and color, because in this way contamination from other objects and cosmic rays can be reduced. The size of these empty regions was adjusted so as to provide a high S/N ratio and to minimize the influence of the residuals produced by the flat-field error are not contributing too much and becoming a major issue.

Finally we calculated the mean of all apertures of one tidal feature and adopted it as measured color. The standard deviation of the magnitudes in the different apertures was assigned as the corresponding standard deviation of the measured color in the individual tidal features. Additionally, we performed a subtraction of the local background. The mode in close-by empty regions was examined and subtracted from the flux measurements. Furthermore the SB as well as the colors were corrected for Galactic foreground extinction.

4.5 MEASURING THE SIGNAL-TO-NOISE RATIO

In order to examine the S/N of the measurements which is due to Poisson statistics of the source and background (BG), the read-out-noise (RDNOISE) of the electronics, it is necessary to determine these parameters as well as the number of pixels (N_{pix}), over which the photometry is performed, and the detector gain. The formula

$$S/N = \frac{(Counts * N_{pix} * Gain)}{\sqrt{(Counts * N_{pix} * gain) + (BG * N_{pix} * gain) + (N_{pix} * RDNOISE^2)}} \tag{4.2}$$

gives the S/N for every used aperture, if the image is scaled to an exposure time of 1 second.

4.6 SERSIC PROFILES

The distribution of light of the detected CDG can be used to classify their nature. Elliptical galaxies can be clearly distinguished from spiral galaxies by the luminosity profile and the values of the found CDG should lie in a given parameter range. Later on the measured Sérsic index *n* can help to distinguish background ellipticals from CDG.

The center and ellipticity of the CDG were examined with SE, the values from the color measurement which include the PA could be used for this step again. In order to perform a surface brightness profile (SBP) fit to the CDG the SB was measured as function of the galactocentric distance along the semi major axis (SMA).

We estimated the SBP of each CDG with the isophotes computed by `ellipse`, by plotting the isophote intensity as a function of their SMA. The error on the isophote intensity as provided by `ellipse` was translated into an error on the surface brightness.

In order to study the structural properties of the CDG the SBP is fitted with a Sérsic profile (Sersic 1968):

$$\mu(r) = \mu_0 + 1.086 * (r/h)^{1/n} \tag{4.3}$$

(Cellone 1999) where μ is the SB, μ_0 is the central surface brightness (CSB), r is the distance from the galaxy center along the semi-major axis, h the scale length and n the Sérsic index.

The fit was performed outside the central regions of the CDG out to the SMA whose corresponding surface brightness is 3σ above the background. If the signal was too faint and thus the SB too low, the SMA was extended to SBs which are only 1σ above the background. We used a non-linear least-squares fit with the Levenberg-Marquardt algorithm and the fit is plotted over the measured SBP.

4.7 IMAGE PROCESSING

After the data reduction the produced images need to be processed in order to highlight the faint substructures surrounding the targeted spiral galaxies. Here we describe how we visualized these features.

4.7.1 ADAPTSMOOTH

The visualization of faint features can be done with different smoothing or masking techniques. Usually this has also side effects, as often the resolution is reduced due to the fact that the algorithms work on every part of the image.

ADAPTSMOOTH (Zibetti 2009) has a different approach, this program is able to smooth astronomical images in an adaptive fashion. The idea is to increase the S/N, therefore regions are smoothed to reach a previously fixed S/N value. The great advantage of ADAPTSMOOTH is that the spatially resolved photometric information is preserved, as everywhere in the image only the minimal smoothing is being performed to achieve the S/N limit. In other words, only locations with low S/N are smoothed and regions with high signal remain untouched.

This command-line based tool only needs the gain, the background and the desired S/N. During each iteration an additional mask is created which records the smoothing. This is important if the target will be studied in different filters. ADAPTSMOOTH can be used with an input mask, this was very helpful for this study as the targets were imaged in two filters. As there are differences in the S/N of observations in different filters a homogeneous smoothing in all used filters is necessary for color measurements. For the image observed in the second filter we used the mask of the previously smoothed image. Therefore it was possible to smooth observations in different filters the same way. For the later color measurements flux conservation was also ensured. Depending on the chosen S/N many faint features stand out much more clearly after they were processed with ADAPTSMOOTH.

4.7.2 COLOR IMAGES

People realize the nature and the world around them with the eyes and brain usually in color, thus it is much more comfortable to look at color images. The IRAF tool `rgbsun` can produce colorful images in rasterfile format with three channels, which are red, green and blue. Unfortunately we only observed in two filters, therefore for the third missing channel we took the mean of the images in the two available filters. It can still be recognized that the dynamical range (color depth) is not large enough and images are looking unreal, but nevertheless it is still improving the visual appearance in contrast to only gray-scale images. The differences between red and blue regions which gives basic informations about the underlying stellar populations are highlighted well enough. The color images can be found in the appendix.

5

NGC 7331 - A CASE STUDY

This chapter is a modified version of Ludwig et al. (2012).

To test the feasibility of this project we observed NGC 7331, an SAb galaxy at a distance of 14.2 Mpc viewed under an inclination angle $i = 77°$. Its inferred luminosity is $M_B = -20.4$ mag (de Vaucouleurs et al. 1991) and its maximum rotational velocity is (245.5 ± 5.2) km s^{-1} (taken from Hyperleda[1], based on the catalog from Bottinelli et al. 1982). These quantities are similar to the properties of the MW and M31. NGC 7331 contains a large-scale dust ring with a radius of about 6 kpc (Regan et al. 2004) and its observed H I distribution shows a warp in the outskirts of the disk (Bosma 1981). The latter could be a sign of past interactions.

NGC 7331 is located in a sparse group with a density of 0.33 galaxies Mpc^{-3} down to $M_V = -16$ mag (Tully & Fisher 1988). Other luminous group members include the disk galaxies NGC 7217, NGC 7320, NGC 7292, NGC 7457, UGC 12060, UGC 12082, UGC 12212, UGC 12311, and UGC 12404 (see Figure 5.1). The galaxies of this group are within ±170 km s^{-1} from NGC 7331, which itself has a radial velocity $v = (816 \pm 1)$ km s^{-1} (Haynes et al. 1998). NGC 7331 is the most luminous galaxy of this group. The other late-type galaxies span the magnitude range $-16 \lesssim \mathrm{M}_B \lesssim -20$ mag. In comparison with the Local Group the NGC 7331 group has only one member brighter than $\mathrm{M}_B = -20$ mag. The NGC 7331 group is classified as a stable group (Materne & Tammann 1974) and is part of the Pegasus Spur (Tully & Fisher 1988).

Figure 5.1 gives an overview of the NGC 7331 galaxy group, underlining the loose, extended character of this group, which resembles the nearby Sculptor group (e.g., Karachentsev et al. 2003a). When measuring the projected distances from NGC 7331 to the other members we get typical distances of 1 Mpc and for the most distant member, UGC 12404, 2.16 Mpc.

5.1 OBSERVATIONS

The observations were performed in October 2009 with the Wisconsin Indiana Yale NOAO (WIYN) 0.9m telescope at Kitt Peak National Observatory in Arizona equipped with the MOSAIC imager. This instrument is a wide-field imager with eight single CCDs, providing a total area of (8192×8192) pixels^2. The total field of view is one deg^2 with a pixel scale of $0.43''$ pixel^{-1}.

---

[1] http://leda.univ-lyon1.fr/

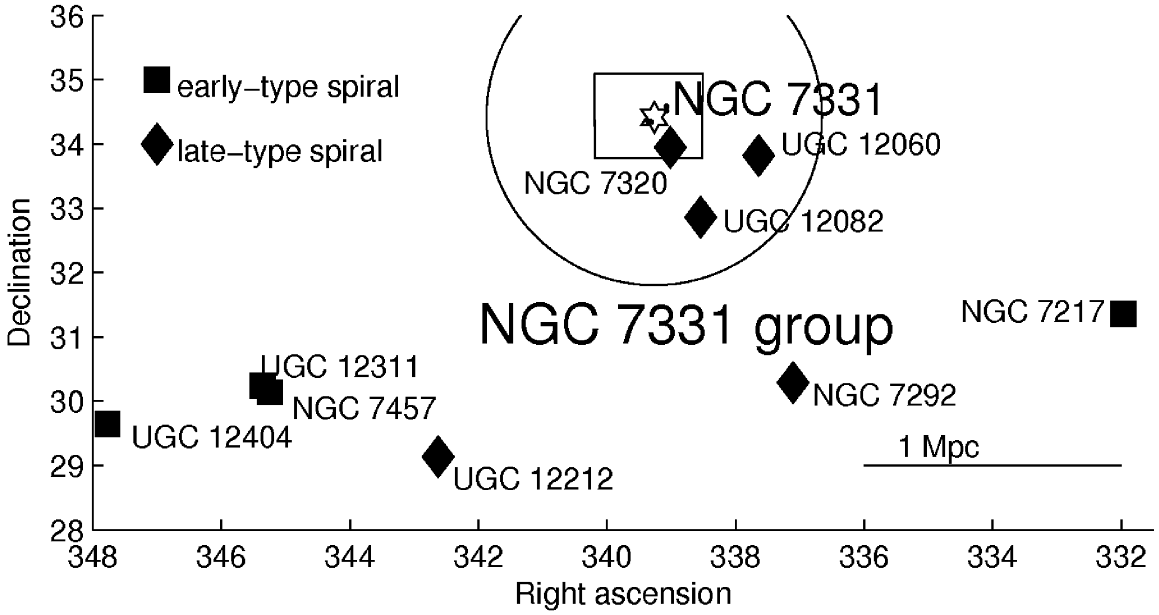

Figure 5.1: The wider NGC 7331 group environment. The star symbol represents the centroid of NGC 7331. The dots around it are our dwarf galaxy candidates. The open rectangle marks our field of view. Filled squares show other massive, yet less luminous early-type spiral galaxies in the NGC 7331 group and in its immediate surroundings. Filled lozenges show late-type spirals in the group and in its vicinity. The open circle indicates a virial radius of 1.3 Mpc around NGC 7331.

We imaged NGC 7331 for 3.5 hrs (9 × 1200 s + 2 × 900 s) in the Sloan Digital Sky Survey (SDSS) g-band and 4.17 hrs (11 × 1200 s + 2 × 900 s) in the SDSS r-band. The dither pattern was chosen with a step size of $400''$ in right ascension and declination so that the galaxy would lie in each of the central four CCDs.

Due to the dither pattern we obtain a final image size of 11148 pixels × 11756 pixels with a resulting field of view of 1.3° × 1.4°, where the edges of the final image have a lower total exposure time (fewer exposures) and a higher noise than the central regions. The area with complete overlap of all stacks is 5440 pixels × 4640 pixels resulting in a field of view of $33' \times 38'$. The final image is characterized by an average point-spread function (PSF) with a full width at half maximum (FWHM) of $1.3''$ in each filter.

For the photometric calibration we used stars in common between our final image and the SDSS Data Release 7 (DR7) (Abazajian et al. 2009). We only used stars that are not saturated in our science images but bright enough to have a good signal-to-noise (S/N) ratio. In the SDSS g-band we used stars between 16.5 and 18 mag and derived a zeropoint of (22.24 ± 0.04) mag, while in the SDSS r-band we selected stars between 16 and 17.5 mag and obtained a zeropoint of (22.19 ± 0.03) mag.

We used the extinction maps of Schlegel et al. (1998) and the extinction law of Cardelli et al. (1989) with $R_V = 3.1$ to calculate the Galactic foreground extinction at the central wavelength of the SDSS g- and r-bands (R_V is the ratio of total to selective extinction in the V-band). All the magnitudes and surface brightnesses derived in the next sections are given already corrected for Galactic foreground extinction.

In deep imaging Galactic cirrus can act as an intervening contaminant. Therefore, the occurrence of cirrus imposes a limit on surface photometry as it is a Galactic foreground that cannot be removed (e.g., Sandage 1976).

In our observed region Galactic cirri are visible. Interestingly cirrus clouds show very red broadband colors (Szomoru & Guhathakurta 1998). Typical $(B-R)$ values range from 1.0 to 1.7 mag (Guhathakurta

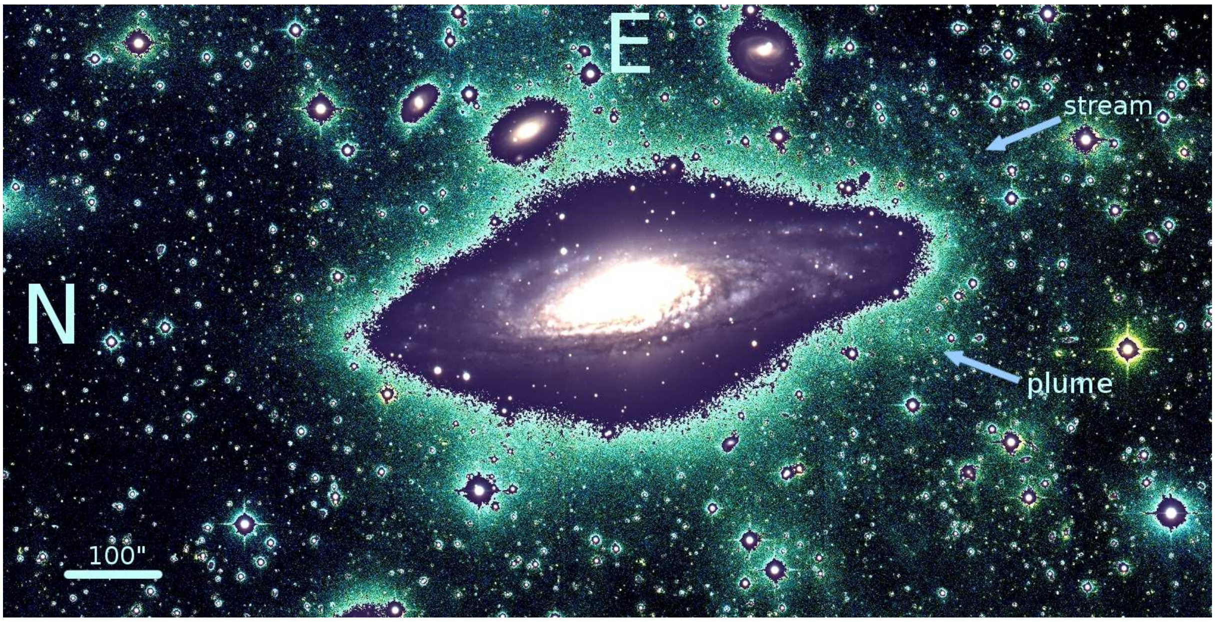

Figure 5.2: An optical view of the inclined spiral galaxy NGC 7331 (center). The image is composed of deep images in the SDSS g- and r-bands obtained with the 0.9m WIYN telescope and has a total size of $22.5' \times 11.4'$, where $100''$ correspond to 7 kpc. A number of luminous background galaxies and foreground stars are visible as well. The outer, grainy-looking regions are contrast-enhanced in order to make faint features visible. In the outskirts faint tidal debris structure can be seen and is highlighted by the arrows.

& Cutri 1994) and translate into $(g-r) = 1.33$ to 2.03 mag when using the color transformation $(B_J - R) = (g-r) + 0.33$ from Fukugita et al. (1995). Therefore, on the basis of their measured colors, faint and blue galaxy features can be distinguished from red Galactic cirrus clouds.

The extinction maps of Schlegel et al. (1998) do not take into account the presence of small scale dust features which can be seen in emission as “cirrus". Therefore our reddening correction does not remove any effect associate with source obscuration by dust associated with cirrus. A careful visual inspection of our images indicates that no cirrus is in close proximity to the objects discussed below, so cirrus reddening is unlikely to be a significant effect.

Observationally, the angular resolution is the most limiting factor for detecting faint, distant dwarf galaxies or streams. Due to the pixel scale of $0.43''$ pixel^{-1} and the need to have several pixels in order to resolve structures we are able to detect objects with a minimum size of 0.3 kpc at the distance of NGC 7331.

5.2 BASIC PROPERTIES OF NGC 7331

A color composite image of NGC 7331 is shown in Figure 5.2. Two images with different contrast levels are overlaid. The white-blue high-surface-brightness inset shows the brighter regions of NGC 7331, highlighting its overall structure, especially its spiral arms and bulge. The underlying green low S/N image reveals the low-surface-brightness features of the galaxy, including a candidate tidal stream and a plume, which are marked with arrows in Figure 5.2 and are discussed further below.

5.3 CANDIDATE DWARF GALAXIES AROUND NGC 7331

5.3.1 IDENTIFICATION OF CANDIDATE DWARF GALAXIES

In order to identify possible dwarf galaxy candidates around NGC 7331, a first analysis was done via visual inspection of the science images. We selected dwarf galaxy candidates on the basis of their low apparent surface brightness, diffuse structure, and angular extent of at least 7″, which is five times the typical point spread function. This was necessary in order to be able to distinguish extended objects from point sources. With spectroscopic follow-up studies Chiboucas et al. (2010) confirm that these selection criteria have a good success rate in identifying true dwarf galaxies. Our field of view and sensitivity do in principle permit us to detect all objects within a galactocentric distance of up to 170 kpc around NGC 7331 and down to a surface brightness $\mu_g = 27$ mag arcsec^2.

We identified four candidate dwarf galaxies, which we named with capital Latin letters in alphabetical order according to increasing projected distance to NGC 7331. Thus the nearest one is called NGC 7331 A, the second nearest NGC 7331 B, and so forth.

5.3.2 PHOTOMETRY OF THE CANDIDATE DWARF GALAXIES

We ran SExtractor (Bertin & Arnouts 1996) on images with a size of 180 × 180 pixels centered on each candidate in order to measure the integrated g and r magnitudes of the candidates after an accurate estimate of their local background. We configured SExtractor to measure isophotal magnitudes in two different apertures defined by the detection thresholds of 1 and 3 σ above the background. The resulting apparent integrated magnitudes are given in Table 5.1, together with their errors computed from SExtractor, which also takes into account the uncertainty on the photometric calibration. The absolute magnitudes were calculated assuming the same distance modulus (30.70 ± 0.32 mag) for the dwarf galaxy candidates as for NGC 7331. Their associated errors also include the error in the distance modulus.

We see that these four candidates fall in the magnitude range $-13 \lesssim M_r \lesssim -11$ typical of the classical dSph galaxies in the Local Group (Grebel et al. 2003). We checked the H I data obtained for NGC 7331 by Walter et al. (2008), and found no H I emission at the position of the four candidates, indicating that there may be no gas for future star formation available. This would be consistent with the properties of the majority of known dSphs in the Local Group. Only NGC 7331 A could possibly be classified as a transition object, because its core, being slightly bluer than its outer parts (see Section 5.3.3), could have recently undergone some star formation.

As the S/N ratio is different for the g- and r-bands, the integrated magnitudes computed by SExtractor sample different areas within each galaxy candidate. In the next Section we will use the IRAF task `ellipse` to compute the integrated color over the same region for each candidate and filter.

5.3.3 SURFACE BRIGHTNESS PROFILES

At first we measured the photometric center of our four dwarf candidates with the IRAF tool `center` in the DIGIPHOT package. The resulting centers are needed to run `ellipse`, where we kept the ellipticity and position angle parameters fixed at the values measured by eye (see Figure 5.3).

In order to measure the surface brightness as a function of galactocentric distance along the semi major axis, we set up `ellipse` to fit a series of concentric isophotes to the stamp images of the four candidates with the length of the semi-major axis gradually increasing with a linear step of a factor of 1.1 (see Figure 5.3).

The surface brightness profiles (SBPs) derived in the r-band are shown in Figure 5.4 with open circles and the error bars computed by `ellipse`. The maximum length of their semi-major axis is defined by the

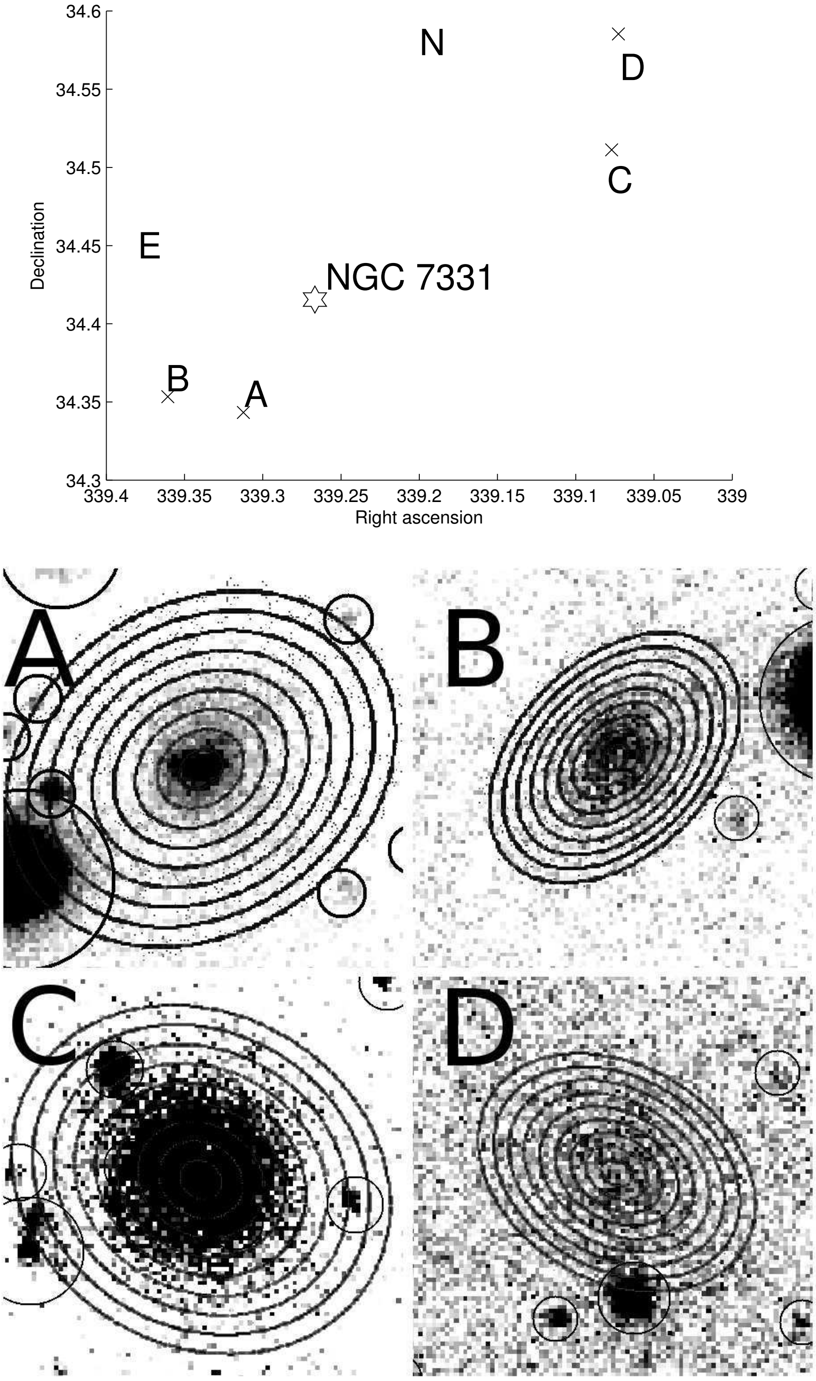

Figure 5.3: Top: The positions of the dwarf galaxy candidates. Bottom: Images of the dwarf galaxy candidates in the SDSS *g*-band obtained with the WIYN 0.9m telescope. These are cut-outs of the final stacked image of our observations with sizes of 180 pixels × 180 pixels. North is left and east is up. The concentric elliptical annuli centered on each of the dSph candidates indicate a subset of the regions within which the surface brightness was measured. The open circles mark presumed background objects that were masked out.

Table 5.1: Observational properties of the dwarf galaxy candidates

Property	NGC 7331 A	NGC 7331 B	NGC 7331 C	NGC 7331 D
RA [J2000] [h m s] (1)	22:37:14.98	22:37:26.56	22:36:18.49	22:36:17.46
Dec [J2000] [° m s] (2)	34:20:35.86	34:21:12.23	34:30:40.37	34:35:07.20
g_0 (1σ) [mag] (3)	18.48 ± 0.04	20.01 ± 0.05	18.30 ± 0.04	20.65 ± 0.05
g_0 (3σ) [mag] (4)	19.91 ± 0.04	20.82 ± 0.20	18.53 ± 0.04	—
r_0 (1σ) [mag] (5)	17.80 ± 0.03	18.75 ± 0.03	17.58 ± 0.03	20.21 ± 0.04
r_0 (3σ) [mag] (6)	19.14 ± 0.03	19.75 ± 0.03	17.90 ± 0.03	—
A_g [mag] (7)	0.34	0.32	0.33	0.33
A_r [mag] (8)	0.25	0.23	0.24	0.24
$(g-r)_0$ (1σ) [mag] (9)	0.57 ± 0.05	0.63 ± 0.06	0.55 ± 0.05	0.75 ± 0.06
$(g-r)_0$ (3σ) [mag] (9)	0.39 ± 0.05	0.62 ± 0.20	0.54 ± 0.05	—
$\mu_0(r)$ [mag arcsec^{-2}] (10)	23.33 ± 0.10	24.10 ± 0.06	23.76 ± 0.03	25.20 ± 0.08
h_r [pc] (11)	325 ± 33	456 ± 15	592 ± 16	516 ± 27
n (12)	1.28 ± 0.11	0.62 ± 0.07	0.71 ± 0.03	0.52 ± 0.07
M_r (1σ) [mag] (13)	-12.90 ± 0.32	-11.95 ± 0.32	-13.12 ± 0.32	-10.48 ± 0.32
R (NGC 7331)$_{\text{projected}}$ [kpc] (14)	20 ± 2	25 ± 3	45 ± 5	58 ± 7

Rows (1) and (2) are the coordinates (J2000 right ascension and declination) where we give hours, minutes, and seconds in row (1) and degrees, minutes, and seconds in row (2). Rows (3) to (6) are the apparent magnitudes in the SDSS *g*- and *r*-band with 1σ and 3σ thresholds above the background detections. In rows (7) and (8), A_g and A_r are the extinction values for the SDSS *g*- and *r*-band. Row (9) contains the extinction-corrected color in the SDSS *g*- and *r*-bands. Row (10) shows the central surface brightness in the *r*-band, $\mu_0(r)$. Row (11) lists the exponential scale length, h_r. Row (12) provides the Sérsic index, *n*, row (13) the absolute magnitude in the *r*-band, M_r, when assuming a distance modulus of 30.70± 0.32, and row (14) the projected distance to NGC 7331, *R*.

corresponding surface brightness being just 1σ above the background. To characterize the structural parameters of the four candidates, we fitted their SBPs with the Sérsic profile (Sersic 1968):

$$\mu(r) = \mu_0 + 1.086 * (r/h)^{1/n} \tag{5.1}$$

(Cellone 1999) where μ is the surface brightness, μ_0 is the central surface brightness, r is the distance from the galaxy center along the semi-major axis, h the scale length and n the Sérsic index. We cut each SBP at the semi-major axis whose corresponding surface brightness is just 3σ (1σ for NGC 7331 D because of its low surface brightness) above the background in order to minimize the uncertainty on the best fitting Sérsic profile. We used a non-linear least-squares fit with the Levenberg-Marquardt algorithm. The best fitting Sérsic profiles are plotted in Figure 5.4 with a solid line, and their parameters (n, μ_0, h_r) are shown in Table 5.1.

The Sérsic indices n obtained for the four candidates range from 0.5 to 1.3, and are in good agreement with those measured by Chiboucas et al. (2009) for the dSphs and dIrrs in the M81 group ($0.21 \lesssim n \lesssim 1.0$). The estimated μ_0 of the four candidates varies between 23 – 25 mag arcsec^{-2} and is consistent with the central surface brightness of the dwarfs in the M81 group as derived by Chiboucas et al. (2009).

We used the SBPs to determine the semi-major axes $r_{1\sigma}$ and $r_{3\sigma}$ at which μ is just 1σ and 3σ, respectively, above the background. For our data $r_{1\sigma}$ and $r_{3\sigma}$ are smaller in the *g*-band, therefore we used their values in the *g*-band ($5.5'' < r_{1\sigma} < 11.0''$ and $2.5'' < r_{3\sigma} < 9.0$) to compute the integrated $(g-r)_0$ colors of each candidate. These colors are reported in Table 5.1.

For each candidate except NGC 7331 A, the colors derived for the 1 and 3 σ thresholds are very similar; in the case of NGC 7331 A the color for the 3 σ threshold is bluer than that for 1 σ. This

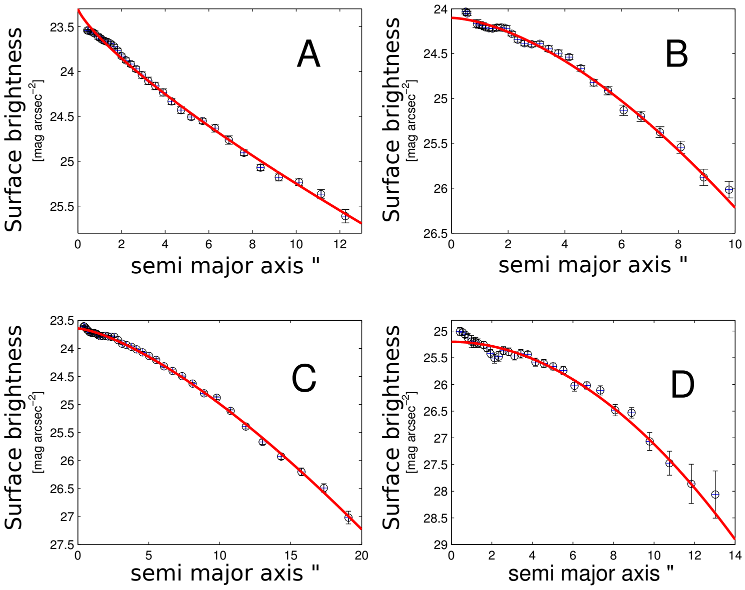

Figure 5.4: Surface brightness profile fits to the dwarf galaxy candidates of NGC 7331 in the SDSS *r*-band.

indicates that this galaxy is bluer in its center, perhaps akin to what is observed in some of the more massive "blue-core dwarf ellipticals" (dE(bc) as classified by Lisker et al. 2006) in the Virgo cluster. For these dE(bc) galaxies, Lisker et al. (2006) were able to show spectroscopically that they did experience star formation in their centers less than a Gyr ago. Similar examples – again among the more luminous dEs – are also known from the Local Group, where the close M31 dE companions NGC 185 (e.g., Hodge 1963; Butler & Martínez-Delgado 2005) and NGC 205 (e.g., Cappellari et al. 1999; Monaco et al. 2009) show recent star formation in their centers. NGC 7331 A may be a lower-luminosity nucleated dSph counterpart of these systems. Note that some Galactic dSph galaxies, in particular Fornax, also show relatively recent star formation that occurred just a few 100 Myr ago, though at the current time they are no longer active (Grebel & Stetson 1999; Saviane et al. 2000).

The $(g-r)_0$ colors of the four dSph candidates around NGC 7331 range from 0.55 to 0.75 mag. In order to compare them with the dwarfs in the Local Group, we used the color transformation equations from Jordi et al. (2006) for Population II stars to translate the $(g-r)_0$ colors of the four candidates into $(B-V)$ colors, i.e., we apply the transformation relation $(B-V) = 0.918 \cdot (g-r) + 0.224$. The resulting $(B-V)$ values vary between 0.7 and 0.9 mag and are consistent with the $(B-V)$ colors measured for LGS 3, And I and Leo I in the Local Group (Mateo 1998).

5.3.4 CANDIDATE DWARF GALAXIES IN THE SDSS

We checked that the four dwarf galaxy candidates found in our WIYN data are also visible in the SDSS images available for NGC 7331. We were able to recover them, although they have a much lower S/N in the SDSS data than in our own data. With a detection limit of $\mu_0(g) \approx 27.0$ mag arcsec^{-2} the WIYN data are slightly deeper than the SDSS in the individual filters.

According to the NASA Extragalactic Database (NED[2]), NGC 7331 has the same morphological type as M31, yet is more than one magnitude brighter in the optical (V-band) and in the near-infrared

---

[2] URL: http://ned.ipac.caltech.edu

(H-band). It may thus be more massive than M31 (see also Section 5.1). We then might expect it to be surrounded by a number of close dE companions similar to those found near M31. Interestingly we did not detect any bright dE across of the field of view of our WIYN data. We then decided to search for dE candidates in the SDSS images covering the surroundings of NGC 7331 out to a distance of 1 Mpc. The depth of the SDSS imaging data in the g-band reaches surface brightnesses as faint as $\mu_0(g) \approx 26.0$ mag arcsec^{-2} to 26.5 mag arcsec^{-2} (Kniazev et al. 2004). Therefore dEs, which have a typical μ_r between 21 and 24 mag arcsec^{-2} and a $(g-r)$ color between 0.2 to 0.8 mag (Lisker et al. 2007, 2008) should be easily detectable in the SDSS images.

We retrieved from the SDSS DR7 photometric catalog (Abazajian et al. 2009) all objects with a Petrosian radius larger than $10''$, $0 \lesssim (g-r) \lesssim 1.5$ mag, and 21 mag arcsec$^{-2} \lesssim \mu_g \lesssim 26$ mag arcsec^{-2}, in order to sample the parameter space of dEs and dSphs. The limits in color and surface brightness were chosen from the properties of dEs in the Virgo Cluster (Lisker et al. 2007, 2008). Smaller Petrosian radii do not allow one to carry out a proper analysis of the object's morphology. A visual inspection of the selected objects revealed no dE or bright dSph candidates.

5.3.5 DWARF GALAXIES IN THE FRAMEWORK OF GALAXY EVOLUTION MODELS

Hierarchical models of galaxy evolution (e.g., White & Frenk 1991) suggest that the halos of giant galaxies contain large numbers of low-mass dark-matter halos. If populated by baryonic matter as well, these halos may be observable as dwarf galaxies. It is well established, however, that even in the case of the MW the number of known dwarf companions is less than the predicted number of satellite halos (e.g., Moore et al. 1999; Kravtsov 2010). While observations of the Local Group and other nearby groups (e.g., Karachentsev 2005) show a high number of dwarf galaxy companions and some tidal interactions (e.g., Miskolczi et al. 2011), the numbers are consistently lower than the model predictions. This missing satellite problem indicates that on the mass scale of galaxies, observations do not reveal luminous versions of the expected substructures.

The possibility therefore exists that only a minority of low-mass satellite dark matter halos contain stars (e.g., Madau et al. 2008). An interesting question is how common such observable luminous structures are, and whether they follow well-defined patterns associated with either host galaxy or galaxy group properties in the nearby universe. Thus we selected nearby galaxy groups for study in GGADDS as these provide the most common environments within which sub-halos should exist in the present-day universe.

5.3.6 THE NGC 7331 GALAXY GROUP

NGC 7331 is a member of a filamentary group of galaxies (see Figure 1). It contains two giant spirals, NGC 7217 and NGC 7331, as well as the luminous S0 galaxy NGC 7457. If we consider the virial radii of typical galaxy groups to be $R_{vir} \leq 1.3$ Mpc (Karachentsev 2005), then the NGC 7331 group appears to consist of three subgroups: 1) the relatively empty zone surrounding the SAb galaxy NGC 7217; 2) a subsystem containing the late-type galaxies NGC 7320, UGC 12060, and UGC 12082 associated with NGC 7331; and 3) a third grouping around the S0 galaxy NGC 7457, which is accompanied by a dwarf S0/dE. The NGC 7457 subgroup is noteworthy in containing early-type disk galaxies, suggesting that it is dynamically more evolved. In contrast to that, the NGC 7331 subgroup is dominated by gas-rich late-type galaxies, indicating that it is likely to be in an earlier dynamical evolutionary phase (see Figure 5.5).

Overall, the NGC 7331 subgroup therefore resembles the loose groupings of late-type giant galaxies found in the Sculptor group or the Canes Venatici cloud (Jerjen et al. 1998; Karachentsev et al. 2003a,b; Karachentsev 2005). Karachentsev (2005) finds that the M94 group and the Sculptor group are not

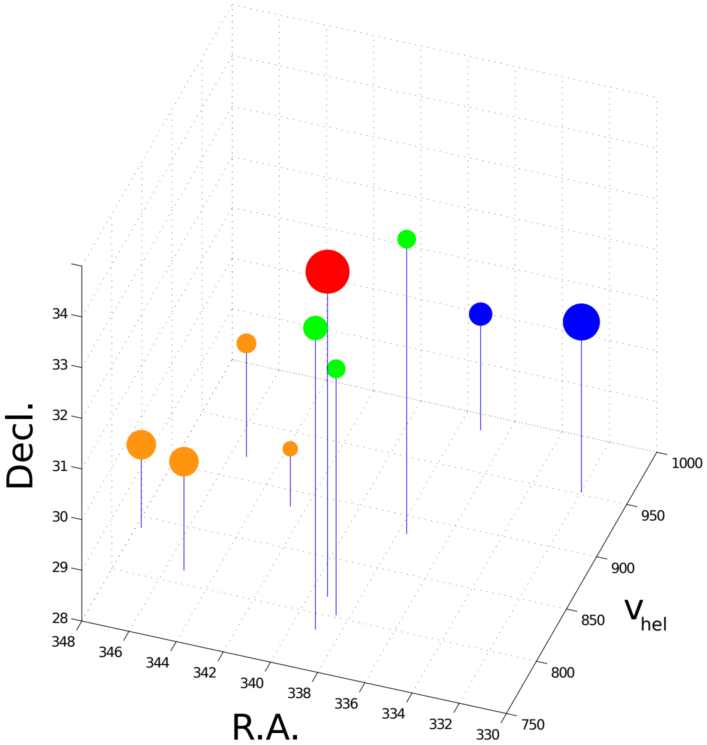

Figure 5.5: Overview of the NGC 7331 group. The red dot stands for NGC 7331. The blue dots mark the subgroup around NGC 7217, the green ones show other spiral and irregular galaxies belonging to the NGC 7331 subgroup, and the yellow dots indicate the NGC 7457 subgroup (the dot size represents the luminosity of each galaxy). The right ascension (RA) and the declination (Dec) are given in degrees. The heliocentric velocity, v_{hel} is given in km s^{-1}.

in a state of dynamical equilibrium, a situation that likely applies to the overall NGC 7331 group. In comparison the Local Group, with its two giant spirals separated by ~ 0.8 Mpc is a denser and likely more massive galaxy group than the NGC 7331 subgroup. Such a more massive and richer galaxy group should have a shorter crossing time, and offer more opportunities for internal interactions within the typical group radius of approximately 1 Mpc.

5.3.7 THE NGC 7331 DWARF SAMPLE COMPARED TO M31 AND OTHER NEARBY GALAXIES

Our study of the region surrounding NGC 7331 reveals four candidate dwarf companions. Three of them have $M_r \leq -13$ mag and are located within a projected radius of 160 kpc from NGC 7331. As this corresponds to the same region covered by the main Pan-Andromeda Archaeological Survey (Richardson et al. 2011), it is interesting to compare results. With our sensitivity we would detect the compact elliptical satellite M32 and all three bright dEs around M31 (i.e., NGC 147, NGC 185, and NGC 205). Obviously any counterparts of such galaxies are missing from our survey zone surrounding NGC 7331. We also would detect at least two of the brighter M31 dSph companions, And I and And II; thus our data are suggestive of roughly comparable luminous dSph populations in the two systems. This result is re-enforced by our finding that the NGC 7331 dwarf galaxy candidates have colors and structures of typical dSph galaxies.

As the absolute H-band magnitude for NGC 7331 (Aaronson 1977) is ≈ 1 mag brighter than that for M31, it is likely that M31 has less stellar mass than NGC 7331. In addition the bulge-to-disk luminosity ratio for NGC 7331 is B/D ≈1 (Bottema 1999) versus B/D ≈ 0.5 for M31 (Geehan et al. 2006). Thus if the dSph population were tied to bulge luminosity, we might expect richer dwarf populations in NGC 7331 as compared to M31. Yet apparently this is not the case, at least within our magnitude limit and with R≤160 kpc. The deficiency of early-type dwarf satellites associated with NGC 7331, however, is more pronounced if we consider the lack of equivalents to the three classical, luminous dE M31 companions. If we compare the stellar masses of more luminous early-type dwarf companions, excluding the anomalous M32 system, then the detected stellar mass in the form of candidate satellite galaxies around NGC 7331 is about 2% of that found in the same radius and absolute magnitude limit around M31. It thus seems possible that the presence of dE-type satellites could be linked to some parameter other than the (stellar) mass of the host galaxy, such as group density, as suggested by earlier studies (e.g., Ferguson & Sandage 1991).

We conclude that unless dE companions to NGC 7331 have been missed at larger radii, where they should have been detected as candidate dwarfs in the SDSS images, NGC 7331 has substantially less stellar material in the form of satellites than the less massive M31 system. Moreover, NGC 7331 lacks luminous nearby companions like the Magellanic Clouds around the Milky Way. Such irregular companions, however, are generally found to be rare (e.g., Guo et al. 2011).

The statistics for dSphs with $M_r \leq -14$ are not well constrained. Our few detections only sample the counterparts of the most luminous counterparts of the “classical” dSphs in the Local Group. When comparing NGC 7331 and M31 in this respect, it seems possible that similarly numerous populations of such dSph satellites may exist around both spiral galaxies. The differences and similarities between the populations of inner satellite galaxies around NGC 7331 as well as in the Sculptor group and in the Local Group is further illustrated in Figure 5.6.

5.4 ANALYSIS OF THE STELLAR STREAM

In the south-eastern outer regions of NGC 7331 we find hints of a very low-surface-brightness structure in our WIYN images that we interpret as a stellar stream (Figure 5.7). We measured the length of the stream with the SAOImage DS9 tool ‘projection’ by placing a rectangular aperture, $29'' \times 85''$, along the stream in a combined g-and r-band image. This gives the mean counts along the stream. This produced an average brightness profile of the stream, and its length was estimated as the distance between the two edges of the stream where the brightness is less than 1σ above the background.

Similarly, we determined the width of the stream with a box of $29'' \times 65''$ placed across the stream in a region free of bright stars. The resulting brightness profile was fitted with a Gaussian function (see Figure 5.8). Its FWHM was used to define the width of the stream. In this manner we obtained a length of 5 kpc and a width of 802 pc for the stream (assuming the same distance modulus as for NGC 7331).

We defined a set of twelve circular apertures, $10''$ in diameter, to estimate an average background in the surroundings of the stream, and three apertures of the same size centered on the brightest regions of the stream to derive its surface brightness. After correcting for the local background, we obtained $\mu_{g,0} = (26.88 \pm 0.11)$ mag arcsec^{-2}, $\mu_{r,0} = (26.63 \pm 0.10)$ mag arcsec^{-2} and $(g - r)_0 = (0.16 \pm 0.16)$ mag, at a S/N of about 7. We discuss the possible origin of the stellar stream in Section 5.

Since many dwarf galaxies in groups and clusters show color gradients (e.g., Kormendy & Djorgovski 1989; Chaboyer 1994; Harbeck et al. 2001), it is interesting to check whether the stream also shows such a color variation. In order to do so we used `pvector` on an area of 354 kpc ×5 kpc aligned with the stream and extracted the average surface brightness of the stream in each filter (see Figure 5.7). The resulting

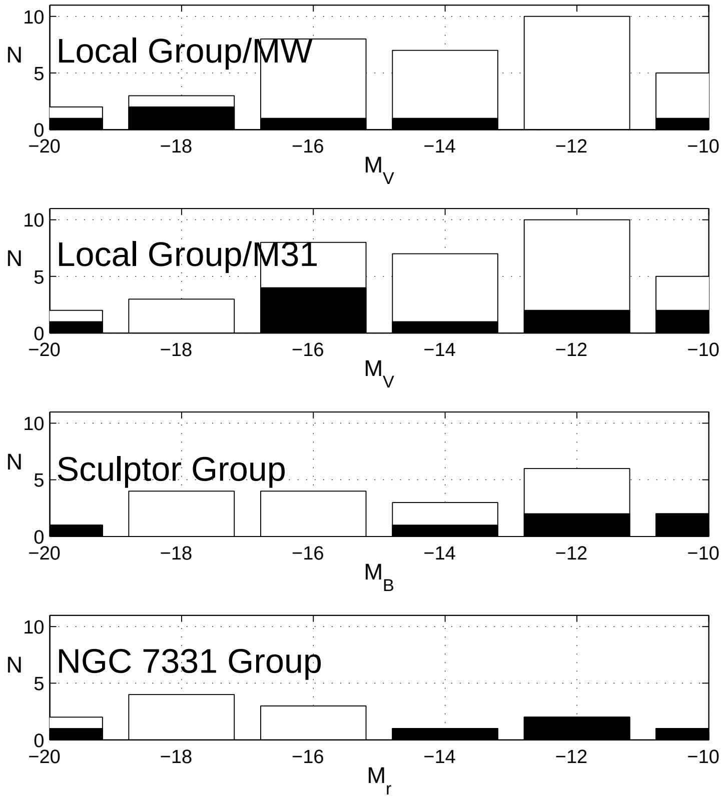

Figure 5.6: The luminosity function of the NGC 7331 subgroup (bottom panel) compared to the Milky Way and M31 subgroups in the Local Group (upper two panels) and the NGC 253 subgroup in the Sculptor group (third panel). The white (unfilled) histogram bars show the total number of detected member galaxies in a given group. The black (filled) histogram bars in the panels indicate what we would measure if we take into account only the likely dwarf satellites of one massive disk galaxy (the Milky Way and M31 for the Local Group and NGC 253 for Sculptor) to permit a direct comparison with NGC 7331.

color profile is plotted in the top panel of Figure 5.9, where the solid line represents the mean color obtained after a 1 σ clipping of the data. We also binned the color profile with a bin size of 13 pixels in order to improve the S/N; the result is shown in the bottom panel in Figure 5.9, where the solid line traces again the average color across the stream (0.15 ± 0.06 mag). This is in good agreement with the color previously obtained with aperture photometry. Integrating the surface brightness profile of the stream we derived $g_0 = (20.03 \pm 0.46)$ mag and $r_0 = (19.87 \pm 0.69)$ mag corresponding to $\mathrm{M}_r = (-10.83 \pm 0.76)$ mag at the distance of NGC 7331.

We also checked the SDSS images in the *g*- ,*r*-, and *i*-band, but we were not able to clearly detect the stream. Also the stacked *gri*-band image does not show a recognizable stream, indicating that the SDSS data are not deep enough and do not provide a high enough S/N ratio to study the stream.

In addition to the stream, another faint feature – a plume – can be detected in the southwest outer regions of NGC 7331 (see Figure 5.2). We performed aperture photometry (three apertures with $r = 5''$) of the plume and derived average surface brightnesses of these apertures of $\mu_{g_0} = (26.29 \pm 0.46)$ mag and

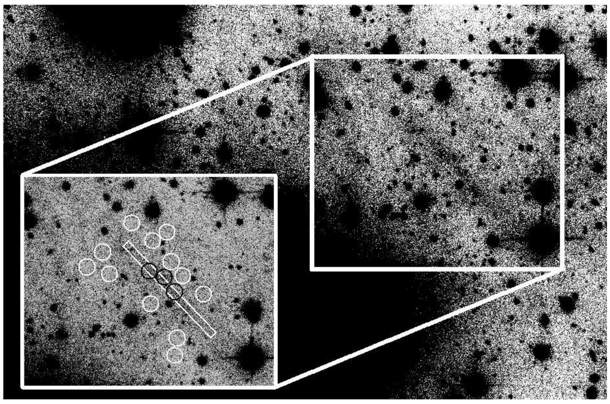

Figure 5.7: The faint stellar stream near NGC 7331. The inset shows the analyzed region. The black circles mark the brightest regions of the stream where we measured the magnitudes and white circles represent the areas of the local background estimation. The white rectangle indicates the region where the color profile was measured.

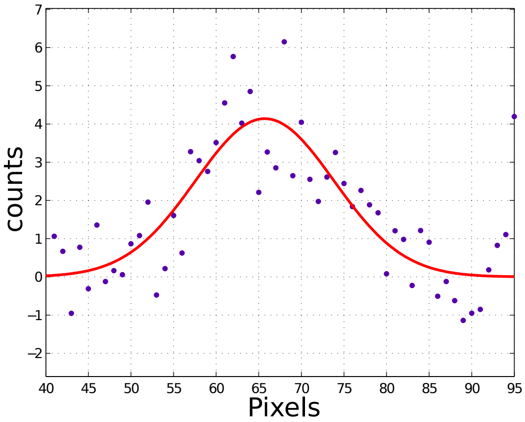

Figure 5.8: The Gaussian fit to the width of stream. For the fit we used the stacked g- and r-band image.

μ_{r_0} = (25.79 ± 0.30) mag with a resulting color of $(g - r)_0 = 0.50 \pm 0.17$. The errors correspond to the fluctuations of the calculated magnitudes in the different apertures. In its surface brightness this feature is similar to the northern spur that can be seen around M31 (Ferguson et al. 2002). This feature could be the result of another accretion event. Given their relatively blue colors, the stream and the plume cannot be mistaken for Galactic cirrus clouds, because, as discussed in Section 5.1, the latter have a typical $g-r$ color between 1.3 and 2 mag.

5.4.1 STELLAR STREAMS AROUND MASSIVE SPIRALS

Stellar streams extending out of the planes of disk galaxies are well established as indicators of past interactions. Given the low density of the NGC 7331 galaxy group, the presence of stellar streams in NGC 7331 then is somewhat surprising. We focus our discussion on the western stream, but note that additional features are seen to the southwest of the galaxy. As the streams appear to be discontinuous and given that the estimated color of the southwestern feature is different from that of the western stream, we cannot tell whether these are two parts of one single stream or constitute two separate structures.

If the western stellar stream is tidal debris, then the galaxy producing it might be detectable. A system with the luminosity of $M_r = -10.8$ mag that we measured in the western stream segment located away from the obscuring main body of NGC 7331 would be included in our sample, but obviously was not found. The blue color of this stream segment, $(g - r)_0 = 0.15$ mag, suggests that it might have been produced by a star-forming galaxy (possibly a dIrr or a dIrr/dSph transition-type galaxy), even though no H I is seen today to be associated with the stream. The narrow projected width of the NGC 7331 stream indicates that such a progenitor would have had a low internal stellar velocity dispersion (Johnston et al. 2008). We thus speculate that the accreted galaxy could have been a low-mass dIrr or dIrr/dSph transition-type galaxy, consistent with the modest luminosity and low surface brightness ($\mu_{r,0} = 26.6 \pm 0.1$ mag arcsec^{-2}) of the western stream segment.

According to the color transformations of Fukugita et al. (1995) [$(B-V) = (g-r) + 0.07$, computed for irregular galaxies], the $(g-r)$ color of the stream translates into $(B-V) = 0.23$ mag, comparable with

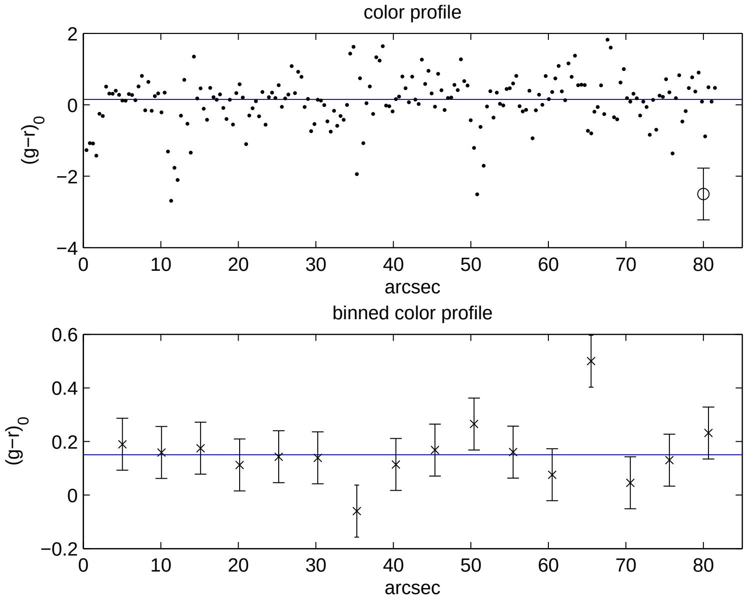

Figure 5.9: The color profile of the stream. The upper plot shows the individual color estimates per pixel. The bottom plot is binned with a bin size of 13 pixels. In both panels the line represents the calculated mean. Within the 1 σ errors no color gradient can be detected.

the colors of the bluest dIrrs in the Local Group (e.g., DDO210, Leo A, Sex A, SagDIG, from Mateo 1998). The observed blue color could alternatively be produced by old, extremely metal-poor stellar populations, which in addition may possess very blue horizontal branches. However, a comparison with the integrated $B - V$ colors of Galactic globular clusters from Harris (1996, (2010 edition)) does not reveal any comparable objects even at low metallicities. The ultra-compact dSph galaxies detected around the Milky Way in recent years (e.g., Zucker et al. 2006; Belokurov et al. 2006) tend to be even more metal-poor than globular clusters, but contain so few stars that they would not leave a recognizable stellar stream with the surface brightness of our stream candidate. The blue color of the stream could also indicate tidally triggered star formation caused by the disruption event if indeed the progenitor was a gas-rich dIrr galaxy. Such young stellar debris was found, for instance, in the halo of the peculiar elliptical galaxy NGC 5128 (Centaurus A), and its A-star colors resemble those of our candidate (Peng et al. 2002).

The time scale since formation of the stream is uncertain. If the NGC 7331 stream is the result of a interaction with a gas-rich dwarf contributing either young blue stars or undergoing tidally triggered star formation, which might suggest a fairly recent interaction a few Myr ago (see Peng et al. 2002). In the Local Group, stars with ages possibly as young as 800 Myr have been detected in the central regions of the Sgr dSph galaxy (Siegel et al. 2007), which is merging with the Milky Way. These stars formed long *after* Sgr began disrupting, but represent only a tiny fraction of the overall stellar populations of Sgr. In any case, interactions involving or leading to recent star formation may not be unusual. Alternatively, such a blue feature might, in principle, form from gas accreted from an intra-group medium. But the observed narrowness of the stream makes this scenario questionable. While star formation has been observed in tidal debris (Makarova et al. 2002; de Mello et al. 2008; Werk et al. 2008), to our knowledge it is not seen in the cases where *diffuse* H I is thought to be accreted onto galaxies (e.g., Sancisi et al. 2008), and therefore is a less likely possibility.

5.5 CONCLUSIONS

Summarising the first resultes of our survey for candidate tidal features and dwarf galaxies in a 160 kpc radius region surrounding the giant SAb spiral NGC 7331, located at an approximate distance of 14.2 Mpc. NGC 7331 is the primary member of a subgroup within a larger filamentary and relatively diffuse galaxy group of the same name. Our deep *g*- and *r*-band images reveal four dwarf galaxy candidates that have colors and structures consistent with dSph satellites close to NGC 7331. No examples of more luminous dE-like companions are found. Moreover, a faint western stellar stream is detected, which has a blue color and low surface brightness, possibly indicative of having had a star-forming, low-mass dIrr/dSph transition-type galaxy or a gas-rich dIrr undergoing tidally triggered star formation as its progenitor. There is also a more diffuse and less well-defined feature to the southwest, but it is unclear whether it is connected with the western stream.

Even though NGC 7331 is a giant spiral with higher total and bulge luminosities than M31, it apparently lacks M31's retinue of comparatively luminous dE satellites, as well as something like its compact elliptical companion M32. The absence of such luminous, massive dE companions means that the stellar mass in the form of inner satellites is 2% or less of that around M31.

On the other hand our few candidate dSph detections are consistent with NGC 7331 and M31 having comparable populations of (classical) dSph companions. The results of our study therefore agree with surveys showing highly variable numbers of moderate-luminosity satellites of giant galaxies, while suggesting that dSph satellites may be more closely tied to the properties of the main galaxy. The source of the large variance in spheroidal satellite stellar masses in galaxy groups remains an interesting question and a potential clue to the origin of these galaxies.

Given the paucity of neighboring galaxies, the detection of what appears to be a bluish stellar tidal debris stream is unexpected. The most straightforward explanation is that NGC 7331 interacted with and at least partially disrupted a star-forming low-mass transition-type dwarf, or that the accretion of a gas-rich dIrr triggered star formation. One of the four dSph candidates discovered in our study shows a blue core similar to more massive, nucleated dEs with recent central star formation found in the Virgo cluster, or similar to transition-type dwarfs with residual centralized star formation activity as observed in the Local Group. Deeper optical and H I observations would be useful in order to obtain a better understanding of the dwarfs and stream(s) around NGC 7331. In low-density groups like the diffuse, extended NGC 7331 group with its many late-type galaxies, interactions with gas-rich dwarfs may be more common than in higher-density environments.

6

ON THE CHARACTERIZATION OF TIDAL FEATURES

In order to characterize the nature of different tidal interactions a set of interacting galaxies has been observed with the 4m Mayall telescope. The initial aim was to check whether the different features, ranging from plumes and clouds to large shells and their origin can be distinguished by their observational properties with only performing photometry.

6.1 OBSERVATIONS

The observations were performed with the Mayall 4m telescope at Kitt Peak National Observatory during a four-night run in December 2010. The rebuilt MOSAIC 1.1 wide-field imager provides a field of view of $36' \times 36'$ with a pixel scale of $0.26''$ pixel^{-1}. In order to fill the gaps between the CCDs of the mosaic imager we took 5-6 exposures which were dithered with an offset of a few arcseconds. The targets were imaged through the SDSS g- and r-filters and the exposure time ranged from 36 to 60 minutes.

The properties of the observations can be found in Table 6.1. The distance range of the galaxies goes from 11.3 to 31.90 Mpc, and therefore the projected observed area varies between 127 kpc $\times$ 131 kpc and 496 kpc $\times$ 346 kpc. Given that the seeing varied from 0.97 to $1.43''$ during the run, it is now possible to detect faint substructures as extended as 60 up to 200 pc.

If the observed region was also imaged by the SDSS, the photometric calibration was done with photometry data from the SDSS DR7 (Abazajian et al. 2009). In our science images non-saturated stars were selected that have a sufficiently high enough signal-to-noise (S/N) ratio, and were matched to the corresponding SDSS magnitudes. This method was used to estimate the zeropoint for each filter. If the observed target galaxy could not be found in the SDSS, zeropoints from other galaxies were taken that we observed in the same night.

In this chapter the results for the different galaxies will be presented. In order to measure the surface brightness and the color of the observed tidal features the following technique was used. Each tidal feature was sampled with a number of small apertures distributed all around its area and avoiding foreground stars and background galaxies This is helpful because the influence of foreground stars and other objects could therefore be removed. The IRAF tool `imstat` was run in the selected boxes in order to get a statistical photometrical analysis on the basis of photon counts. After the comparison of the mean, mode

Table 6.1: Observational properties.

Name (1)	field of view (2)	t_{obs} g [min] (3)	t_{obs} r [min] (4)	DM [mag] (5)	distance (Mpc) (6)	field of view [kpc] (7)	seeing [$''$] g (r) (8)
NGC 2460	$53' \times 37'$	42	37	32.45±0.81	31.90	496 × 346	1.15 (1.39)
NGC 3227	$40' \times 40'$	60	38	31.6±0.04	20.85	242 × 242	1.25 (1.07)
NGC 3521	$39' \times 41'$	60	38	30.35±0.53	12.08	138 × 144	1.39 (1.43)
NGC 3628	$39' \times 40'$	60	36	30.2±0.6	11.3	127 × 131	1.16 (0.97)

Column (1) gives the name of the target, (2) gives the total field of view of all stacked observations of one target, (3) and (4) the total observing time in the SDSS *g*- and *r*-bands. The distance modulus (5) is listed together with the metric distance (6) which was taken from NED. Finally, the physical size of the field of view is given in column (7) as well as the seeing measured in the final stacked images in the *g*-band (in brackets in the *r*-band) in column (8).

and median value, later on the median value of each aperture was used (this way the influence of background objects, cosmic rays and foreground stars was reduced). Each box had a size of 60 ×60 pixels. This size turned out to be the optimum between the error of the count statistics of the individual pixels and the large-scale fluctuations caused by flat-field errors. With this technique, the surface brightness in the SDSS *g*- and *r*-band as well as the resulting colors could be measured. Due to the fact that several boxes for each feature were used, it was possible to measure the fluctuations of the measured values (Figure 6.1 – 6.8).

6.2 NGC 2460

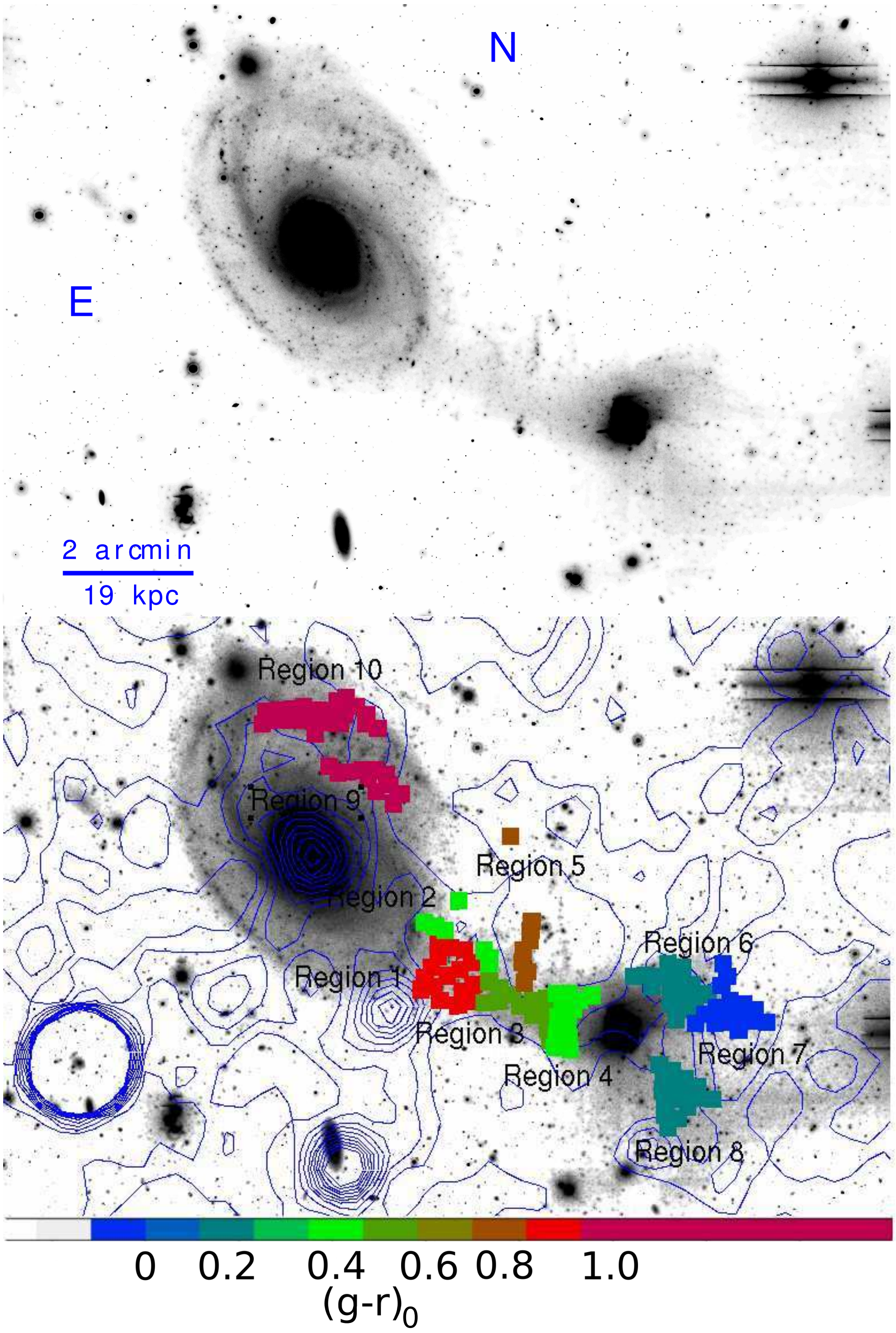

Figure 6.1: On top an image of NGC 2460 is shown. The lower panel shows how apertures were distributed in order to sample the tidal features of NGC 2460. These apertures are color-coded on the basis of their average $(g-r)_0$ color as given in the color bar at the bottom. Every aperture box has a size of 60 pixels.

NGC 2460 is an SAa galaxy at a distance of 31.9 Mpc. In Figure 6.1 the tidal interaction of this galaxy with the Sb galaxy IC 2209 can be seen. In order to characterize the different features their $(g-r)_0$ color was measured and corrected for Galactic foreground extinction. In Region 1 a red color of about 0.9 mag was obtained, which could be explained by an accreted late-type dwarf galaxy. In contrast a blue color of ~ 0.4 mag characterizes the bridge between these two galaxies (Region 2 to Region 4). Region 5 is the faintest region with a very low surface brightness of 26.32 mag arcsec^{-2} and also a red color of 0.72 mag. The different color of this faint feature is a hint that the progenitor may also have been a dwarf galaxy. Region 6, 7 and 8 cover the outskirts of IC 2209. The measured blue colors between -0.08 and 0.21 suggest that these regions may have experienced recent or ongoing star formation. Region 9 and 10 were only used for comparison of the spiral arms of NGC 2460 to the outer faint regions, the measured red colors could be explained by dust.

Typical S/N values per pixel averaged over all apertures ranged from 2.1 for the brightest regions to 0.67 for the faintest feature. This is only a lower limit, as we have used apertures covering many pixels. In total four different types of tidal debris can be observed around this target, showing that merging galaxies produce or are accompanied by very different tidal features. In Figure 6.2 the measured colors of the different faint features are plotted together with the corresponding surface brightness for the four studied galaxies.

NGC 2460 shows a bridge connecting it with its interaction partner IC 2209. Interestingly, blue colors were measured in these areas, which is typical for regions with recent or ongoing star formation. Region 3 and the neighboring regions 1 to 4 show a wide range of colors, which shows that the observed stellar populations can be very different. Around IC2209 in Region 6 to 8 even bluer colors are observed, which correspond to the tidal tails at the other end of the merging pair. Region 9 and 10 are used for consistency checks of the measured colors and for comparison to the spiral arms. The measured colors are much redder there and the spread is much smaller, we suggest that the red colors could be explained by dust.

Table 6.2: Measurements for NGC 2460

Region (1)	$\mu_{g,0}$ (2)	$\mu_{r,0}$ (3)	$(g-r)_0$ (4)
1	25.53 ± 0.38	24.64 ± 0.48	0.89 ± 0.20
2	25.49 ± 0.25	25.11 ± 0.21	0.38 ± 0.05
3	24.83 ± 0.28	24.35 ± 0.29	0.47 ± 0.13
4	24.02 ± 0.60	23.57 ± 0.64	0.45 ± 0.15
5	26.32 ± 0.73	25.60 ± 0.72	0.72 ± 0.20
6	24.17 ± 0.63	23.96 ± 0.68	0.21 ± 0.14
7	25.36 ± 0.38	25.44 ± 0.47	-0.08 ± 0.10
8	24.61 ± 0.32	24.48 ± 0.46	0.13 ± 0.22
9	23.71 ± 0.33	22.25 ± 0.32	1.46 ± 0.03
10	23.75 ± 0.53	22.45 ± 0.49	1.29 ± 0.10

The measured values for the different regions shown in Figure 6.1. Column (1) gives the numbered region, in (2) and (3) the corresponding SB are given in the SDSS *g*- and *r*-band together with the measured fluctuations. The measured color and the corresponding standard deviation is noted in column (4). All errors are the standard deviation of the different values measured in the apertures of each region.

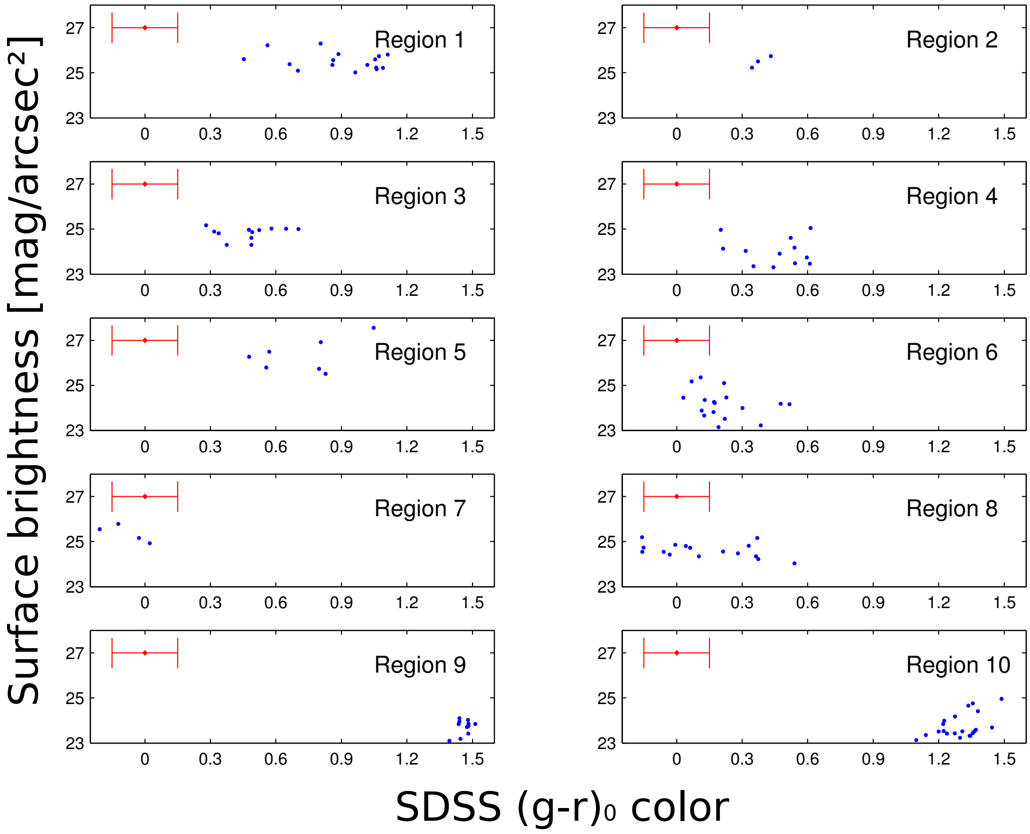

Figure 6.2: In this Figure a surface brightness (g-band) versus SDSS $(g - r) - 0$ color plot is shown for the faint tidal debris regions. For every studied region a graph is plotted, where each point represents one aperture with the measured SB and the corresponding color. The red error bar represents the typical error for the measurements (error of the photometric calibration and photometry).

6.3 NGC 3227

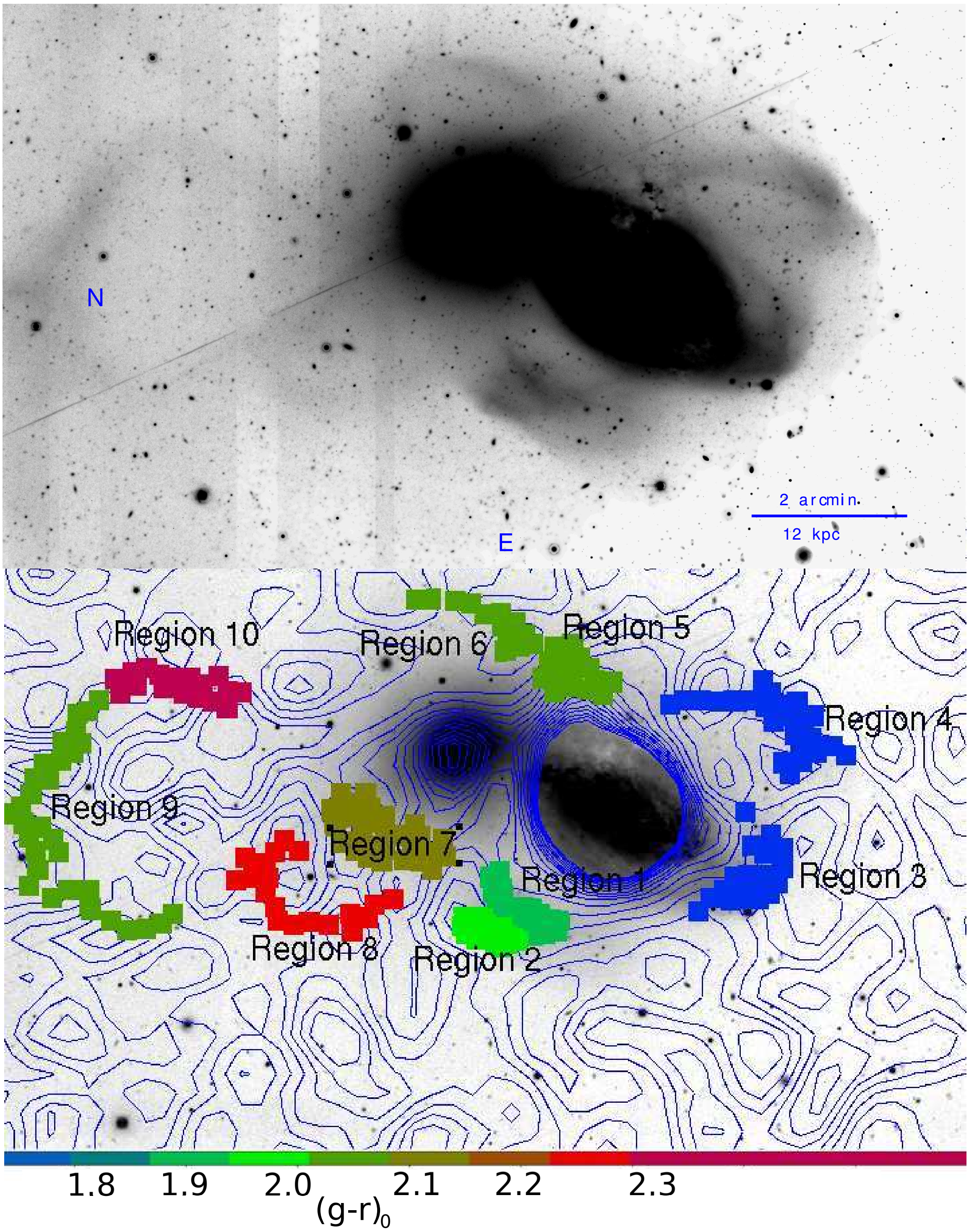

Figure 6.3: On top an image of NGC 3227 (right) together with NGC 3226 (left) is presented. In the lower panel the measured colors in the different regions are overplotted over a black and white image of the same size. Each box has a size of 60 pixels. The blue contours show the measured HI around these galaxies.

NGC 3227 is an SAB(s)a pec galaxy at a distance of 20.8 Mpc. Figure 6.3 shows an image of the ongoing major merger between NGC 3227 and the elliptical E2 galaxy NGC 3226, and a huge variety of tidal debris around these interacting galaxies is visible. Region 1 and 2 are some of the brightest substructures that can be detected in the outskirts and are connecting NGC 3227 and NGC 3226. The measured surface brightness and color help to distinguish between the two slightly different features. The measured color of $(g-r)_0 = 1.9$ cannot be explained by old stellar populations. Instead such extremely red colors are often produced by dust and HI clouds. Indeed HI observations confirm that a large amount of gaseous material can be seen around the merging system. An HI mass of the total system of $1.1 \times 10^9\ M_\odot$ is measured (Mundell et al. 1995). The similar color of Region 1 and 2 suggest that they have the same origin. In Region 3 a nice umbrella can be seen coming out of NGC 3227, which seems to be falling back. An arc coming out of the prime galaxy NGC 3227 is marked by Region 4. Region 5 is a diffuse structure between the two merging galaxies and Region 6 samples an arc connected to NGC 3226. The outer halo of NGC 3227 is studied in Region 7 and another arc which is pointing to NGC 3226 is marked by Region 8. Additionally, an extended arc far in the outskirts can be identified, it is marked by Region 9 and 10.

We measured also lower limits for the S/N per pixel for every aperture. The averaged values for the different regions were varying by a large factor. The faintest regions show on average a S/N ~1.7 and the bright features have high values of ~13.5. All features show similar colors, which suggests that across all regions dust and HI are the main reason for the red colors. Therefore it is not possible to characterize the stellar populations in the tidal debris features.

In Figure 6.4 the measured colors of the different faint features are plotted together with the corresponding surface brightness for the four studied galaxies. The colors measured around NGC 3227 are in contrast to the previous galaxy very red. They appear to consist mostly of material like stars and dust that was probably torn out during the merging process. As argued before, the color range of the red colors is narrow. We see these trend in every region investigated here. Region 3 and 4 are following the previous trend, but these regions are slightly bluer than the rest as they are on the side of NGC 3227 that points away from the interaction direction and additionally show a wider color range as well.

Table 6.3: Measurements for NGC 3227

Region (1)	$\mu_{g,0}$ (2)	$\mu_{r,0}$ (3)	$(g-r)_0$ (4)
1	20.18 ± 0.17	18.28 ± 0.16	1.9 ± 0.04
2	20.84 ± 0.47	18.91 ± 0.46	1.92± 0.04
3	20.02 ± 0.95	18.32 ± 0.94	1.71± 0.05
4	21.86 ± 0.68	20.21 ± 0.79	1.65± 0.12
5	20.50 ± 0.63	18.47 ± 0.63	2.03± 0.03
6	21.61 ± 0.58	19.57 ± 0.64	2.03± 0.06
7	20.67 ± 0.58	18.59 ± 0.57	2.07± 0.05
8	22.93 ± 0.43	20.74 ± 0.45	2.19± 0.13
9	22.92 ± 0.49	20.88 ± 0.48	2.04± 0.11
10	23.60 ± 0.10	21.08 ± 0.11	2.53± 0.04

The measured values for the different regions shown in Figure 6.3. Column (1) gives the numbered region, in (2) and (3) the corresponding SB are given in the SDSS *g*- and *r*-bands together with the measured fluctuations. The measured color and the corresponding standard deviation is noted in column (4).

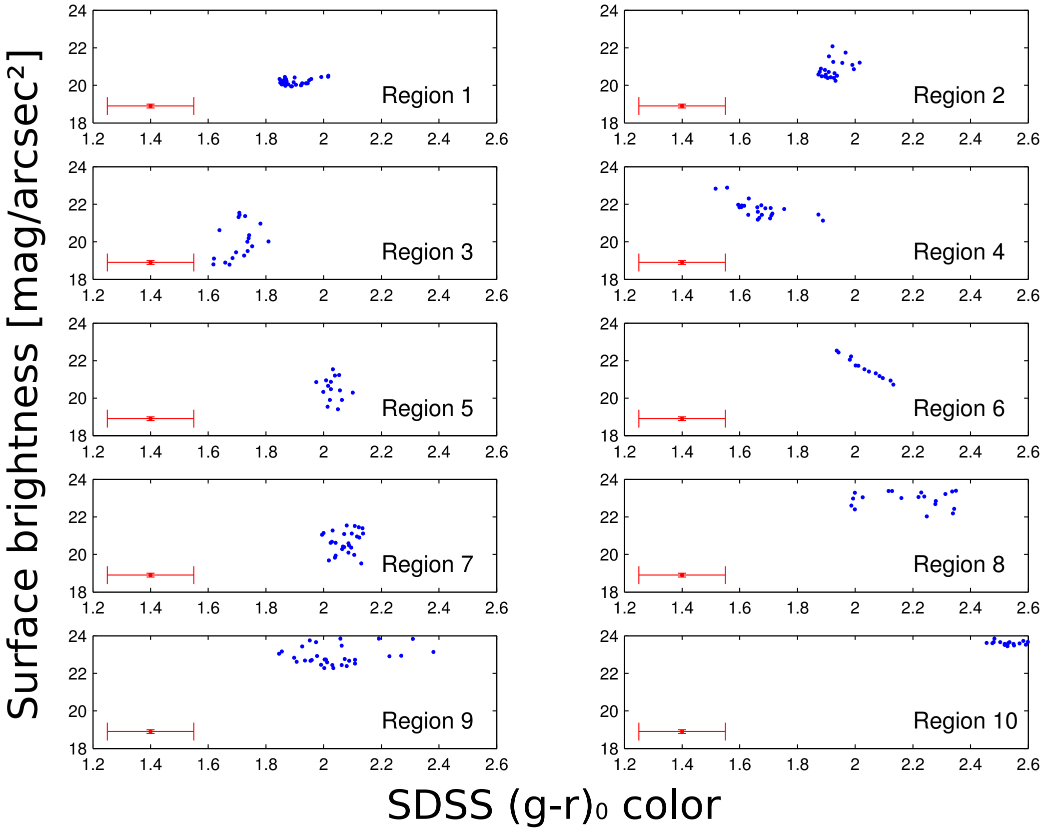

Figure 6.4: In this Figure a surface brightness (g-band) versus SDSS $(g - r) - 0$ color plot is shown for the faint tidal debris regions. For every studied region a graph is shown, where each point represents one aperture with the measured SB and the corresponding color. The red error bar represents the typical error for the measurements (error of the photometric calibration and photometry).

6.4 NGC 3628

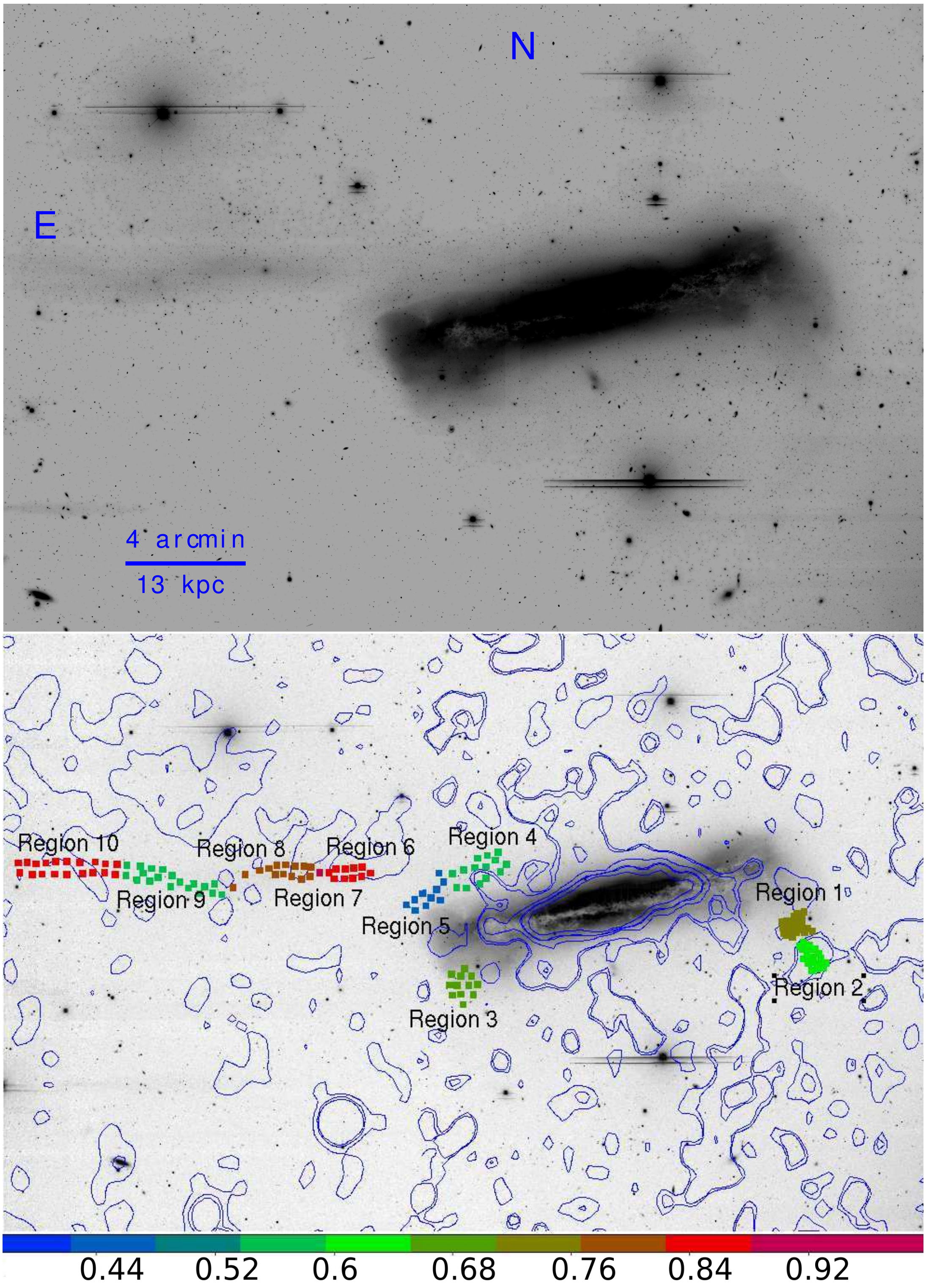

Figure 6.5: On top a smoothed image of NGC 3628 in the *g*-band is shown. In the lower panel the measured colores in the different regions were highlighted. The blue contours show the measured HI around these galaxies.

NGC 3628 is an Sb pec galaxy at a distance of 11.3 Mpc showing different tidal debris structures, which are either filamentary or diffuse. In Region 1 and 2 clearly one can see a diffuse structure with an intermediate color $(g-r)_0 \approx 0.65$ mag. On the other side of the disk a similar feature can be identified which is labeled Region 3. Their similar colors may indicate that the features in Regions 1, 2 and 3 arose from a past merging event. The same could be said for Regions 4 and 5 on the basis of their colors, though in Region 5 a common bluer color is measured. The tidal interaction with a surrounding dwarf satellite is studied with Region 6 to 10, within the error they all show the same range of observed colors. The extended long and thin structure of the stream suggests that this feature was produced by a disrupted satellite. Region 7 marks the densest region, the slightly redder color and higher brightness as well as the compact appearance could be a hint that Region 7 is the core of the former satellite.

The tidal debris features show very different values of the SB, thus the averaged S/N per pixel over all apertures is ~0.3 for the faintest regions and ~4.0 for the brightest ones, again these are only lower limits.

In Figure 6.6 the measured colors of the different faint features are plotted together with the corresponding surface brightness for the four studied galaxies.

Around NGC 3628 the same trends as in the other targets are observed. The observational error of the color estimation was much more uncertain due to larger errors in the photometric zeropoints, thus the color ranges are wider from the beginning. This galaxy is in an advanced state of the merging process, as all the colors of the widely distributed features are similar. Only the faint lance coming out of NGC 3628 is a bit different compared to the other features, as the origin is most likely another interaction event. The spread of the color distribution is much wider, this could be a hint that the material is coming from an accreted dwarf companion.

Table 6.4: Measurements for NGC 3628

Region (1)	$\mu_{g,0}$ (2)	$\mu_{r,0}$ (3)	$(g-r)_0$ (4)
1	22.14 ± 0.45	21.42 ± 0.47	0.71 ± 0.04
2	24.11 ± 0.57	23.48 ± 0.67	0.62 ± 0.13
3	21.28 ± 0.58	20.59 ± 0.59	0.69 ± 0.04
4	23.01 ± 0.31	22.44 ± 0.42	0.57 ± 0.12
5	23.75 ± 0.68	23.29 ± 0.74	0.45 ± 0.10
6	24.54 ± 0.26	23.71 ± 0.35	0.83 ± 0.11
7	23.57 ± —	22.59 ± —	0.99 ± —-
8	24.01 ± 0.25	23.24 ± 0.28	0.77 ± 0.12
9	24.93 ± 0.43	24.35 ± 0.42	0.58 ± 0.10
10	25.61 ± 0.41	24.78 ± 0.73	0.83± 0.41

The measured values for the different regions shown in Figure 6.5. Column (1) gives the numbered region, in (2) and (3) the corresponding SB are given in the SDSS *g*- and *r*-band together with the measured fluctuations. The measured color and the corresponding standard deviation is noted in column (4).

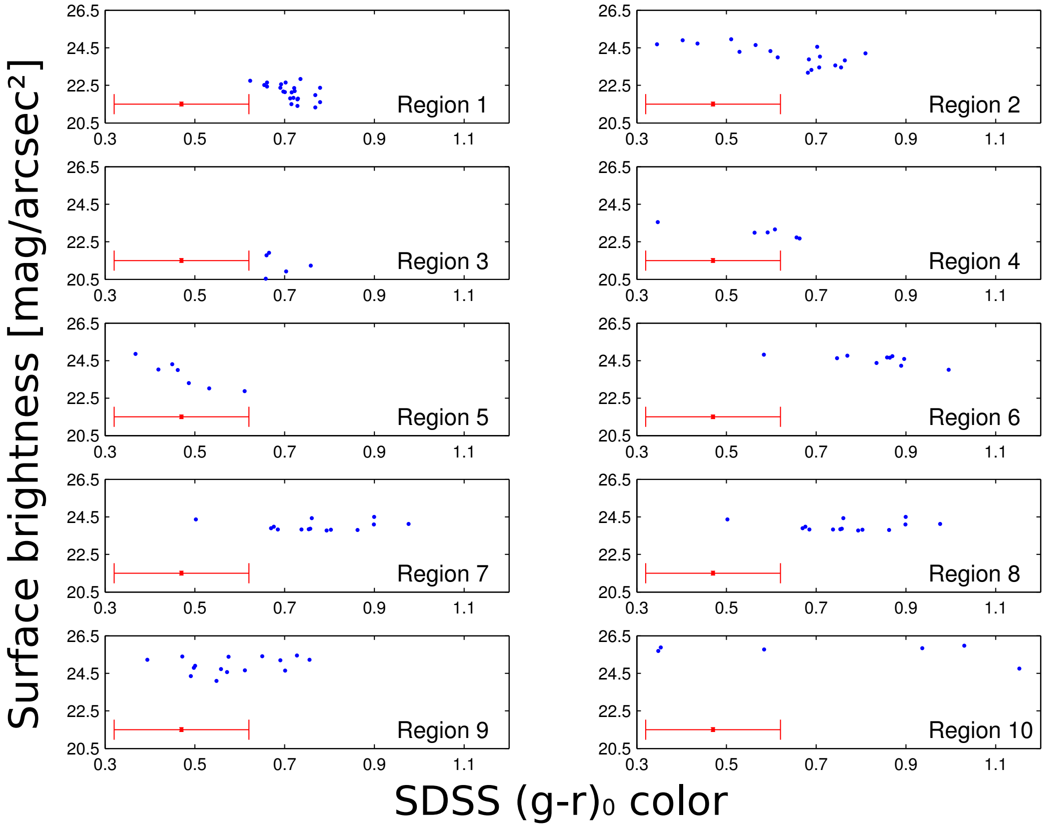

Figure 6.6: In this Figure a surface brightness (*g*-band) versus SDSS $(g-r)-0$ color plot is shown for the faint tidal debris regions. For every studied region a graph is plotted, where each point represents one aperture with the measured SB and the corresponding color. The red error bar represents the typical error for the measurements (error of the photometric calibration and photometry).

6.5 NGC 3521

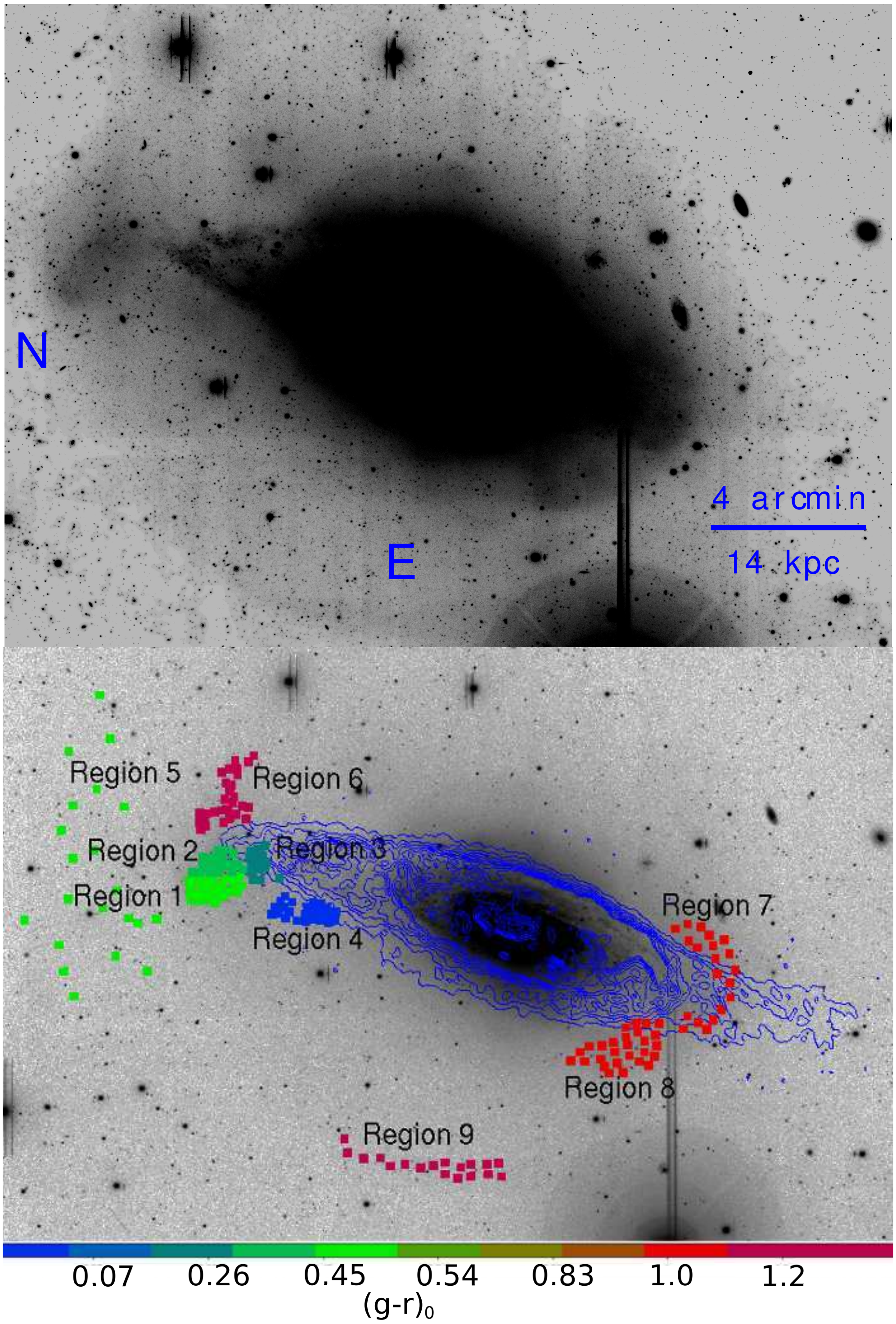

Figure 6.7: A panoramic view around NGC 3521 shown with a gray-scale plot, which was observed in the g-band. In the lower panel the measured $(g-r)_0$ colors in different regions are color-coded as given in the color bar at the bottom. The upper and lower panel are not perfectly aligned and have slightly different scales. The blue contours show the measured HI around the galaxy.

NGC 3521 is an SAB(rs)bc galaxy at a distance of 12.1 Mpc. Around this galaxy we can observe a nice umbrella coming out from the disc, already observed by Martínez-Delgado et al. (2010), who did not perform any color measurement. This was the reason to re-observe this target through two filters. The brightest part of the tidal debris is located in Region 1 and 2. The average color of these regions of $(g - r)_0 \sim 0.4$ mag could hint to a dwarf galaxy as the origin of the umbrella. In the image also a connection from the umbrella to the disk can be detected (Region 3) and a faint extension of the umbrella in the west is marked with Region 6. Additionally, another feature close-by can be seen which is labeled Region 4. Its blue color is a sign of current star formation. Another trace of tidal debris is visible on the other side of the disc, this diffuse structure has been sampled in 7 and 8. Its observed red color $(g - r)_0 \sim 1.1$ mag makes it different from the umbrella. In the outskirts of NGC 3521 a extended and faint arc (Region 9) can be detected, the observed red color of Region 7 to 9 (possibly caused by the same accretion event) could be explained by an accreted dwarf companion which has a very old stellar population.

In order to check the detection of the different faint features we calculated the lower limit of the S/N ratios of the tidal features, averaging over all apertures of each region these range from ~0.7 to ~4.0 for the brightest tidal debris components. In Figure 6.8 the measured colors of the different faint features are plotted together with the corresponding surface brightness for the four studied galaxies.

The stellar populations which can be seen around NGC 3521 are much more complex as compared to the other interacting systems. The measured colors can be used to set a very rough estimate of the underlying stellar populations in the observed regions. The Regions 1-4 show very blue colors. Again this could be interpreted as signs for ongoing or recent star formation. The other regions show much redder colors. Especially Region 6 and 9 show interesting trends, the measured surface brightness is decreasing with increasing color. This again supports the proposed interpretation of recent or ongoing star formation, as populations without star formation and comparable stellar mass are usually less bright. In summary very different colors can be detected, which may be a hint that the studied features have a different origin. Looking at this diversity a side-step onto the HI-distribution can be quite interesting. Around a clearly pronounced warp in the HI (the HI data were taken from Walter et al. 2008) mostly red and old stellar populations are observed. In contrast to that on the other side the HI is much more smooth and less dense and a bright umbrella with blue colors can be seen. The reason for that could be that on the "blue" side with the bright tidal debris feature the gas is at a higher density and thus star formation started. On the other side the gas density was not high enough and the interacting event could only disturb the HI distribution.

Table 6.5: Measurements for NGC 3521

Region (1)	$\mu_{g,0}$ (2)	$\mu_{r,0}$ (3)	$(g-r)_0$ (4)
1	22.33 ± 0.71	21.84 ± 0.85	0.50 ± 0.18
2	23.05 ± 0.38	22.75 ± 0.42	0.30 ± 0.06
3	23.50 ± 0.90	23.26 ± 1.35	0.23 ± 0.27
4	23.99 ± 0.48	23.97 ± 0.83	0.02 ± 0.36
5	23.23 ± 0.62	22.73 ± 0.64	0.50 ± 0.15
6	21.04 ± 1.06	19.80 ± 0.96	1.23 ± 0.16
7	21.29 ± 1.11	20.21 ± 1.18	1.08 ± 0.08
8	21.84 ± 0.76	20.73 ± 0.69	1.11 ± 0.07
9	24.49 ± 1.94	23.10 ± 1.62	1.38 ± 0.36
10	22.32 ± 1.04	21.09 ± 1.05	1.23 ± 0.09

The measured values for the different regions shown in Figure 6.7. Column (1) gives the numbered region, in (2) and (3) the corresponding SB are given in the SDSS *g*- and *r*-band together with the measured fluctuations. The measured color and the corresponding standard deviation is noted in column (4).

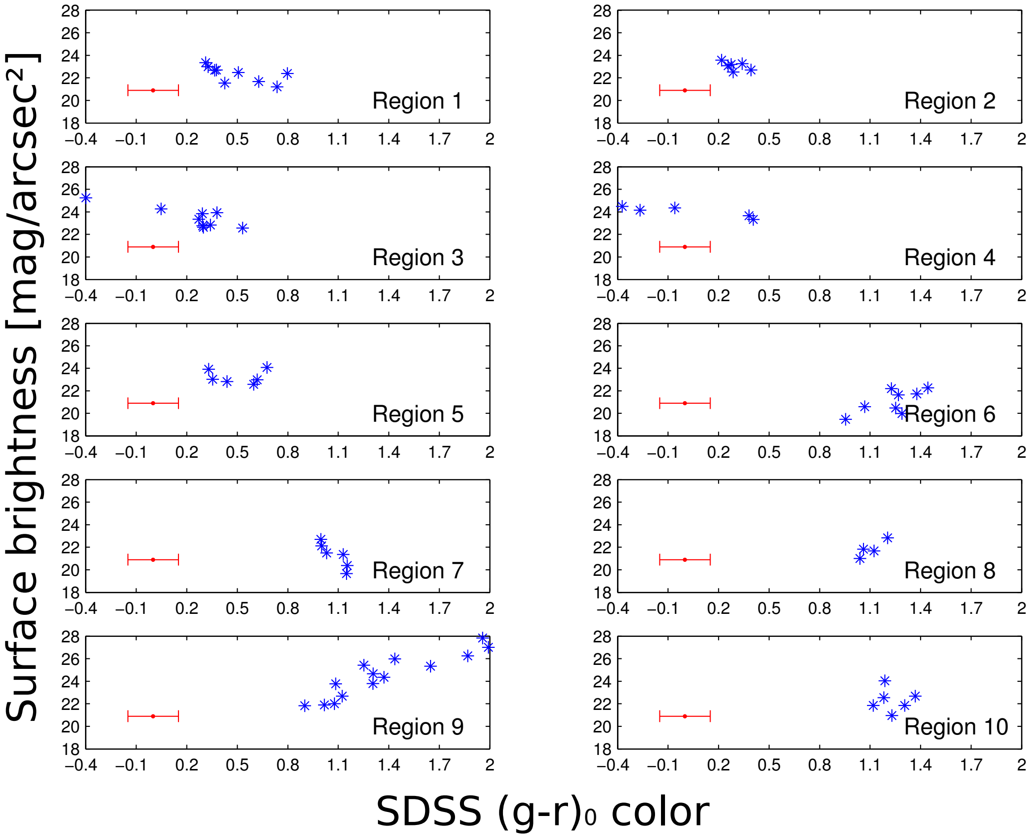

Figure 6.8: In this Figure a surface brightness (*g*-band) versus SDSS $(g-r)-0$ color plot is shown for the faint tidal debris regions. For every studied region a graph is shown, where each point represents one aperture with the measured SB and the corresponding color. The red error bar represents the typical error for the measurements (error of the photometric calibration and photometry).

6.6 CANDIDATE DWARF GALAXIES

The benefit of using a wide-field imager is that also close-by companions can be detected. In the following section we will report on candidate dwarf galaxies that were found near the observed targets. Around each galaxy several candidate dwarf galaxies (CDG) were detected. Candidates were selected by visual inspection of the images and the observed morphology, e.g. a smooth and extended light distribution with low SB for dSphs, was the main criteria in order to classify them as possible satellites. Also the size of the CDGs played an important role, due to the limited resolution only targets with sizes larger than five times the typical seeing could be resolved in order to classify its morphology. The available field of view limits the observations only to the inner regions of the host galaxy environment. Typical distances of the dwarf galaxy candidates to the central galaxy vary from 10 to 120 kpc.

In order to perform photometry on the candidates SExtractor was used to measure the basic properties like the center of the object, ellipticity, magnitude and surface brightness. If the signal was high enough all measurements were 3σ above the background, only for the faintest CDG a lower limit of 1σ was set. The SExtractor ellipticity was used as input for the IRAF tool `ellipse`, that was run on the candidates in order to fit isophotes as a function of semi-major axis and to construct the candidates surface brightness profiles and integrated $(g-r)$ colors (integrated over a common area with a radius where the signal in the *g*-band is 1σ above the background). Then the surface brightness profile (SBP) of the candidates were fitted with a Sérsic function, to characterize their structural parameters.

Stamp images (on the left hand side) and the corresponding SBP (right) fit of the selected dwarfs galaxy candidates are shown in figures 6.9 – 6.35. The red ellipse in the stamp images highlights the area of the galaxy that lays 1 σ above the background. The plotted ellipse visualizes the CDG's ellipticity and the position angle measured as described before. The structural parameters of the best-fitting Sérsic profile for the observed SB profile are listed in the lower left hand corner; *n* is the Sérsic index, *csb* is the central surface brightness and *r* is the scale length. All measured parameters agree very well with other confirmed dwarf galaxies in previous studies (see section 7.1).

The optical appearance and the estimated structural parameters finally support the claim that the observed targets are dwarf galaxies, but in order to confirm these as true satellites spectroscopic measurements are needed to estimate their redshifts.

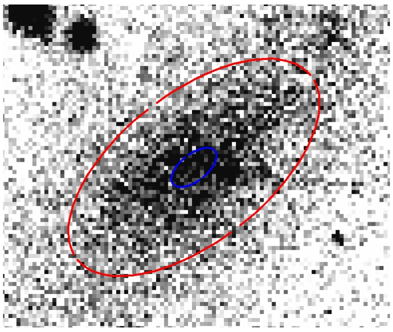

Figure 6.9: CDG NGC 2460 A

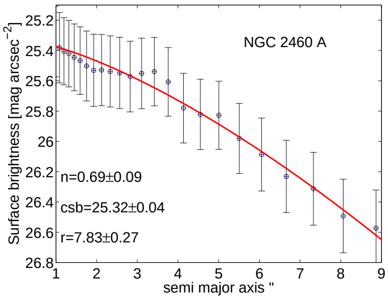

Figure 6.10: SBP of NGC 2460 A

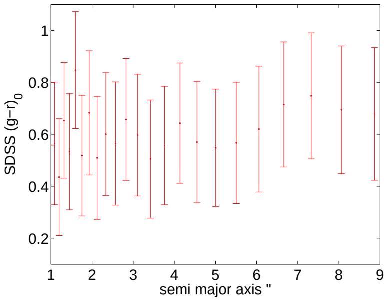

Figure 6.11: Color profile of NGC 2460 A

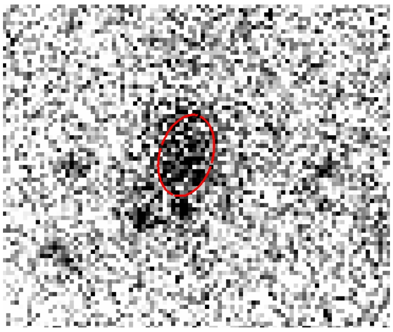

Figure 6.12: CDG NGC 2460 B

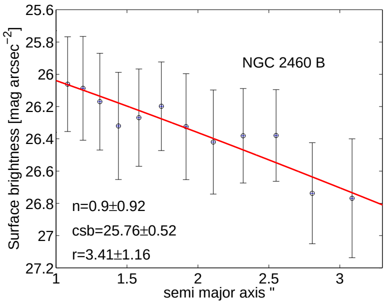

Figure 6.13: SBP of NGC 2460 B

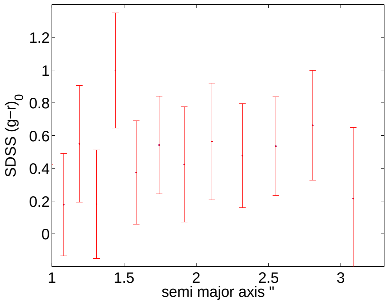

Figure 6.14: Color profile of NGC 2460 B

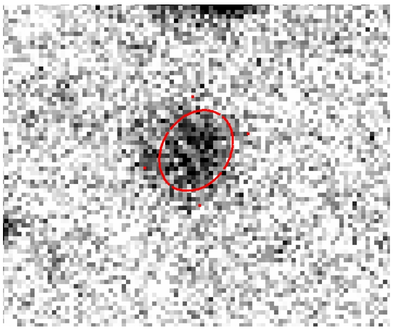

Figure 6.15: CDG NGC 2460 C

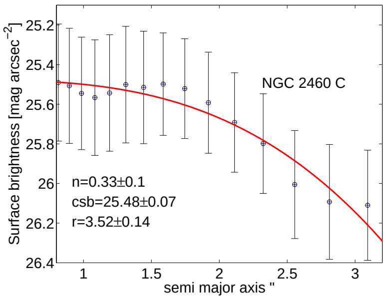

Figure 6.16: SBP of NGC 2460 C

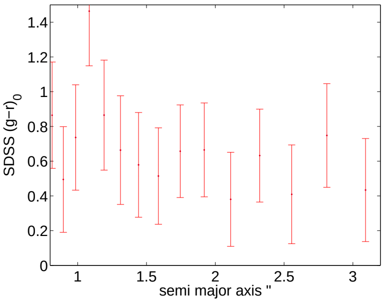

Figure 6.17: Color profile of NGC 2460 C

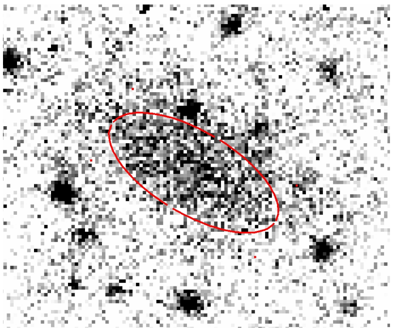

Figure 6.18: CDG NGC 3227 A

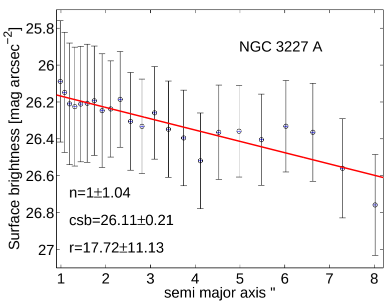

Figure 6.19: SBP of NGC 3227 A

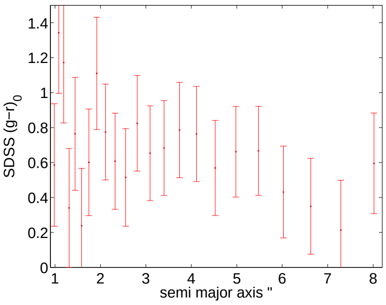

Figure 6.20: Color profile of NGC 3227 A

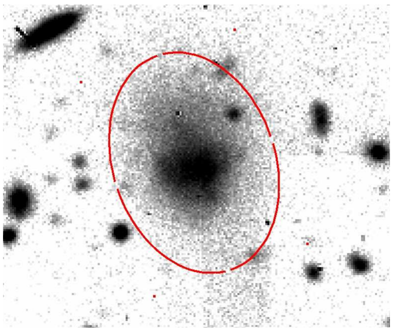

Figure 6.21: CDG NGC 3227 B

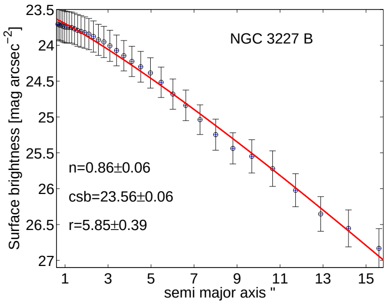

Figure 6.22: SBP of NGC 3227 B

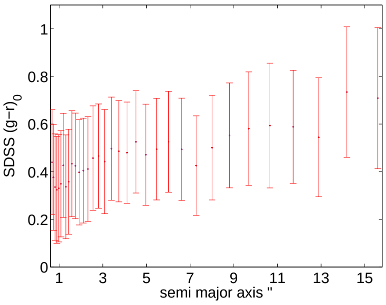

Figure 6.23: Color profile of NGC 3227 B

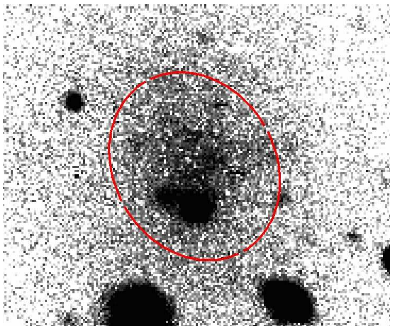

Figure 6.24: CDG NGC 3521 A

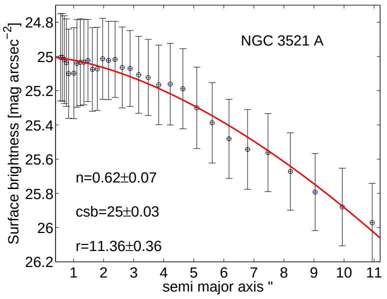

Figure 6.25: SBP of NGC 3521 A

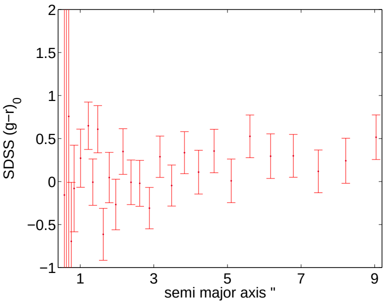

Figure 6.26: Color profile of NGC 3521 A

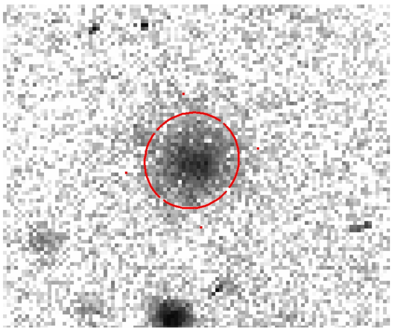

Figure 6.27: CDG NGC 3521 B

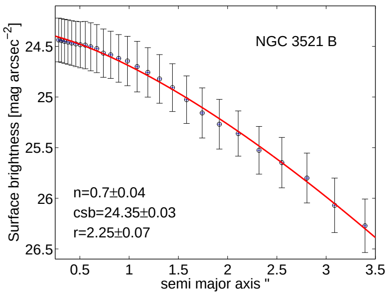

Figure 6.28: SBP of NGC 3521 B

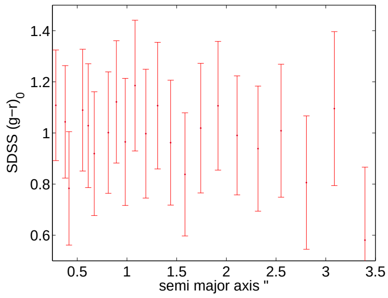

Figure 6.29: Color profile of NGC 3521 B

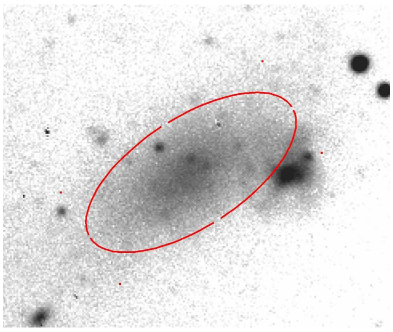

Figure 6.30: CDG NGC 3628 A

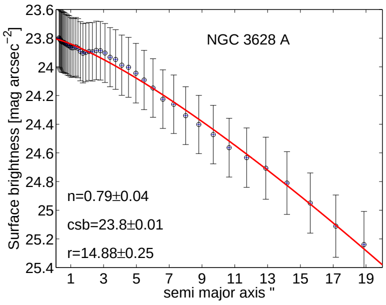

Figure 6.31: SBP of NGC 3628 A

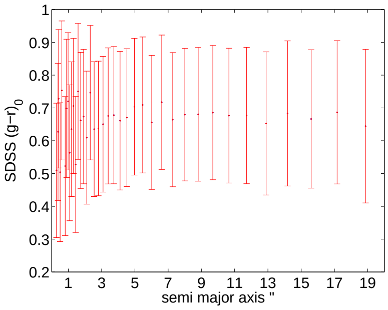

Figure 6.32: Color profile of NGC 3628 A

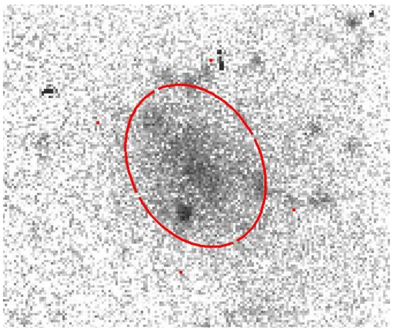

Figure 6.33: CDG NGC 3628 B

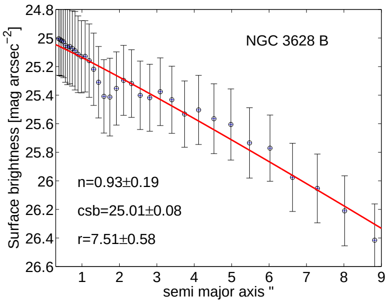

Figure 6.34: SBP of NGC 3628 B

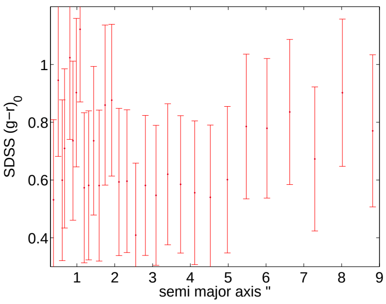

Figure 6.35: Color profile of NGC 3628 B

Figure 6.9 – 6.35: On the left hand side, stamp images of the CDG are displayed. The red circle marks the ellipse that corresponds to an isophote with a signal of 1 σ above the background. The shown ellipses visualize the measured ellipticity and the position angle. In the middle the surface brightness profile of the CDG can be seen. The parameters of the fit of a Sérsic function to the light profile is shown in the left lower corner. The red ellipses on the left highlight the semi-major axis out to which the fit was performed. The color profile of the CDG can be found on the right hand side. We do not find any color gradient in any of the candidates, only scatter around the measured color can be seen.

Table 6.6: Dwarf galaxy candidates

Name (1)	$g_0(1\sigma)$ (2)	$g_0(3\sigma)$ (3)	$r_0(1\sigma)$ (4)	$r_0(3\sigma)$ (5)	D_{cent}[kpc] (6)	$(g-r)_0$ (7)	$M_{r,0}$ (8)
NGC 2460 A	20.19	22.54	19.44	21.00	32	0.70	-13.176
NGC 2460 B	23.32	—	22.86	—	36	0.51	-9.756
NGC 2460 C	23.07	—	21.59	—	53	0.56	-11.026
NGC 3227 A	21.63	—	21.68	—	11	0.55	-9.972
NGC 3227 B	18.86	19.18	18.41	18.86	12	0.535	-13.242
NGC 3521 A	19.86	19.93	18.97	19.11	80	1.03	-11.561
NGC 3521 B	22.71	22.68	21.68	21.53	81	0.97	-8.851
NGC 3628 A	18.16	18.50	18.25	18.79	10	0.67	-12.012
NGC 3628 B	20.66	23.00	20.89	22.49	70	0.71	-9.372

Column (1) gives the name of each candidate. The apparent magnitude in the SDSS *g*-band is given in column (2) at 1 σ above the background and at 3 σ in column (3). The same is listed for the SDSS *r*-band in column (4) and (5). In column (6) the projected distance to the central galaxy D_{cent} is reported, assuming that the dwarf is roughly at same distance from the observer as the central galaxy. (7) gives the SDSS $(g-r)_0$ color corrected already for Galactic foreground extinction and (8) the absolute magnitude in the *r*-band.

6.7 THE GROUP ENVIRONMENT

In order to study the environment of our selected massive spiral galaxies NED[1] was used to search for the nearest neighbors.

The search radius was limited to 750 kpc in right ascension and declination and to $\sim \pm 300$ km s^{-1} in radial velocity, which should cover most of the members of the observed groups when following the definition for the virial radius of groups in Karachentsev (2005).

An overview of the different groups is shown in figures 6.36 – 6.39. When comparing the different groups one can easily realize that NGC 3521 is in a low density area, NGC 2460 and NGC 3227 are part of filamentary structure and NGC 3628 is living in a very rich group. Besides these differences in the environment we found no significant difference in the number and properties of dwarf galaxies which can be found around the massive spiral galaxies. This suggests that the population of dwarf galaxies detected in our data does not significantly depend on galaxy environment.

6.8 CHARACTERISATION OF TIDAL INTERACTIONS

In the last years sensitive detectors have enabled scientists a new view on the evolution of galaxies and their outskirts. Besides the well-known bright and more or less homogeneous structures like spiral arms and elliptical isophotes also very disturbed faint features can be seen in the outskirts of galaxies. These features range from faint streams to big tidal tails of merging galaxies. Four different interaction stages are presented in this chapter, which follow roughly the Toomre sequence (Toomre 1977). The Toomre sequence illustrates the merger process of spiral galaxies, after the first approach follows the

---

[1] URL: http://ned.ipac.caltech.edu

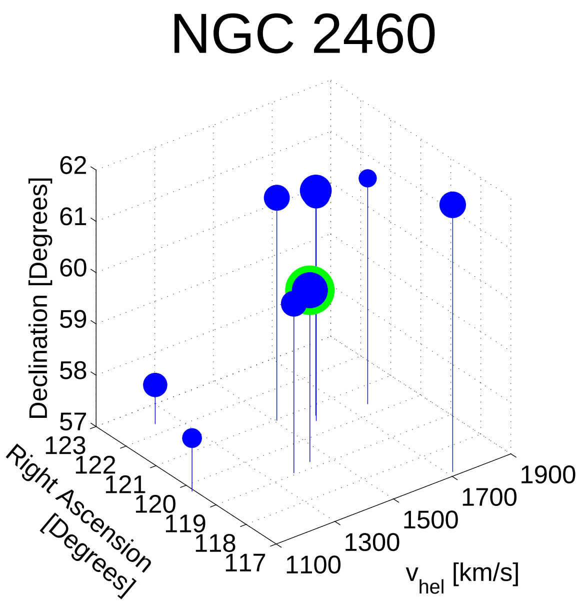

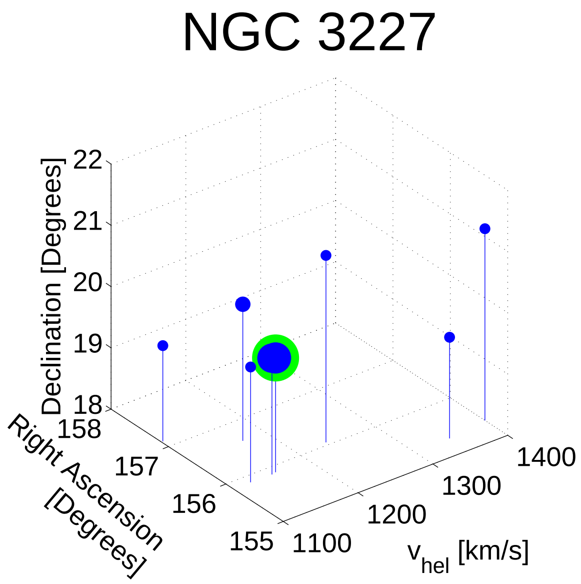

Figure 6.36: The environment around NGC 2460

Figure 6.37: The environment around NGC 3227

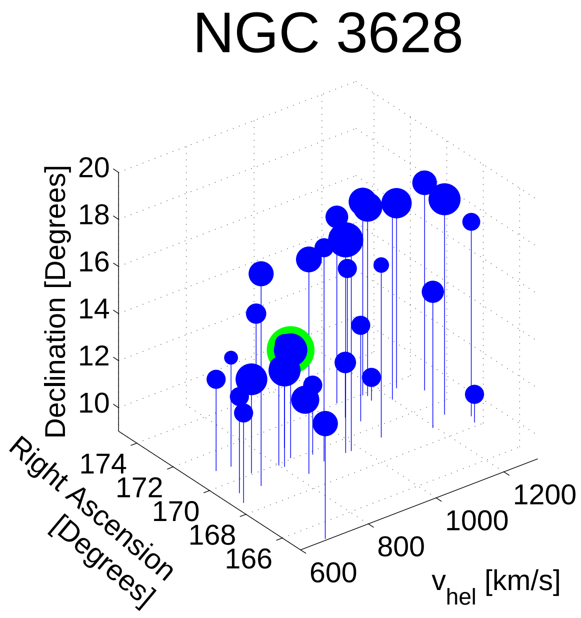

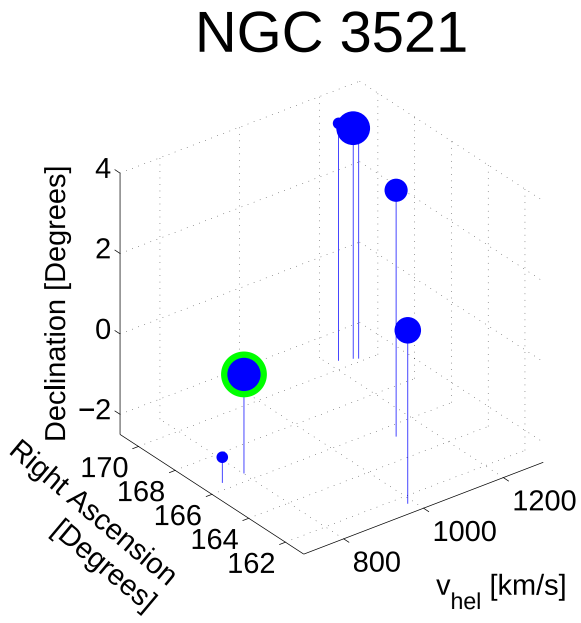

Figure 6.38: The environment around NGC 3628

Figure 6.39: The environment around NGC 3521

Figure 6.36 – 6.39: The environment around the observed galaxies. All neighboring galaxies are displayed down to $M_B \leq -16$. The dot size is scaled to the luminosity of each target. The green circle marks the studied galaxy.

actual merger process. In the next step the central merging has finished, after the galaxy stabilized again, finally, little evidence for the interaction can be seen. In NGC 2460 the interaction has just started. It seems that the interacting companion is on the first passage, and therefore this is the initial stage of a minor merger.

NGC 3227 is a very complex system of different structures, which suggests that it is a first stage of a major merger. Also an elliptical galaxy is involved in this merging system. NGC 3628 shows a more advanced phase of a merger. Big disturbances of the disc are still visible, but the galaxy has regained a regular morphology. Therefore we classified NGC 3628 as an evolved minor merger where the companion has been highly stretched. The last galaxy of this sample is NGC 3521. Its companion is not visible any longer. Thus it is in the final coalescence state of a merger, only faint features are still visible and the disc as completely stabilized again.

Tidal debris comes in various forms and over a huge variety with respect to appearance and luminosity. The main question now is whether there is a common origin of these features. Clearly this depends mostly on the parameter space which is given by the interacting galaxies in form of masses, orbits and infalling velocity angles.

One idea is that there is a clear distinction of features with different luminosity. A basic description would be that bright features belong to minor or major mergers and faint tidal debris structures are produced by accretion of small satellite companions.

In order to study these different scenarios the sample galaxies were selected for a comparison among different merging and accretion events. Therefore deep imaging of merging and accreting galaxies was performed in the SDSS g- and r-band for a rough characterization of the underlying stellar populations and the origin of tidal features.

The color measurements were used to highlight that with this technique it is possible to study the origin of this features. The measured color is an indicator of the stellar populations which can be found in these features.

Summarizing the measured colors and brightness of all targets one can learn from these different stages of merging galaxies that the observed spread of colors is very wide, ranging from blue star forming regions to older stellar populations with $g - r > 1.0$. We find also hints that different merging/accretion events can be observed around some targets. Comparing the measured colors to other observations (Knierman et al. 2013; Wehner et al. 2006), blue colors and regions with ongoing or recent star formation are observed, on the other side streams can also show red colors (Beaton et al. 2013; Chonis et al. 2011) and the same variation of distributed colors from blue to red (Miskolczi et al. 2011). Taking into account these results, the observations of debris structures around merging galaxies cannot rule out that many of the observed streams are a relict of such merging events. So the origin of faint features around massive spiral galaxies will still be a matter of debate.

The lifetime of bright tidal debris features together with the merger rate at $z = 0$ can be used for an approximation of what is expected to be observed in the nearby universe. Following Johnston et al. (2001), faint features lose more than 2 magnitudes per gigayear. Taking into account that the major merger rate is a strong function of redshift and that the minor merger rate is only marginally dependent on redshift we see that the frequency of left-overs from merging galaxies is in the same order as tidal debris around galaxies (19% of all galaxies show faint features, Miskolczi et al. 2011)

Interestingly, the results show that the initial properties of scenarios which can lead to faint tidal debris structures can be very different. As the analysis shows, all kind of expected properties ranging from young and blue to old and red stellar populations can be found in the faint debris regions. Therefore many different processes must be responsible for the creation of such structures. The observations show that the origin of the studied features can be thrown out stellar material from the merging counterparts as well as newly formed stars.

It should be noted here as well that all galaxies with faint debris in the outskirts show always warps or even more disturbances. Therefore one can usually detect a morphological change in the appearance of the central galaxies. This point cannot be turned the other way round, as not all disturbed galaxies show the studied tidal debris. The short lifetime of tidal debris also makes it difficult to argue about the frequency of mergers.

The limited one color study can tell only very roughly the nature of the stellar populations which can be found in the studied tidal debris features. For a detailed study of the origin and further properties of the stellar populations observations in different bands would be necessary. Especially the connection to the HI distribution could give very useful hints to disentangle the origin. Many galaxies show a clear distinction between the disturbance of stellar material on the one hand and on the other of the HI distribution. This makes it necessary that the origin could be different to the proposed scenarios of tidal debris which is produced by major/minor mergers and accretion events. Thinkable are for example galactic fountains which can produce young star forming regions which are triggered by merging galaxies or HI reservoirs where shocks induce the same effects. For old and red populations it is a bit more difficult to think about alternatives, but in principle the interacting galaxies do not need to be destroyed and tidal effects could be responsible that one observes old material removed from the merging partners without a full merger of the two counterparts.

6.9 CANDIDATE DWARF GALAXIES IN THE MERGER ENVIRONMENT

In the Local Group many dwarf galaxy companions to the spiral galaxies are observed. Additionally, it is often argued that many parts of the Local Group are in tidal interaction with each other. A very interesting question is whether this is affecting the abundance and the properties of the dwarf galaxy companions.

For this comparison an approximation is performed in order to examine how many dwarf galaxies would have been found if the MW and the M31 would have been observed at the same distance as the studied galaxies. Therefore the Local Group was virtually moved to the distance range of the studied galaxies. The most influencing limits are the resolution and the field of view. Taking the resolution, the field of view, the limiting magnitude and surface brightness into account, it is expected to find about two dwarf galaxies around each target, as galaxies with larger distances would only show the most massive companions and ones with smaller distances will only show the most close-by dwarf galaxies. Interestingly all the observed galaxies show two or more candidates. This result could suggest that there is no major change in the luminosity function of galaxies caused by merging events as no change on the luminosity function is detected within the sensitivity range covered here (see discussion in 8.2).

7

DWARF GALAXIES IN NEARBY GALAXY GROUPS

In this chapter there will be a report on the survey using the WFI camera. We will first highlight the results from other studies to which the proposed candidates will be compared. CDG were selected first by visual inspection of the science images. Their morphology was the basis in order to consider them as candidates. Later on photometry of the targets was used to calculate the magnitudes, the color, the SBP and the color profile of each candidate. These examined parameters are helpful in order to classify them as CDG or declare them as background object. This method is the only way how CDG can be found. Chiboucas et al. (2010) demonstrate with follow-up spectroscopic observations that this strategy is very successful in predicting CDG. We categorized the CDG into three classes:

1. **CDG A** are all candidates which are most likely dwarf companions based on their color and structure.

2. **CDG B** are possible candidates which show most of the expected properties.

3. **CDG C** are likely background galaxies, but could be confused with BCDs or transition dwarf companions.

7.1 DWARF GALAXIES IN THE LOCAL GROUP AND AROUND OTHER NEARBY GALAXIES

Many observations of dwarf galaxies around massive close-by galaxies can be found. We will list here the measured parameters like color and Sérsic index in order to present the basis upon which the candidates were classified as CDG. Jerjen et al. (2000) report on dwarf galaxies around Centaurus A and Sculptor. They find $(B-R)_0$ between 0.8 and 1.7 and Sérsic indices ranging from 0.63 to 1.9. Also the color profiles are used in order to classify our candidates as dwarf companions. Dwarf galaxies in the Local Group have Sérsic indices ranging from 0.5 to 1.7 and $(B-R)_0$ values from 0.7 to 1.6 (Mateo 1998).

Chiboucas et al. (2009) studied dwarf galaxies in the M81 group. They report about Sérsic indices ranging from 0.21 to 1.0. Makarova et al. (2005) surveyed southern nearby dwarf galaxies and finds a

$(B-R)_0$ color range of 0.4 to 1.2. Another study of Local Volume dwarf galaxies can be found in Sharina et al. (2008). They report colors of $0.4 \lesssim (B-R)_0 \lesssim 1.4$.

The references listed above are only a excerpt of the many studies of close-by dwarf galaxies. The reported values define our classification system of possible CDG. The range of expected properties for prospective CDG is $0.4 \lesssim (B-R)_0 \lesssim 1.7$ and $0.2 \lesssim$ Sérsic index $n \lesssim 1.9$.

7.2 NGC 134

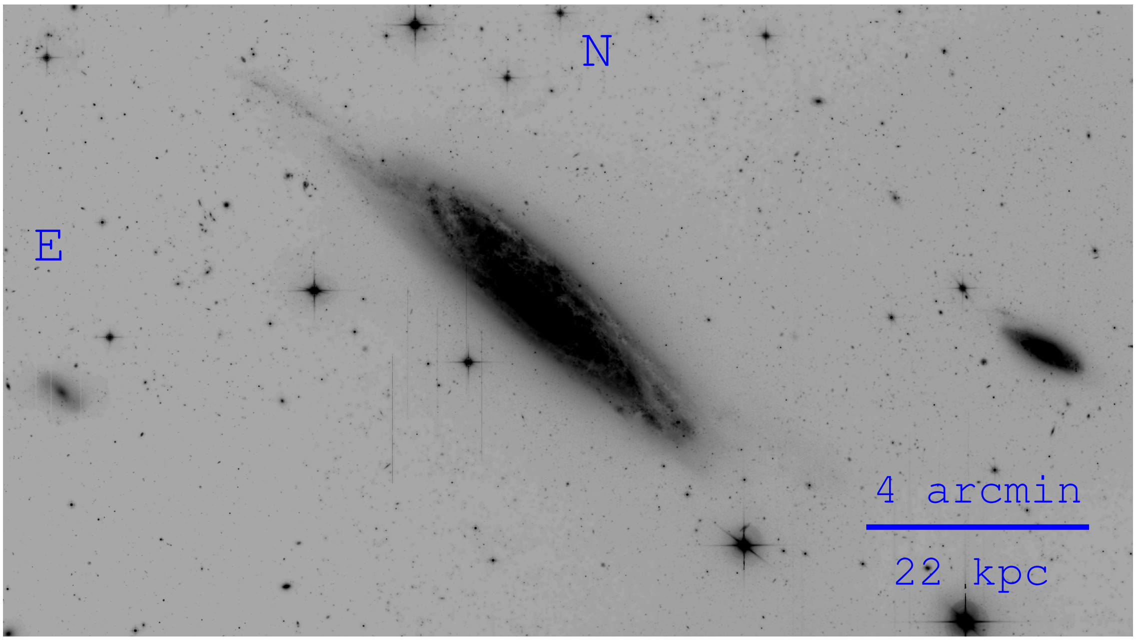

Figure 7.1: The environment around NGC 134

NGC 134 is an Sbc galaxy located at a distance of 18.7 Mpc[1]. Similar to NGC 7331 an outstanding warp is visible. In the northeast direction an extended tidal tail can be observed. A similar feature can be observed in the opposite direction, but there the brightness is much fainter. In proximity in projection the spiral galaxy NGC 131 can be observed (right hand side in Figure 7.1), but this galaxy has a radial velocity of 1410 km s^{-1} (compared to a radial velocity of 1582 km s^{-1} of NGC 134). Therefore a tidal interaction with it is unlikely.

The analysis of the imaging data revealed two CDG, which we classified as dSph. The observed properties like n, CSB and color agree with the expected parameters and classify NGC 134 1 and NGC 134 2 as CDG A (see Figure 7.2). The measured color profiles (Figure 7.2 and 7.7) do not show any gradient, the measured color for each isophote is varying around the measured color. The low S/N of both candidates causes these fluctuations.

Additionally, a dE candidate can be found in this system. According to the measured color, the luminosity and color profile it is categorized as CDG A.

---

[1] all distances are taken from the NASA Extragalactic Database (NED) URL:http://ned.ipac.caltech.edu

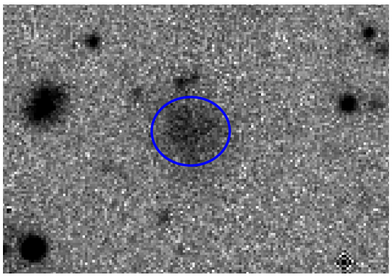

Figure 7.2: CDG NGC 134 1

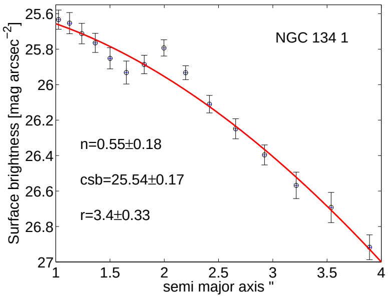

Figure 7.3: SBP of NGC 134 1

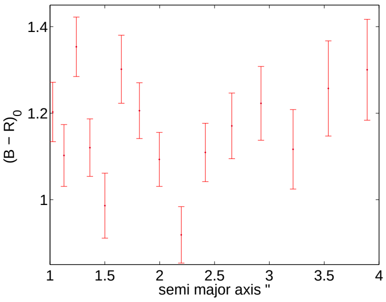

Figure 7.4: Color profile of NGC 134 1

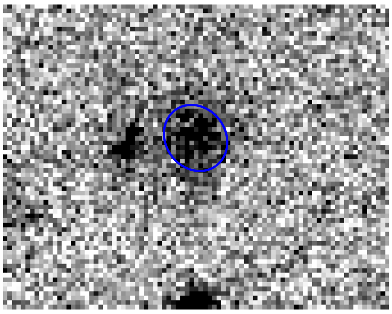

Figure 7.5: CDG NGC 134 2

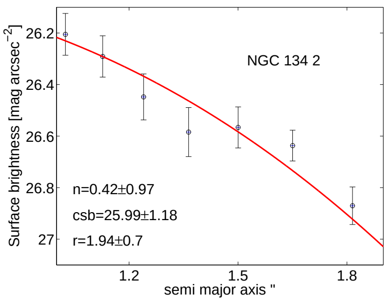

Figure 7.6: SBP of NGC 134 2

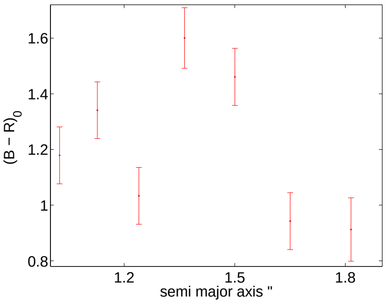

Figure 7.7: Color profile of NGC 134 2

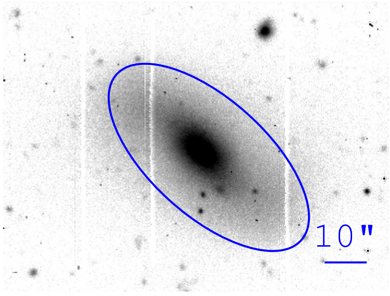

Figure 7.8: CDG NGC 134 dE

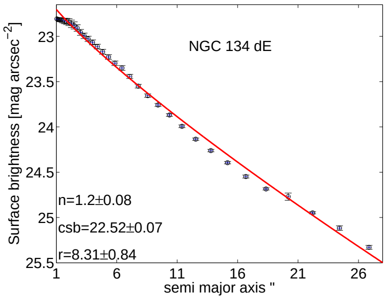

Figure 7.9: SBP of NGC 134 dE

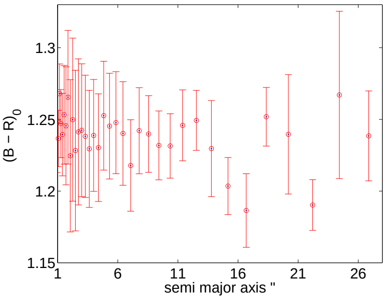

Figure 7.10: Color profile of NGC 134 dE

7.3 NGC 908

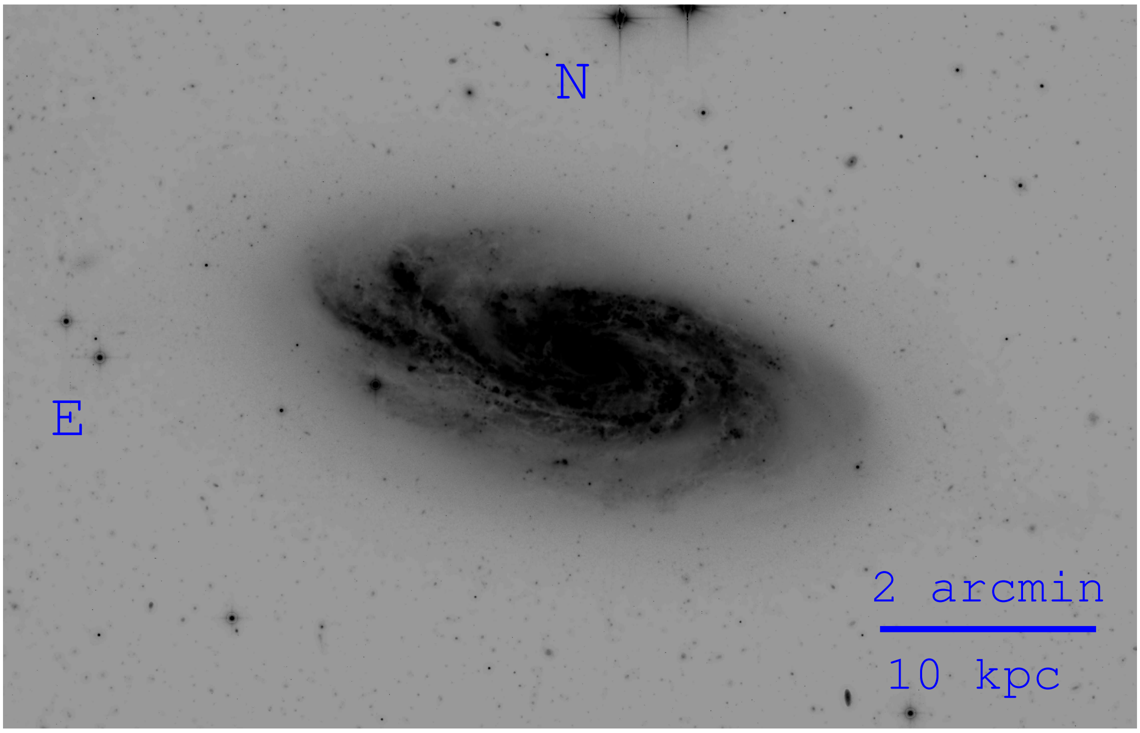

Figure 7.11: The environment around NGC 908

NGC 908 is an Sc galaxy at a distance of 17.5 Mpc. A bright elliptical bulge can be observed together with three extended spiral arm structures. The arm pointing to the east is much more open than the others, which results in a warped appearance of the whole galaxy. The arms do not show a homogeneous structure and many obvious star-forming regions can be recognized (Eskridge et al. 2002).

Though this galaxy looks relaxed but not symmetric in structure, it is not possible to find any hints of tidal debris features down to the observing limits.

We found three CDG around NGC 908. The first candidate is most likely a dIrr (CDG A) galaxy because of its irregular appearance. Note that the bright region is slightly off-centered. This is not unusual for this galaxy type. The SBP shows typical values for a CDG. The color profile highlights that in the central bright region recent or ongoing star formation can be observed, this would explain the blue colors measured in the center. Towards larger radii much redder colors can be observed. This clear color gradient highlights that in the outer parts no or much less HI is located and therefore the stellar populations are much older there.

The second CDG is categorized as CDG C, most likely it is a background elliptical galaxy. Although the observed color put it in the range of a CDG, the *n* and the core are not matching these criteria. Also the color profile shows hints that there is a gradient which shows redder colors in the center, such gradients can often be observed in E. Though the measured parameters are not matching all expected properties, it could alternatively maybe explained by a nucleated dE. Therefore the nature of NGC 908 2 is not clear.

The third candidate looks like a typical dSph, all criteria match the properties of dSphs and therefore it is classified as CDG A. Due to the low SB the color profile does show a clear trend. The scatter around the measured color makes it impossible to interpret the structures in this CDG.

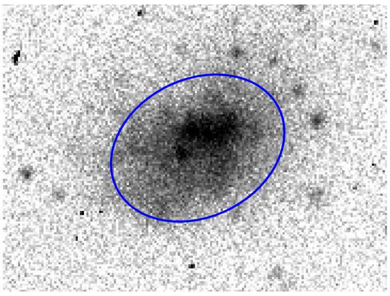

Figure 7.12: CDG NGC 908 1

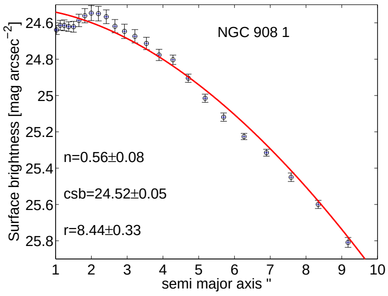

Figure 7.13: SBP of NGC 908 1

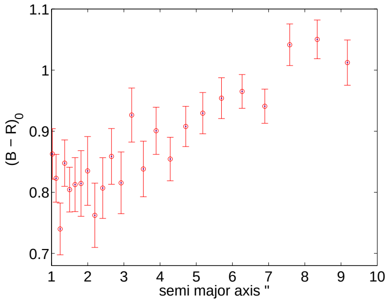

Figure 7.14: Color profile of NGC 908 1

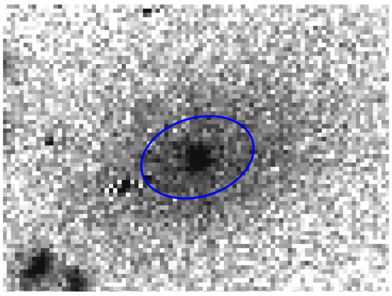

Figure 7.15: CDG NGC 908 2

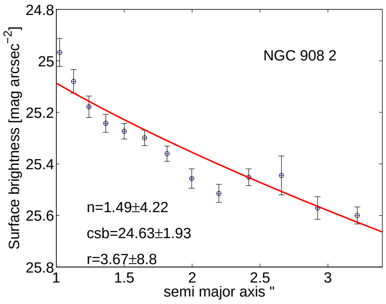

Figure 7.16: SBP of NGC 908 2

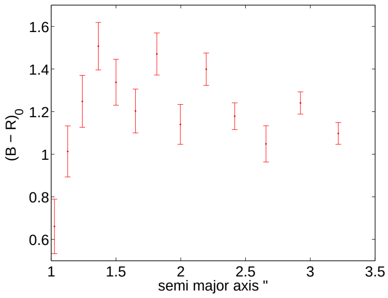

Figure 7.17: Color profile of NGC 908 2

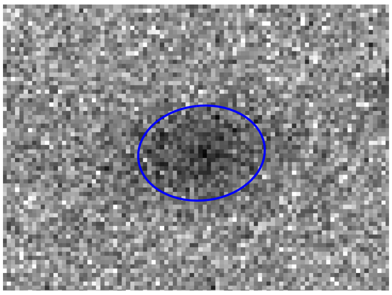

Figure 7.18: CDG NGC 908 3

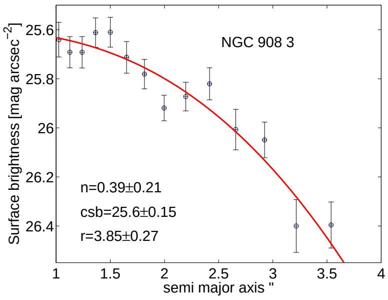

Figure 7.19: SBP of NGC 908 3

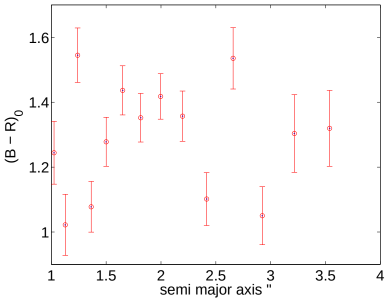

Figure 7.20: Color profile of NGC 908 3

7.4 NGC 1365

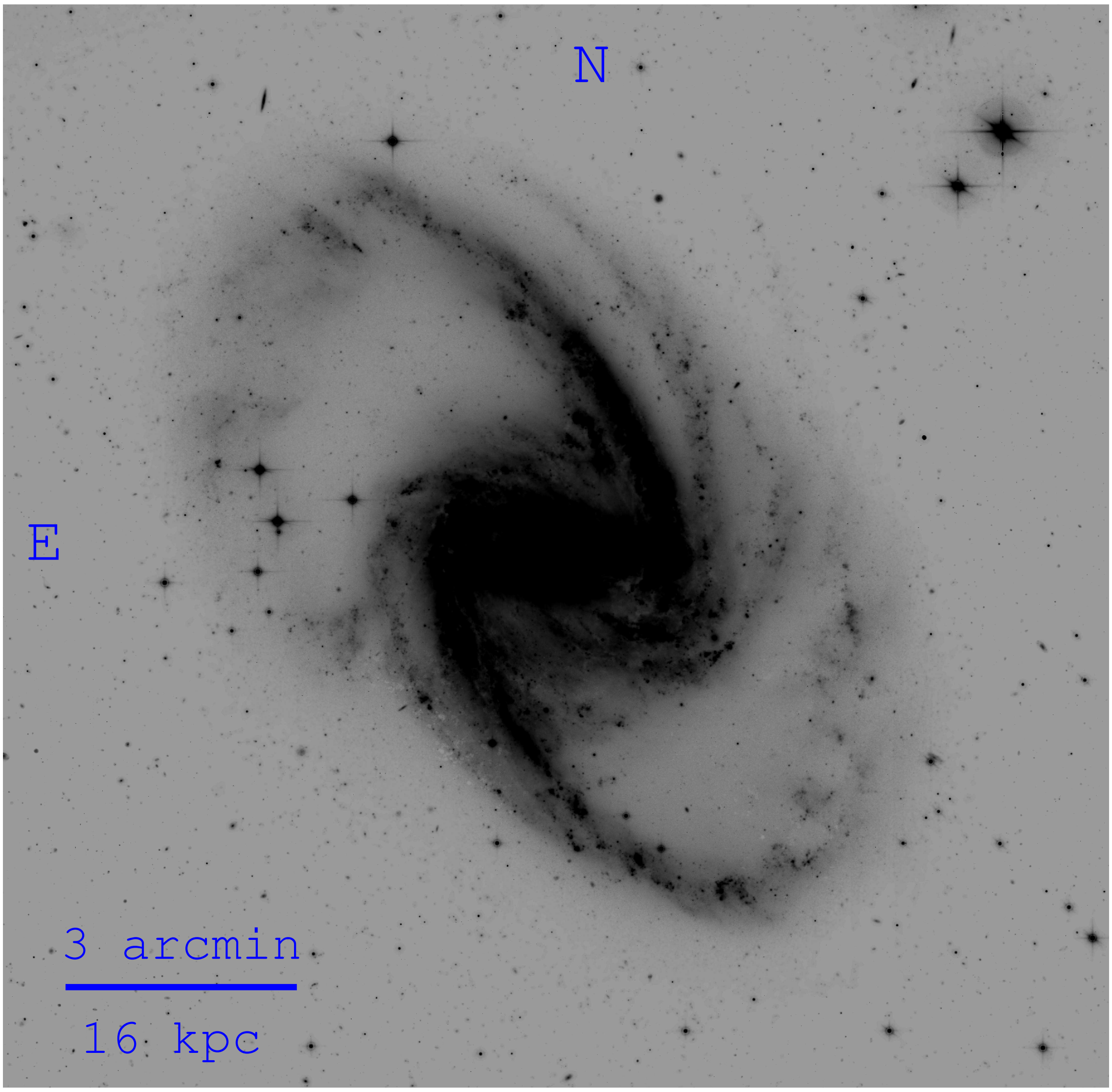

Figure 7.21: The environment around NGC 1365

NGC 1365 is an Sb galaxy at a distance of 17.9 Mpc. Its position and redshift classify this galaxy as a member of the Fornax Cluster, but the membership is often questioned as it has a very large angular size (Sandage & Bedke 1994). Therefore it was included into the survey as the density is very high and it makes it a very good object for a comparison to galaxies in less dense environments.

Signs of tidal debris can not be found via inspection of the images, apart from a spiral arm which is extending far beyond the the remaining spiral structure. The SB of this feature is going down rapidly in the outskirts.

In the environment of NGC 1365 three CDG can be identified. The first one could be classified as a likely dSph galaxy. The observed parameters categorize it as CDG A. The bright objects were masked out and are assumed to be background objects. The color profile does not show any gradient. In the inner parts noise is visible as the fitted area is quite small and in the outer parts the S/N is decreasing.

NGC 1365 2 (CDG A) shows the same parameters as usual dSphs, but in the center a core can be

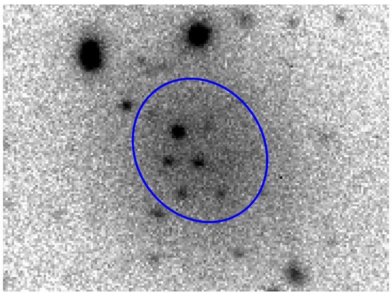

Figure 7.22: CDG NGC 1365 1

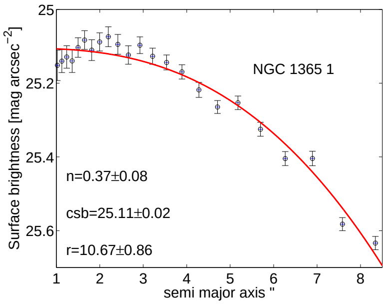

Figure 7.23: SBP of NGC 1365 1

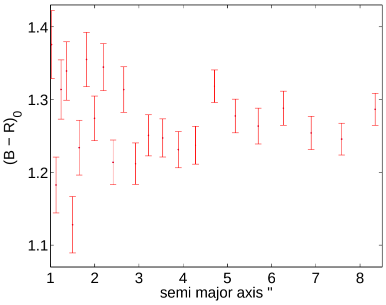

Figure 7.24: Color profile of NGC 1365 1

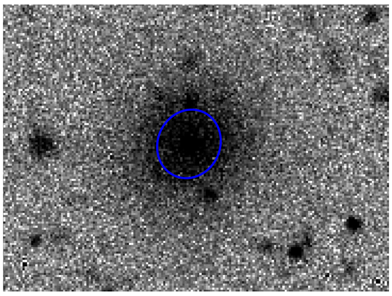

Figure 7.25: CDG NGC 1365 2

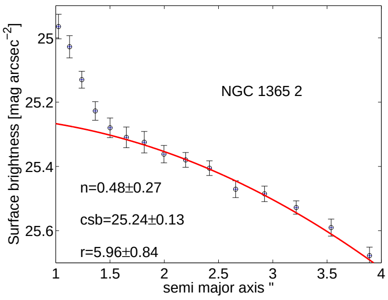

Figure 7.26: SBP of NGC 1365 2

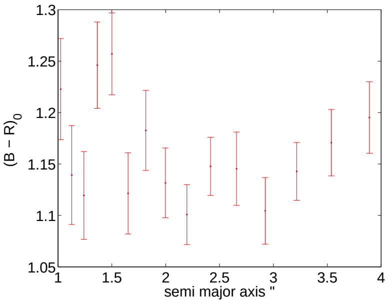

Figure 7.27: Color profile of NGC 1365 2

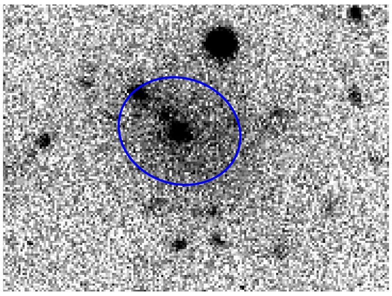

Figure 7.28: CDG NGC 1365 3

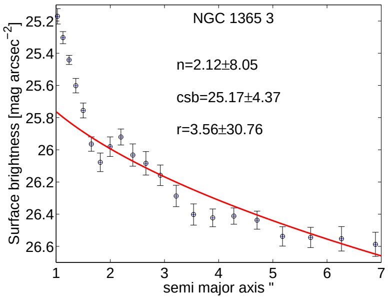

Figure 7.29: SBP of NGC 1365 3

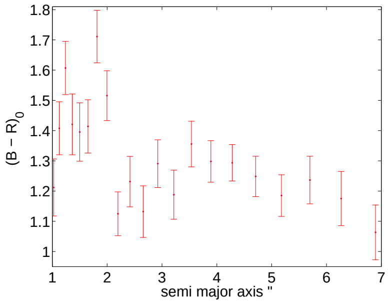

Figure 7.30: Color profile of NGC 1365 3

identified. Therefore the core was not used for the SBP fit. Using this exclusion the profile follows the expected shape for a CDG. A color gradient can not be clearly recognized there.

The third CDG (CDG B) does not confirm completely the properties of usual dwarf companions. The color and morphology show properties of dSphs, but the SBP clearly reveals a core in the center. We classify it therefore as nucleated dE. Even when fitting a profile without the center to the light distribution, a unusual high *n* is measured. The color profile is highlighting the difference of the core and the rest of CDG, in the center the core is much redder than the outer parts. A clear break between these two regions can be recognized. This could also be a low SB spiral galaxy with a bulge or maybe a background object or a background galaxy projected on dSph. The results show that the classification as CDG is questionable for this candidate.

7.5 NGC 1421

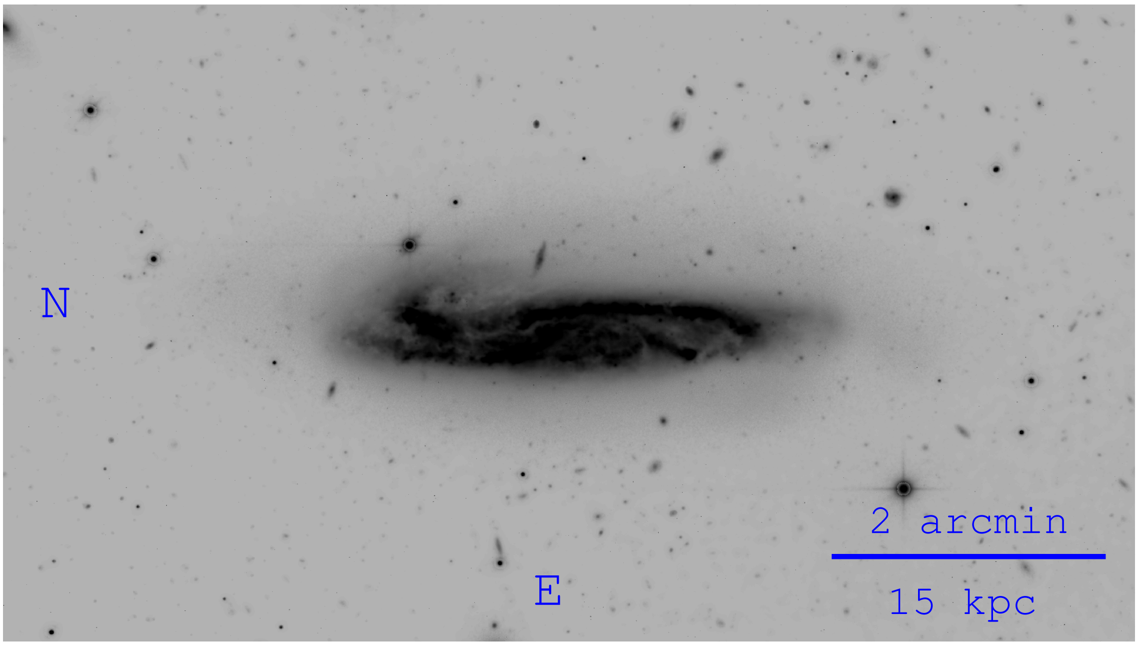

Figure 7.31: The environment around NGC 1421

NGC 1421 is classified as Sbc with a distance of 25.8 Mpc. The system shows two bright arms and a nucleus. All these structures show HSB HII regions (Meurer et al. 2006). The galaxy is clearly warped. Far beyond the disk to the north on one side and to the south on the other side faint substructures are visible.

Interestingly, Meurer et al. (2006) show that there is a dwarf companion which would have been classified as background galaxy by our criteria, especially because of the two HSB nuclear HII regions. According to the classification of the HIPASS survey this is clearly a dwarf companion which is classified as dE. It could also be a transition type dwarf, the inner complex structure and the slightly blue core as well as HI content are usual signs of this type.

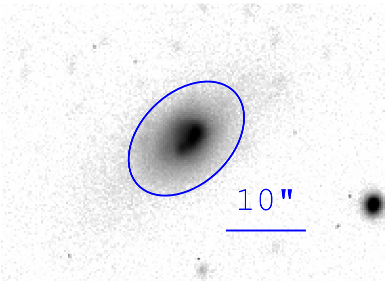

Figure 7.32: CDG NGC 1421 1

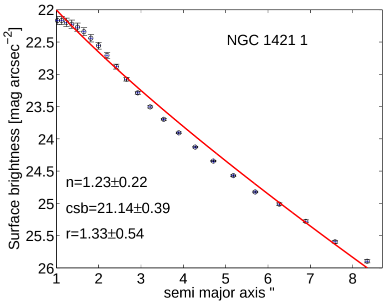

Figure 7.33: SBP of NGC 1421 1

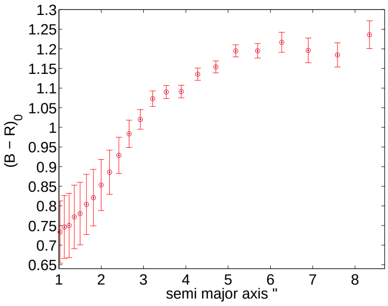

Figure 7.34: Color profile of NGC 1421 1

7.6 NGC 7314

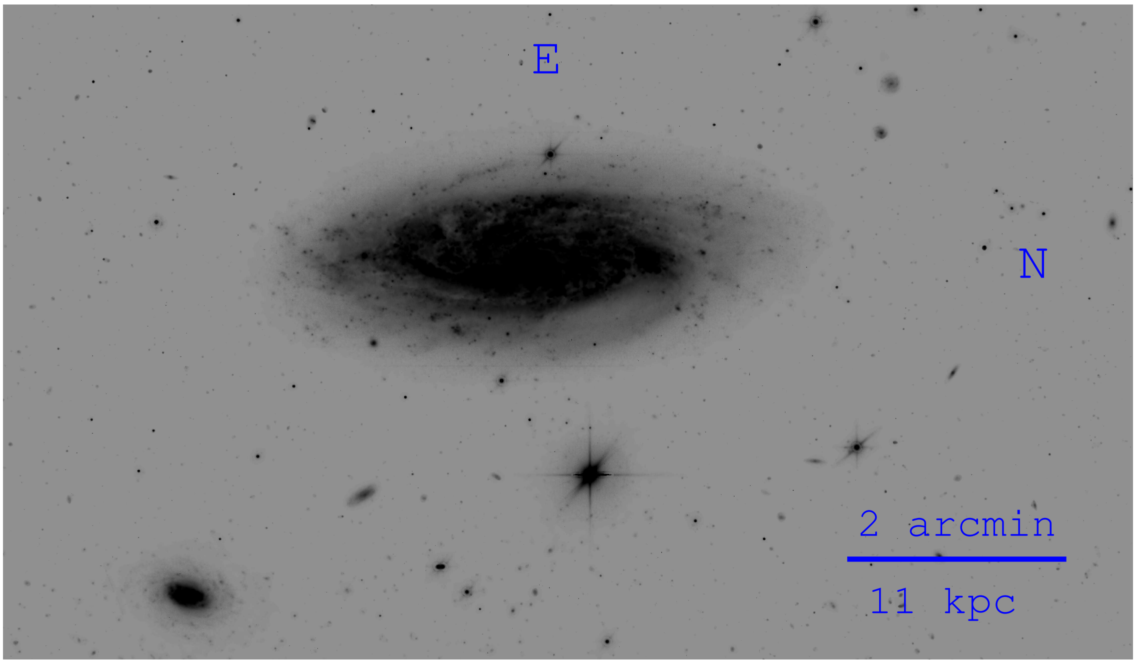

Figure 7.35: The environment around NGC 7314

The Sbc galaxy NGC 7314 is located at a distance of 18.6 Mpc. Many giant HII regions can be found in the spiral arms and in the nucleus an optically thick component can be detected (Evans et al. 1996). Down to the SB limit of this survey no signs of tidal debris or streams can be detected. The galaxy is in an isolated region with a density of 0.08 galaxies Mpc^{-3} (all densities are taken from Tully & Fisher 1988). In contrast to other targets this object is extremely homogeneous, no signs of warps or similar features can be seen. Such regularly shaped spiral galaxies are rare, but the isolated environment where the galaxy is located could be an explanation of these observations.

NGC 7314 1 is classified as a dE galaxy. The observed parameters and the SBP categorizes the target as CDG A. The measured color profile does not show any gradient, the plot only shows scatter around the measured color.

The second CDG has an optical appearance and observed properties of dSph (CDG B). The extremely low SB of this object makes the SBP fit difficult. It is unclear why at an SMA of 2.3” a steep decline can be seen, which is limited to a small area. The reason could be that there is a unresolved background object or substructure. Also a centering problem can lead to such results, but this seems unlikely due to the rest of the profile. The color profile visualizes the same problem again, no clear gradient can be detected and therefore the hints that the color is redder in the center is not stated well enough to constrain it as real feature.

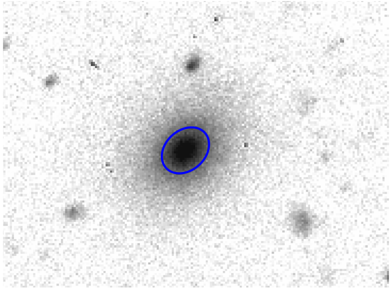

Figure 7.36: CDG NGC 7314 1

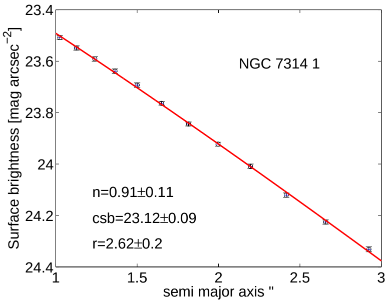

Figure 7.37: SBP of NGC 7314 1

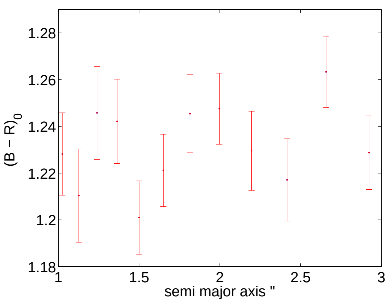

Figure 7.38: Color profile of NGC 7314 1

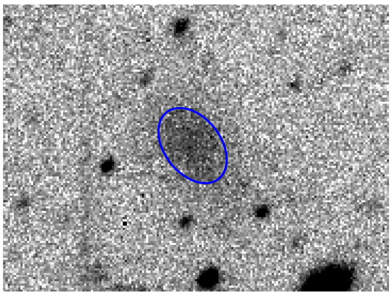

Figure 7.39: CDG NGC 7314 2

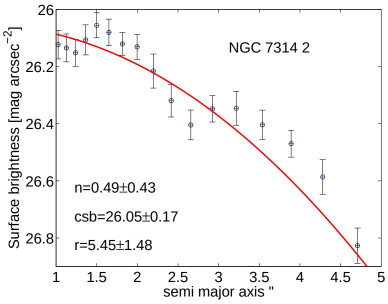

Figure 7.40: SBP of NGC 7314 2

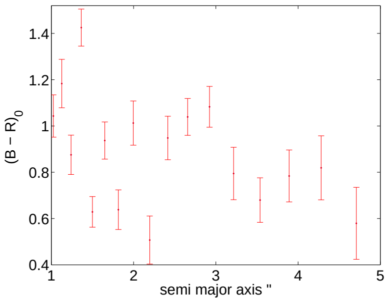

Figure 7.41: Color profile of NGC 7314 2

7.7 NGC 7599

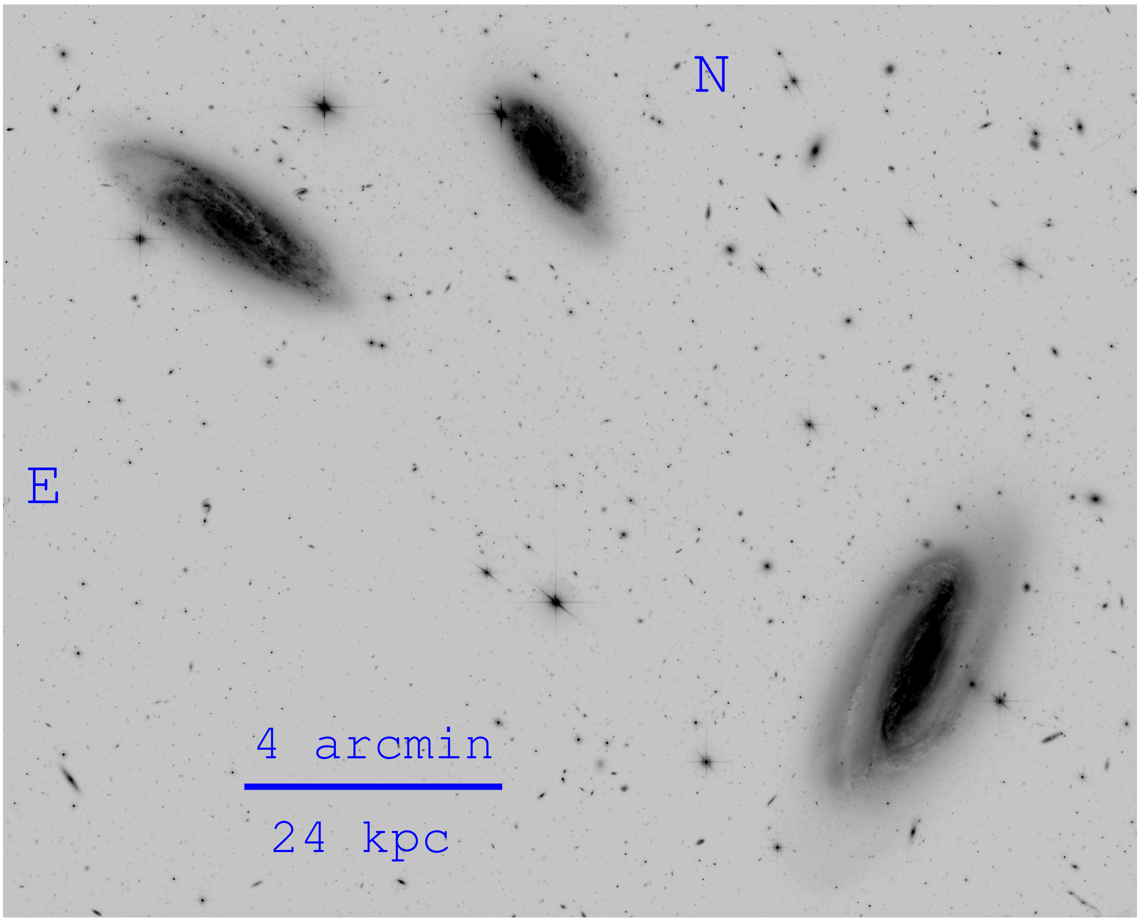

Figure 7.42: The image shows NGC 7582 (right bottom), NGC 7590 (in the middle of the top of the image) and NGC 7599 (in the top left corner).

On the left hand side in the top corner of Fig.7.42 NGC 7599, which is an Sc galaxy at a distance of 20.4 Mpc, can be seen. Close-by are NGC 7590 (25.6 Mpc) in the middle of the top edge and at the right bottom of the image the bright NGC 7582 (20.9 Mpc). They are located in a dense environment of 0.43 galaxies Mpc^{-3}. Interestingly, de Vaucouleurs et al. (1976) do not find an obvious interaction between NGC 7599 and NGC 7582, although NGC 7599 is not relaxed. NGC 7599 has a very open spiral arm pointing east, therefore this target appears disturbed and might have undergone a tidal interaction with another candidate. The other two galaxies of this group appear much more regularly shaped, whereas a warp can be seen in the disk structure of NGC 7590. In none of this targets faint tidal debris structures can be detected.

In total seven CDG can be found around the three galaxies. Due to the proximity of several massive galaxies and missing redshift data a clear membership cannot be examined, therefore all CDG have designations starting with NGC 7599, this is a random selection and in principle every candidate could be a satellite of any of the shown massive spirals.

The first CDG is classified as dIrr, clearly irregular formed regions with recent or ongoing star formation can be recognized. The color profile shows very blue colors in the center, which supports the classification as dIrr (CDG A) with the assumed star formation. A color gradient can be detected with much redder colors in the outer regions, therefore star formation must have stopped there.

NGC 7599 2 (CDG A) is a typical dSph candidate with an extremely smooth appearance, which can be also seen in the SBP. In the color profile there is no gradient visible, many dSph have no detectable gradient in the stellar populations. Another dIrr can be seen in NGC 7599 3. Many subregions with a high SB can be recognized. The SBP categorizes it as CDG A and in the color profile the typical color gradient for dIrr is visible, recent or ongoing star formation in the central regions cause bluer colors towards the center. NGC 7599 4 to 7 are all classified as dSphs, the properties of the SBPs categorize them as CDG A. In none of the color profiles gradients can be seen. Only scatter caused by the low S/N is visible.

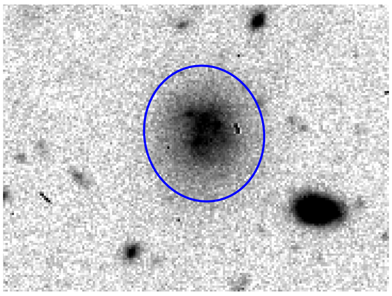

Figure 7.43: CDG NGC 7599 1

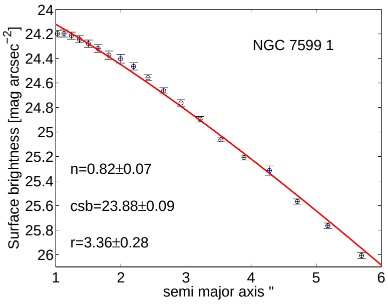

Figure 7.44: SBP of NGC 7599 1

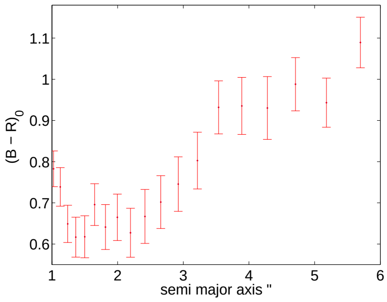

Figure 7.45: Color profile of NGC 7599 1

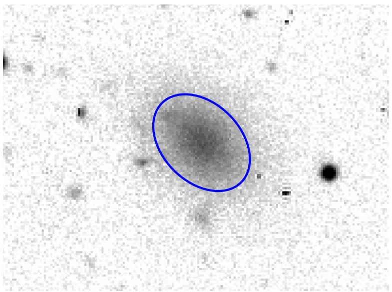

Figure 7.46: CDG NGC 7599 2

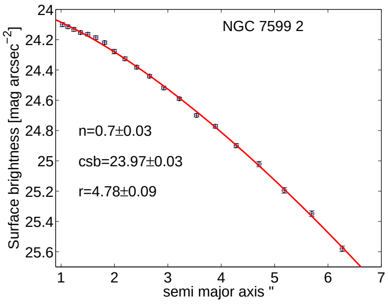

Figure 7.47: SBP of NGC 7599 2

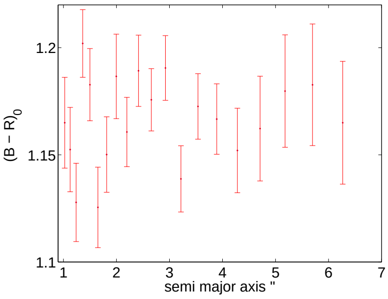

Figure 7.48: Color profile of NGC 7599 2

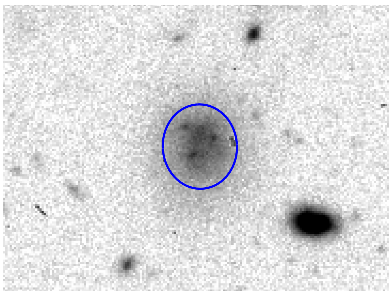

Figure 7.49: CDG NGC 7599 3

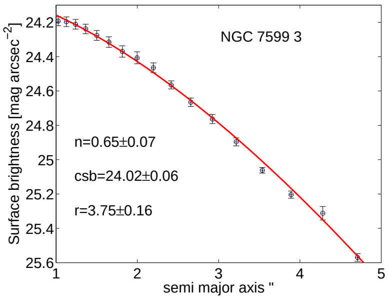

Figure 7.50: SBP of NGC 7599 3

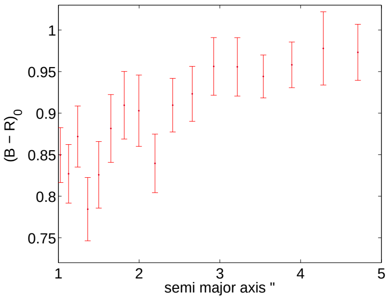

Figure 7.51: Color profile of NGC 7599 3

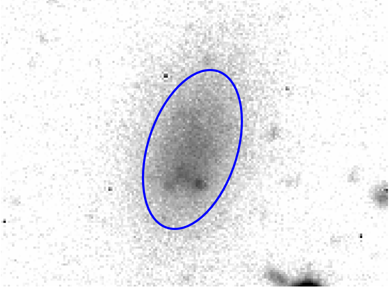

Figure 7.52: CDG NGC 7599 4

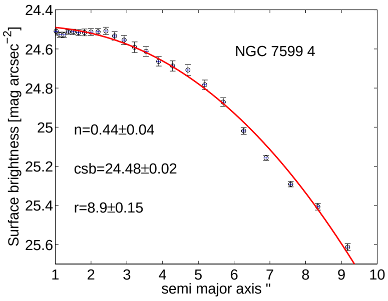

Figure 7.53: SBP of NGC 7599 4

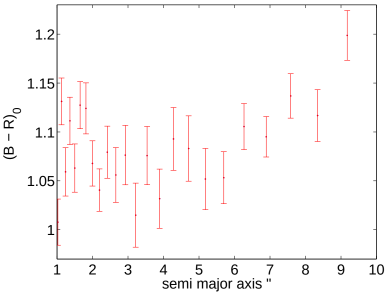

Figure 7.54: Color profile of NGC 7599 4

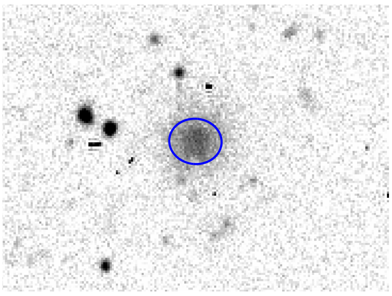

Figure 7.55: CDG NGC 7599 5

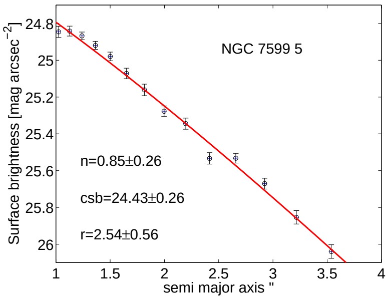

Figure 7.56: SBP of NGC 7599 5

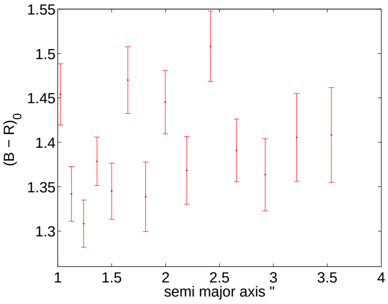

Figure 7.57: Color profile of NGC 7599 5

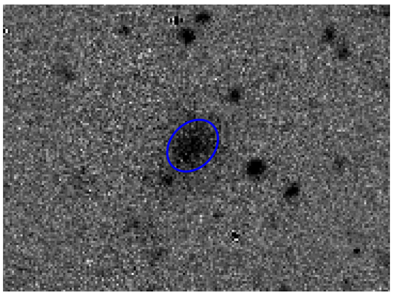

Figure 7.58: CDG NGC 7599 6

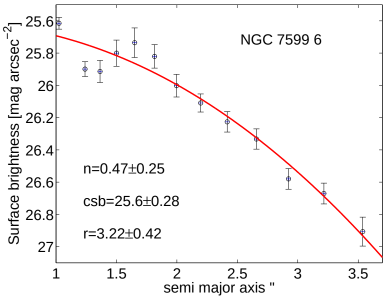

Figure 7.59: SBP of NGC 7599 6

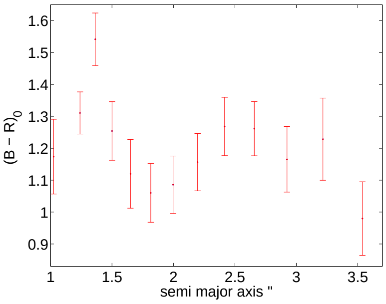

Figure 7.60: Color profile of NGC 7599 6

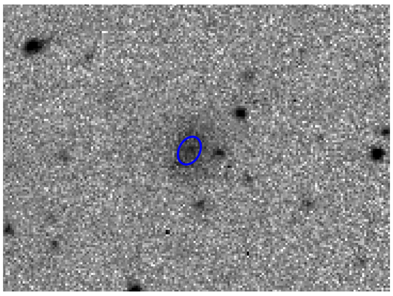

Figure 7.61: CDG NGC 7599 7

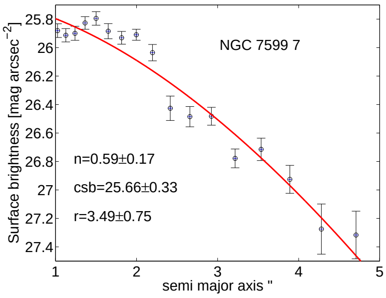

Figure 7.62: SBP of NGC 7599 7

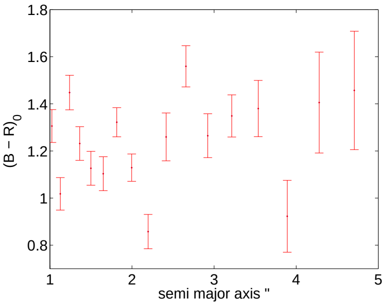

Figure 7.63: Color profile of NGC 7599 7

7.8 NGC 7721

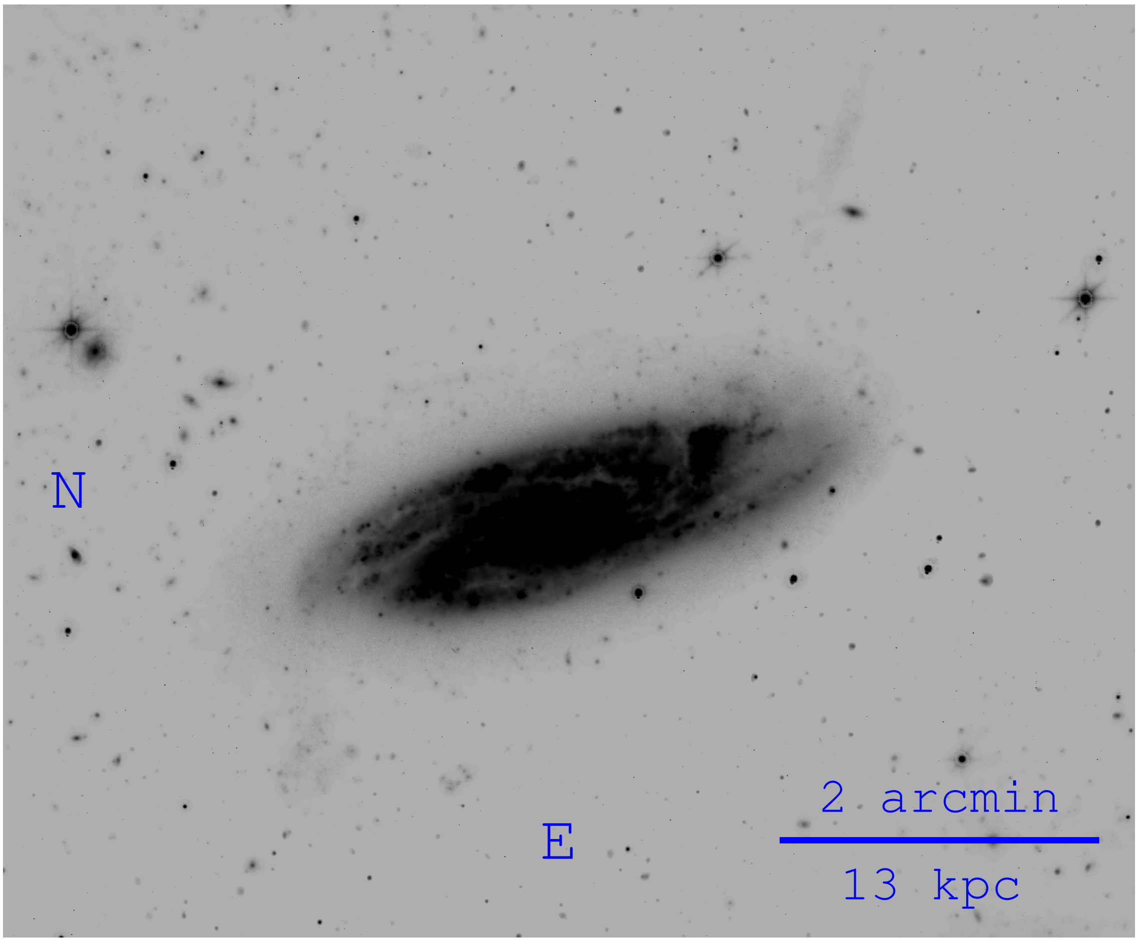

Figure 7.64: The environment around NGC 7721

NGC 7721 is an Sc galaxy at a distance of 22.13 Mpc. The spiral structure of this galaxy is very disturbed. A warp and many bright regions with star formation can be seen in the spiral arms. In the southwest a tidal stream is detected, which clearly is the sign of a tidal interaction. Additionally a cloud can be seen in the faint outskirts of the spiral arms in the opposite direction of the stream in the northeast. The cloud is in contrast to the stream directly connected to the spiral structure. The cloud could have the same origin as the stream, the opposite position of these features could be explained by the accretion of a satellite galaxy after the first orbit.

One CDG can be found around NGC 7721 in the observed region. It is classified as a dSph (CDG A) galaxy with typical properties of dwarf companions. The SBP follows the light distribution that is expected for CDG and the color profile does not reveal a clear color gradient.

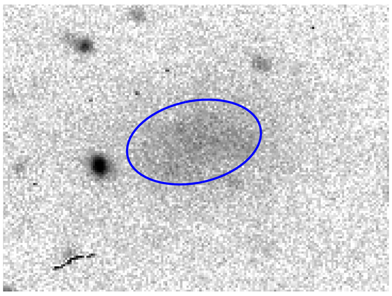

Figure 7.65: CDG NGC 7721 1

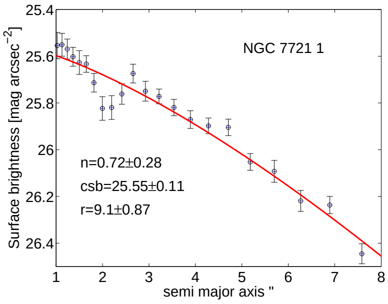

Figure 7.66: SBP of NGC 7721 1

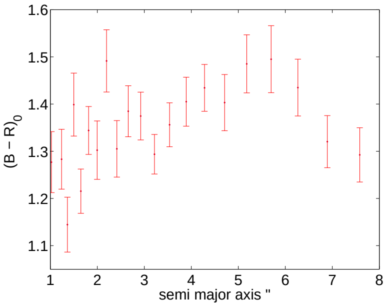

Figure 7.67: Color profile of NGC 7721 1

7.9 IC 4721

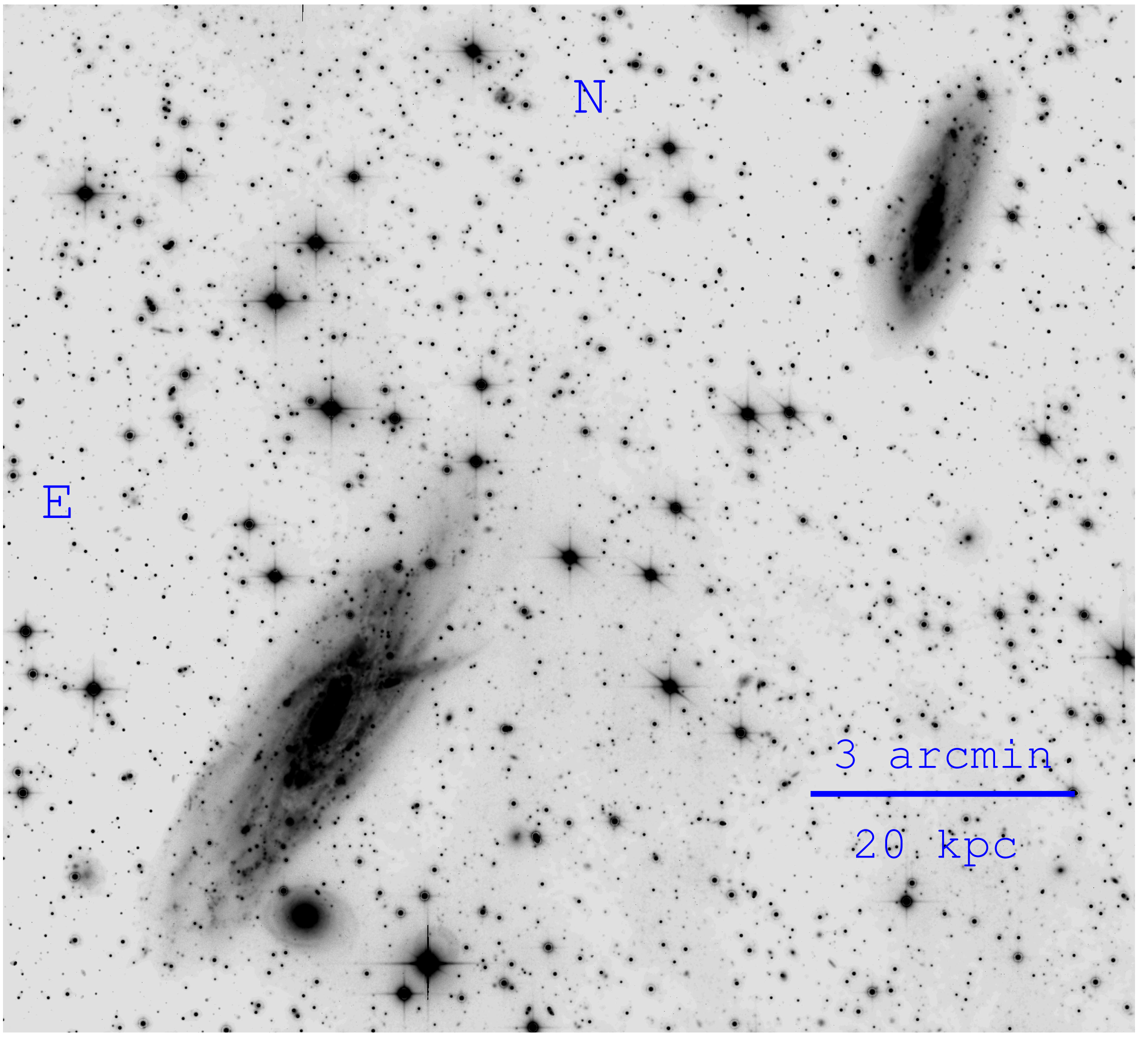

Figure 7.68: The environment around IC 4721

IC 4721 is an Scd galaxy at a distance of 22.9 Mpc. It forms an interacting galaxy pair together with IC 4720 (in Figure 7.68 in the top right). Both galaxies appear noticeably disturbed, IC 4721 shows a clear warp and appears lopsided and the other member of the galaxy pair is much more confused. In the faint outskirts of IC 4721 an obvious plume directing west and in the north a faint extended cloud can be recognized. Compared to the other studied galaxies this target is much less massive. Interestingly, a high number of dIrr CDG can be identified in close proximity, which is a clear difference from the observations of the other targets.

The first CDG (CDG A) is observed close-by to the spiral galaxy. In the center bright disturbed regions can be seen, the SBP shows typical properties of dwarf companions. In the measured color profile no clear gradient can be identified. IC 4721 2 (CDG A) is classified as dIrr, a central nucleus and a lot of diffuse structure can be seen over the whole candidate. The fitted Sérsic profile shows typical properties of this galaxy type. The color profile shows a complex structure. In the nucleus a steep gradient with redder colors at larger radii can be identified, then at intermediate radii the color is getting bluer, shows another peak with redder colors and is decreasing to bluer values again. This double-peak structure is most likely produced by different stellar subpopulations.

The third CDG is labeled as dSph and shows a smooth light distribution. The SBP supports the classification as CDG A and the color profile shows no clear gradient, only at larger radii the colors are on average redder.

An extended dIrr can be seen in IC 4721 4, especially in the center diffuse structure together with a nucleus is visible. The parameters of the fit to the SBP categorizes it as CDG A. The color profile is typical for a dIrr. In the center at the location of the diffuse structure, a color gradient with redder colors at larger radii can be identified, ongoing or recent star formation in the central regions of the CDG can cause bluer colors there. From intermediate radii to the edge of this CDG a constant color is measured. This candidate can be labeled as standard dIrr galaxy.

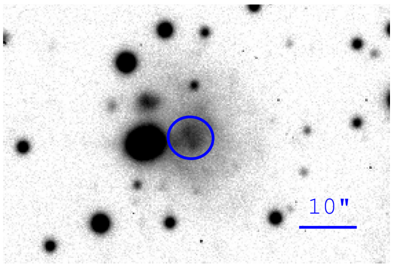

Figure 7.69: CDG IC 4721 1

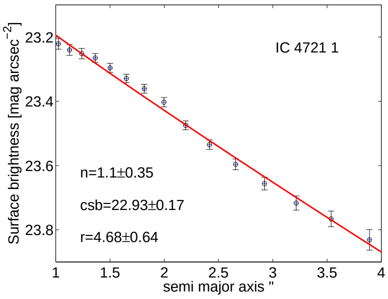

Figure 7.70: SBP of IC 4721 1

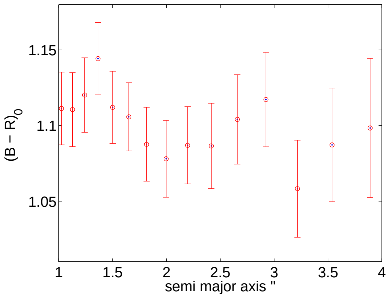

Figure 7.71: Color profile of IC 4721 1

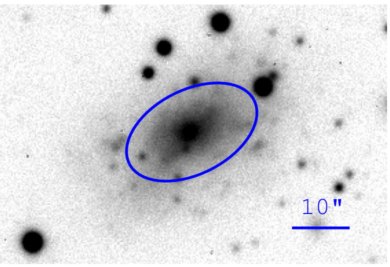

Figure 7.72: CDG IC 4721 2

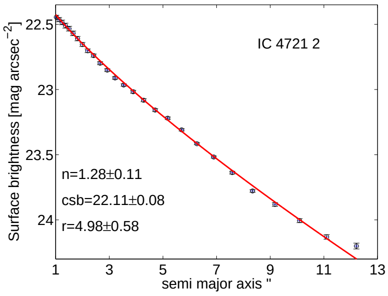

Figure 7.73: SBP of IC 4721 2

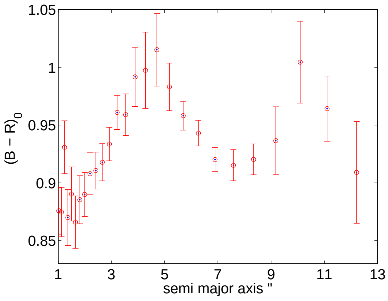

Figure 7.74: Color profile of IC 4721 2

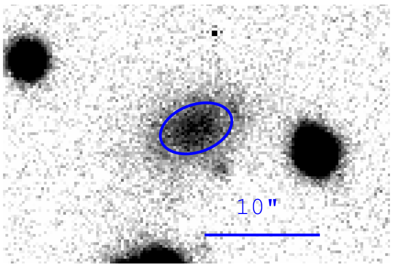

Figure 7.75: CDG IC 4721 3

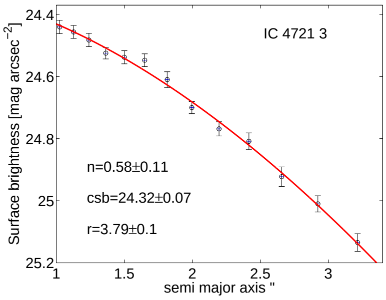

Figure 7.76: SBP of IC 4721 3

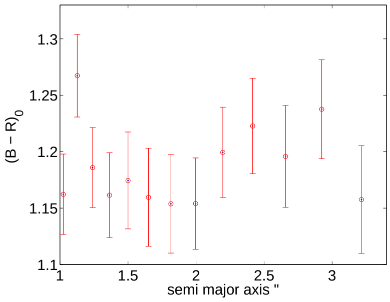

Figure 7.77: Color profile of IC 4721 3

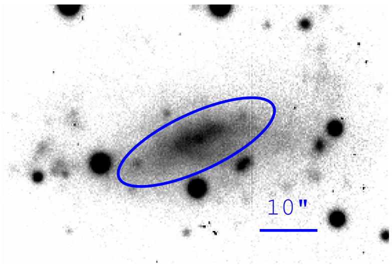

Figure 7.78: CDG IC 4721 4

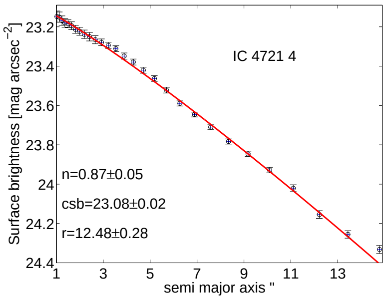

Figure 7.79: SBP of IC 4721 4

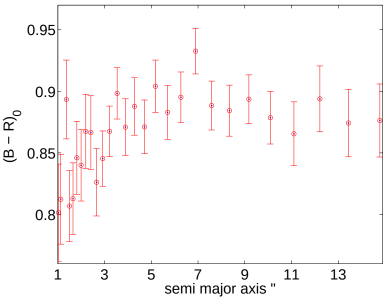

Figure 7.80: Color profile of IC 4721 4

7.10 NGC 7727

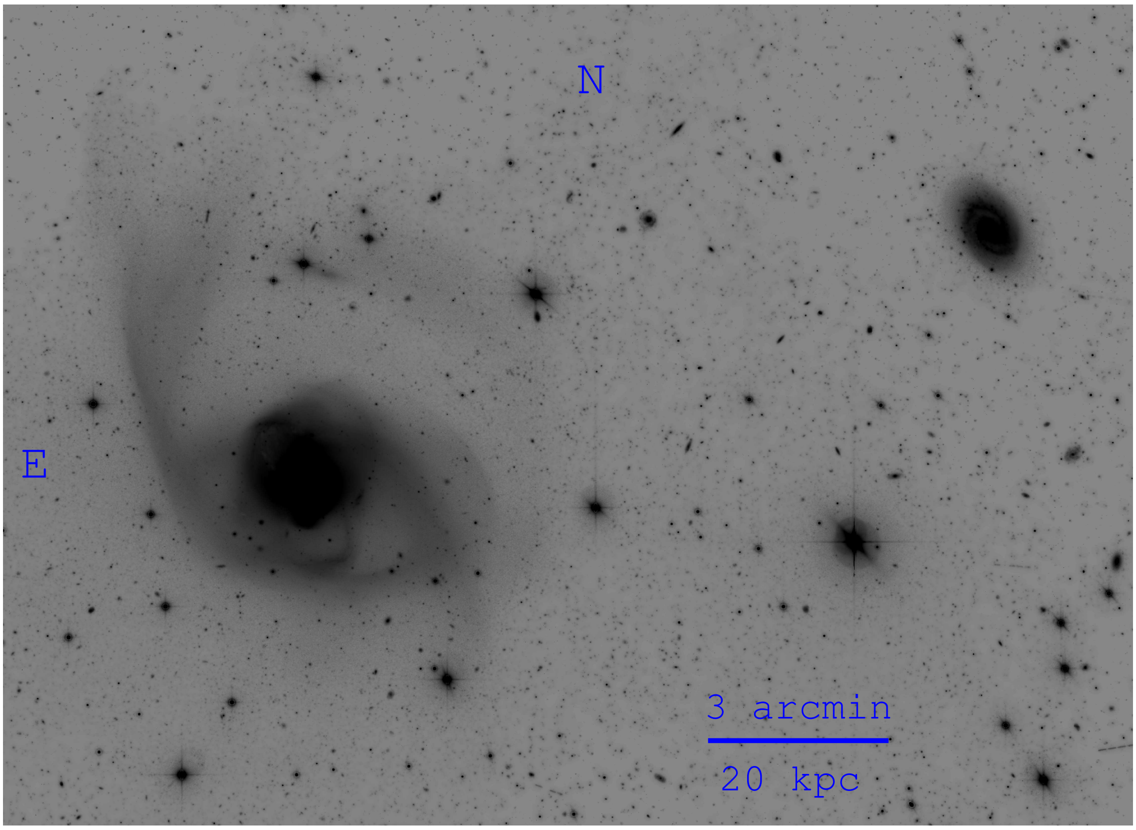

Figure 7.81: The environment around NGC 7727

NGC 7727 (Arp 222) is an Sa galaxy at a distance of 23.3 Mpc. It is the remnant of a merger of two disk galaxies after 1 Gyr and it will evolve to an elliptical galaxy, and interestingly, it shows a bright second nucleus in the inner region (Crabtree & Smecker-Hane 1994). Observations in the K-Band (Rothberg & Joseph 2004) show that the SBP can be described by de Vaucouleurs $r^{1/4}$ law. This can be interpreted as violent relaxation since the merging process. An analysis of the discrete structure of the galaxy reveals plumes coming out from the nucleus and this indicates that the system is not completely relaxed, like it would be expected for a mature elliptical galaxy (Brassington et al. 2007).

In the optical images tidal tails can be observed. A less pronounced one can be seen in the southwest, however many substructures can be seen in this part. Towards the northeast an extended tidal tail is visible, additionally a shell is connecting the tidal tails. The close-by Sb galaxy NGC 7724 is more than 10 Mpc more distant, therefore a tidal interaction with the merging system seems unlikely.

At the same height of the shell, in the north of NGC 7727 a tidal dwarf galaxy candidate (TCDG) can be found which is categorized as CDG A. This would be a location where the formation of TDG would be expected (Wetzstein et al. 2007; Duc et al. 2000). However, the measured color of 1.12 ± 0.09 mag is unusually red for a TDG. The observed colors of TDG are often blue (e.g. a list of observed colors can be found in Weilbacher et al. 2000), but e.g. Duc et al. (2000) report on a TCDG with B-R=0.96. NGC 7727 1 is shaped unregularly, which can also be a hint that it is either formed during the merging process or alternatively that it is interacting with NGC 7727 and starting to get stripped.

In order to fit an SBP to the light distribution of the TCDG the bright objects were masked out, but still the impact of other objects and the distortion of the core could not be completely removed.

Nevertheless, the values for the Sérsic index and the CSB seem reasonable for a CDG (see Fig.7.83).

In order to find gradients in the distribution of the stellar populations the color profile was studied. The profile is shown in Fig.7.84. It does not reveal a clear color gradient. In the center the fluctuations are big due to a very limited amount of counts, in the outer part the values are slightly rising. But as the S/N is small there and therefore the errorbars are big, this trend may not be real.

In the field of view which is covered by the observations no additional CDG can be detected down to the resolution and SB limit of 27 mag arcsec^{-2}. Interestingly, this is an example of a nearly isolated environment. It is still unclear if the local environment and the merging process influences the faint end of the luminosity function.

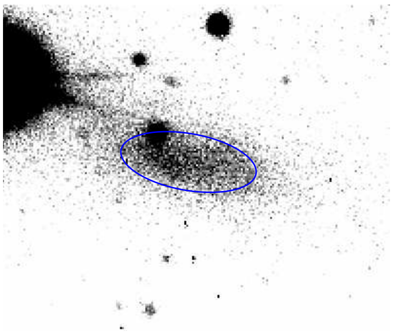

Figure 7.82: CDG found around NGC 7727

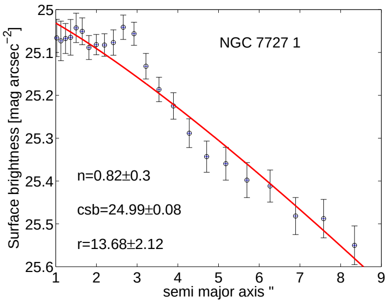

Figure 7.83: SB Profile

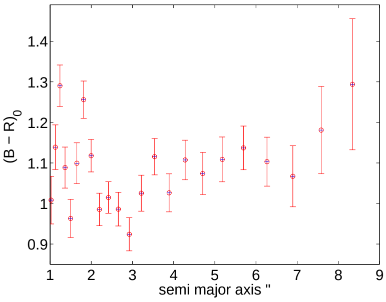

Figure 7.84: color profile

7.11 UGCA 071

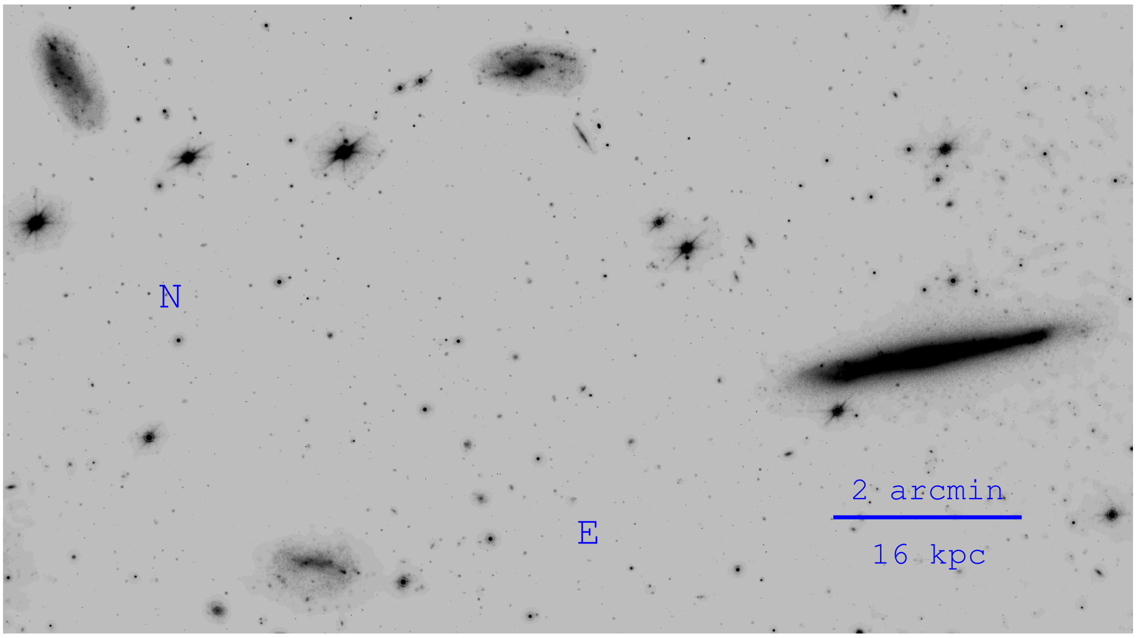

Figure 7.85: The environment around UGCA 071

UGCA 071 is an Sd galaxy at a distance of 27.8 Mpc. This central galaxy is with $M_B \sim 17$ about three magnitudes fainter than the other targets investigated in this thesis. The extremely undisturbed disk and the number of several neighboring irregular galaxies were the reasons for the selection. Therefore it is possible to compare the sample of dwarf galaxies around massive spiral galaxies to a loose group of intermediate mass galaxies. This region has an enormous local galaxy density, it could therefore be classified as a semi-compact group.

The first of this sample is UGCA 071 1 (CDG A), a dIrr candidate. Many star forming regions across the whole candidate can be detected. Two gradients are visible in the color profile. In the center blue colors are produced by bright regions with ongoing or recent star formation. Moving outwards the observed colors are getting redder and in the outskirts another star forming region causes blue colors.

The second CDG is also classified as dIrr (CDG A). Several irregular structures can be recognized. The color profile does not show a clear gradient, only at intermediate radii a bright region with ongoing or recent star formation is causing a gradient with bluer colors at these radii. UGCA 071 3 (CDG A) shows an extremely irregular structure with different bright knots of star forming regions. The dIrr shows a clear gradient in the color profile. In the outer regions two bright regions are causing the bluer colors there. Similar features can be seen in the dIrr UGCA 071 4 (CDG A). Its color profile shows the same properties as the previous candidate.

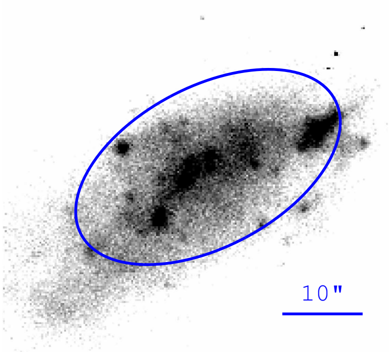

Figure 7.86: CDG UGCA 071 1

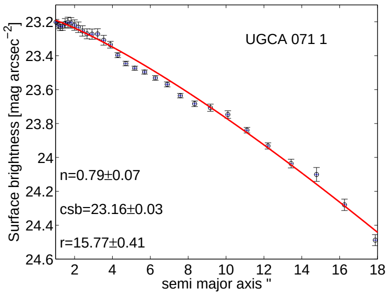

Figure 7.87: SBP of UGCA 071 1

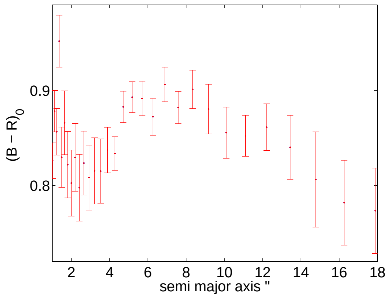

Figure 7.88: Color profile of UGCA 071 1

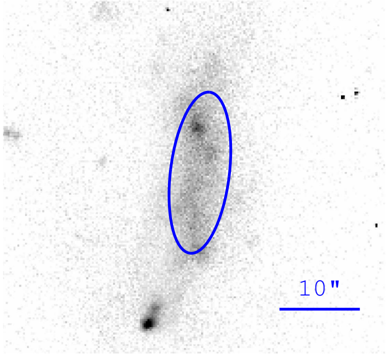

Figure 7.89: CDG UGCA 071 2

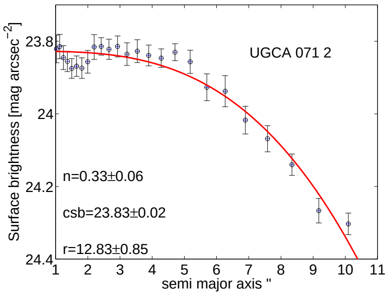

Figure 7.90: SBP of UGCA 071 2

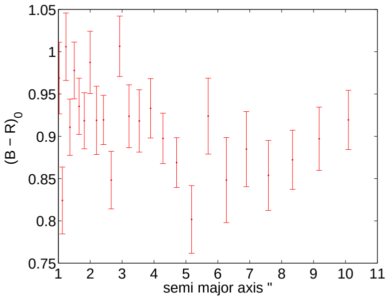

Figure 7.91: Color profile of UGCA 071 2

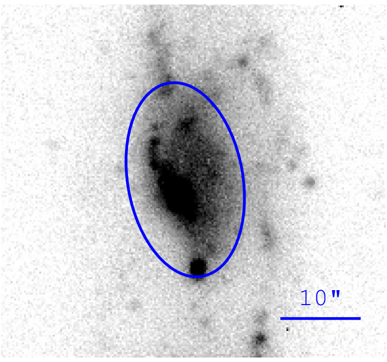

Figure 7.92: CDG UGCA 071 3

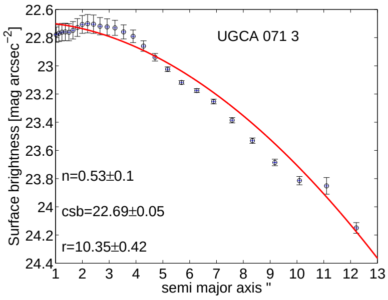

Figure 7.93: SBP of UGCA 071 3

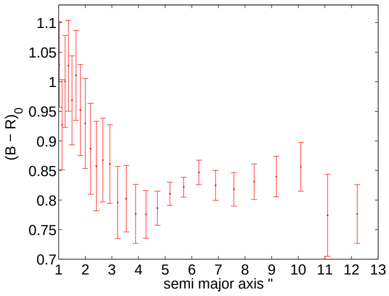

Figure 7.94: Color profile of UGCA 071 3

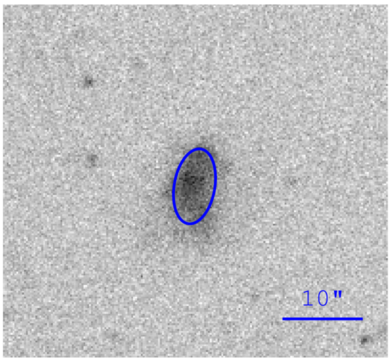

Figure 7.95: CDG UGCA 071 4

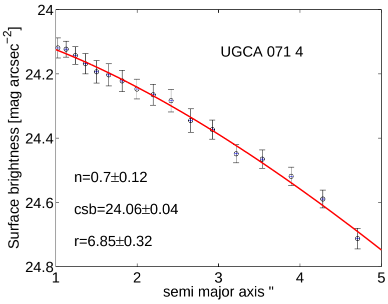

Figure 7.96: SBP of UGCA 071 4

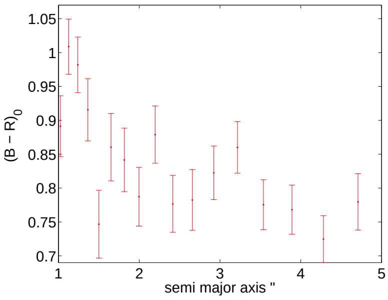

Figure 7.97: Color profile of UGCA 071 4

7.12 NGC 150

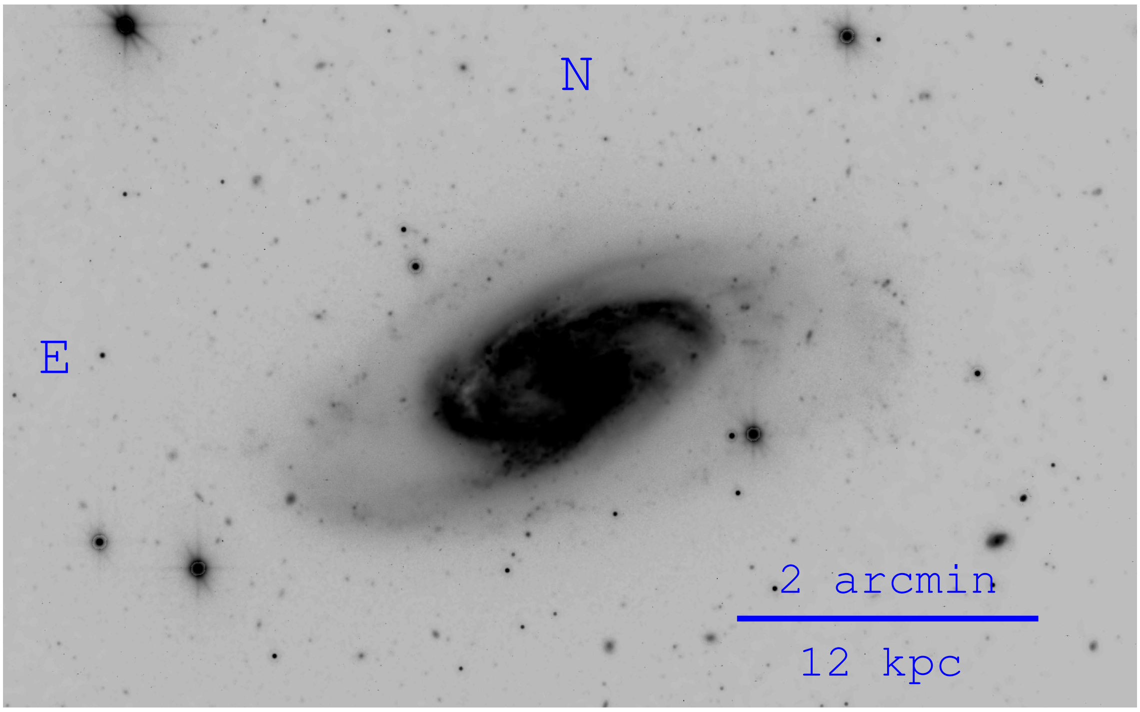

Figure 7.98: The environment around NGC 150

NGC 150 is an Sb galaxy at a distance of 20.5 Mpc. It shows a two arm grand-design spiral structure with asymmetric arms as well as regions with strong star formation, which are located where the arms and the bar are connected (Eskridge et al. 2002). The spiral arms are extending far into the faint outskirts of the galaxy. The arm in the west is very smooth and seems to be dissolving. A tidal interaction could be responsible for this feature.

In the observational data two CDG can be found. NGC 150 1 (CDG A) could be a quenched dIrr, as the optical appearance is not as smooth as for dSphs and the color profile shows a hint of a color gradient with a redder color in the outskirts. Due to the low SB and thus also very low S/N the SBP was fitted out to isophotes with values only 1 σ above the background. The second candidate was classified as dE. The fitted SBP categorizes it as CDG A. The color profile does not reveal any gradient in the stellar populations and it could possibly be a post-burst galaxy due to the big error bars. In the faint outskirts the left-over of tidal tails can be detected, a clear imbalance is visible there.

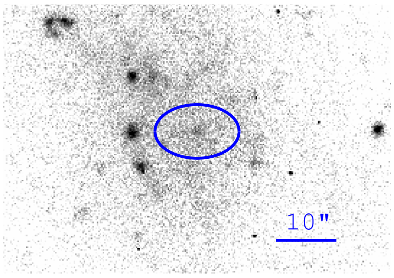

Figure 7.99: CDG NGC 150 1

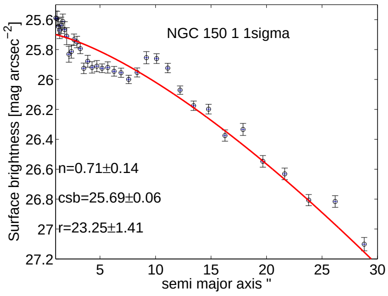

Figure 7.100: SBP of NGC 150 1

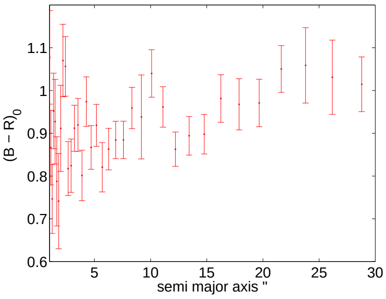

Figure 7.101: Color profile of NGC 150 1

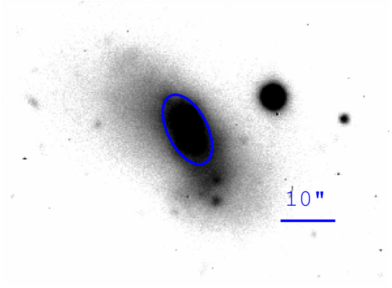

Figure 7.102: CDG NGC 150 2

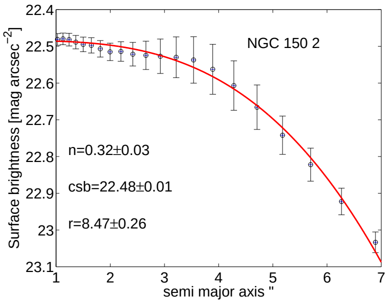

Figure 7.103: SBP of NGC 150 2

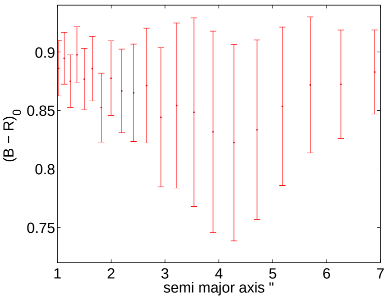

Figure 7.104: Color profile of NGC 150 2

7.13 NGC 578

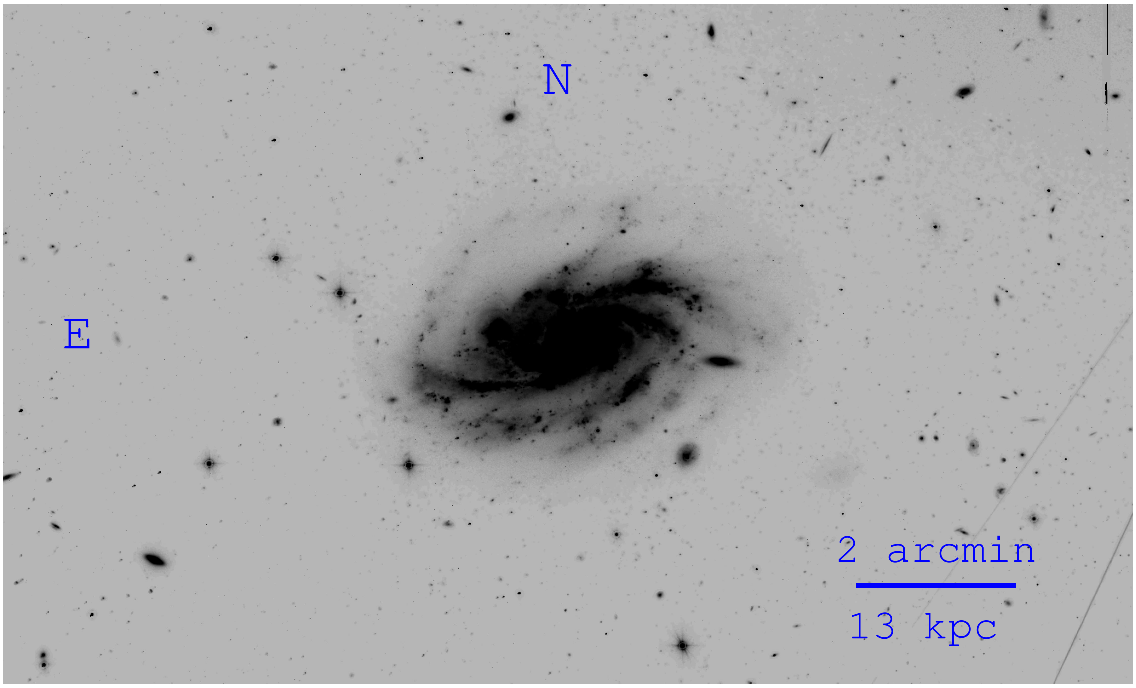

Figure 7.105: The environment around NGC 578

NGC 578 is an Sc galaxy at distance of 21.7 Mpc. The bar connects to several spiral arms and in the arms several bright HI regions can be seen. The spiral arms are extending into the outskirts with very low SB. Tidal debris or streams cannot be detected around NGC 578. In the southwest a very faint feature can be seen, but it is too distant to be caused by a tidal interaction, no connection to the central galaxy can be detected. Most likely this feature is caused by flats or a galactic cirrus region.

NGC 578 1 is classified as a dSph, the smooth light distribution categorizes it together with the fitted parameters of the SBP as CDG A. The color profile shows very constant color values, the redder color measurements in the center are not reliable because in the center the scatter can be high. The second CDG shows typical properties of a dSph. The SBP fit reveals a high *n*, therefore this candidate could be a background galaxy as well. The color profile does not show a clear gradient. The results suggest that this candidate is questionable (CDG B).

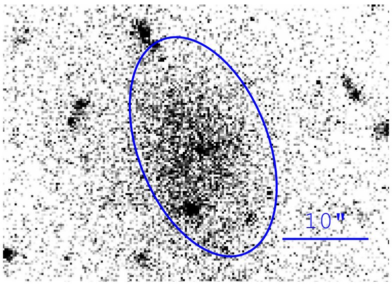

Figure 7.106: CDG NGC 578 1

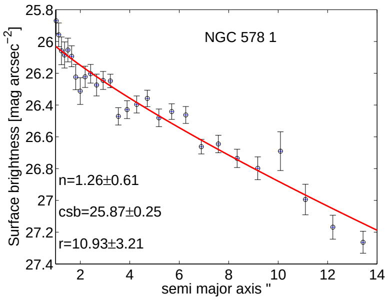

Figure 7.107: SBP of NGC 578 1

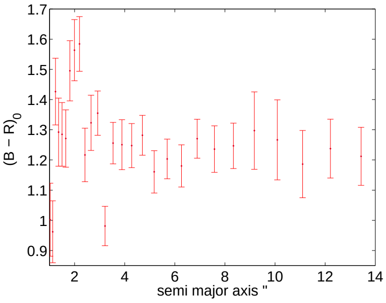

Figure 7.108: Color profile of NGC 578 1

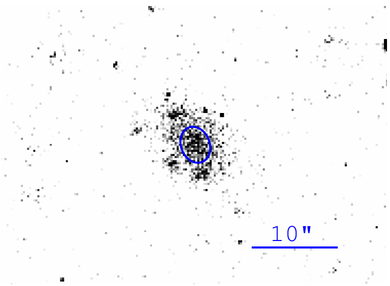

Figure 7.109: CDG NGC 578 2

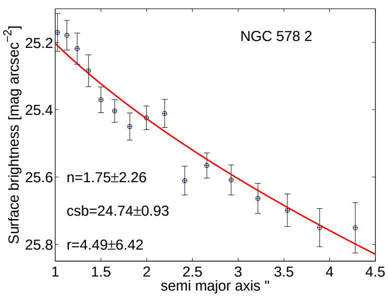

Figure 7.110: SBP of NGC 578 2

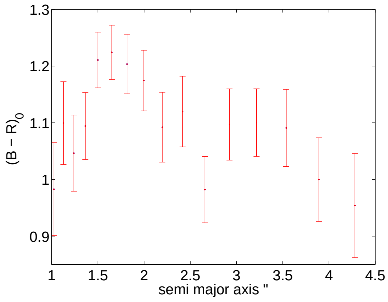

Figure 7.111: Color profile of NGC 578 2

7.14 NGC 755

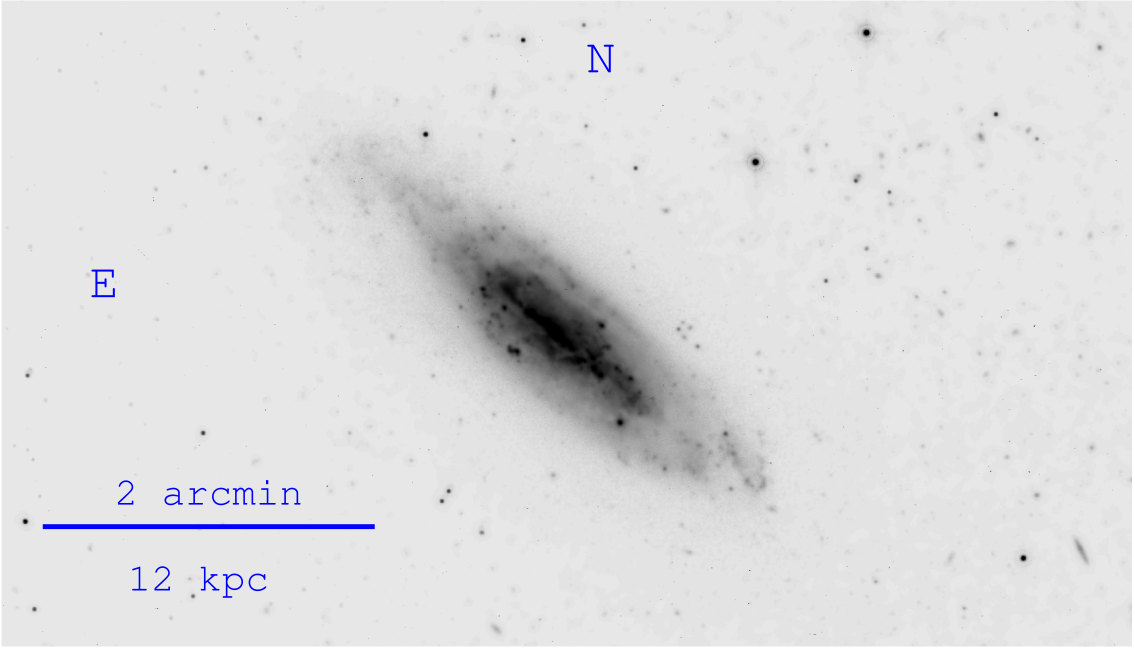

Figure 7.112: The environment around NGC 755

The Sb galaxy NGC 755 is located at a distance of 20.1 Mpc. The galaxy is fainter than many of the other targets ($M_B \sim -18$), but the faint smooth outskirts made this target interesting for studying tidal debris. The galaxy shows a clear warp, the low SB in the outskirts of the spiral structure is very extended. Despite the disturbed appearance of this target no signs of tidal debris or streams can be found down to the observational limits. The environment around this object exhibits no dwarf companion. This could be explained by the lower mass in contrast to the other targets, but is still a very interesting observation.

7.15 NGC 1425

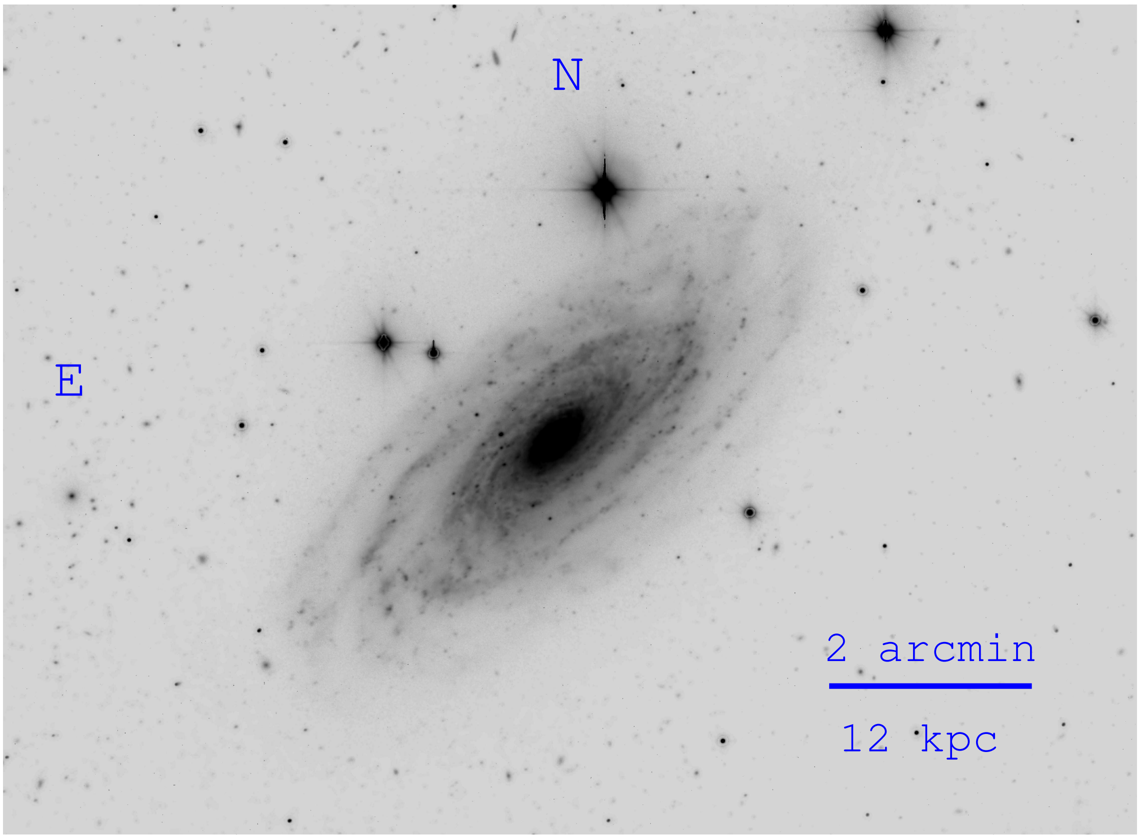

Figure 7.113: The environment around NGC 1425

NGC 1425 is an Sb galaxy with a distance of 21.2 Mpc and a member of the Fornax cluster. The galaxy is also in close proximity to the Eridanus group, but compared to Fornax Eridanus is at a larger distance (Mould et al. 2000). Despite the survey was clearly focused at the group environment, this target was interesting due to its high local density of 0.83 galaxies Mpc^{-3}. The galaxy is very regularly shaped, only in the southeast the spiral arms are more open. Interestingly, no sign of tidal debris or streams can be detected.

Despite of the high density local environment only one CDG can be found. It is a dSph with a nucleus, which can clearly be seen in the image. The SBP also highlights the core, as this is the reason that the profile is extremely steep in the inner regions, therefore it could also be a foreground star superimposed on the CDG. Due to this bright feature the fit is only performed in the outer regions, a smooth distributions of light can be seen in the profile there. The color profile is also disturbed by the core, as a clear gradient is going from a blue center with recent or ongoing star formation to redder colors in the outer regions. The blue center makes it relatively unlikely that the nucleus is a foreground star. Similar features can be seen in blue core dEs in the Virgo cluster (Lisker et al. 2008). All measured parameters categorizes NGC 1425 1 as CDG A.

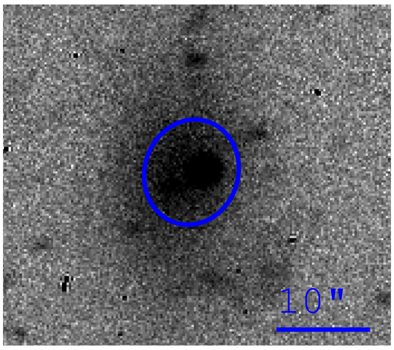

Figure 7.114: CDG NGC 1425 1

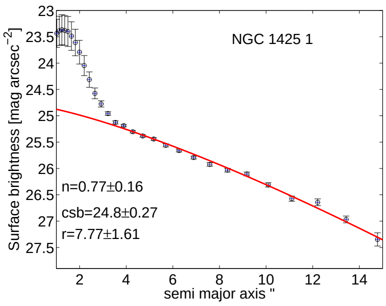

Figure 7.115: SBP of NGC 1425 1

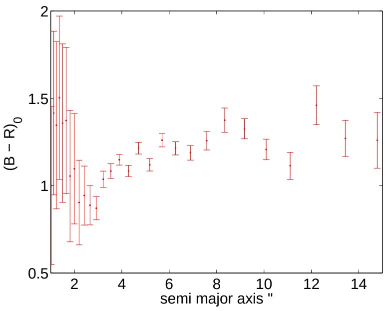

Figure 7.116: Color profile of NGC 1425 1

7.16 NGC 1532

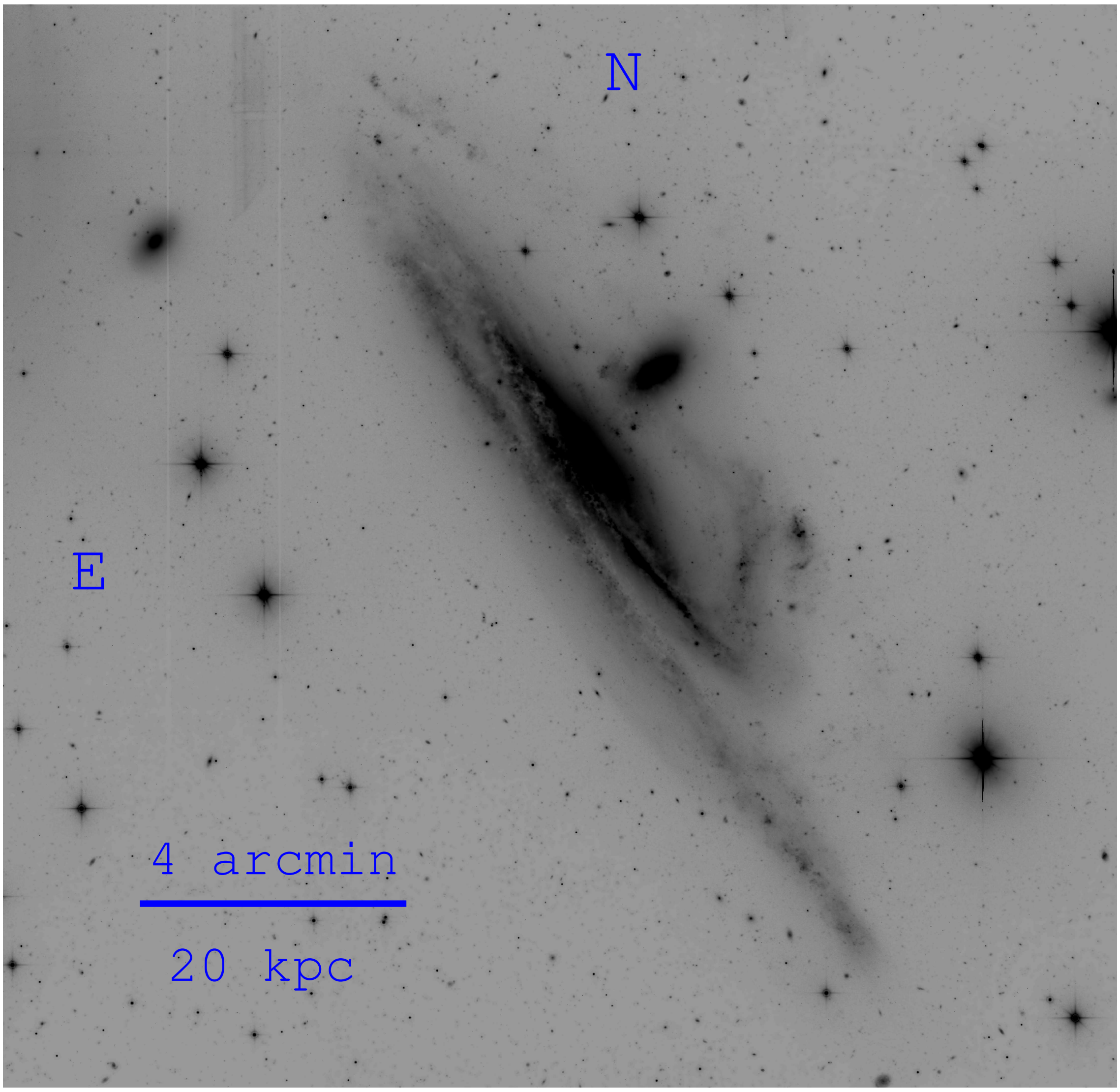

Figure 7.117: The environment around NGC 1532

NGC 1532 is an Sb galaxy at a distance of 17.1 Mpc. Sandage & Bedke (1994) already noted that the amorphous companion NGC 1531 caused the perturbation and tidal distortion. The merging system is comparable to M82. The faint features in the outer regions traces the interaction, especially the faint arm in the north and the tilted spiral arm in west suggest that the encounter has caused these features.

The CDG NGC 1532 1 (CDG A) is a dSph with a nucleus in the center. In the SBP the central isophotes show a steep profile. The fit was only performed to the outer smooth light distribution. The resulting parameters are in the range of dwarf galaxies. The color profile does not reveal any gradient. The color is nearly constant at all radii, only statistical fluctuations are visible.

The second CDG (CDG A) looks very similar to the first one, this dSph has also a nucleus in the center and the SBP shows the same light distribution as well as the color profile appears constant. The observed properties could also hint that this CDG is a transition type dwarf.

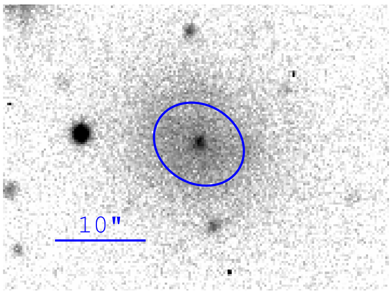

Figure 7.118: CDG NGC 1532 1

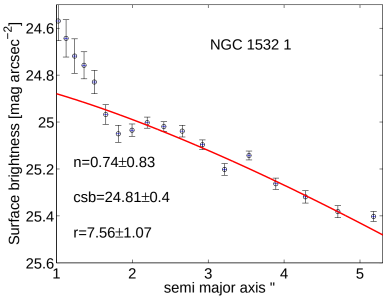

Figure 7.119: SBP of NGC 1532 1

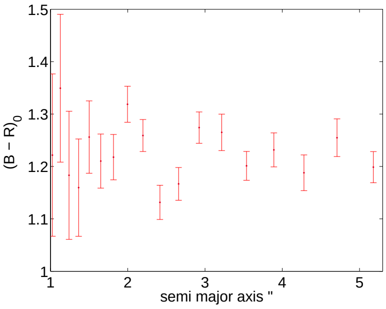

Figure 7.120: Color profile of NGC 1532 1

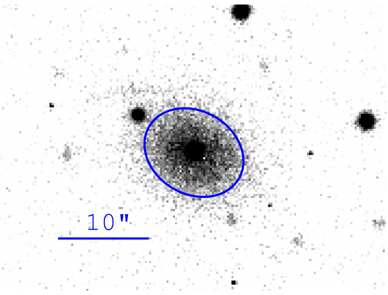

Figure 7.121: CDG NGC 1532 2

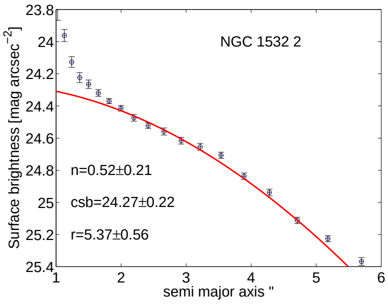

Figure 7.122: SBP of NGC 1532 2

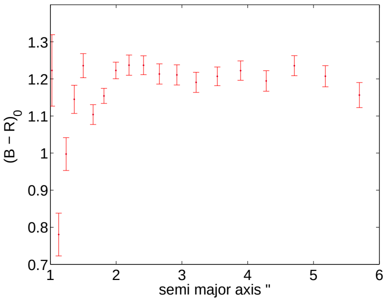

Figure 7.123: Color profile of NGC 1532 2

7.17 NGC 1964

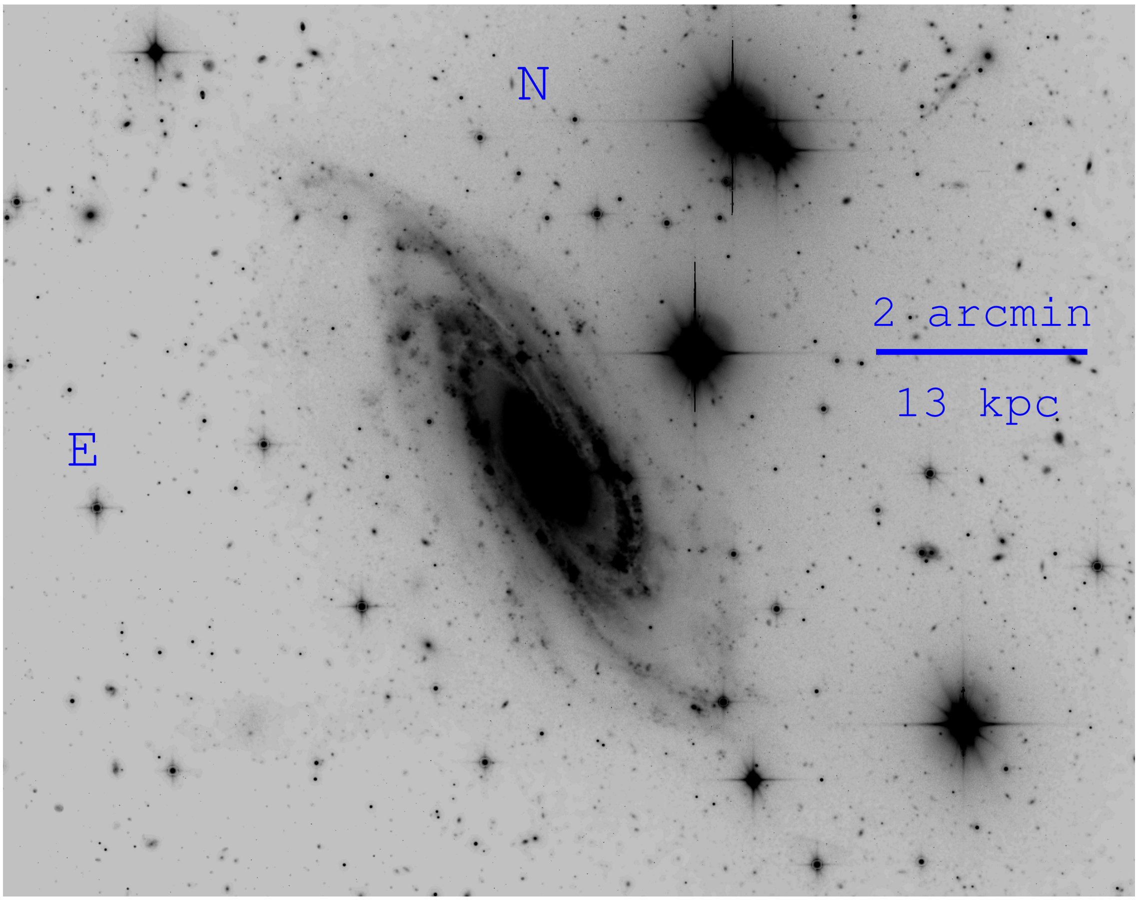

Figure 7.124: The environment around NGC 1964

NGC 1964 is Sb galaxy located in a distance of 21.4 Mpc. The galaxy shows signs of warp. The spiral arm in the north is much brighter than the opposite one. The spiral structure shows knots with high star formation in the central parts and towards larger radii the SB is going down rapidly. Signs of tidal debris can not be detected, though the galaxy appears slightly distorted.

NGC 1964 1 is classified as dIrr (CDG A). Two central bright regions with recent or ongoing star formation can be identified. These two regions are responsible that the SBP does not show a smooth distribution in the center. The color profile therefore shows a gradient with blue colors in the central parts and redder colors towards larger radii.

The second CDG is a dSph (CDG A) with a smooth light distribution highlighted with the SBP. The color profile does not show any gradient, only scatter around the measured color is visible. NGC 1964 3 (CDG A) shows a very smooth light distribution with a central core, therefore this CDG is labeled as a dSph with a nucleus. The SBP and the color profile show fluctuations due to low S/N caused by the low SB, therefore it is not possible to detect any gradient in the color profile.

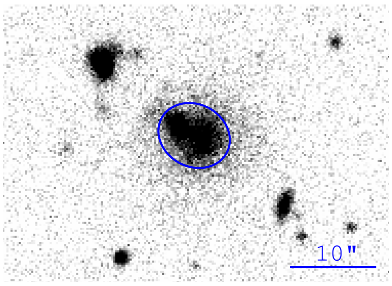

Figure 7.125: CDG NGC 1964 1

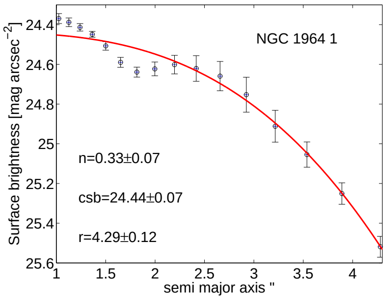

Figure 7.126: SBP of NGC 1964 1

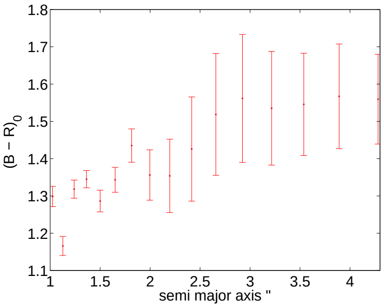

Figure 7.127: Color profile of NGC 1964 1

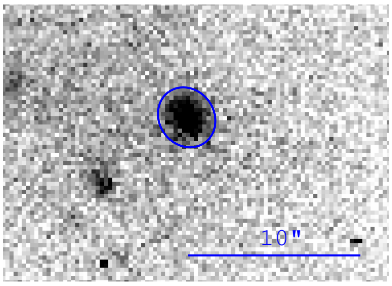

Figure 7.128: CDG NGC 1964 2

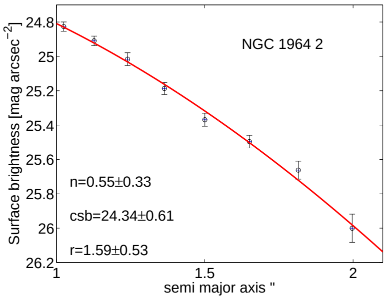

Figure 7.129: SBP of NGC 1964 2

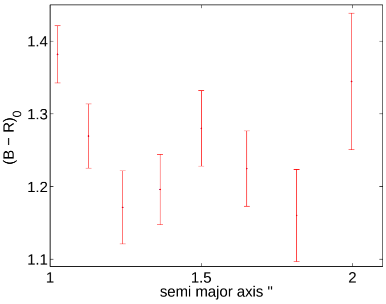

Figure 7.130: Color profile of NGC 1964 2

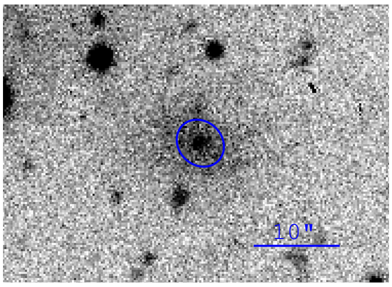

Figure 7.131: CDG NGC 1964 3

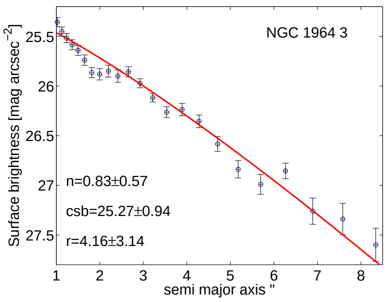

Figure 7.132: SBP of NGC 1964 3

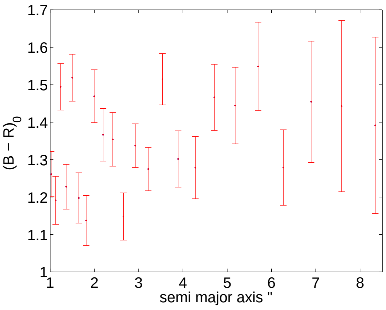

Figure 7.133: Color profile of NGC 1964 3

7.18 NGC 2310

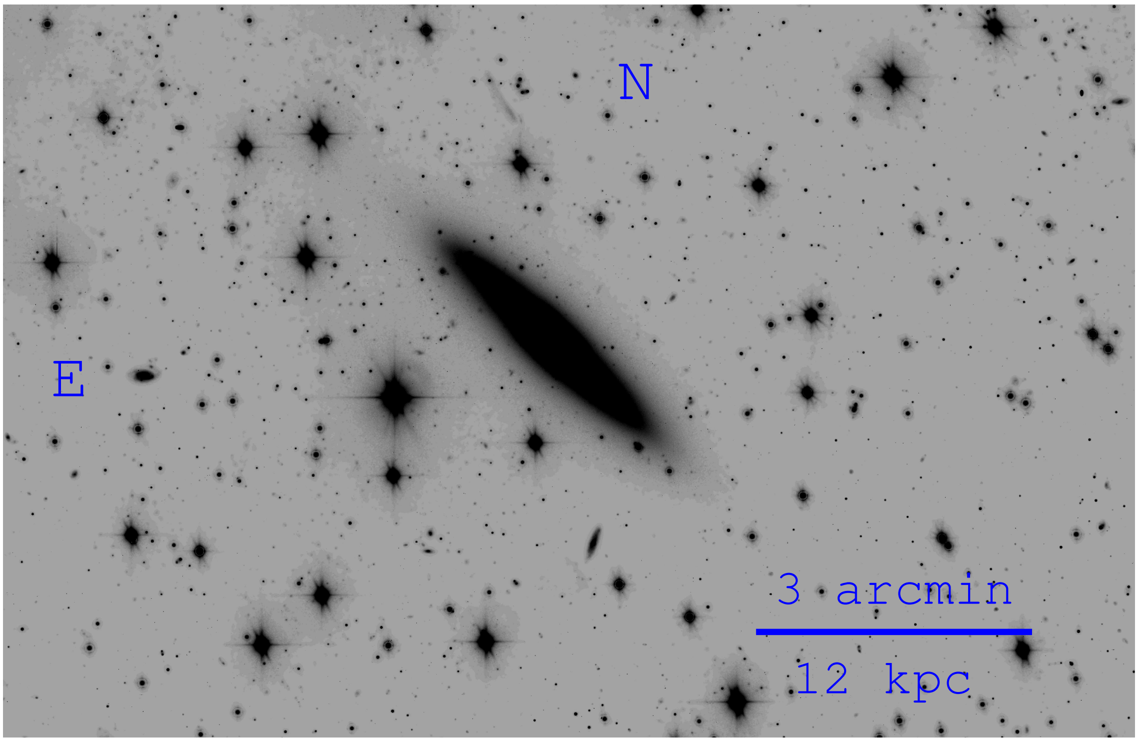

Figure 7.134: The environment around NGC 2310

The S0 galaxy NGC 2310 is located at a distance of 13.6 Mpc. The very symmetrical design shows a very undisturbed galaxy, only the northeast arm seems to be slightly wider than the opposite one. In the faint outskirts no signs of tidal debris nor streams can be detected down to the observational limits.

Our first CDG, NGC 2310 1, (CDG C) was allocated to the background objects after the analysis. The reason for showing the results is to demonstrate that the allocation of a CDG is reliable with the presented parameters. First of all, the SBP shows an exponential light distribution like it is expected for elliptical background galaxies with $n \sim 4$. The total measured color is extremely red and the color profile shows immensely red colors in the center, this is only expected for very old stellar populations at large redshifts. Also dust can cause such red colors. A clear gradient with bluer colors in the outskirts is not observed in any other CDG with a comparable steepness. Also all the observed parameters are not in the range of values expected for a CDG. This shows that the criteria for CDG are sorting out successfully background targets.

The CDG NGC 2310 2 is classified as dIrr due to several bright star forming regions distributed over the whole measured area. The fit to the SBP categorizes it as CDG A with expected parameters for this type. In contrast to other dIrrs no color gradient is visible, this is most likely due to the fact that radii regions with recent or ongoing star formation are distributed throughout this galaxy. This explains the constant blue color in the color profile and therefore all parameters support the assumption that this CDG could be a dIrr.

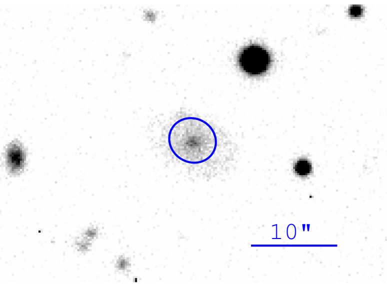

Figure 7.135: CDG NGC 2310 1

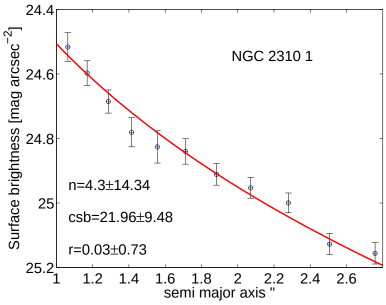

Figure 7.136: SBP of NGC 2310 1

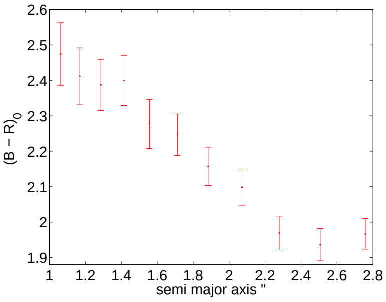

Figure 7.137: Color profile of NGC 2310 1

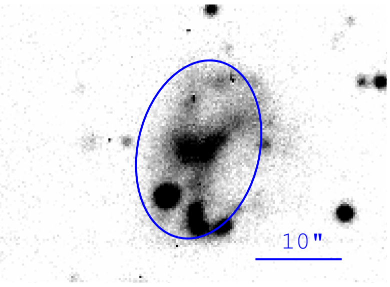

Figure 7.138: CDG NGC 2310 2

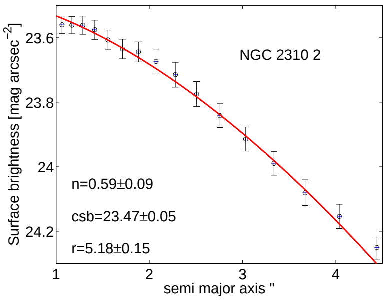

Figure 7.139: SBP of NGC 2310 2

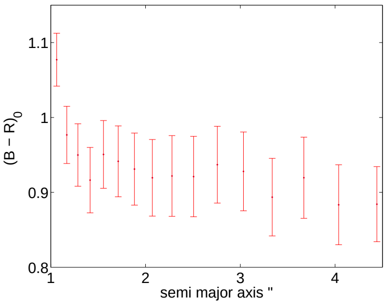

Figure 7.140: Color profile of NGC 2310 2

7.19 NGC 3717

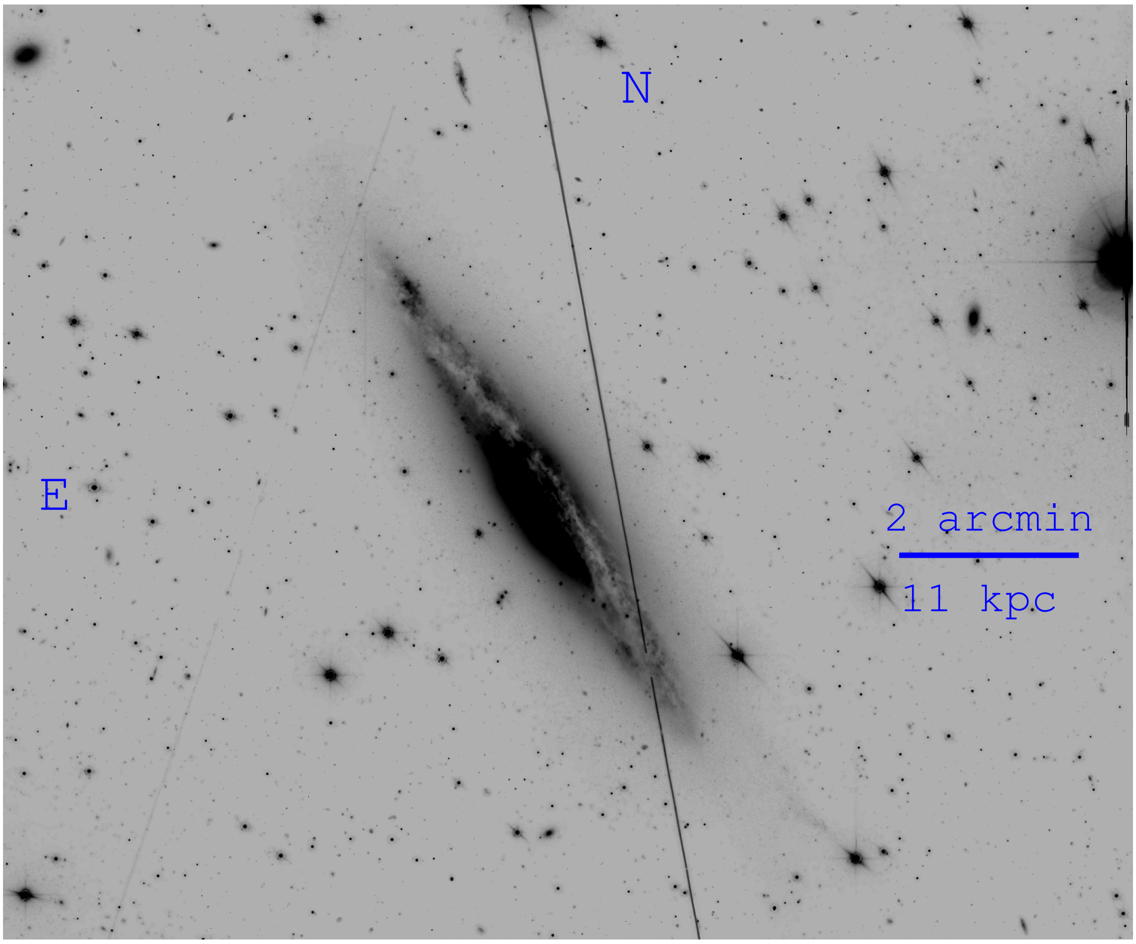

Figure 7.141: The environment around NGC 3717

NGC 3717 is an Sb galaxy seen edge on at a distance of 18.7 Mpc. Arp & Madore (1977) note that in close proximity a relatively bright compact galaxy can be observed (IC 2913). The target shows a warp in the spiral structure and hints of disturbances can be found. Especially in the faint outskirts of the object in the southwest of the spiral structure an extremely low SB feature can be seen at the same height of the disk.

In the observed environment two CDG can be found. NGC 3717 1 is labeled as dSph and the fitted parameters of the Sérsic profile to the SBP categorizes it as CDG A. The color profile shows a clear gradient with redder colors in the center.

The second CDG is classified as dIrr galaxy (CDG A). Its diffuse structure was inspected by eye. The color profile shows an extreme gradient with blue colors in the center of the CDG, this can be interpreted as tracers or signs of ongoing star formation. After the steep profile in the center the color tends to get slightly redder from intermediate to larger radii, therefore this CDG could maybe as well a transition type dwarf candidate. The measured parameters are in overlap with the expected range for CDG.

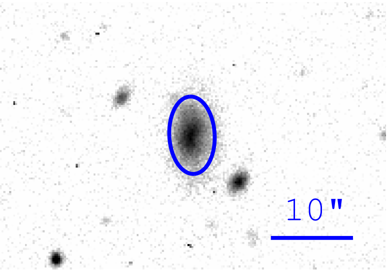

Figure 7.142: CDG NGC 3717 1

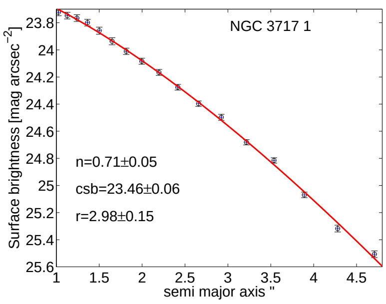

Figure 7.143: SBP of NGC 3717 1

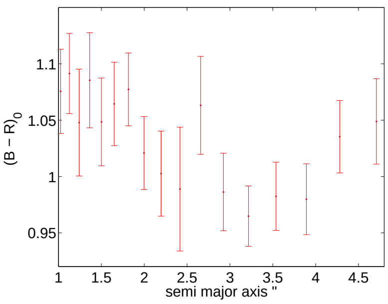

Figure 7.144: Color profile of NGC 3717 1

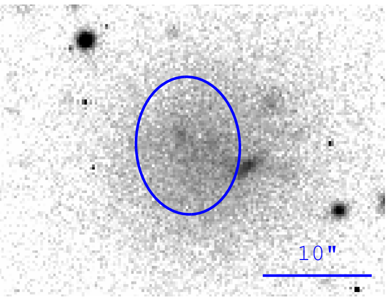

Figure 7.145: CDG NGC 3717 2

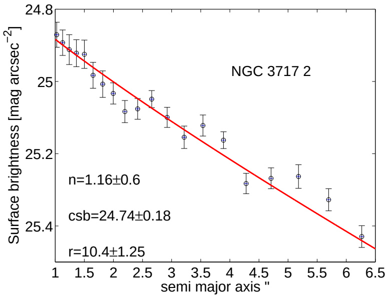

Figure 7.146: SBP of NGC 3717 2

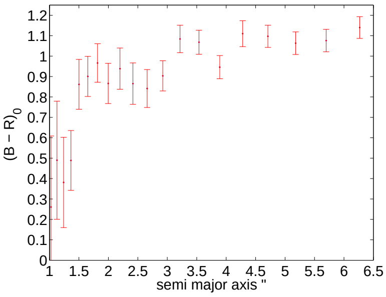

Figure 7.147: Color profile of NGC 3717 2

7.20 NGC 3936

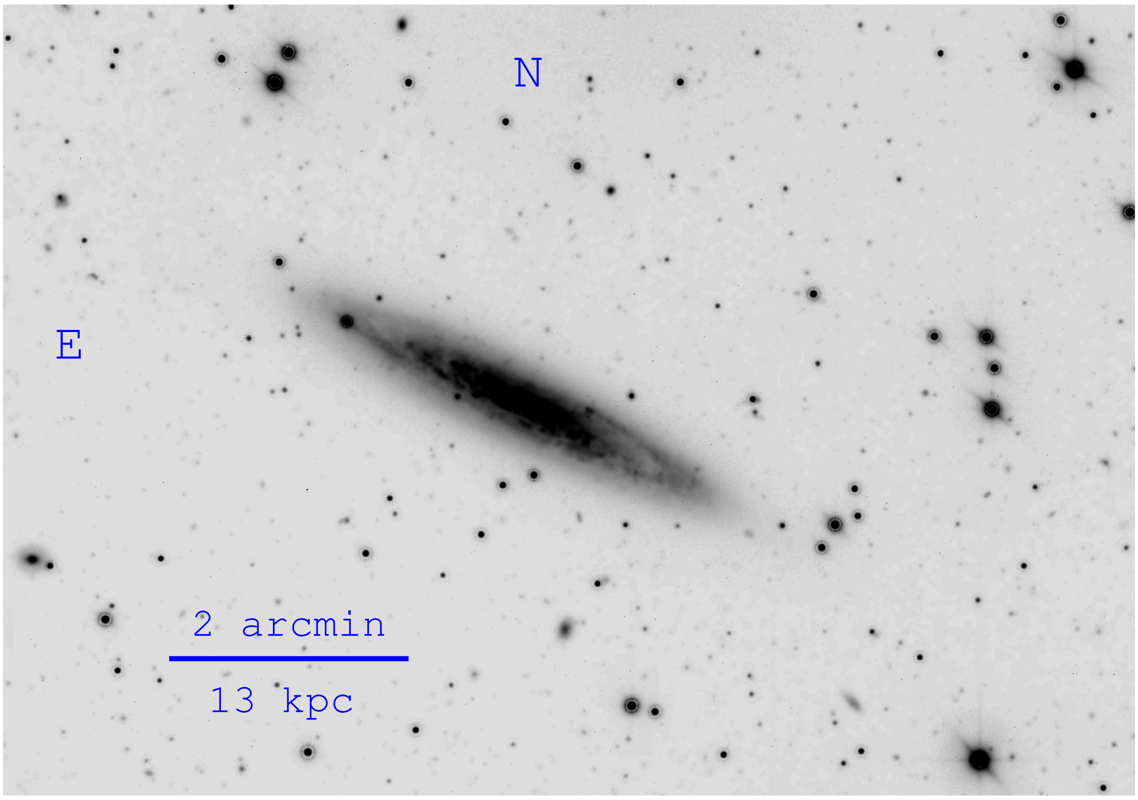

Figure 7.148: The environment around NGC 3936

NGC 3936 is an Sbc galaxy seen edge-on. The spiral arms show an extraordinary symmetric structure, only the arm in the southeast shows a higher SB than the arm in the opposite direction. The faint outskirts thus do not reveal any signs of tidal debris features, therefore no recent interaction or accretion event can be found around this target.

One CDG can be found in the observed field. Its optical appearance marks it as dE (CDG A). The SBP shows that the CDG has two components, a central core out to a semi-major-axis of 3.5″ (a cut in SBP can be detected) and a very smooth light distribution at larger radii. The color profile shows two gradients, a slight increase of the color to intermediate radii, in the outskirts a decline of the color to bluer regions can be seen. The profile suggests that this CDG has older stellar populations at intermediate regions and younger ones to larger radii.

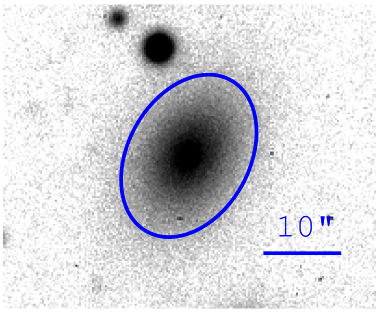

Figure 7.149: CDG NGC 3936 1

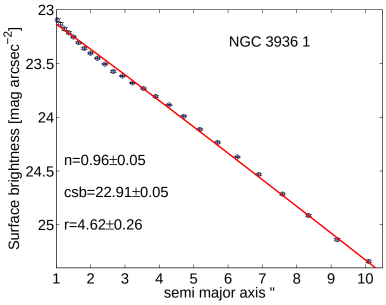

Figure 7.150: SBP of NGC 3936 1

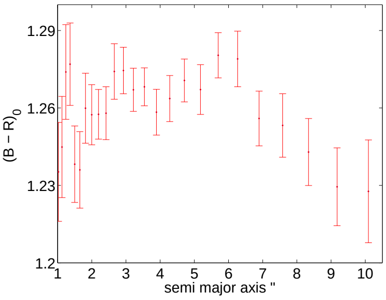

Figure 7.151: Color profile of NGC 3936 1

7.21 NGC 3956

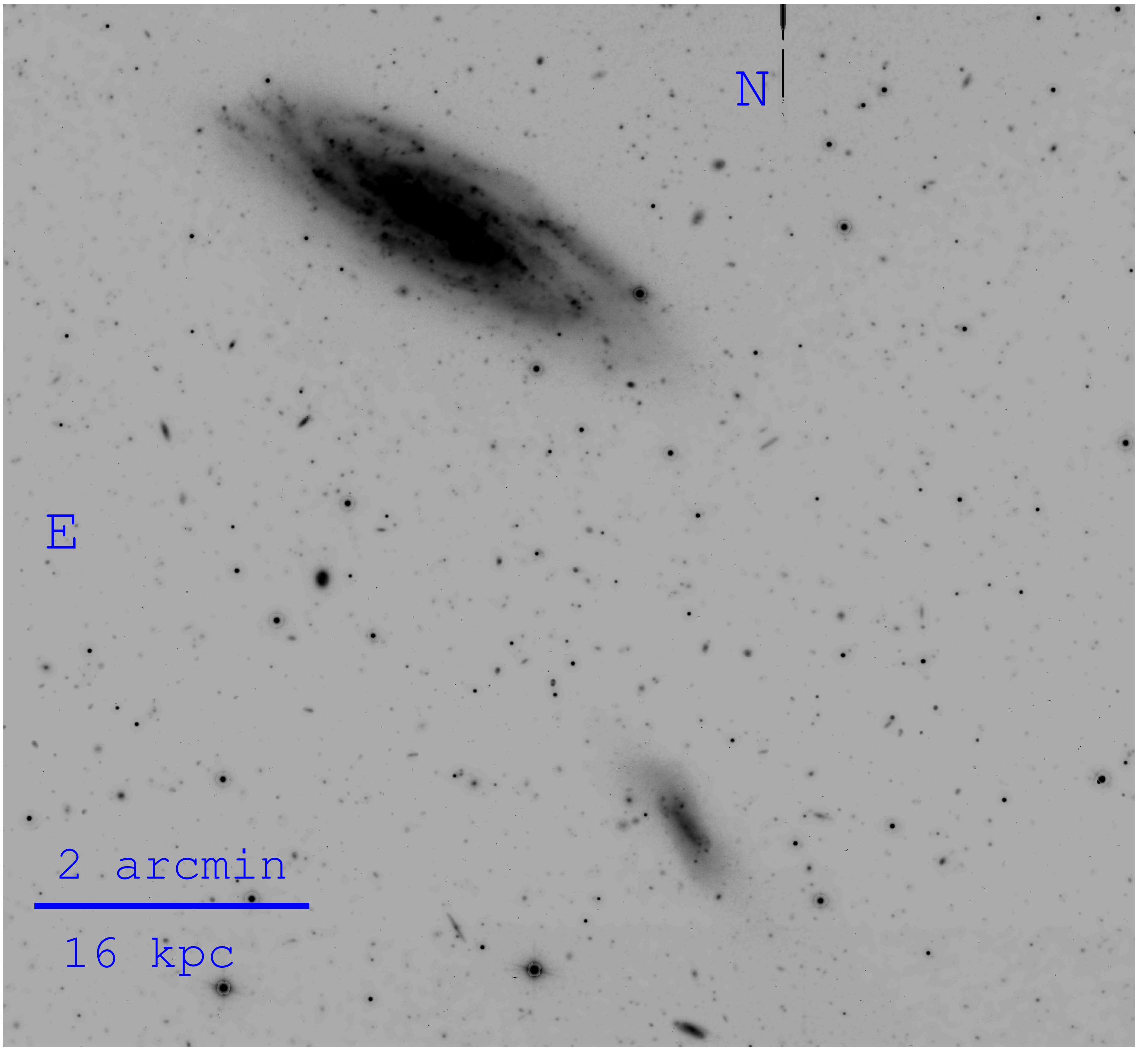

Figure 7.152: The environment around NGC 3956

NGC 3956 is an Sc galaxy at a distance of 27.3 Mpc. It appears lopsided and the spiral structure shows warp. Especially the arm in the northeast is much brighter than the opposite one and in all spiral arms bright knots with star formation can be seen. Despite the similarity to the MW or NGC 7331 no signs of tidal debris or streams can be observed in the regions around this target. Close-by the dIrr ESO 572-G011 can be seen. Very few hints suggest that it could be in tidal interaction with NGC 3956. In the faint outskirts of this CDG two features which look similar to tidal tails can be seen, it appears definitely disturbed.

Sandage & Bedke (1994) notes that NGC 3956 is in a region with a number of galaxies, together with the S0 NGC 3957 and the Sbc galaxy NGC 3981 (will be discussed in the next section) this is an analog to the Local Group when comparing the measured heliocentric velocity and the measured distance of every member to each other to the properties of the Local Group. Additionally, in the region around and between them many dE, Im and Sm CDG can be observed (Sandage & Bedke 1994).

In close proximity to NGC 3956 three CDG can be found. The first one shows a bright off-center region with recent or ongoing star formation. Therefore it was classified as dIrr. The parameters of the

Sérsic function fit to the light distribution supports the classification as CDG. The color profile shows a linear gradient with bluer colors towards larger radii, this is most likely caused by the bright region with star formation at the border of the studied area. This color profile with a linear gradient is different from the profiles of our CDG sample. Therefore it is marked only as CDG B.

NGC 3956 2 (CDG A) is a dSph, the low SB and very smooth light distribution can be seen in the stamp image. The SBP is scattering around the fit, but this is not unusual given the low S/N. Therefore also the color profile shows only scatter around the examined color of this CDG.

Visual inspection suggests that the third CDG is classified as dSph (CDG A) with a nucleus. The bright central region is also the reason that a break can be found in the SBP at an SMA of 2″. The Sérsic fit is only performed at larger radii to fit only the outer component. Interestingly, though two components can be seen in this CDG, there is no gradient in the color profile.

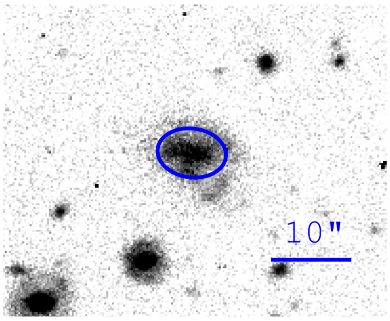

Figure 7.153: CDG NGC 3956 1

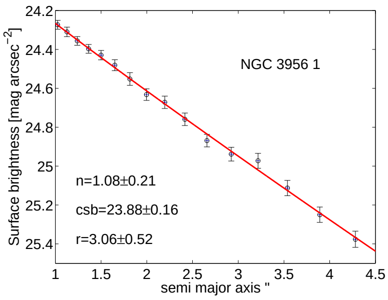

Figure 7.154: SBP of NGC 3956 1

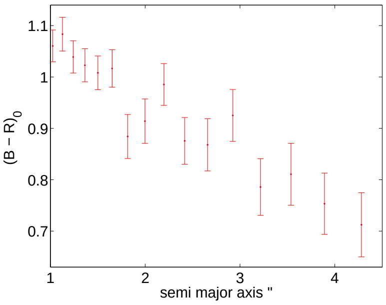

Figure 7.155: Color profile of NGC 3956 1

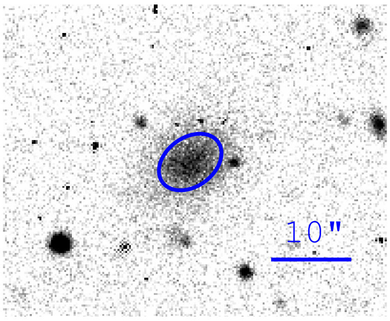

Figure 7.156: CDG NGC 3956 2

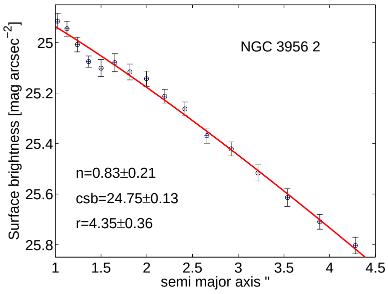

Figure 7.157: SBP of NGC 3956 2

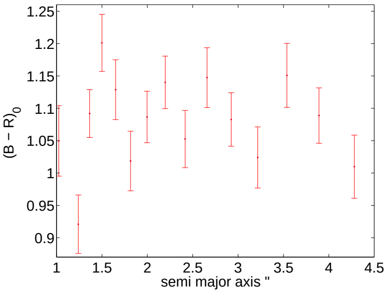

Figure 7.158: Color profile of NGC 3956 2

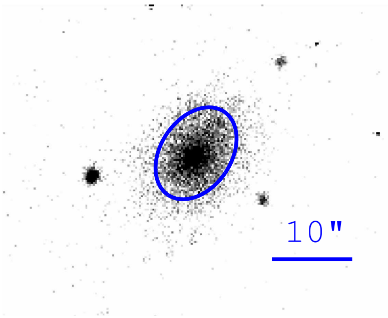

Figure 7.159: CDG NGC 3956 3

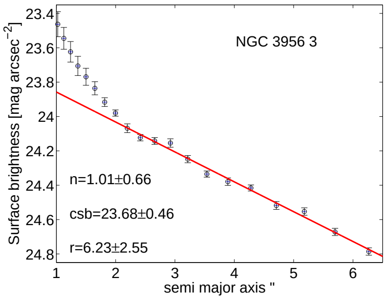

Figure 7.160: SBP of NGC 3956 3

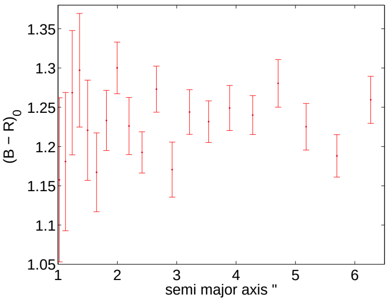

Figure 7.161: Color profile of NGC 3956 3

7.22 NGC 3981

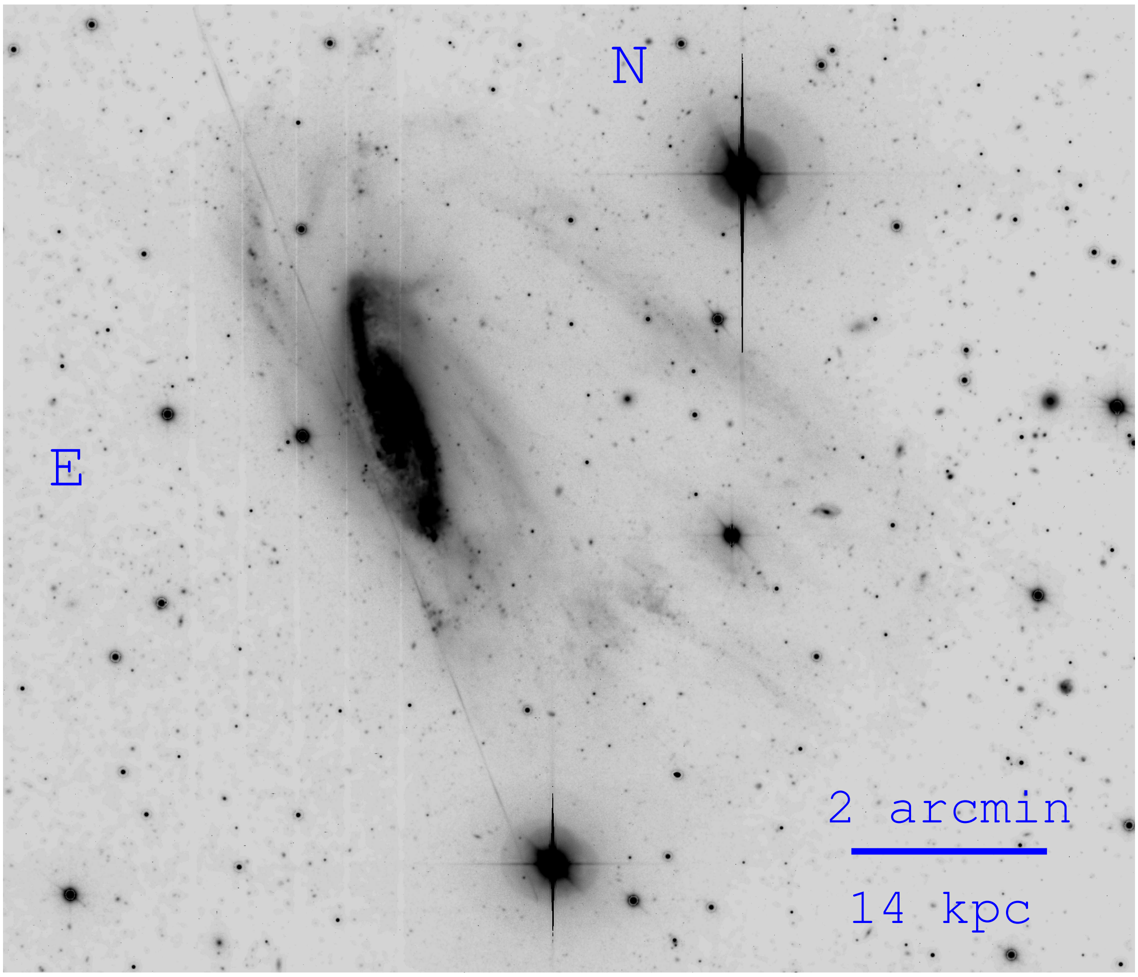

Figure 7.162: The environment around NGC 3981

NGC 3981 is an Sbc galaxy located at a distance of 23.8 Mpc, it is in the same group as the previously presented galaxy. The galaxy is extremely disturbed. This galaxy is or was clearly in interaction with another galaxy. In the central regions the spiral structure appears slightly warped and lopsided, especially at the end of the arm directing south an extremely bright region with star formation. At larger radii the spiral arms are spread wide into the outskirts of the galaxy. Three main features of tidal debris can be seen, in the east the extension of a spiral arm forms a shield like structure. In the opposite direction to the west a similar feature can be detected, but in contrast to the previous one no connection to any spiral arm can be identified. The third feature is a very extended cloud in the south. A lot of material must have been thrown out during the merging process.

Two CDG have been found in the observed field. The first one is a typical dSph (CDG A) with a smooth light distribution and a low SB. Like for many other observed dSphs no gradient is visible in the color profile, due to the low S/N, which is caused by the faint SB, only scatter around the measured color can be seen there.

NGC 3981 2 (CDG B) shows many bright off-center regions with recent or ongoing star formation. This dIrr appears extremely disturbed and seems to be in interaction. The SBP is problematic, many different features can be seen there. There is a nucleus in the center. This extremely bright feature shows a steep luminosity profile, therefore this could also be a superimposed foreground star. The measured PSF would be consistent with a foreground star. To larger radii a smooth light distribution can be found, but suddenly is decreasing rapidly again until it is getting constant at the largest radii again. Therefore the fit of an Sérsic function to this complicated light profile is difficult. The same features appear in the color profile, in the center where the nucleus is located red colors can be observed. Then there is an extraordinarily steep decline in color and at larger radii the blue color stays constant with maybe a subtle decrease in color. The nature of this target is questionable, the steep color decline in the central region could be a hint that the central core feature is a projected compact elliptical. Nevertheless, it would be also possible that a faint dIrr is in a merging process with this cE. Nevertheless, a background merger seems unlikely because no spiral structure can be detected.

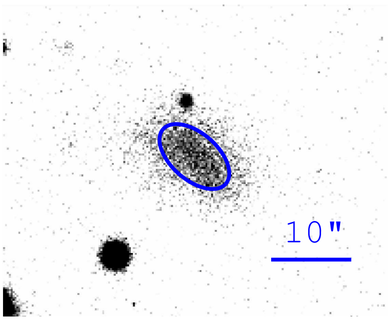

Figure 7.163: CDG NGC 3981 1

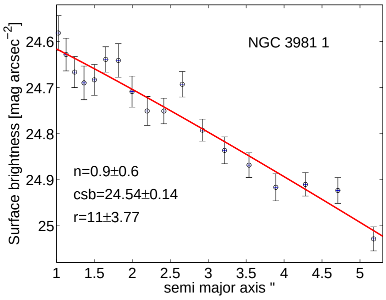

Figure 7.164: SBP of NGC 3981 1

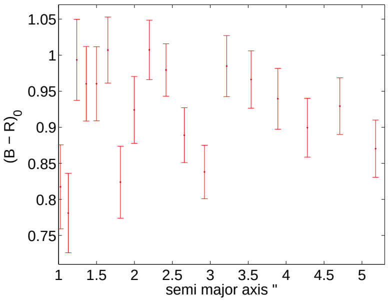

Figure 7.165: Color profile of NGC 3981 1

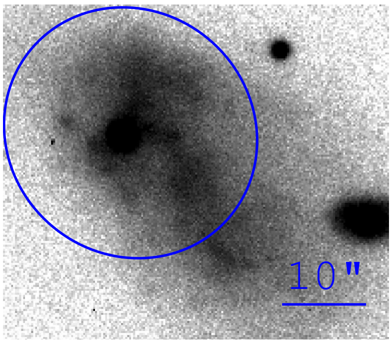

Figure 7.166: CDG NGC 3981 2

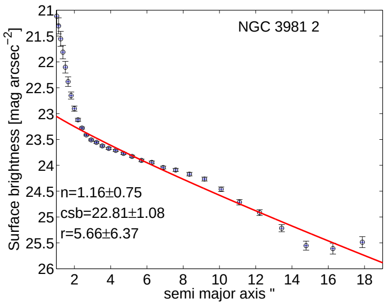

Figure 7.167: SBP of NGC 3981 2

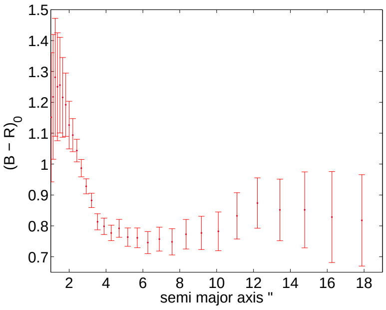

Figure 7.168: Color profile of NGC 3981 2

7.23 NGC 4219

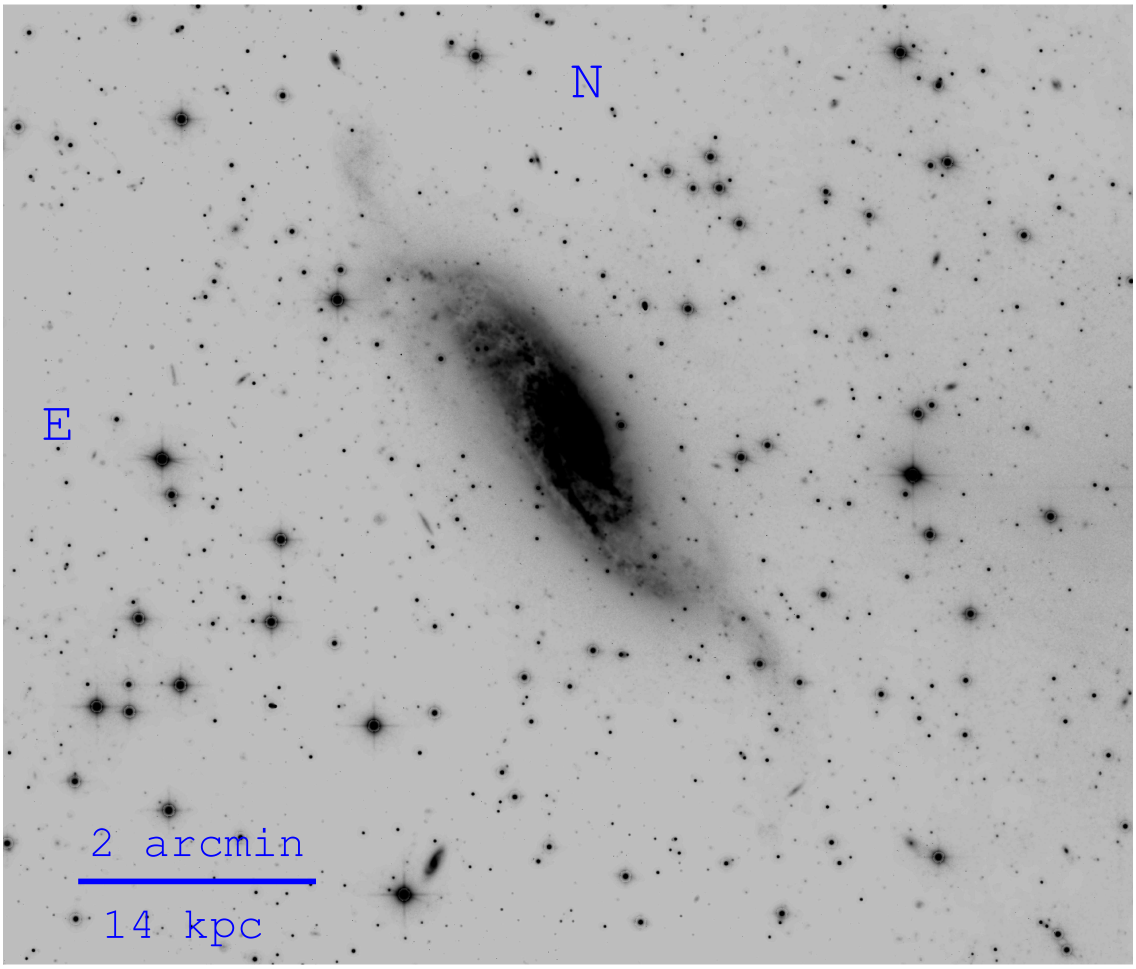

Figure 7.169: The environment around NGC 4219

NGC 4219 is located at a distance of 23.3 Mpc and typified as Sbc. Its spiral structure shows thin main spiral arms together with a two-armed inner spiral pattern, additionally, a compact bulge with a crescent-shaped structure is visible (Heraudeau et al. 1996). A warp can be identified and in the faint outskirts a lot of disturbances are visible. The spiral arms extend very far into the low SB regions of the galaxy. At both sides of the galaxy faint tidal debris in form of a plume can be detected. The structures are connecting to the spiral arms and in the southwest the plume is much more extended. The signs of tidal debris show that this object has overgone a severe tidal interaction.

One CDG can be found in the observed field around the target, its very smooth and fuzzy appearance marks it as dSph (CDG A). The SBP is noisy due to the low S/N of this candidate, but the Sérsic profile fit results typical dwarf galaxy parameters. In the color profile the measured color stays constant with only fluctuations around the average value, which is not surprising given the faint SB of this object.

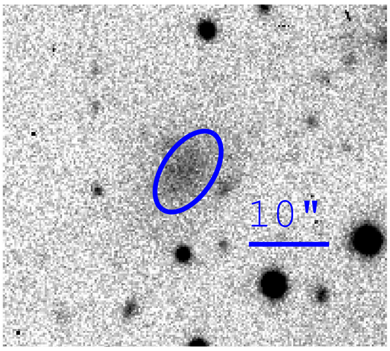

Figure 7.170: CDG NGC 4219 1

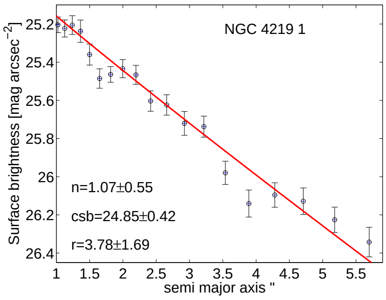

Figure 7.171: SBP of NGC 4219 1

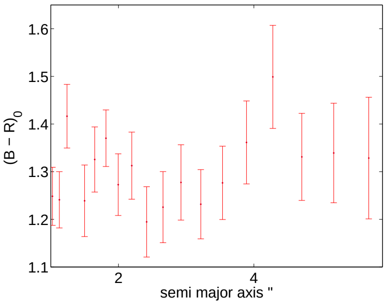

Figure 7.172: Color profile of NGC 4219 1

7.24 NGC 4835

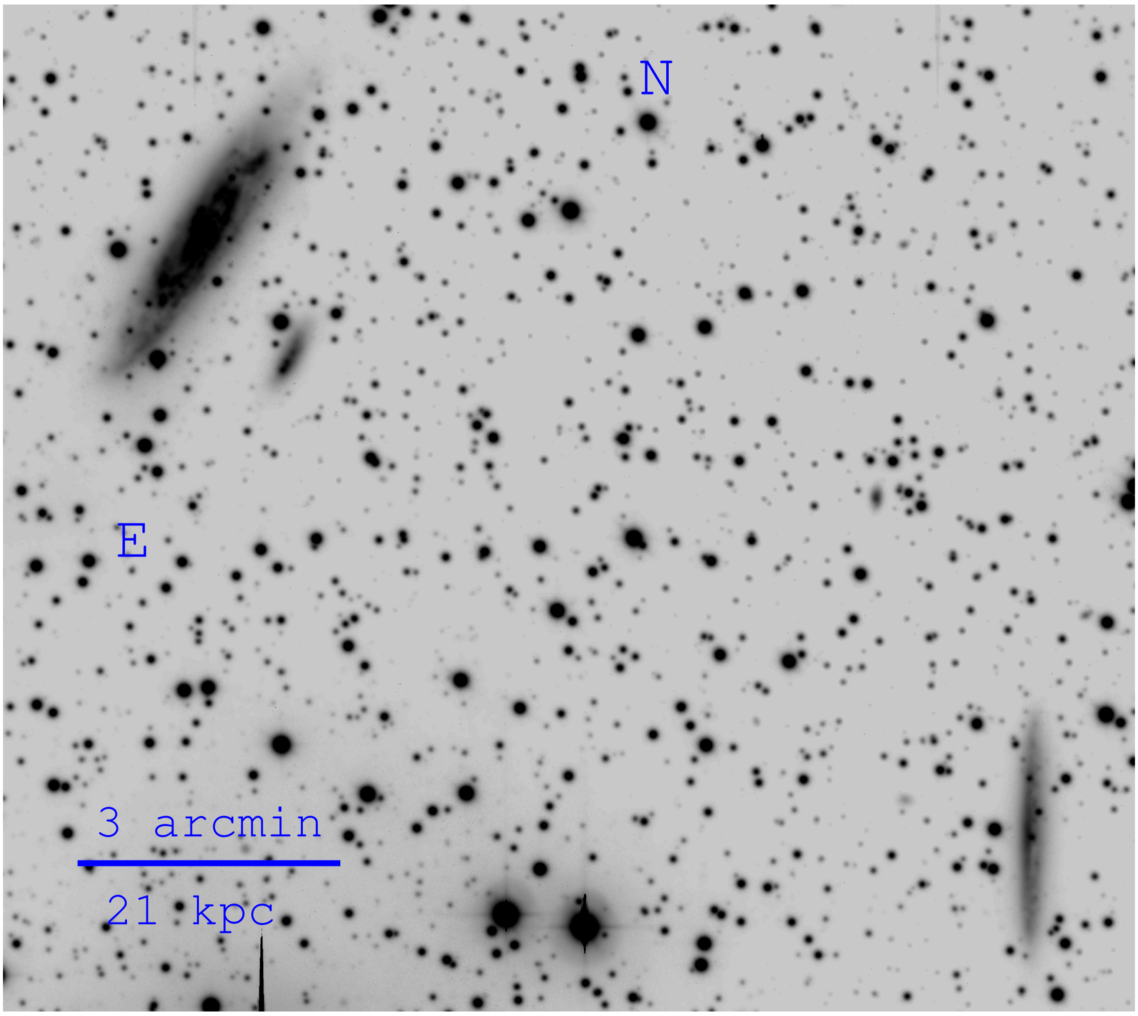

Figure 7.173: The environment around NGC 4835

The Sbc galaxy NGC 4835 is observed at 24.3 Mpc. Sandage & Bedke (1994) note that this is a galaxy pair with a dwarf companion classified as Im and that the resolution of the knots (HII) in NGC 4835 and the dwarf companion are the same, thus most likely both are at the same distance. Another faint spiral, NGC 4835A, is visible in the lower left, but with a distance of 46.9 Mpc it is not member of the observed system.

NGC 4835 has thin spiral arms and shows disturbances in its faint outskirts, especially at the north edge of the target a plume which connects to the spiral structure can be observed. Therefore an ongoing or past tidal interaction must have shaped this feature.

In the observed field around this object three CDG were found. The first one is a dSph with a smooth light distribution, which can also be seen in the SBP. Toghether with the color all measured parameters categorize it as CDG A. No gradient can be seen in the color profile, only scatter around the mean measured color is visible there. NGC 4835 2 (CDG C) is classified as dSph as well due to the smooth light distribution and the parameters of the Sérsic profile fit to the SBP are in the range observed for dSphs. But the color profile is unusual, because a steep linear gradient with bluer colors at larger radii can be identified. Therefore the nature of this object is unclear and it could represent also a rarely seen low SB background galaxy. The third CDG (CDG B) shows a diffuse structure with a nucleus and additional bright off center regions. Its color profile shows a lot of scatter in the inner regions. This could be caused by the diffuse structure and the small area of fitted isophotes. Moving outwards, a clear gradient with bluer colors at larger radii is visible. It is assumed that this effect is caused by star formation in different regions. These locally limited regions at intermediate radii and the properties of the stellar populations there would also explain why at the edge the color is getting redder again.

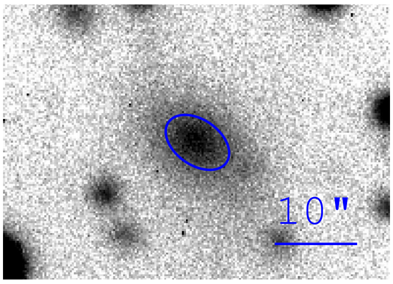

Figure 7.174: CDG NGC 4835 1

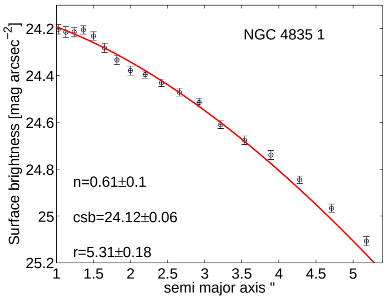

Figure 7.175: SBP of NGC 4835 1

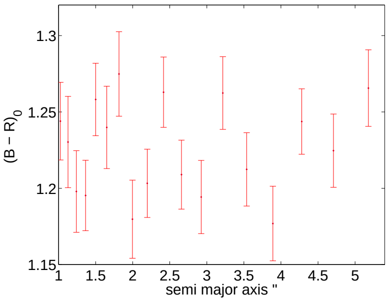

Figure 7.176: Color profile of NGC 4835 1

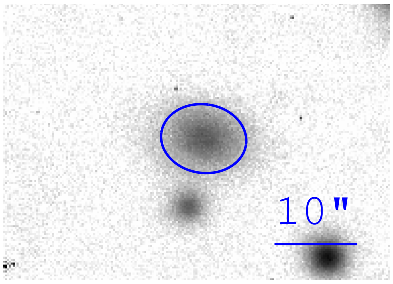

Figure 7.177: CDG NGC 4835 2

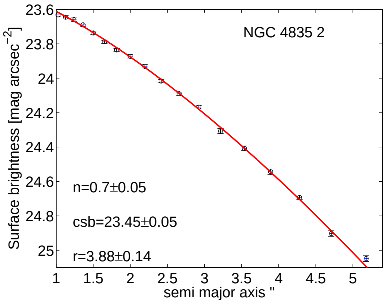

Figure 7.178: SBP of NGC 4835 2

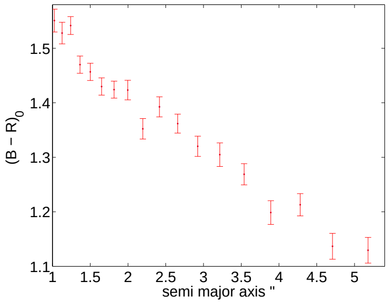

Figure 7.179: Color profile of NGC 4835 2

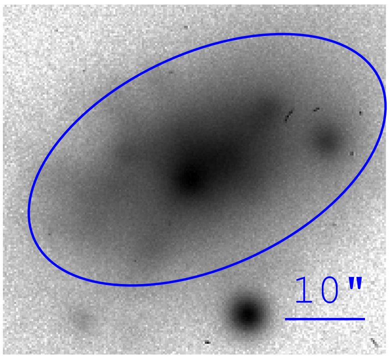

Figure 7.180: CDG NGC 4835 3

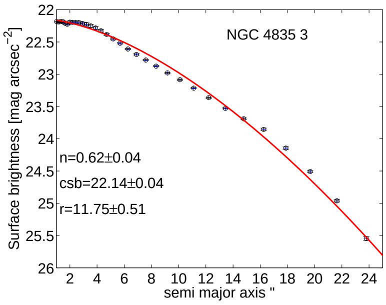

Figure 7.181: SBP of NGC 4835 3

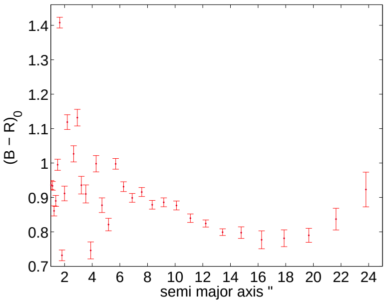

Figure 7.182: Color profile of NGC 4835 3

7.25 NGC 6810

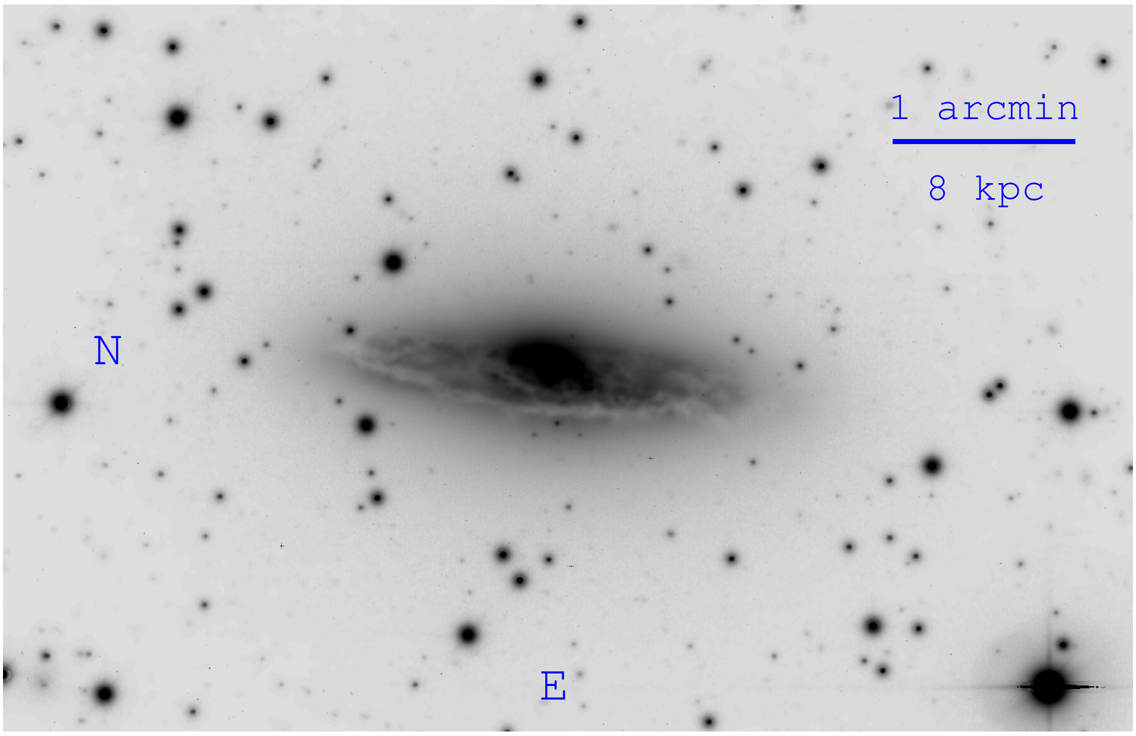

Figure 7.183: The environment around NGC 6810

NGC 6810 is Sab galaxy located at a distance of 27.2 Mpc.

It is seen edge-on and the spiral structure turns out to be lopsided and warped. Heraudeau et al. (1996) report that this highly inclined galaxy shows a large-scale dust lane and a complex central structure with a bright disk as well as a crescent-like bright feature can be seen on the far side which is the unobscured half of the innermost bulge. Interestingly, the spiral arms connect to these inner regions and a large bulge which is shaping the spiral structure give this target an impressive behavior (Heraudeau et al. 1996). In the faint outskirts no signs of tidal debris or accretion events can be identified.

Two CDG are found in the observations of this survey. Both are classified as dIrrs due to their diffuse appearance and off-center bright regions with recent or ongoing star formation. The first CDG (CDG A) shows a typical light distribution and in the color profile a linear gradient with bluer colors at larger radii can be recognized. This could be caused by the nuclear feature in the center, which appears less spherical as in other CDG. NGC 6810 2 (CDG A) has a more fuzzy light distribution due to more concentrated and a higher number off-center regions than other dIrrs. The color profile shows that it has two components. In the inner region the measured color is about 1.14 mag (could be also a steep gradient if there are some major fluctuations). At a radius of $6''$ a clear break can be identified. In the outer regions a constant bluer color is observed. This could be explained by the bright outer regions, whose stellar populations are completely different because they could have recent or ongoing star formation.

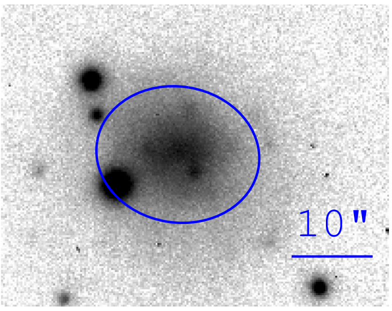

Figure 7.184: CDG NGC 6810 1

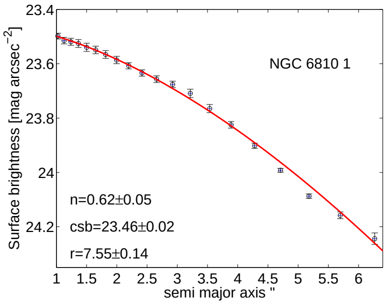

Figure 7.185: SBP of NGC 6810 1

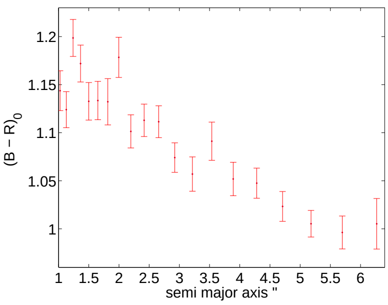

Figure 7.186: Color profile of NGC 6810 1

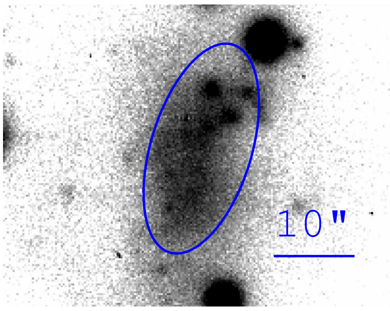

Figure 7.187: CDG NGC 6810 2

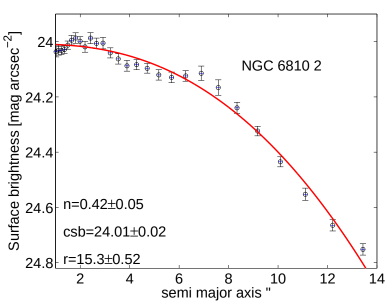

Figure 7.188: SBP of NGC 6810 2

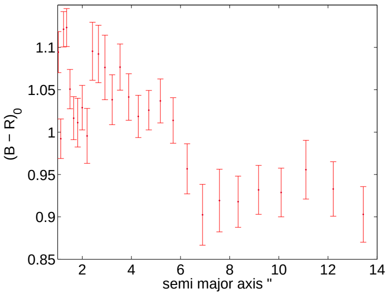

Figure 7.189: Color profile of NGC 6810 2

7.26 PROPERTIES OF THE OBSERVED CDG

At the end of this chapter we visualize the results of the CDG found in this work. All magnitudes and B-R colors in the presented figures are corrected for galactic foreground extinction. In the following figures only members of the CDG A and CDG B classification are taken into account. In the figures 7.190 – 7.194 we show histograms of the measured values of all CDGs. The selection criteria for candidates set basically the border at both ends of the histograms, but overall background targets are expected to show completely different values, so this supports the assumption that the parameter range is well chosen.

As a second step we checked if there are relationships between the measured properties of our CDG sample. A clear relationship has only been found for the central surface brightness and the absolute magnitude M_B (see Figure 7.195). That the luminosity is a strong function of the observed surface brightness was already reported by many other studies (e.g. Caldwell et al. 1992; Jerjen et al. 2000; Sharina et al. 2008; Makarova et al. 2009, and in many more studies).

Figures 7.197 and 7.199 show only a weak dependence of the color on the central surface brightness and M_B. Scatter is most likely caused by photometric errors and calibration uncertainties. The measured properties of the CDGs do not show any dependence on the projected distance (see Figure 7.198 and 7.196). A possible reason that we do not find any relationship is that our field of view is limited and therefore we are concentrating at the closest-by dwarfs. Moreover, we only have projected distances. Only a few outliers would make it already very difficult as our dwarf sample is limited.

Structural parameters of the Sérsic profile fit to the luminosity distribution show no hints of any relationships 7.200 – 7.202. This suggests that structural properties of the luminosity distribution are not specific for any luminosity or color of the studied CDG.

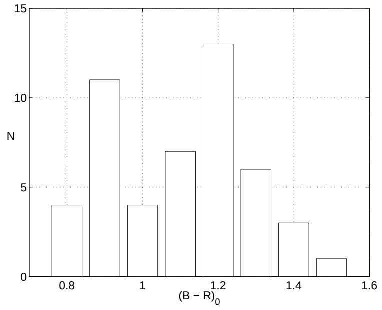

Figure 7.190: Overview of distribution of all measured colors.

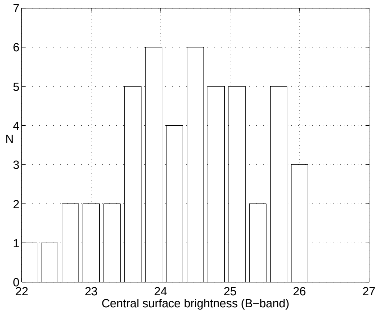

Figure 7.191: The central surface brightness of the CDG.

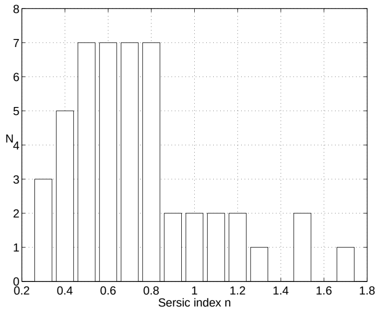

Figure 7.192: The Sérsic indices from the SBP fits.

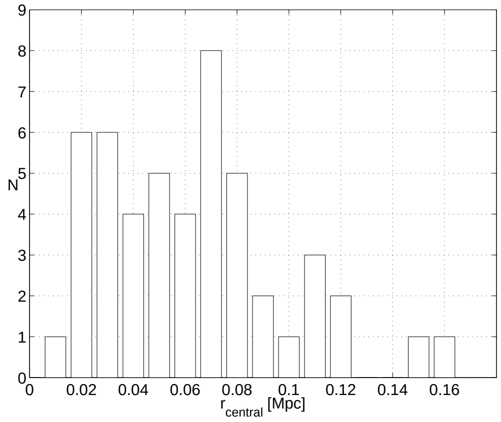

Figure 7.193: Projected distances to the central galaxy with assuming the CDGs to be at the same distance.

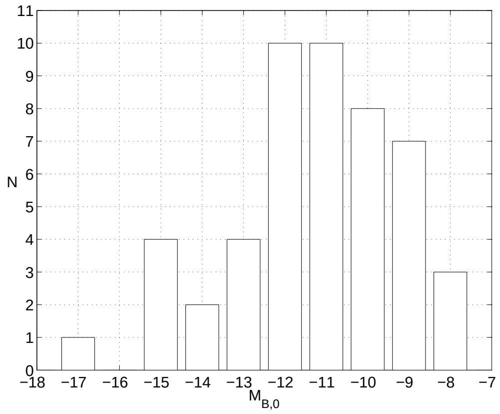

Figure 7.194: The extinction corrected absolute magnitudes with using the same distances modulus as the central spiral galaxy.

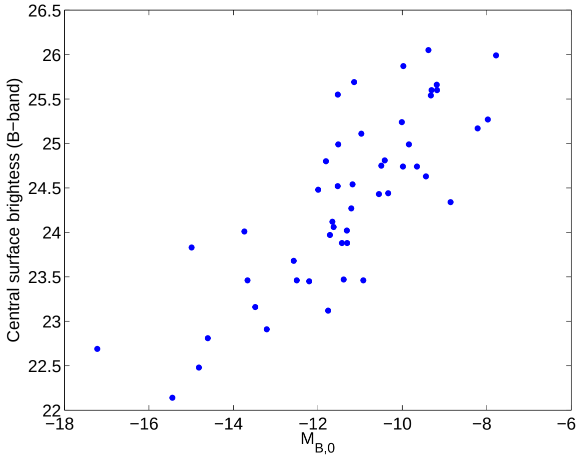

Figure 7.195: The central surface brightness as a function of the absolute magnitudes in the B-band.

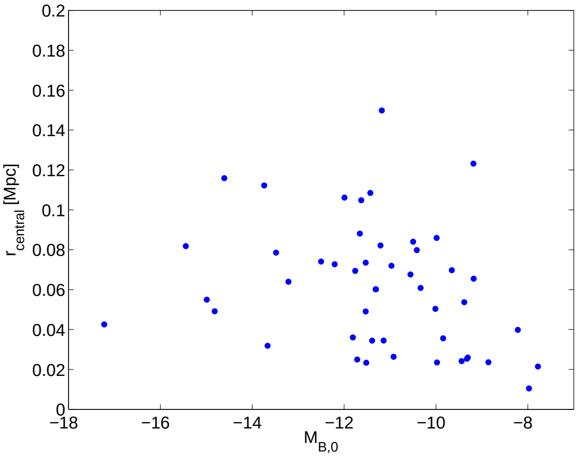

Figure 7.196: The projected distance to the central galax $r_{central}$ as a function of absolute magnitude M_B.

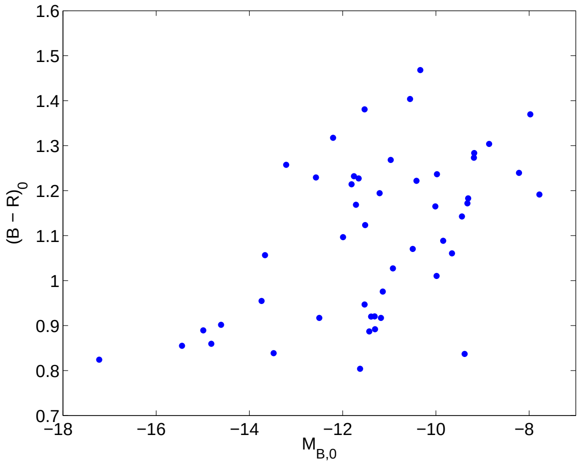

Figure 7.197: The measured color as function of the absolute magnitude M_B.

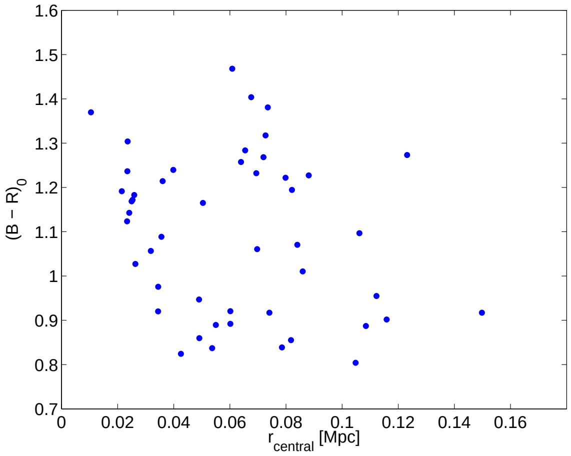

Figure 7.198: The measured B-R color as a function of the projected distance to the central massive spiral.

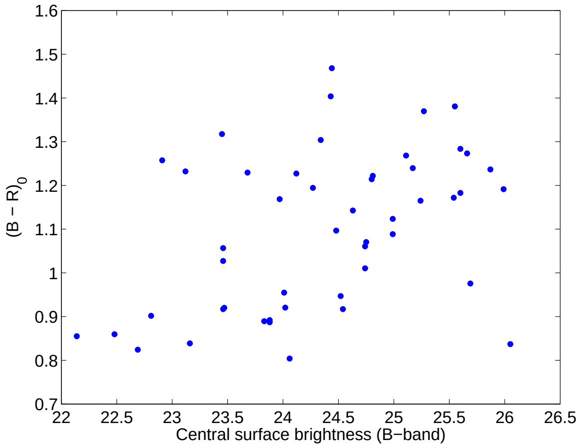

Figure 7.199: Color versus central surface brightness.

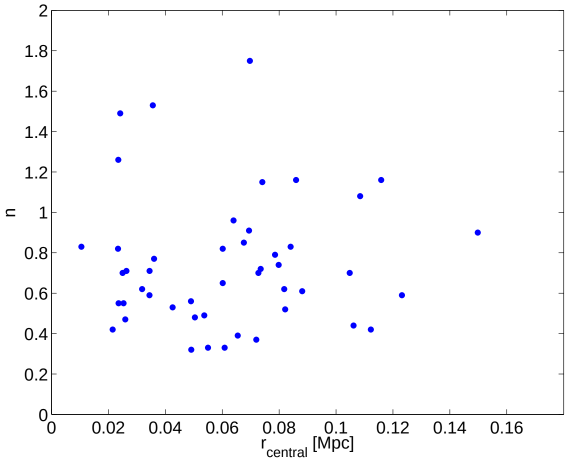

Figure 7.200: The Sérsic index *n*as a function of the projected distance.

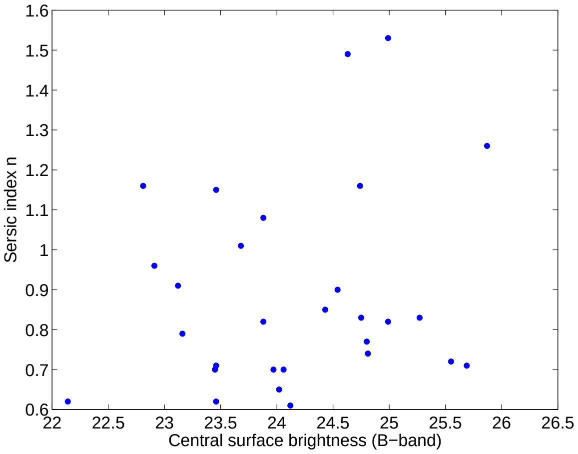

Figure 7.201: The central surface brightness versus n.

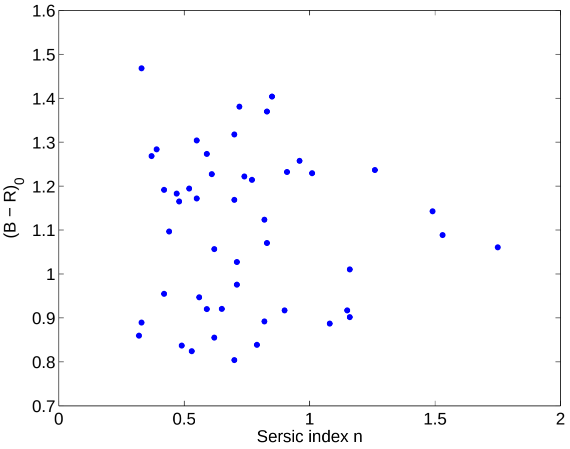

Figure 7.202: The measured B-R color as a function of the Sérsic index n.

Table 7.1: Properties of the detected CDG

Name (1)	RA (2)	Dec (3)	B_0 (4)	R_0 (5)	$M_{B,0}$ (6)	$M_{R,0}$ (7)	$(B-R)_0$ (8)	n (9)	csb (10)	r (11)	r_{cen} (12)	type (13)	class (14)
NGC 1425 1	3:42:03.41	-29:48:01.92	19.82 ± 0.03	18.46 ± 0.02	-11.81	-13.17	1.21	0.77 ± 0.16	24.8 ± 0.27	7.77 ± 1.61	36	dSph	CDG A
NGC 1964 1	5:33:40.74	-21:48:01.87	21.31 ± 0.06	18.96 ± 0.03	-10.33	-12.68	1.47	0.33 ± 0.07	24.44 ± 0.07	4.29 ± 0.12	60	dIrr	CDG A
NGC 1964 2	5:33:33.63	-21:59:20.56	22.78 ± 0.12	21.28 ± 0.08	-8.86	-10.36	1.30	0.55 ± 0.33	24.34 ± 0.61	1.59 ± 0.53	24	dSph	CDG A
NGC 1964 3	5:33:26.80	-21:57:57.55	23.67 ± 0.18	21.55 ± 0.09	-7.97	-10.09	1.37	0.83 ± 0.57	25.27 ± 0.94	4.16 ± 3.14	10	dSph	CDG A
UGCA071 1	3:25:12.07	-16:04:53.28	18.72 ± 0.02	16.34 ± 0.01	-13.48	-15.86	0.84	0.79 ± 0.07	23.16 ± 0.03	15.77 ± 0.41	79	dIrr	CDG A
UGCA071 2	3:25:33.82	-16:07:33.88	17.21 ± 0.01	17.51 ± 0.02	-14.99	-14.69	0.89	0.33 ± 0.06	23.83 ± 0.02	12.83 ± 0.85	55	dIrr	CDG A
UGCA071 3	3:25:12.15	-16:09:48.60	14.98 ± 0.01	16.25 ± 0.01	-17.22	-16.03	0.82	0.53 ± 0.1	22.69 ± 0.05	10.35 ± 0.42	43	dIrr	CDG A
UGCA071 4	3:25:25.65	-16:01:08.91	20.57 ± 0.04	19.66 ± 0.03	-11.63	-12.63	0.80	0.7 ± 0.12	24.06 ± 0.04	6.85 ± 0.32	105	dIrr	CDG A
NGC 150 1	0:33:51.38	-27:50:26.62	20.40 ± 0.04	21.03 ± 0.07	-11.14	-10.51	0.98	0.71 ± 0.14	25.69 ± 0.06	23.25 ± 1.41	34	dIrr	CDG A
NGC 150 2	0:33:38.29	-27:47:48.73	16.72 ± 0.01	15.83 ± 0.01	-14.82	-15.71	0.86	0.32 ± 0.03	22.48 ± 0.01	8.47 ± 0.26	49	dE	CDG A
NGC 1532 1	4:11:15.09	-33:04:45.88	20.73 ± 0.05	19.26 ± 0.03	-10.42	-11.89	1.22	0.74 ± 0.83	24.81 ± 0.4	7.56 ± 1.07	80	dSph	CDG A
NGC 1532 2	4:10:47.35	-32:49:01.10	19.94 ± 0.03	18.67 ± 0.02	-11.21	-12.48	1.19	0.52 ± 0.21	24.27 ± 0.22	5.37 ± 0.56	82	dSph	CDG A
NGC 2310 1	6:54:15.60	-40:50:00.45	21.60 ± 0.08	18.95 ± 0.03	-9.07	-11.72	2.25	4.3 ± 14.34	21.96 ± 9.48	0.03 ± 0.73	18	BG	CDG C
NGC 2310 2	6:53:08.07	-40:51:05.69	19.28 ± 0.02	18.57 ± 0.02	-11.39	-12.10	0.92	0.59 ± 0.09	23.47 ± 0.05	5.18 ± 0.15	34	dIrr	CDG A
NGC 578 1	1:30:14.61	-22:41:41.73	21.67 ± 0.07	19.78 ± 0.04	-9.98	-11.87	1.24	1.26 ± 0.61	25.87 ± 0.25	10.93 ± 3.21	23	dSph	CDG A
NGC 578 2	1:30:22.52	-22:51:00.47	21.00 ± 0.08	21.12 ± 0.07	-9.65	-10.56	1.06	1.75 ± 2.26	24.74 ± 0.93	4.49 ± 6.42	70	dSph	CDG B
NGC 7727 1	23:39:52.37	-12:14:08.03	20.32 ± 0.04	19.33 ± 0.03	-11.52	-12.51	1.12	0.82 ± 0.3	24.99 ± 0.08	13.68 ± 2.12	23	dSph	CDG A
NGC 7721 1	23:39:34.61	-6:31:28.87	20.18 ± 0.04	19.34 ± 0.03	-11.53	-12.37	1.38	0.72 ± 0.28	25.55 ± 0.11	9.1 ± 0.87	74	dSph	CDG A
NGC 7599 1	23:18:50.41	-42:23:48.90	20.23 ± 0.03	19.42 ± 0.03	-11.31	-12.12	0.89	0.82 ± 0.07	23.88 ± 0.09	3.36 ± 0.28	61	dIrr	CDG A
NGC 7599 2	23:19:39.46	-42:17:54.51	19.83 ± 0.03	18.75 ± 0.02	-11.71	-12.79	1.17	0.7 ± 0.03	23.97 ± 0.03	4.78 ± 0.09	25	dSph	CDG A
NGC 7599 3	23:18:50.41	-42:23:48.90	20.23 ± 0.03	19.43 ± 0.03	-11.31	-12.11	0.92	0.65 ± 0.07	24.02 ± 0.06	3.75 ± 0.16	60	dIrr	CDG A
NGC 7599 4	23:17:45.97	-42:18:36.89	19.55 ± 0.03	18.51 ± 0.02	-11.99	-13.03	1.10	0.44 ± 0.04	24.48 ± 0.02	8.9 ± 0.15	106	dSph	CDG A
NGC 7599 5	23:20:12.77	-42:09:12.15	20.99 ± 0.05	19.71 ± 0.04	-10.55	-11.83	1.40	0.85 ± 0.26	24.43 ± 0.26	2.54 ± 0.56	68	dSph	CDG A
NGC 7599 6	23:19:02.44	-42:18:05.08	22.23 ± 0.09	21.10 ± 0.07	-9.31	-10.44	1.18	0.47 ± 0.25	25.6 ± 0.28	3.22 ± 0.42	26	dSph	CDG A
NGC 7599 7	23:17:34.84	-42:22:06.24	22.36 ± 0.09	21.09 ± 0.07	-9.19	-10.45	1.27	0.59 ± 0.17	25.66 ± 0.33	3.49 ± 0.75	123	dSph	CDG A
NGC 7314 1	22:36:23.26	-26:12:46.44	19.57 ± 0.03	18.33 ± 0.02	-11.76	-12.00	1.23	0.91 ± 0.11	23.12 ± 0.09	2.62 ± 0.2	69	dE	CDG A
NGC 7314 2	22:36:25.01	-26:07:45.11	21.95 ± 0.08	21.07 ± 0.07	-9.38	-10.26	0.84	0.49 ± 0.43	26.05 ± 0.17	5.45 ± 1.48	54	dSph	CDG B

Name (1)	RA (2)	Dec (3)	B_0 (4)	R_0 (5)	$M_{B,0}$ (6)	$M_{R,0}$ (7)	$(B-R)_0$ (8)	n (9)	csb (10)	r (11)	r_{cen} (12)	type (13)	class (14)
NGC 1365 1	3:32:29.78	-36:05:17.40	20.27 ± 0.04	19.12 ± 0.03	-10.97	-12.13	1.27	0.37 ± 0.08	25.11 ± 0.02	10.67 ± 0.86	72	dSph	CDG A
NGC 1365 2	3:32:48.62	-36:09:11.24	21.23 ± 0.06	19.48 ± 0.03	-10.01	-11.76	1.16	0.48 ± 0.27	25.24 ± 0.13	5.96 ± 0.84	50	dSph	CDG A
NGC 1365 3	3:34:07.88	-36:04:11.42	23.02 ± 0.13	21.25 ± 0.07	-8.22	-9.99	1.24	2.12 ± 8.05	25.17 ± 4.37	3.56 ± 30.76	40	dSph	CDG B
NGC 908 1	2:23:22.37	-21:05:19.83	19.67 ± 0.03	18.86 ± 0.03	-11.53	-12.34	0.95	0.56 ± 0.08	24.52 ± 0.05	8.44 ± 0.33	49	dIrr	CDG A
NGC 908 2	2:23:24.51	-21:13:03.36	21.76 ± 0.07	20.43 ± 0.05	-9.44	-10.77	1.14	1.49 ± 4.22	24.63 ± 1.93	3.67 ± 8.8	24	dSph	CDG C
NGC 908 3	2:23:59.22	-21:12:10.71	22.02 ± 0.08	20.56 ± 0.06	-9.18	-10.65	1.28	0.39 ± 0.21	25.6 ± 0.15	3.85 ± 0.27	65	dSph	CDG A
NGC 134 1	0:29:59.98	-33:15:18.72	22.03 ± 0.08	20.79 ± 0.06	-9.32	-10.56	1.17	0.55 ± 0.18	25.54 ± 0.17	3.4 ± 0.33	25	dSph	CDG A
NGC 134 2	0:30:38.13	-33:16:40.23	23.57 ± 0.17	24.33 ± 0.31	-7.78	-7.02	1.19	0.42 ± 0.97	25.99 ± 1.18	1.94 ± 0.7	21	dSph	CDG A
NGC 134 dE	0:31:02.77	-33:16:14.75	17.30 ± 0.01	15.79 ± 0.01	-14.19	-15.56	1.23	1.20 ± 0.08	22.52 ± 0.07	8.31 ± 0.84	47	dE	CDG A
IC 4889 1	19:45:18.98	-54:16:16.58	22.36 ± 0.10	21.35 ± 0.08	-9.84	-10.85	1.09	1.53 ± 2.48	24.99 ± 0.86	5 ± 3.78	36	dSph	CDG B
IC 4889 2	19:44:55.25	-54:11:56.95	19.70 ± 0.03	18.98 ± 0.03	-12.50	-13.23	0.92	1.15 ± 0.18	23.46 ± 0.17	2.83 ± 0.56	74	dIrr	CDG A
NGC 3717 1	11:31:54.19	-30:19:03.60	20.42 ± 0.04	19.52 ± 0.04	-10.92	-11.82	1.03	0.71 ± 0.05	23.46 ± 0.06	2.98 ± 0.15	26	dSph	CDG A
NGC 3717 2	11:32:44.22	-30:16:09.22	21.36 ± 0.06	20.53 ± 0.06	-9.99	-10.81	1.01	1.16 ± 0.6	24.74 ± 0.18	10.4 ± 1.25	86	dIrr	CDG A
NGC 3936 1	11:52:39.64	-27:03:11.81	18.52 ± 0.02	17.23 ± 0.01	-13.21	-5.19	1.26	0.96 ± 0.05	22.91 ± 0.05	4.62 ± 0.26	64	dE	CDG A
NGC 3956 1	11:53:02.46	-20:34:56.82	20.72 ± 0.05	20.18 ± 0.05	-11.43	-11.97	0.89	1.08 ± 0.21	23.88 ± 0.16	3.06 ± 0.52	108	dIrr	CDG B
NGC 3956 2	11:53:44.58	-20:24:08.96	21.65 ± 0.07	20.74 ± 0.06	-10.50	-11.41	1.07	0.83 ± 0.21	24.75 ± 0.13	4.35 ± 0.36	84	dSph	CDG A
NGC 3956 3	11:55:53.85	-20:11:32.12	19.58 ± 0.03	18.27 ± 0.02	-12.57	-13.88	1.23	1.01 ± 0.66	23.68 ± 0.46	6.23 ± 2.55	276	dSph	CDG A
NGC 3981 1	11:54:36.00	-19:56:26.00	20.69 ± 0.05	20.21 ± 0.05	-11.18	-11.66	0.92	0.9 ± 0.6	24.54 ± 0.14	11 ± 3.77	150	dSph	CDG A
NGC 3981 2	11:54:59.96	-19:58:54.79	17.26 ± 0.01	16.49 ± 0.01	-14.61	-15.38	0.90	1.16 ± 0.75	22.81 ± 1.08	5.66 ± 6.37	116	dIrr	CDG B
NGC 4835 1	12:57:19.28	-46:25:03.11	20.24 ± 0.04	18.82 ± 0.03	-11.66	-13.08	1.23	0.61 ± 0.1	24.12 ± 0.06	5.31 ± 0.18	88	dSph	CDG A
NGC 4835 2	12:57:21.42	-46:22:16.37	19.70 ± 0.03	18.37 ± 0.02	-12.21	-13.53	1.32	0.7 ± 0.05	23.45 ± 0.05	3.88 ± 0.14	73	dSph	CDG C
NGC 4835 3	12:58:09.19	-46:04:18.10	16.45 ± 0.01	15.60 ± 0.01	-15.45	-16.30	0.86	0.62 ± 0.04	22.14 ± 0.04	11.75 ± 0.51	82	dIrr	CDG B
NGC 6810 1	19:44:02.52	-58:37:41.65	18.48 ± 0.02	17.66 ± 0.02	-13.67	-14.49	1.06	0.62 ± 0.05	23.46 ± 0.02	7.55 ± 0.14	32	dIrr	CDG A
NGC 6810 2	19:44:54.18	-58:29:42.35	18.40 ± 0.02	17.93 ± 0.02	-13.74	-14.21	0.95	0.42 ± 0.05	24.01 ± 0.02	15.3 ± 0.52	112	dIrr	CDG A
NGC 4219 1	12:15:28.66	-43:07:09.48	23.35 ± 0.18	21.15 ± 0.08	-8.48	-10.68	1.31	1.07 ± 0.55	24.85 ± 0.42	3.78 ± 1.69	111	dSph	CDG A
IC 4721 1	18:34:45.85	-58:31:33.43	19.51 ± 0.01	18.42 ± 0.01	-12.26	-13.36	1.10	1.1 ± 0.35	22.93 ± 0.17	4.68 ± 0.64	22	dIrr	CDG A
IC 4721 2	18:35:29.04	-58:36:26.96	17.34 ± 0.01	16.61 ± 0.01	-14.43	-15.16	0.95	1.28 ± 0.11	22.11 ± 0.08	4.98 ± 0.58	71	dIrr	CDG A
IC 4721 3	18:32:54.26	-58:22:41.81	21.46 ± 0.07	20.16 ± 0.05	-10.31	-11.61	1.19	0.58 ± 0.11	24.32 ± 0.07	3.79 ± 0.1	92	dIrr	CDG A
IC 4721 4	18:35:02.50	-58:17:05.31	18.13 ± 0.02	16.35 ± 0.01	-13.65	-15.42	0.88	0.87 ± 0.05	23.08 ± 0.02	12.48 ±0.28	91	dIrr	CDG A

In Column (1) we give the name of the CDG and in Column (2) and (3) the J2000 coordinates for RA and Dec. Column (4) and (5) lists the Galactic foreground extinction corrected magnitudes in the B- and R-band as measured by SExtractor. The shown errors are calculated by SExtractor. , the additional calibration error from the zeropoints of 0.06 was not taken into account in order to show the quality of the measurement by SExtractor, but in principle needs to be included. Column (6) and (7) consists of the corresponding luminosity assuming the same distance modulus as the observed host galaxy. Column (8) gives the measured Galactic foreground extinction corrected $(B-R)_0$ color when using ellipse (details are listed in Section 4.3), typical errors are about 0.09 mag. Column (9) – (11) lists the measured parameters of the Sérsic fit to the SBP, namely the Sérsic index n, the CSB and the scale length r with the corresponding errors. In Column (12) we show the projected distance to the central massive spiral r_{cen} assuming the CDG to be at the same distance as the host galaxy. Column (13) gives the classified morphology and Column (14) the CDG class.

8

SUMMARY AND OUTLOOK

We performed deep imaging on nearby massive spiral galaxies in order to investigate their dwarf satellites and the resulting environmental effects on the host galaxies. First of all we will summarize the frequency of tidal debris in this survey. Later on we will discuss the abundance of dwarf galaxies around massive spirals and compare our studied targets to other observations. Finally, we will discuss the observational limits and give an outlook on how future observational facilities can improve this project.

8.1 ON THE FREQUENCY OF TIDAL DEBRIS

We find a variety of different faint features in the outskirts of our studied galaxies. Thus the tidal features in our survey are separated into broad categories of streams, clouds/plumes and bridges/tails. It is important to take into account that observational limits in SB and detectability of faint features are influencing the statistical analysis of imaging data in order to find tidal features there. To summarize our results, we find the following.

About 54% of all studied galaxies in our survey show signs of tidal interactions. In 35% of all targets signs of tidal tails or bridges can be identified, 11% show plumes or clouds and only 8% show streams. We note that our survey is biased in the sense that only late-type galaxies were selected, preferentially objects with signs of interactions. Several other surveys have studied the frequency of tidal debris, but every single one has an individual approach and covers a different redshift space. Thus a direct comparison is difficult.

Miskolczi et al. (2011) used the SDSS for these studies. They find that about 6% of all galaxies show streams and in total 19% of their targets have faint features. Although their work based on the SDSS is more limited in SB than our work, they find similar abundances of streams and their quoted number of 19% of galaxies which show faint features is similar to the number if in this work only faint features would be taken into account.

A much wider redshift range ($0.04 < z < 0.2$) was studied by Atkinson et al. (2013). They find that 37% of all their galaxies show tidal features. These are then subdivided into clear tidal features (12%), convincing weaker tidal features (6%), marginal features (8%) and hint for a potential tidal feature (11%). Given that many of the studied galaxies in our work were selected with a strong bias, especially those which show major interactions, roughly the statistics agree to each other.

A study of tidal features around elliptical galaxies can be found in Tal et al. (2009). 73% of all their studied galaxies contain tidal disturbances. Whether their higher detection rate, compared to the rate we found in our work, is due to their observational limits or due to morphological class of their objects remains uncertain.

Cosmological simulations trace the build-up of halos with time. Cooper et al. (2010) demonstrate that the number of accreted satellites rapidly decreases with their mass, therefore the probability of observing bright streams around spirals is low. Given the fast decay of the observed surface brightness (Johnston et al. 2001) the frequency of the tidal features which are observed around galaxies suggests that the observations are in agreement with the CDM model.

Taking into account the low surface brightness levels of tidal features, in principle deeper observations should reveal a higher number of tidal features. The limit of ultra deep observations is several magnitudes deeper than what is covered by our and the other surveys mentioned. Mouhcine et al. (2010) demonstrated that with modern telescopes ultra faint deep imaging can be performed. Their observed stream can also be resolved into single stars with $i \approx 26.8 - 27.0$ mag, they show e.g. that around NGC 891 tidal features at such faint SB can be found. Additionally, Mihos et al. (2005) highlight that also in the cluster environment ultra deep imaging could provide new insights into the study of galaxy interactions. They report on an observed SB limit of 28.5 mag arcsec^{-2} in the V-band. These studies suggest that the search for tidal features around galaxies could be improved by ultra deep imaging.

8.2 ABUNDANCE OF DWARF GALAXIES AROUND MASSIVE NEARBY SPIRALS

Galaxy groups undergo several phases in their evolution. In filamentary large-scale structures field galaxies can be observed. The low-density parts of large-scale structures can be also described as associations. The massive galaxies in these associations do not seem to interact with other members, and only a few or none dE are present there. Most of our observed galaxies are in these stage, therefore usually about two or three dSphs down to a surface brightness limit of μ_B =27 mag arcsec^{-2} can be found there. UGC 071 is one of our target galaxies in so called associations. Interestingly, there a high number of dIrrs are found. These observations highlight that the group just started to agglomerate and the dwarf companions have not yet been modified by interactions with their environment. Tully et al. (2006) report on several associations consisting only of dwarf galaxies. Therefore associations of dwarf galaxies must be taken into account when the evolution of galaxies is studied. The Canes Venatici I cloud is described as amorphous filament, which is populated mostly by late-type dwarf galaxies (Karachentsev et al. 2003b). This is comparable to the galaxy population which we observed around UGC 071 and IC 4721.

The next phase in the evolution of groups is the stage of a young group. In our data such environments are represented e.g. in NGC 134. These groups typical have a mixture of dSph, dIrr and dE galaxies. At this point the group started to stabilize and dwarf companions were already processed by their hosts. The next step in the evolution can be seen in the LG. The status can be described by mature groups. In our survey this can be seen especially in the environment around NGC 7599. Like in the LG two dominant spiral galaxies are observed close-by, additionally, many dSph dE/dIrr are found in these regions. Another LG analog is the NGC 3956 - NGC 3981 system. Several dSph and dIrr can be found around these. Typical dE galaxies cannot be observed there. Mechanisms like dynamical friction can cause that massive close-by companions are accreted or downsized, as these effects are a strong function of the distance to the central galaxy. Over the stage of compact groups galaxies evolve to fossil groups. These targets are not included in this survey, as they are observed at a much larger distance.

In total around two to three CDG are found around each target. Given the observational limits of the limited field of view and the resolution of the detector this is in agreement what would have been observed if the LG massive spirals or nearby groups like Sculptor or Centaurus A would have been observed at the same distance. We would have missed most of the dSphs due to the low resolution of our camera.

The initial question of how common are features and companions seen around the MW and M31 can be answered with detailed observations. The studied massive nearby spirals show similar properties in terms of abundance of dwarf companions inside the observational limits, but the evolutionary stage can be very different (see section about dwarfs around NGC 7331). This highlights the past evolution the LG was going trough. Especially the close proximity of the Magellanic clouds and the high number of dE around M31 mark these local examples as members of a mature group and thus they are different from most of the nearby galaxies studied in our survey. In the future many interactions will happen in the LG, e.g. the MW will merge with M31, also the recent infall of the Magellanic clouds show that the LG is moving into a turbulent phase of group evolution.

Summarizing the abundance of dwarf galaxies around nearby massive spirals, a similar amount of dwarf galaxies can be found around them. Previously known discrepancies like the missing satellite problem, which describes that a much higher number of subhalos should be found around the halos, cannot be solved by the observations of this survey. But other mechanisms like photoionisation already show that different processes could be responsible for suppressing the number of observable dwarf companions.

The studied properties of the galaxies show (only roughly in this survey) that the abundance of dwarf satellites is not a function of the environment or the morphology of a galaxy. Instead it seems mainly to be a function of the mass of the central galaxy. This is already suggested by numerical simulations (see e.g. Elahi et al. 2013). Observations in the LG show that a certain fraction of dwarf companions can be found close-by, in Figure 8.1 (Grebel 2005) it is highlighted how many of the dwarfs can be found at which radii. In order to compare the MW to the studied galaxies in this survey two main limits have to be taken into account. The covered area as a function of distance is shown in Figure 8.2 and the limitation due to missing resolution is highlighted in Figure 8.3. Both are shown as function of distance. In Figure 8.4 the expected number of dwarf galaxies is plotted for each distance bin if the MW would have been observed at same distance with similar limitations like the studied targets. Given that the MW has some very bright massive companions (which is a not common for galaxies like the MW, see e.g. Busha et al. 2011), the number of CDG observed is quantitatively in agreement with the expected number of dwarf companions.

Trentham & Tully (2002) demonstrate that in dynamically more evolved systems a lower number of dIrr is found and a higher number of dE is being observed. This ratio is used to argue that many of the observed systems in this survey suggest that a reasonable amount of late-type dwarf galaxies could be a sign of more evolved systems. It must also be taken into account, that we only have projected distances for the CDGs, therefore these are only a lower limit for the real distance of the studied companions to the host galaxy.

8.3 OBSERVATIONAL LIMITS

Our work demonstrates impressively that small to medium sized telescopes can be used for deep imaging of nearby galaxies. Our observational limit of $B_{R/r} \sim 27$ mag arcsec^{-2} is close to the limit of what could be achieved with modern detectors and this class of telescopes. Longer exposure times would only marginally increase the SB limits because it would take a lot of observing time.

Furthermore, there are more limits than only the pure signal detection. The detector properties itself are setting restrictions, previously reported by the flat-field calibration. This limitation is given by the detector technique and e.g. with the use of a higher number of detectors this issue will require further and intensive correction mechanisms. Stray light from the telescope and detector constructions are a major issue as well, because bright sources like stars and the studied massive galaxies themselves produce features in the science images. Also many telescope - detector combinations show pupil ghosts. These

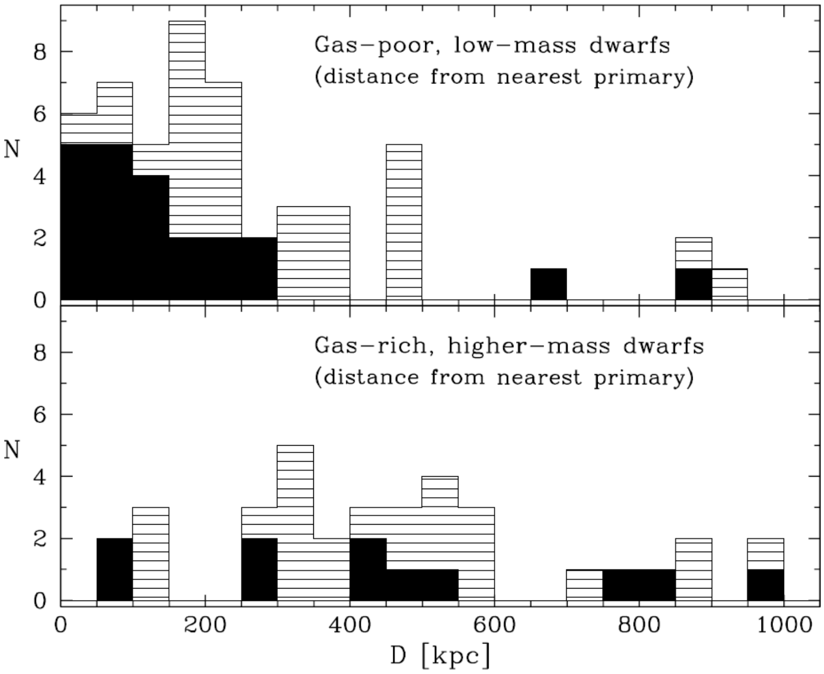

Figure 8.1: The observed radii of different dwarf galaxies in the LG, taken from Grebel (2005).

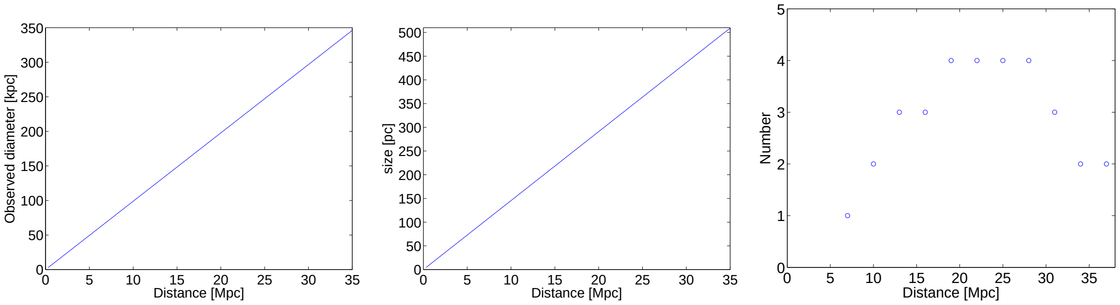

Figure 8.2: The covered field of view versus distance.

Figure 8.3: The size of dwarf galaxies which can be resolved as a function of distance.

Figure 8.4: The number of expected dwarf galaxies when moving the MW virtually to the given distances and applying our observational limits of resolution and field of view. It stands out that our chosen distance range (majority of the targets is between 15 and 30 Mpc) is very well chosen in order to find possible dwarf companions around the targets with the given limits of the telescope-detector combination.

can be more or less pronounced depending on the used filters and studied objects.

There are additional intrinsic limits. Earthbound observations are limited mostly by the atmosphere. Modern techniques like adaptive optics can correct e.g. the effect of dissolving light paths when light is moving through the different layers of the atmosphere, but still reflecting light coming from artificial sources are influencing deeper observations. Even if imagers with the same resolution and field of view would be used in space-telescopes, there are still existing observational limits on the achievable depth. In close proximity to the sun zodiacal light contributes distinctly to the limiting background. This effect could only be minimized at larger radii from the sun. Also Galactic cirrus clouds intrinsically restrict the detection of ultra-faint features. Only a small number of studies have studied these in detail, in order to distinguish real faint features belonging to the studied galaxies from these cirrus clouds extensive information about cirrus is necessary (see section 5.1 for a further discussion of cirrus). Finally, galactic stellar halos will affect the observations at ultra deep imaging of faint substructures of galaxies. Tidal features like streams decrease extremely fast in the luminosity and observable surface brightness, therefore it will get impossible to identify these without resolving them single stars.

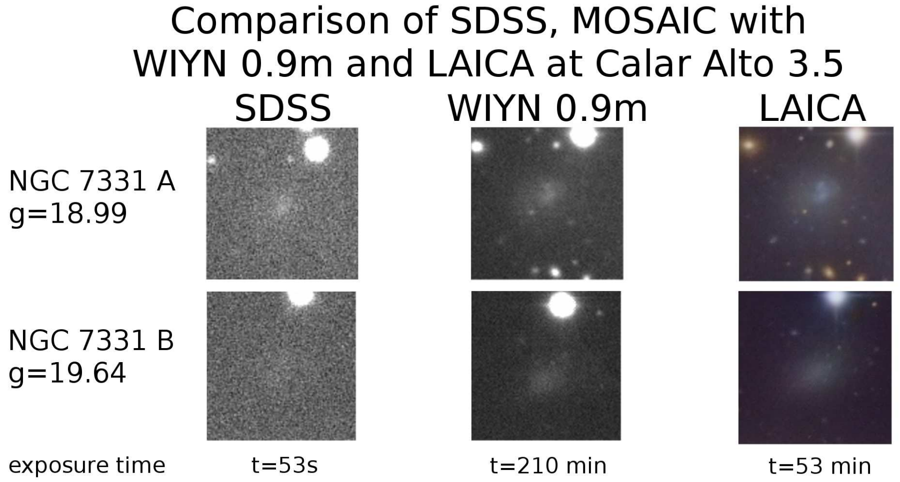

Figure 8.5: The observations of the same CDG with different filters. The same targets are observed with SDSS, the 0.9m (MOSAIC) and the Calar Alto 3.5m (LAICA imager) telescope. Besides the different SB limits the influence of resolution onto the details of CDG is highlighted in this image.

In order to highlight the differences of observational depth and resolution of the detector telescope combination the observations of the same dwarf galaxies but with different facilities are compared in Figure 8.5. The SDSS has a lower observational depth, but the SB limit of the 0.9m data and the Calar Alto 3.5m data are similar. The comparison shows that the this survey is much deeper than the SDSS and on the other side demonstrates how better resolution helps to classify the morphology and structure of the CDG.

8.4 OUTLOOK

This survey includes data for about 60 galaxies. Data analysis is performed on all observations and the thesis reports on a considerable number of CDG. In order to confirm these as dwarf companions spectroscopic observations are necessary. The data include a high number of potential candidates although the morphology cannot be defined clearly by the available resolution. These candidates could complement the dwarf galaxy population of the studied galaxies, but only redshift measurements can unveil the nature of these objects.

It is planned to make the analyzed data publicly available, future similar studies could therefore use the agglomerated data.

This project also was initiated in order to test the feasibility of modern imaging detectors, which offer a much bigger field of view and therefore consist of much more single CCDs. The start with MOSAIC on the WIYN 0.9m demonstrates that deep imaging is possible with even small telescopes and was planned as a direct test for the One Degree Imager (ODI). Both cover roughly the same observational solid angle of one degree. The increased resolution of ODI (which will be on the WIYN 3.5m) helps to resolve fainter and smaller substructures and increases the field of view compared to MOSAIC on the 4m. The study of the faint end of the luminosity function can be improved by a substantial factor. The thesis demonstrates that the nearby universe shows very interesting targets for these kinds of studies. Another instrument which improves the outlined properties is the camera of the dark energy survey (DECam). With its field of view of 2.2 degrees on the 4m Blanco telescope it is a perfect instrument to not only study the distribution of very high redshift objects but also the environment of nearby galaxies. Another very interesting instrument is Hyper Suprime cam, which works on the 8m Subaru telescope. With its observational diameter of 1.5 degrees a very wide field of view is combined with the resolution of a 8m class telescope. The studied topic of this work would tremendously benefit if similar objects would be studied with this detector.

At the moment the quality of the imaging data of this new detectors is not reported. The most challenging task is the data reduction of 900 Megapixel data (570 for DECam). The experience of this work demonstrates that fully automatic pipelines cannot provide high quality data. During the reduction steps instantaneous adaption of different parameters is necessary. In addition, permanent quality control is necessary to ensure that corrupted calibration files are not used. The extreme amount of data will need the development of completely new data and reduction management.

In the future the most modern instruments will help to understand the intriguing life of galaxies and their companions. This thesis highlights the treasures that can be found in nearby galaxies, the new class of detectors could bring new insights into this topic and would be the next step in this project.

9

APPENDIX

9.1 IRAF REDUCTION SCRIPTS

9.1.1 COORDINATE TRANSFORMATION

```
real ra,dec
    int i1
    string name,*list1,*list2,ra_string,dec_string
    struct *flist, *flist2
    flist = ”N7314_B.list”
    while (fscan (flist, name) != EOF) {
    hselect (name//"[1]",fields="ra",expr=yes, » "ex3")
    hselect (name//"[1]",fields="dec",expr=yes, » "ex2")
    list1 = ("ex3") # associate temporary file with list variable
    list2 = ("ex2")
    j=fscan (list1,ra) # read the value of the airmass in the file into parameter air
    j=fscan (list2,dec) # read the value of the airmass in the file into parameter air
    delete ("ex3",verify=no) # delete file ex3
    delete ("ex2",verify=no) # delete file ex3
    for(i1=1;i1<=8;i1+=1) {
    printf("%h\n",ra)| scanf ("%s",ra_string)
    printf("%h\n",dec)| scanf ("%s",dec_string)
    hedit (name//"["//i1//"]", "RA", ra_string, add=no, addonly=no, delete=no, verify=no, show=no, update=yes)
    hedit (name//"["//i1//"]", "DEC", dec_string, add=no, addonly=no, delete=no, verify=no, show=no, update=yes) } }
```

9.1.2 HEADER EDITING

```
esohdr ("WFI_Ima*fits", "object", querytype=no, namps=1, ntransient=2, wcsdb="esodb$wcs.db", redo=no, fd1="", fd2="")
```

```
esohdr ("WFI_Flat*.fits", "flat", querytype=no, namps=1, ntransient=2, wcsdb="esodb$wcs.db", redo=no, fd1="", fd2="")
esohdr ("WFI_Dark*.fits", "zero", querytype=no, namps=1, ntransient=2, wcsdb="esodb$wcs.db", redo=no, fd1="", fd2="")
```

9.1.3 BASIC REDUCTION

```
int i1,i2
real hc real cn real cf
string file_name,name,trunc_name, name_zero,name_dflat_R, name_dflat_B, name_sflat_R, name_sflat_B, name_sflat_R_fin, name_sflat_B_fin
struct *flist,*flist2
################## DEFINE NIGHT HERE !!!!! ####################
i2 = 5
##########################################################
########## DEFINE THE FILE NAMES HERE ###################
##########################################################
name_zero="zero_n"//i2//""
name_dflat_R="dflatn"//i2//"_R"
name_dflat_B="dflatn"//i2//"_B"
name_sflat_R="sflat_n"//i2//"R"
name_sflat_B="sflat_n"//i2//"B"
name_sflat_R_fin="sflat_n"//i2//"RBB_Rc_162_ESO844"
name_sflat_B_fin="sflat_n"//i2//"BBB_B_123_ESO878"
ccdproc ("*.fits", output="", bpmasks="", ccdtype=" ", noproc=no, xtalkcor=no, fixpix=no, overscan=yes, trim=yes, zerocor=no, darkcor=no, flatcor=no, sflatcor=no, split=no, merge=no, xtalkfile="", fixfile="", saturation="INDEF", sgrow=0, bleed="INDEF", btrail=20, bgrow=0, biassec="!biassec", trimsec="!trimsec", zero="Zero", dark="Dark", flat="Flat*", sflat="Sflat*", minreplace=1., interactive=no, function="legendre", order=1, sample="*", naverage=1, niterate=1, low_reject=3., high_reject=3., grow=0., fd="", fd2="")
zerocombine ("*Dark*.fits", output=name_zero, combine="median", reject="crreject", ccdtype="zero", process=yes, delete=no, scale="none", statsec="", nlow=1, nhigh=1, nkeep=1, mclip=yes, lsigma=3., hsigma=3., rdnoise="OUTRON", gain="OUTCONAD", snoise="0.", pclip=-0.5, blank=0.)
ccdproc ("*FlatDomeIma*.fits", output="", bpmasks="", ccdtype=" ", noproc=no, xtalkcor=no, fixpix=no, overscan=yes, trim=yes, zerocor=yes, darkcor=no, flatcor=no, sflatcor=no, split=no, merge=no, xtalkfile="", fixfile="", saturation="!saturate", sgrow=0, bleed="mean+3000", btrail=15, bgrow=1, biassec="!biassec", trimsec="!trimsec", zero=name_zero, dark="Dark", flat="Flat*", sflat="Sflat*", minreplace=1., interactive=no, function="legendre", order=1, sample="*", naverage=1, niterate=1, low_reject=3., high_reject=3., grow=0., fd="", fd2="")
flatcombine ("@flats_R.list", output=name_dflat_R, combine="median", reject="ccdclip", ccdtype="FLAT,SCREEN", process=no, subsets=no, delete=no, scale="mode", statsec="", nlow=1, nhigh=1, nkeep=1, mclip=no, lsigma=3., hsigma=3., rdnoise="OUTRON", gain="OUTCONAD", snoise="0.", pclip=-0.5, blank=1.)
flatcombine ("@flats_B.list", output=name_dflat_B, combine="median", reject="ccdclip", ccdtype="FLAT,SCREEN", process=no, subsets=no, delete=no, scale="mode", statsec="", nlow=1, nhigh=1, nkeep=1, mclip=no, lsigma=3., hsigma=3., rdnoise="OUTRON", gain="OUTCONAD", snoise="0.", pclip=-0.5, blank=1.)
ccdproc ("@obj_R.list", output="", bpmasks="@bpm_R.list", ccdtype=" ", noproc=no, xtalkcor=no, fixpix=no, overscan=yes, trim=yes, zerocor=yes, darkcor=no, flatcor=no, sflatcor=no,
```

```
split=no, merge=no, xtalkfile="", fixfile="BPM", saturation="55000", sgrow=1, bleed="mean+20000", btrail=15, bgrow=1, biassec="!biassec", trimsec="!trimsec", zero=name_zero, dark="Dark", flat="Flat*", sflat="Sflat*", minreplace=1., interactive=no, function="legendre", order=1, sample="*", naverage=1, niterate=1, low_reject=3., high_reject=3., grow=0., fd="", fd2="")
ccdproc ("@obj_B.list", output="", bpmasks="@bpm_B.list", ccdtype=" ", noproc=no, xtalkcor=no, fixpix=no, overscan=yes, trim=yes, zerocor=yes, darkcor=no, flatcor=no, sflatcor=no, split=no, merge=no, xtalkfile="", fixfile="BPM", saturation="55000", sgrow=1, bleed="mean+20000", btrail=15, bgrow=1, biassec="!biassec", trimsec="!trimsec", zero=name_zero, dark="Dark", flat="Flat*", sflat="Sflat*", minreplace=1., interactive=no, function="legendre", order=1, sample="*", naverage=1, niterate=1, low_reject=3., high_reject=3., grow=0., fd="", fd2="")
objmasks ("@obj_B.list", "@om_B.list", omtype="numbers", skys="@sky_B.list", sigmas="", masks="", extnames="", logfiles="STDOUT", blkstep=1, blksize=-10, convolve="block 3 3", hsigma=3., lsigma=10., hdetect=yes, ldetect=no, neighbors="8", minpix=6, ngrow=2, agrow=2.)
objmasks ("@obj_R.list", "@om_R.list", omtype="numbers", skys="@sky_R.list", sigmas="", masks="", extnames="", logfiles="STDOUT", blkstep=1, blksize=-10, convolve="block 3 3", hsigma=3., lsigma=10., hdetect=yes, ldetect=no, neighbors="8", minpix=6, ngrow=2, agrow=2.)
sflatcombine ("@obj_B_sf.list", output=name_sflat_B, combine="median", reject="ccdclip", ccdtype=" ", subsets=yes, masktype="!objmask", maskvalue=0., scale="mode", statsec="", nkeep=1, nlow=1, nhigh=1, mclip=yes, lsigma=6., hsigma=3., rdnoise="outron", gain="outconad", snoise="0.", pclip=-0.5, blank=1., grow=3., fd="")
sflatcombine ("@obj_R_sf.list", output=name_sflat_R, combine="median", reject="ccdclip", ccdtype=" ", subsets=yes, masktype="!objmask", maskvalue=0., scale="mode", statsec="", nkeep=1, nlow=1, nhigh=1, mclip=yes, lsigma=6., hsigma=3., rdnoise="outron", gain="outconad", snoise="0.", pclip=-0.5, blank=1., grow=3., fd="")
#########################################################################
#################
################# CREATION OF BAD PIXEL MASK — zero_co_bpm_*
#################
#########################################################################
file_name="zero_n"//i2//".fits"
for(i1=1;i1<=8;i1+=1) {
print(file_name//"["//i1//"]")
imcopy (file_name//"["//i1//"]", "zero_co_bpm_"//i1//".fits")
imreplace ("zero_co_bpm_"//i1//".fits",value=0,lower=INDEF,upper=6)
imreplace ("zero_co_bpm_"//i1//".fits",value=1,lower=6.000001,upper=INDEF)
}
#########################################################################
#################
################# CREATION OF BAD PIXEL MASK — flats_co_bpm_*
#################
#########################################################################
file_name="sflat_n"//i2//"BBB_B_123_ESO878.fits"
for(i1=1;i1<=8;i1+=1) {
print(file_name//"["//i1//"]")
imcopy (file_name//"["//i1//"]", "co_bpm_B_"//i1//".fits")
imreplace ("co_bpm_B_"//i1//".fits",value=1,lower=INDEF,upper=5)
imreplace ("co_bpm_B_"//i1//".fits",value=0,lower=5.01,upper=INDEF)
}
```

```
file_name="sflat_n"//i2//"RBB_Rc_162_ESO844.fits"
for(i1=1;i1<=8;i1+=1) {
print(file_name//"["//i1//"]")
imcopy (file_name//"["//i1//"]", "co_bpm_R_"//i1//".fits")
imreplace ("co_bpm_R_"//i1//".fits",value=1,lower=INDEF,upper=5)
imreplace ("co_bpm_R_"//i1//".fits",value=0,lower=5.01,upper=INDEF)
##### ADD all the BPM together
imarith ("co_bpm_R_"//i1//".fits","+","co_bpm_B_"//i1//".fits","flat_co_bpm_B_R_"//i1//".fits")
imarith ("flat_co_bpm_B_R_"//i1//".fits","+","zero_co_bpm_"//i1//".fits","master_bpm"//i1//".fits")
}
#########################################################################
#########################################################################
#################
################# CORRECTION OF THE BAD PIXELS FOR SFLAT
#################
#########################################################################
ls sflat*.fits » "sflat.list"
flist = "sflat.list"
for(i1=1;i1<=8;i1+=1) {
print ("Starting to replace bad pixels with fixpix of "//name//"["//i1//"] with master_bpm"//i1//".fits", » "logfile_fixpix")
fixpix (name//"["//i1//"]", "master_bpm"//i1//".fits", linterp="INDEF", cinterp="INDEF", verbose=no, pixels=no)
}
}
#########################################################################
ccdproc ("@obj_R.list", output="", bpmasks="", ccdtype="", noproc=no, xtalkcor=no, fixpix=no, overscan=no, trim=no, zerocor=no, darkcor=no, flatcor=yes, sflatcor=yes, split=no, merge=no, xtalkfile="", fixfile="", saturation="!saturate", sgrow=0, bleed="", btrail=15, bgrow=1, biassec="!biassec", trimsec="!trimsec", zero=name_zero, dark="Dark", flat=name_dflat_R, sflat=name_sflat_R_fin, minreplace=1., interactive=no, function="legendre", order=1, sample="*", naverage=1, niterate=1, low_reject=3., high_reject=3., grow=0., fd="", fd2="")
ccdproc ("@obj_B.list", output="", bpmasks="", ccdtype="", noproc=no, xtalkcor=no, fixpix=no, overscan=no, trim=no, zerocor=no, darkcor=no, flatcor=yes, sflatcor=yes, split=no, merge=no, xtalkfile="", fixfile="", saturation="!saturate", sgrow=0, bleed="mean+5000", btrail=15, bgrow=1, biassec="!biassec", trimsec="!trimsec", zero=name_zero, dark="Dark", flat=name_dflat_B, sflat=name_sflat_B_fin, minreplace=1., interactive=no, function="legendre", order=1, sample="*", naverage=1, niterate=1, low_reject=3., high_reject=3., grow=0., fd="", fd2="")
#########################################################################
#################
################# CORRECTION OF THE BAD PIXELS FOR EVERY IMAGE
#################
#########################################################################
ls WFI*Ima*.fits » "FIXPIX.list"
flist = "FIXPIX.list"
while (fscan (flist, name) != EOF){
for(i1=1;i1<=8;i1+=1) {
```

```
print ("Starting to replace bad pixels with fixpix of "//name//"["//i1//"] with master_bpm"//i1//".fits", » "logfile_fixpix")
fixpix (name//"["//i1//"]", "master_bpm"//i1//".fits", linterp="INDEF", cinterp="INDEF", verbose=no, pixels=no)
}
}
##########################################################################
```

9.1.4 WCS SOLUTION

```
real ra,dec int i1 string name,*list1,*list2,ra_string,dec_string,co_name struct *flist, *flist2
flist = "obj_B.list"
while (fscan (flist, name) != EOF) {
mscgetcat (name, "co"//name, magmin=16., magmax=19., catalog="usnob1@noao", rmin=30.)
msccmatch (name, "co"//name, yes, outcoords="outnewco", usebpm=yes, verbose=yes, nsearch=300, search=100., rsearch=0.7, cbox=11, maxshift=15., csig=0.4, cfrac=0.8, listcoords=yes, nfit=4, rms=7., fitgeometry="general", reject=3., update=yes, interactive=no, fit=no, graphics="stdgraph", cursor="")
delete ("outnewco",verify=no) # delete file ex3
}
```

9.1.5 DEPROJECTING IMAGES

```
real ra,dec int i1,i2,i3 string name,*list1,*list2,ra_string,dec_string,trunc_name struct *flist, *flist2
flist = "obj_R.list"
while (fscan (flist, name) != EOF) {
print (name)
i1 = strlen (name)
i2 = i1 - 5
trunc_name = substr (name, 1, i2)
print(trunc_name//"tp.fits", » "tp_obj_R.list")
}
mscimage ("@obj_R.list", "@tp_obj_R.list", format="image", pixmask=no, verbose=")_.verbose", wcssource="image", reference="WFI_Ima.30.fits[7]", ra=INDEF, dec=INDEF, scale=INDEF, rotation=INDEF, blank=0., interpolant="sinc17", minterpolant="linear", boundary="constant", constant=0., fluxconserve=no, ntrim=8, nxblock=1000, nyblock=1000, interactive=no, nx=10, ny=20, fitgeometry="general", xxorder=4, xyorder=4, xxterms="half", yxorder=4, yyorder=4, yxterms="half", fd_in="", fd_ext="", fd_coord="")
```

9.1.6 TRANSPARENCY CORRECTION

```
stsdas
int a, a2
string filename
filename="ngc3227_g0"
struct *flist, *flist2
flist = "3227gnumbers.list"
string te1,te2,te3,te4,comma string ee, photout real x1,xmax,n1,n2
xmax=0
```

```
a=1
while (fscan (flist, a) != EOF) {
rd2xy(filename//a//"bg.fits", 10:23:33.261, 19:53:11.07, hour = yes, » "co_tp")
list=" "
list="co_tp"
printf ("%.s \n", list) | scanf ("%s %s %g %s %s %s %g", te1, te2, n1, comma, te3, te4, n2)
print (n1,n2, »"xyco_"//filename//a//"bg")
delete ("co_tp", verify=no)
}
digiphot
daophot
int a
string filename
filename="ngc3227_g0"
struct *flist, *flist2
flist = "3227gnumbers.list"
string te1,te2,te3,te4,comma, ee, photout
real x1,xmax,n1,n2
xmax=0
a=1
while (fscan (flist, a) != EOF) {
daophot.photpars.aperture=9
phot (image=filename//a//"bg",coords="xyco_"//filename//a//"bg",output="photo_"//filename//a//"bg")
list=" " # define the single output file of daophot task phot
#fields photout 2 > row2 # read in only column 2 in file row2
#tselect row2 sum "row()==5" #prints only row 5 which is the sum of all counts in the set aperture
fields ("photo_"//filename//a//"bg","2", lines="80", quit_if_miss=no, print_file_n=no, > "sum")
list="sum"
j=fscan(list,x1)
printf("%.10g %.1g\n",x1,a, » "gal_counts"//a)
delete ("sum",verify=no) # delete file m3
delete ("photo_"//filename//a//"bg",verify=no) # delete file m3
delete ("xyco_obj"//a//"bg",verify=no)
}
int a
string file_name, filename
filename="ngc3227_g0"
struct *flist, *flist2
flist = "3227gnumbers.list"
flist2 = "3227gnumbers.list"
string te1,te2,te3,te4,comma
string ee, photout
real x1,x2,xmax,n1,n2,tpcor
xmax=0
a=1
while (fscan (flist, a) != EOF) {
list=" "
list="gal_counts"//a
```

```
    j=fscan(list,x1,x2)
    if (x1>xmax) {
    xmax=x1
    print(xmax,"new max value found")
    };
    }
    while (fscan (flist2, a) != EOF) {
    list=" "
    list="gal_counts"//a
    j=fscan(list,x1,x2)
    print(x1,x2) print(xmax)
    tpcor=xmax/x1
    print(tpcor,a, »"logfile_tpcor_g")
    imstat.format=no
    imstat.fields="mean,mode" #configure imstat only to display mode
    imstat (images=filename//a//"bg.fits",binwidt=0.1) # rediredt imstat output to file m3
    imarith (filename//a//"bg.fits","*",tpcor,filename//a//"trp.fits") # use imarith to subtract bg (background) from the image, the result is ...bg.fits
    imstat.format=no
    imstat.fields="mean,mode" #configure imstat only to display mode
    imstat (images=filename//a//"trp.fits",binwidt=0.1) # rediredt imstat output to file m3
    }
```

9.1.7 IMAGE PROCESSING

```
stsdas
    int n,i1,i2,i3
    string list_all_files_mask,list_all_files_gap,mask_im,gap_im,gal_name
    string filename,name,trunc_name
    real air,airmstar,airmend
    real bg,exptime,xx,cf,cf_1,cn_1,hc,cn
    struct *flist, *flist2
    flist = "tp_obj_R.list"
    while (fscan (flist, name) != EOF) {
    i1 = strlen (name) # i = 3
    i2 = i1 - 5
    i3 = 8
    trunc_name = substr (name, 1, i2) # s = "bcd"
    list=" " #initialize the cl list variable
    #ex3="temp.file" #store a temporary file name in string ex3
    print (name," ", »"logfile_airbgcor")
    print ("The mean and mode of "//name//" is:")
    imstat.format=no
    imstat.fields="mean,mode" #configure imstat only to display median and mode
    imstat (images=name,binwidt=0.01) # rediredt imstat output to file m3
    hselect (name,fields="AIRMSTAR",expr=yes, > "ex3")
    list = ("ex3") # associate temporary file with list variable
    j=fscan (list,airmstar) # read the value of the airmass in the file into parameter air
```

```
hselect (name,fields="AIRMEND",expr=yes, > "ex4")
list = ("ex4") # associate temporary file with list variable
j=fscan (list,airmend) # read the value of the airmass in the file into parameter air
air=(airmstar+airmend)/2
print ("AIRMASS: ",airmstar,airmend,air, »"logfile_airbgcor")
x=10* *(0.028*air) # calculate the factor x for the airmass correcation, 0.028 is the extinction factor ex (k=0.07) of filter g times 0.4, (0.4 x ex)
print ("airmass correction: ",x, »"logfile_airbgcor")
hselect (name,fields="EXPTIME",expr=yes)| scan(exptime)
xx = x / exptime
print ("exposure time: "//exptime//" and resulting correction factor: ",xx, »"logfile_airbgcor")
imarith (name,"*",xx,trunc_name//"ex.fits") # use imarith to multiply the image with the airmass correction factor x, the result is ...ex.fits
delete ("ex3",verify=no) # delete file ex3
delete ("ex4",verify=no) # delete file ex3
print ("Image "//name//" is extinction corrected already")
print ("The mean and mode of "//trunc_name//"ex.fits is:")
imstat.format=no
imstat.fields="mean,mode" #configure imstat only to display mode
imstat (images=trunc_name//"ex.fits",binwidt=0.01) # rediredt imstat output to file m3
imstat.fields="mode" #configure imstat only to display mode
imstat (images=trunc_name//"ex.fits",binwidt=0.01, > "m3") # rediredt imstat output to file m3
list = ("m3") # associate temporary file with list variable
j=fscan (list,bg) # read the value in the file into parameter x
print ("background: ",bg, »"logfile_airbgcor")
imarith (trunc_name//"ex.fits","-",bg,trunc_name//"bg.fits") # use imarith to subtract bg (background) from the image, the result is ...bg.fits
delete ("m3",verify=no) # delete file m3
print ("Image "//trunc_name//"bg.fits is background subtracted and extinction corrected already")
print ("the mean and the mode of "//trunc_name//"bg.fits is:")
imstat.format=no
imstat.fields="mean,mode" #configure imstat only to display mode
imstat (images=trunc_name//"bg.fits",binwidt=0.01) # rediredt imstat output to file m3
} # end of for loop
flist = "tp_obj_B.list"
while (fscan (flist, name) != EOF) {
i1 = strlen (name) # i = 3
i2 = i1 - 5
i3 = 8
trunc_name = substr (name, 1, i2) # s = "bcd"
list=" " #initialize the cl list variable
#ex3="temp.file" #store a temporary file name in string ex3
print (name," ", »"logfile_airbgcor")
print ("The mean and mode of "//name//" is:")
imstat.format=no
imstat.fields="mean,mode" #configure imstat only to display median and mode
imstat (images=name,binwidt=0.01) # rediredt imstat output to file m3
hselect (name,fields="AIRMSTAR",expr=yes, > "ex3")
```

```
list = ("ex3") # associate temporary file with list variable
j=fscan (list,airmstar) # read the value of the airmass in the file into parameter air
hselect (name,fields="AIRMEND",expr=yes, > "ex4")
list = ("ex4") # associate temporary file with list variable
j=fscan (list,airmend) # read the value of the airmass in the file into parameter air
air=(airmstar+airmend)/2
print ("AIRMASS: ",airmstar,airmend,air, »"logfile_airbgcor")
x=10* *(0.088*air) # calculate the factor x for the airmass correcation, 0.028 is the extinction factor ex (k=0.22) of filter g times 0.4, (0.4 x ex)
print ("airmass correction: ",x, »"logfile_airbgcor")
hselect (name,fields="EXPTIME",expr=yes)| scan(exptime)
xx = x / exptime
print ("exposure time: "//exptime//" and resulting correction factor: ",xx, »"logfile_airbgcor")
imarith (name,"*",xx,trunc_name//"ex.fits") # use imarith to multiply the image with the airmass correction factor x, the result is ...ex.fits
delete ("ex3",verify=no) # delete file ex3
delete ("ex4",verify=no) # delete file ex3
print ("Image "//name//" is extinction corrected already")
print ("The mean and mode of "//trunc_name//"ex.fits is:")
imstat.format=no
imstat.fields="mean,mode" #configure imstat only to display mode
imstat (images=trunc_name//"ex.fits",binwidt=0.01) # rediredt imstat output to file m3
imstat.fields="mode" #configure imstat only to display mode
imstat (images=trunc_name//"ex.fits",binwidt=0.01, > "m3") # rediredt imstat output to file m3
list = ("m3") # associate temporary file with list variable
j=fscan (list,bg) # read the value in the file into parameter x
print ("background: ",bg, »"logfile_airbgcor")
imarith (trunc_name//"ex.fits","-",bg,trunc_name//"bg.fits") # use imarith to subtract bg (background) from the image, the result is ...bg.fits
delete ("m3",verify=no) # delete file m3
print ("Image "//trunc_name//"bg.fits is background subtracted and extinction corrected already")
print ("the mean and the mode of "//trunc_name//"bg.fits is:")
imstat.format=no
imstat.fields="mean,mode" #configure imstat only to display mode
imstat (images=trunc_name//"bg.fits",binwidt=0.01) # rediredt imstat output to file m3
} # end of for loop
######################################################################
############
############ Producing masks and replacing gaps with zero values
############
######################################################################
###############################################
flist = "tp_obj_R.list"
while (fscan (flist, name) != EOF){
i1 = strlen (name) # i = 3
i2 = i1 - 5
i3 = 8
trunc_name = substr (name, 1, i2) # s = "bcd"
```

```
print("Starting to replace the gaps with 0")
imcopy (trunc_name//"bg.fits", trunc_name//"gap.fits")
imreplace (images=trunc_name//"gap.fits",value=0,lower=INDEF,upper=-0.8)
imcopy (trunc_name//"bg.fits", trunc_name//"mask.fits")
imreplace (trunc_name//"mask.fits",value=1,lower=-0.8,upper=INDEF)
imreplace (trunc_name//"mask.fits",value=0,lower=INDEF,upper=-0.801)
}
flist = "tp_obj_B.list"
while (fscan (flist, name) != EOF){
i1 = strlen (name) # i = 3
i2 = i1 - 5
i3 = 8
trunc_name = substr (name, 1, i2) # s = "bcd"
print("Starting to replace the gaps with 0")
imcopy (trunc_name//"bg.fits", trunc_name//"gap.fits")
imreplace (images=trunc_name//"gap.fits",value=0,lower=INDEF,upper=-0.3)
imcopy (trunc_name//"bg.fits", trunc_name//"mask.fits")
imreplace (trunc_name//"mask.fits",value=1,lower=-0.3,upper=INDEF)
imreplace (trunc_name//"mask.fits",value=0,lower=INDEF,upper=-0.301)
}
#########################################################################
#########
######## COMBINING SINGLE IMAGE TO FINAL IMAGE
#########
#########################################################################
list_all_files_mask=""
list_all_files_gap=""
gal_nam = "N3981"
flist = "obj_R_long.list"
while (fscan (flist, name) != EOF){
i1 = strlen (name) # i = 3
i2 = i1 - 5
i3 = 8
trunc_name = substr (name, 1, i2) # s = "bcd"
list_all_files_mask=list_all_files_mask//trunc_name//"tpmask.fits,"
list_all_files_gap=list_all_files_gap//trunc_name//"tpgap.fits,"
} cf = strlen (list_all_files_mask) # i = 3
cn = strlen (list_all_files_gap) # i = 3
cf_1 = cf - 1
cn_1 = cn - 1
print(cf,cf_1,cn,cn_1)
mask_im = substr (list_all_files_mask, 1, cf_1) # s = "bcd"
gap_im = substr (list_all_files_gap, 1, cn_1) # s = "bcd"
imcombine (input=mask_im,output=gal_nam//"R_mask",combine="sum",offset="wcs")
imcombine (input=gap_im,output=gal_nam//"R_gap",combine="sum",offset="wcs")
imarith (gal_nam//"R_gap","/",gal_nam//"R_mask",gal_nam//"R_f1")
list_all_files_mask=""
list_all_files_gap=""
```

```
flist = "obj_B_long.list"
while (fscan (flist, name) != EOF){
i1 = strlen (name) # i = 3
i2 = i1 - 5
i3 = 8
trunc_name = substr (name, 1, i2) # s = "bcd"
list_all_files_mask=list_all_files_mask//trunc_name//"tpmask.fits,"
list_all_files_gap=list_all_files_gap//trunc_name//"tpgap.fits,"
} cf = strlen (list_all_files_mask) # i = 3
cn = strlen (list_all_files_gap) # i = 3
cf_1 = cf - 1
cn_1 = cn - 1
print(cf,cf_1,cn,cn_1)
mask_im = substr (list_all_files_mask, 1, cf_1) # s = "bcd"
gap_im = substr (list_all_files_gap, 1, cn_1) # s = "bcd"
imcombine (input=mask_im,output=gal_nam//"B_mask",combine="sum",offset="wcs")
imcombine (input=gap_im,output=gal_nam//"B_gap",combine="sum",offset="wcs")
imarith (gal_nam//"B_gap","/",gal_nam//"B_mask",gal_nam//"B_f1")
print ("CONGRATULATIONS: "//gal_nam//" WAS SUCCESSFULLY REDUCED")
```

9.1.8 PHOTOMETRIC ANALYSIS

```
# necessary files : 3628_g_f1; 3628_r_f1; 3628_g_minus_r
stsdas
int xg, yg, d12, xr, yr, xgrkp, ygrkp, xcount
string filename, filename2, fn3, fn4, fn5, te1, te2, comma,te3, te4,image_v, image_gr, struct_name
real x1, y1, x2, y2, x3, y3, ra1, dec1, mean_v, midpt_v, mode_v, stddev_v, npix_v, mean_r, midpt_r, mode_r, stddev_r, npix_r
real zp_g, zp_r, mode_bg_g, mode_bg_r, midpt_bg_g, midpt_bg_r, m_g, m_r, sb_g, sb_r, t_exp_g, t_exp_r, mean_gr, midpt_gr, mode_gr, stddev_gr, npix_gr
t_exp_g=600
t_exp_r=450
# #### photometry calculations
#
# the pixel scale is 0.258 arcseconds per pixel – > area of 0.066564 arcsenonds^2 per pixel
#
# m_g=(-2.5*(log(((midpt_v-mode_bg_g)*npix_v)/t_exp_g)))+zp_g
# m_r=(-2.5*(log(((midpt_r-mode_bg_r)*npix_r)/t_exp_r)))+zp_r
# sb_g=m_g+(2.5*log(npix_v*0.066564))
# sb_r=m_r+(2.5*log(npix_r*0.066564))
zp_g=26.97
zp_r=27.25
#The average background value in the g-band is [midpt] [mode]-22.165152736842 -27.207406921053
#The average background value in the r-band is [midpt] [mode]-27.681152394737 -36.752034803158
mode_bg_g=-39.339335870833
midpt_bg_g=-33.021605191667
```

```
mode_bg_r=-3.9142030833333
midpt_bg_r=-10.104654279167
filename2="3628_g_minus_r_SDSS"
filename="3628_g_minus_r"
fn3="3628_g_f1"
fn4="3628_r_f1"
fn5="3628_g_minus_r"
struct *fn_reg1
struct *fn_reg2
struct *fn_reg3
struct *fn_reg4
struct *fn_reg5
struct *struct_newname
fn_reg1 = "umbrella_regions_1.dat"
fn_reg2 = "umbrella_regions_2.dat"
fn_reg3 = "umbrella_regions_3.dat"
fn_reg4 = "umbrella_regions_4.dat"
fn_reg5 = "umbrella_regions_5.dat"
######################################################################
######### Calculating the S/N ratio of each aperture #################
real bg_g_tot, bg_r_tot, gain, rdnoise, s_to_n_g, s_to_n_r
gain = 0.88
rdnoise = 5.0
bg_g_tot = 5983
bg_r_tot = 10412
#s_to_n_g = (midpt_v*gain)/sqrt((midpt_v*gain)+(bg_g_tot*gain)+(rdnoise**2))
#s_to_n_r = (midpt_r*gain)/sqrt((midpt_r*gain)+(bg_r_tot*gain)+(rdnoise**2))
#midpt_v, mode_v, stddev_v, npix_v
#midpt_r, mode_r, stddev_r, npix_r
######################################################################
### reddening correction
real A_g, A_r, A_g_1, A_g_2, A_g_3, A_g_4, A_g_5, A_g_6, A_g_7, A_g_8, A_g_9, A_r_1, A_r_2, A_r_3, A_r_4, A_r_5, A_r_6, A_r_7, A_r_8, A_r_9
A_g_1=0.216161863918935
A_g_2=0.21420675378739
A_g_3=0.228259107857869
A_g_4=0.229481051690085
A_g_5=0.173882607324276
A_g_6=0.216161863918935
A_g_7=0.195755401920935
A_g_8=0.210174339141078
A_g_9=0.237545880982707
A_r_1=0.155649169473879
A_r_2=0.15424137596818
A_r_3=0.164359891790394
A_r_4=0.165239762731456
A_r_5=0.125205634913132
A_r_6=0.155649169473879
```

```
A_r_7=0.140955324758143
A_r_8=0.151337801862675
A_r_9=0.171046910942465
# set the used radius calculated was 17
d12=30
# read in regions from ds9 region table
#print (fn_reg1_struct)
############ START OF THE SCRIPT ########################################
for (xcount=1; xcount<=11 ;xcount+=1) {
struct_newname="co_regions_"//xcount
A_g=0.241
A_r=0.166
if (xcount == 1) {
A_g = 0.216161863918935
A_r = 0.155649169473879 ;}
else if (xcount == 2) {
A_g = 0.21420675378739 A_r = 0.15424137596818 ;} else if (xcount==3) { A_g=0.228259107857869 A_r=0.164359891790394 ;} else if (xcount==4) { A_g=0.229481051690085 A_r=0.165239762731456 ;} else if (xcount==5) { A_g=0.216161863918935 A_r=0.155649169473879 ;} else if (xcount==6) { A_g=0.195755401920935 A_r=0.140955324758143 ;} else if (xcount==7) { A_g=0.195755401920935 A_r=0.140955324758143 ;} else if (xcount==8) { A_g=0.195755401920935 A_r=0.140955324758143 ;} else if (xcount==9) { A_g=0.210174339141078 A_r=0.151337801862675 ;} else if (xcount==10) { A_g=0.210174339141078 A_r=0.151337801862675 ;} else if (xcount==11) { A_g=0.237545880982707 A_r=0.171046910942465 ;} else if (xcount==12) { A_g=0.237545880982707 A_r=0.171046910942465 ;} else print ("Error");
print (A_g,A_r)
while (fscan(struct_newname, x1, y1) != EOF) {
print (x1) | scan (xg)
print (y1) | scan (yg)
imstat (fn3//"["//(xg-d12)//":"//(xg+d12)//", "//(yg-d12)//":"//(yg+d12)//"]", fields="image, mean, midpt, mode, stddev, npix", lower=INDEF, upper=INDEF, nclip=0, lsigma=3., usigma=3., binwidth=0.01, format=no, cache=no, »"values")
list=" " list="values"
printf ("%.s \n", list) | scanf ("%s %g %g %g %g %g", image_v, mean_v, midpt_v, mode_v, stddev_v, npix_v)
delete ("values", verify=no)
# getting the ra dec coordinates from the g-band image
xy2rd(fn3, x1, y1, hms = no, » "co_r_stars")
list=" "
list="co_r_stars"
printf ("%.s \n", list) | scanf ("%s %s %g %s %s %s %g", te1, te2, ra1, comma, te3, te4, dec1)
delete ("co_r_stars", verify=no)
# calculated the values for the r-band image
rd2xy(fn4, ra1, dec1, hour = no, » "co_tp")
list=" "
list="co_tp"
printf ("%.s \n", list) | scanf ("%s %s %g %s %s %s %g", te1, te2, x2, comma, te3, te4, y2)
#print (x1,y1,x2,y2)
```

```
delete ("co_tp", verify=no)
#print (te1, te2, aa, comma, te3, ab, te4)
print (x2) | scan (xr)
print (y2) | scan (yr)
imstat (fn4//"["//(xr-d12)//":"//(xr+d12)//", "//(yr-d12)//":"//(yr+d12)//"]", fields="image, mean, midpt, mode, stddev, npix", lower=INDEF, upper=INDEF, nclip=0, lsigma=3., usigma=3., binwidth=0.01, format=no, cache=no, »"values")
list=" "
list="values"
printf ("%.s \n", list) | scanf ("%s %g %g %g %g %g", image_r, mean_r, midpt_r, mode_r, stddev_r, npix_r)
delete ("values", verify=no)
# calculate the different colors in the colormaps of the kittpeak color map
#rd2xy(fn5, ra1, dec1, hour = no, » "co_tp")
#
#list=" "
#list="co_tp"
#
#printf ("%.s \n", list) | scanf ("%s %s %g %s %s %s %g", te1, te2, x3, comma, te3, te4, y3)
#print (x1, y1, x2, y2, x3, y3)
#delete ("co_tp", verify=no)
#print (te1, te2, aa, comma, te3, ab, te4)
#print (x3) | scan (xgrkp)
#print (y3) | scan (ygrkp)
#imstat (fn5//"["//(xgrkp-d12)//":"//(xgrkp+d12)//", "//(ygrkp-d12)//":"//(ygrkp+d12)//"]", fields="image, mean, midpt, mode, stddev, npix", lower=INDEF, upper=INDEF, nclip=0, lsigma=3., usigma=3., binwidth=0.01, format=no, cache=no, »"values")
#
#list=" "
#list="values"
#
#printf ("%.s \n", list) | scanf ("%s %g %g %g %g %g", image_gr, mean_gr, midpt_gr, mode_gr, stddev_gr, npix_gr)
#delete ("values", verify=no)
if ((midpt_v-mode_bg_g)>0)
m_g=((-2.5*(log(((midpt_v-mode_bg_g)*npix_v)/t_exp_g)))+zp_g)
else
m_g=0
if ((midpt_r-mode_bg_r)>0)
m_r=((-2.5*(log(((midpt_r-mode_bg_r)*npix_r)/t_exp_r)))+zp_r)
else
m_r=0
if ((midpt_v)>0)
s_to_n_g = (midpt_v*gain)/sqrt((midpt_v*gain)+(bg_g_tot*gain)+(rdnoise**2))
else
s_to_n_g=0
if ((midpt_r)>0)
if ((midpt_r-mode_bg_r)>0)
```

```
s_to_n_r = (midpt_r*gain)/sqrt((midpt_r*gain)+(bg_r_tot*gain)+(rdnoise**2))
else
s_to_n_r = 0;
sb_r=m_r+(2.5*log(npix_r*0.066564))
sb_g=m_g+(2.5*log(npix_v*0.066564))
print(m_g, sb_g, m_r, sb_r, (m_g-m_r), (midpt_v/mode_v), (mean_v/mode_v), (mean_v/midpt_v), (midpt_r/mode_r), (mean_r/mode_r), (mean_r/midpt_r), s_to_n_g, s_to_n_r)
print((midpt_v-mode_bg_g), (midpt_r-mode_bg_r), »"median_g_r")
print(m_g, sb_g, m_r, sb_r, (m_g-m_r), (mode_gr-(A_g-A_r)), (midpt_gr-(A_g-A_r)), (midpt_v/mode_v), (mean_v/mode_v), (mean_v/midpt_v), (midpt_r/mode_r), (mean_r/mode_r), (mean_r/midpt_r))
print(s_to_n_g, s_to_n_r, »"sn") }
print("this was region:", xcount)
print("this was region:", xcount,»"sn")
}
```

9.2 ADDITIONAL OBSERVED GALAXIES

9.2.1 MOSAIC - 4M MAYALL

Figure 9.1: NGC 3044 (SDSS *r*-band)

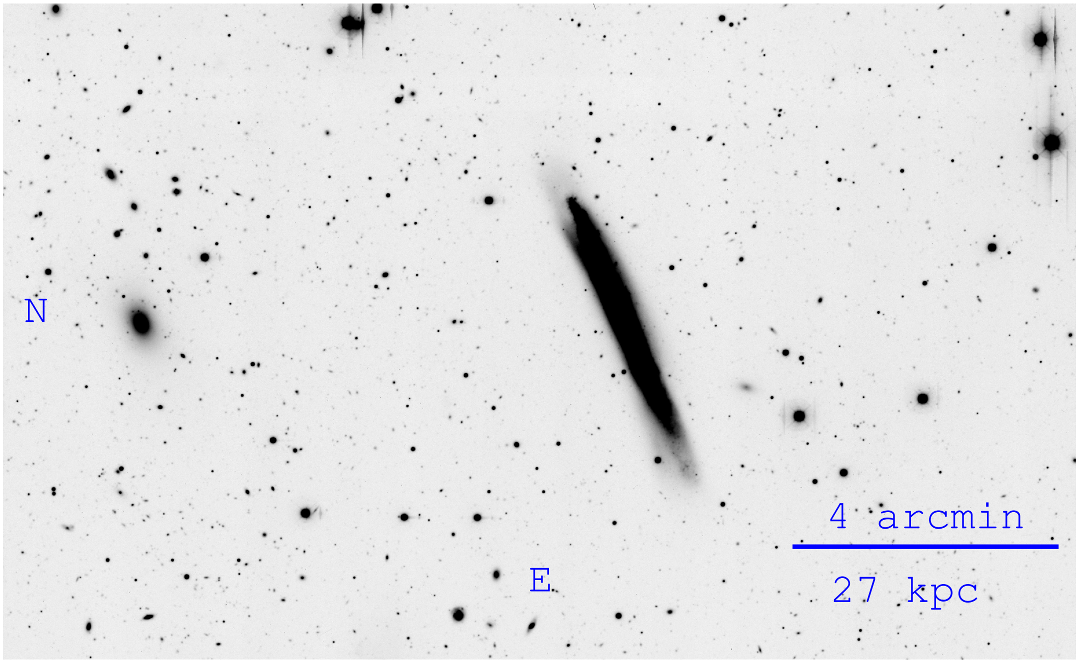

Figure 9.2: NGC 3245 (SDSS *g*-band)

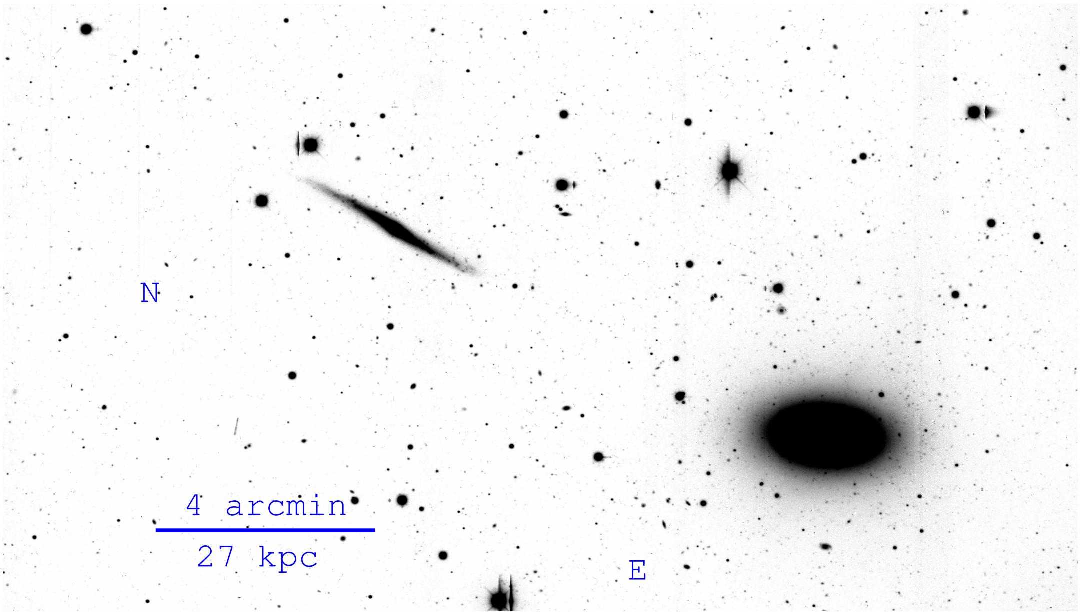

Figure 9.3: NGC 3953 (SDSS *g*-band)

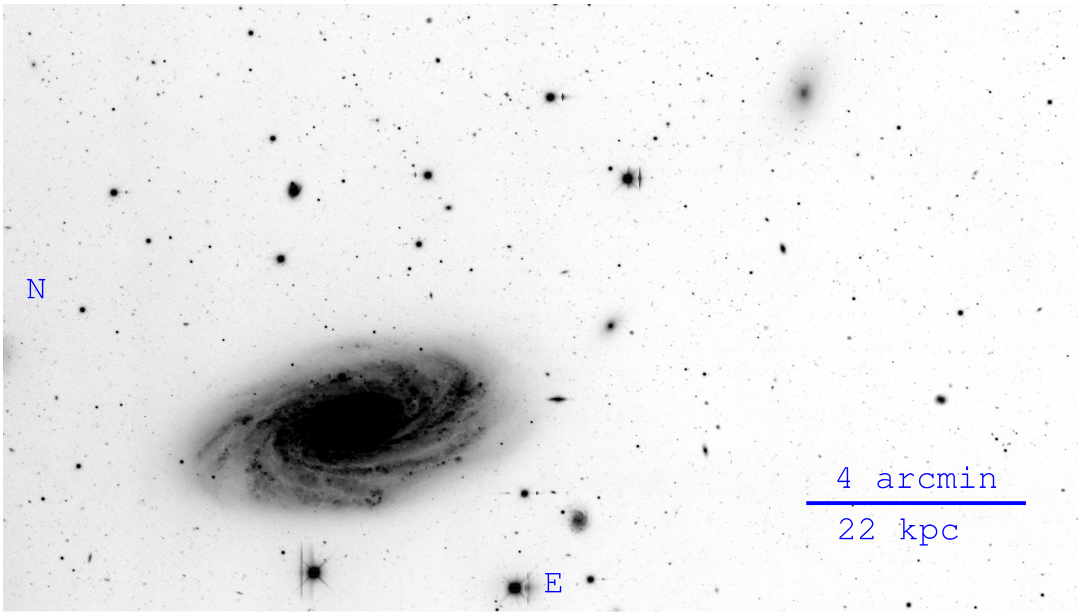

Figure 9.4: UGC 2953 (SDSS *g*-band)

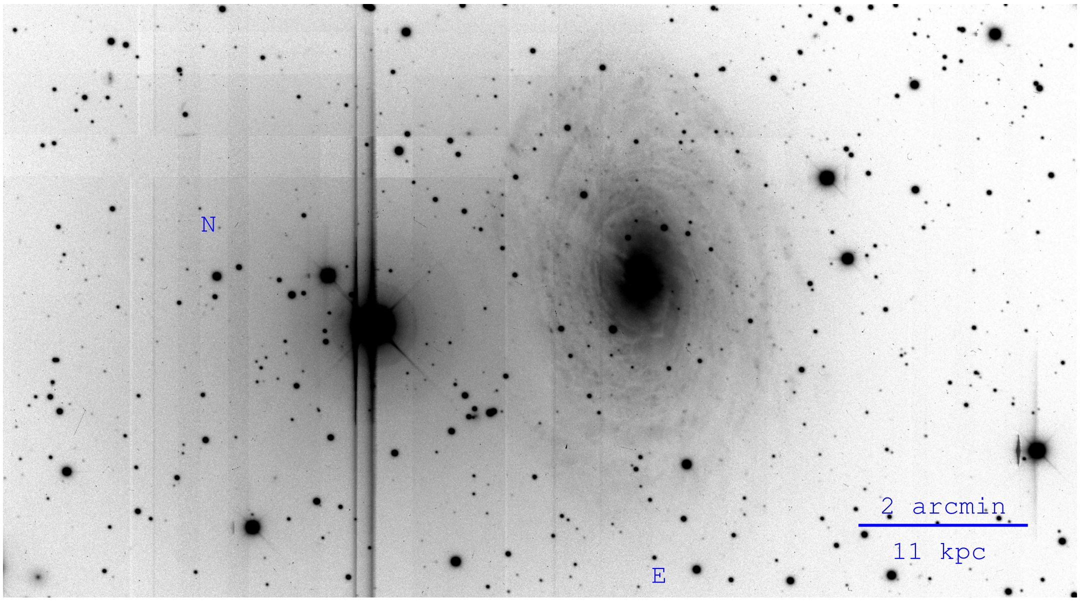

9.2.2 MOSAIC - WIYN 0.9M

Figure 9.5: NGC 524 (SDSS *g*-band)

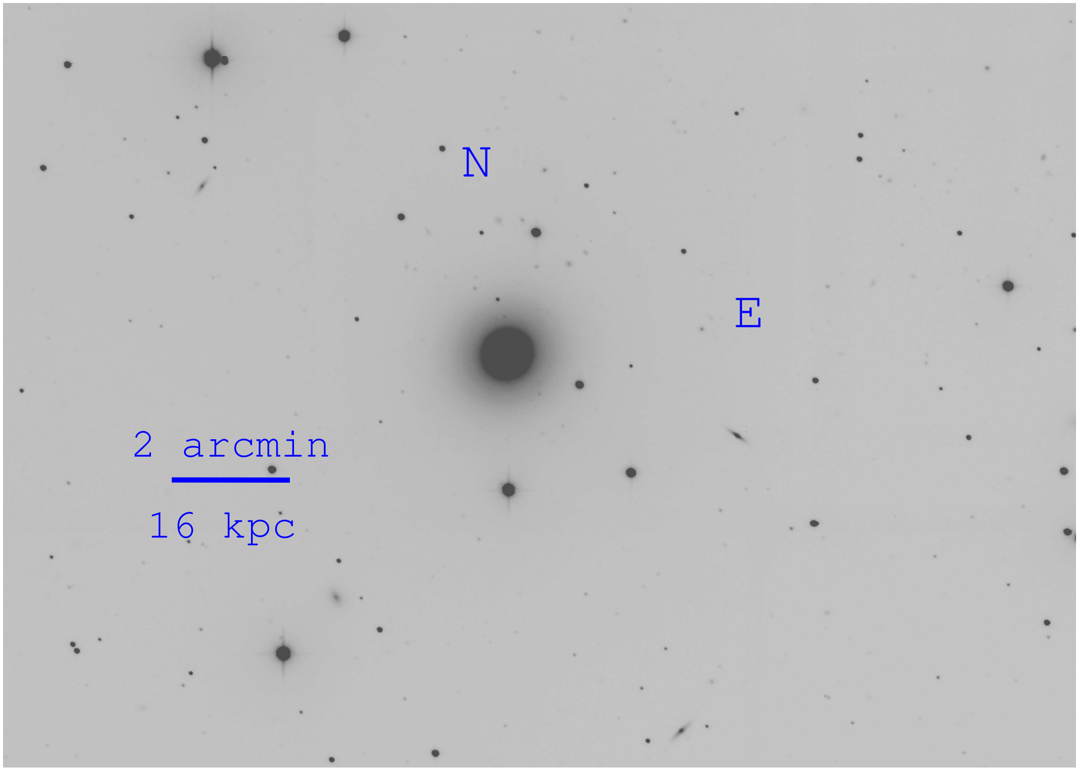

Figure 9.6: NGC 524 Candidate dwarf galaxies (SDSS *g*-band)

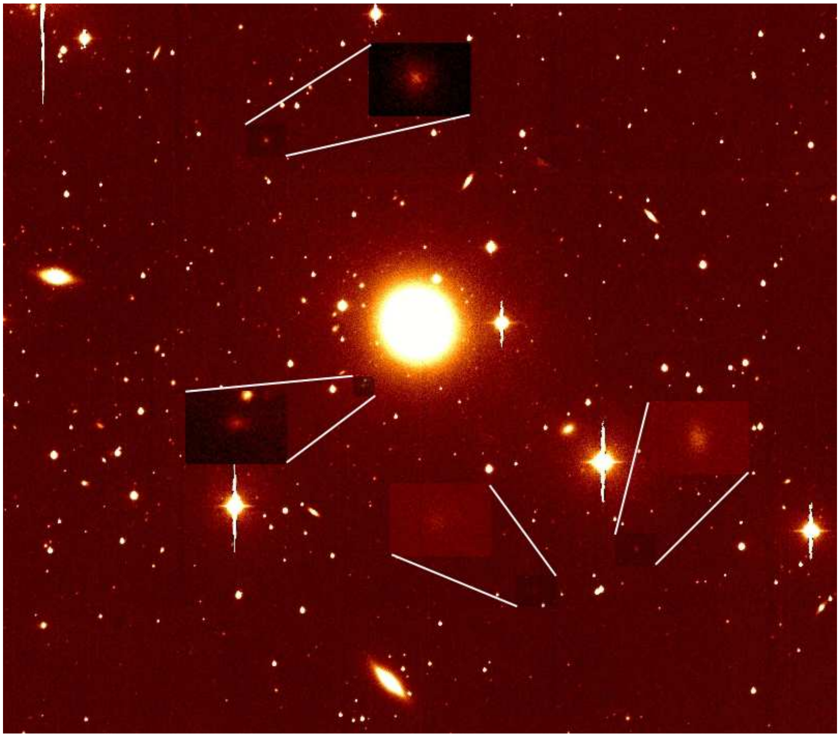

Figure 9.7: NGC 660 (SDSS *r*-band)

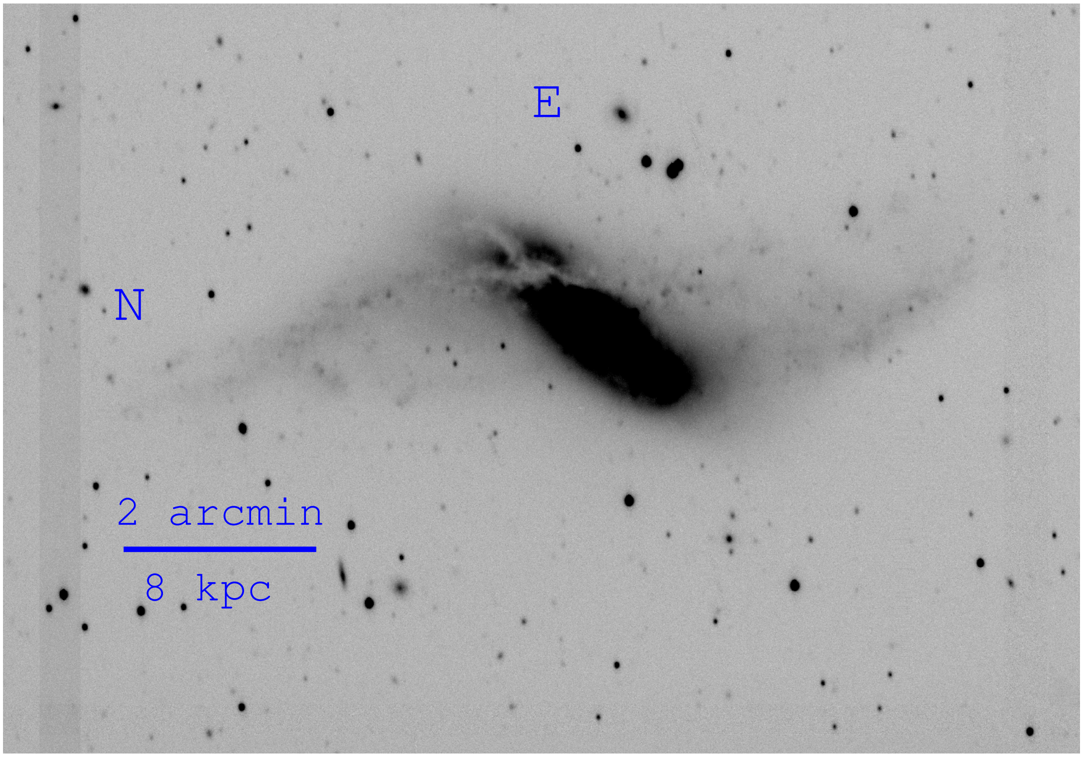

Figure 9.8: NGC 772 (SDSS *g*-band)

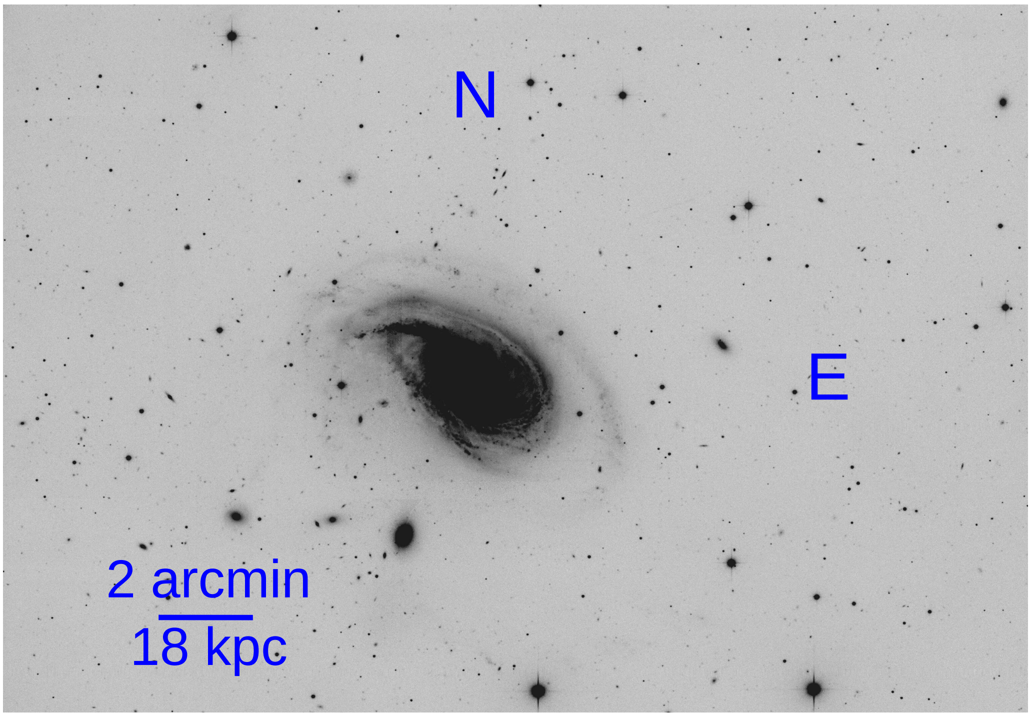

Figure 9.9: NGC 1023 (SDSS *g*-band)

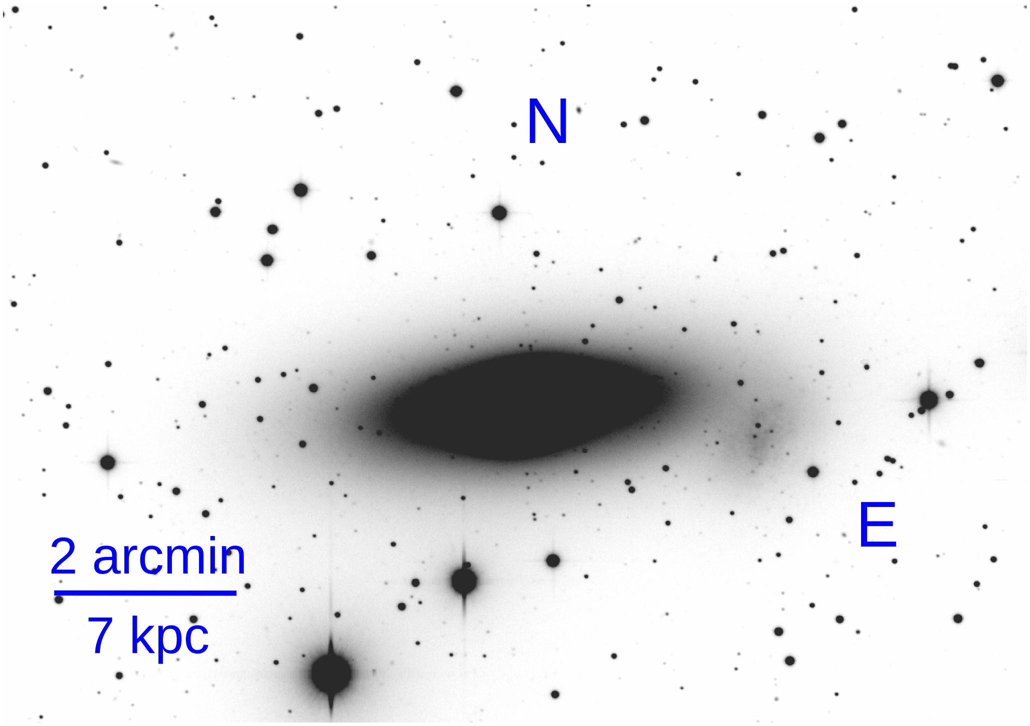

Figure 9.10: NGC 2608 (SDSS *g*-band)

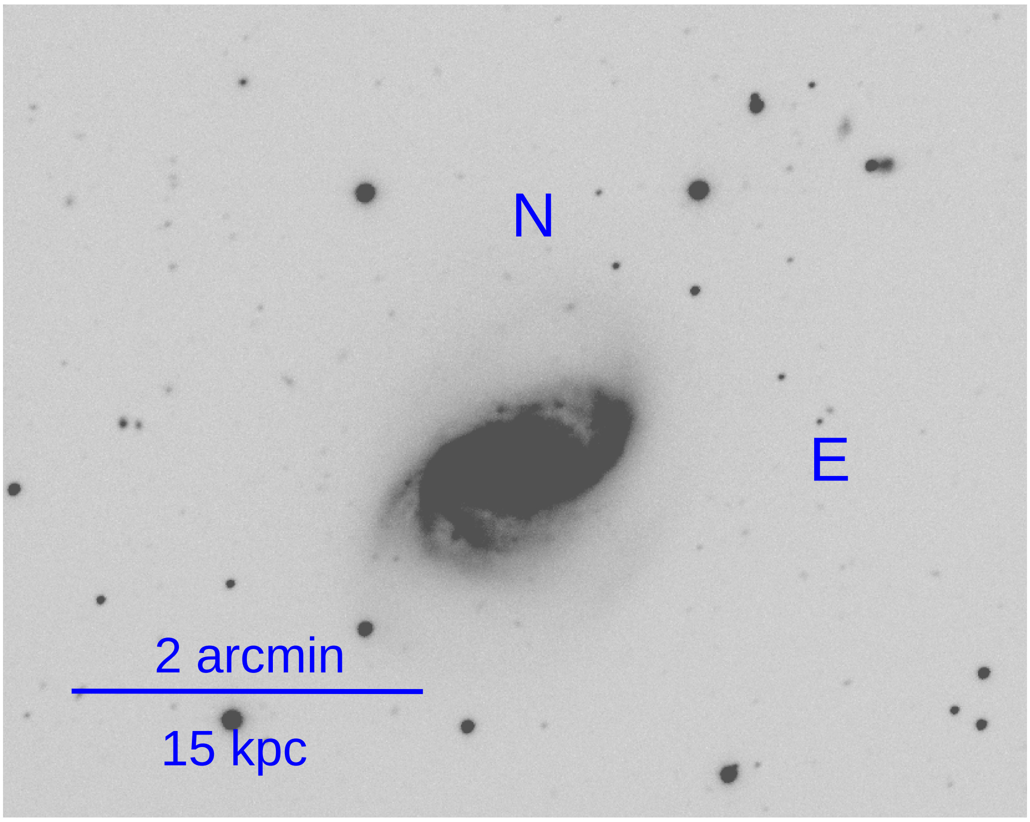

Figure 9.11: NGC 4013 (SDSS *g*-band)

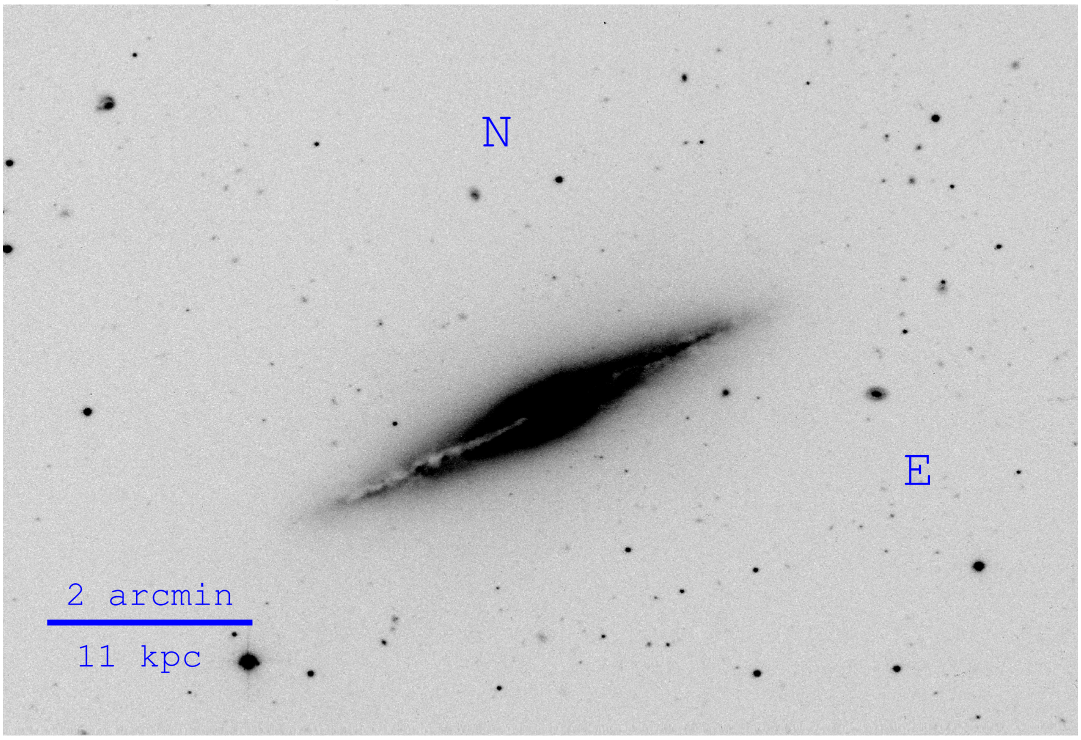

Figure 9.12: NGC 5529 (SDSS *g*-band)

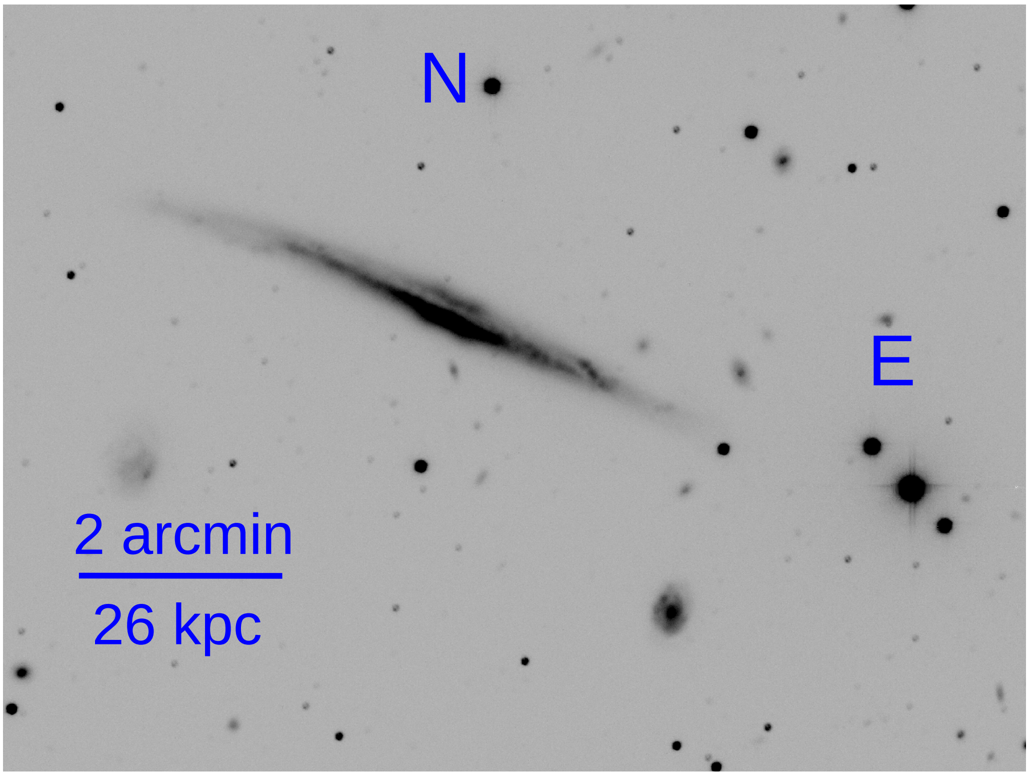

Figure 9.13: NGC 7013 (SDSS *g*-band)

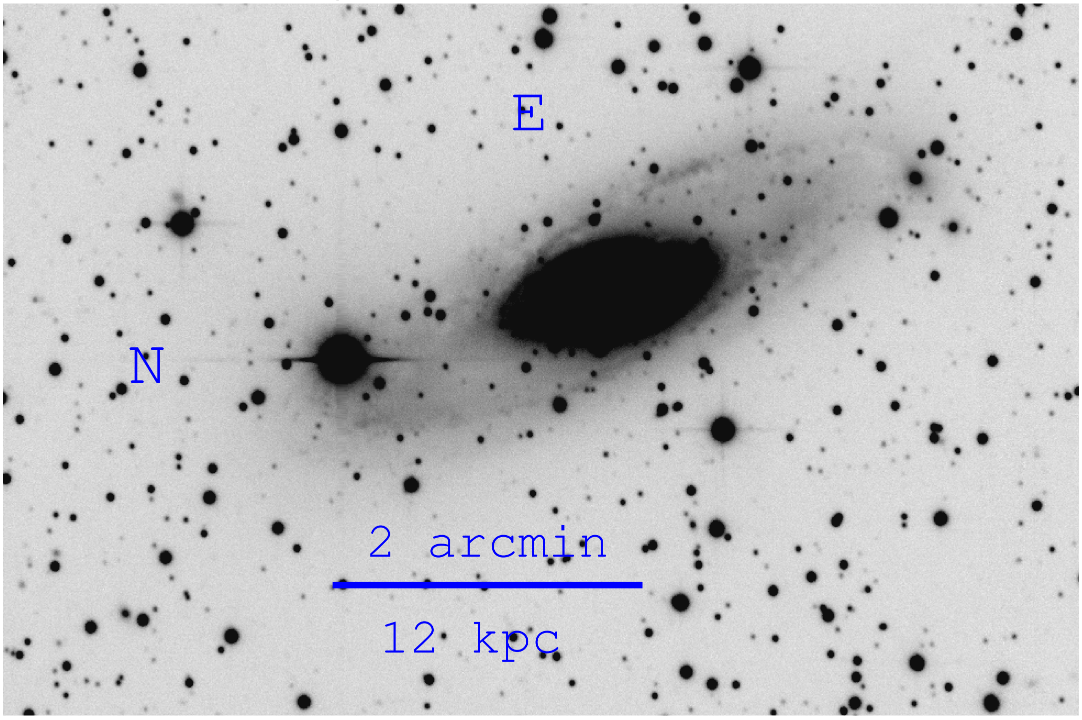

Figure 9.14: NGC 7457 (SDSS *g*-band)

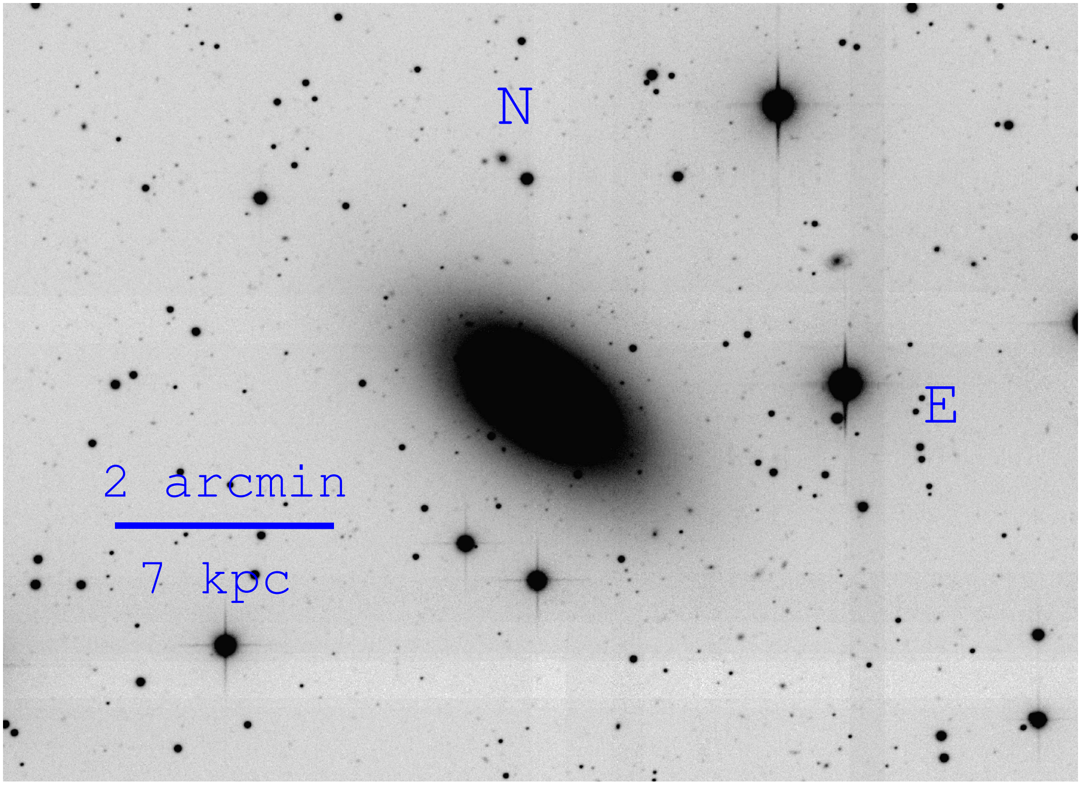

Figure 9.15: UGC 2531 (SDSS *g*-band)

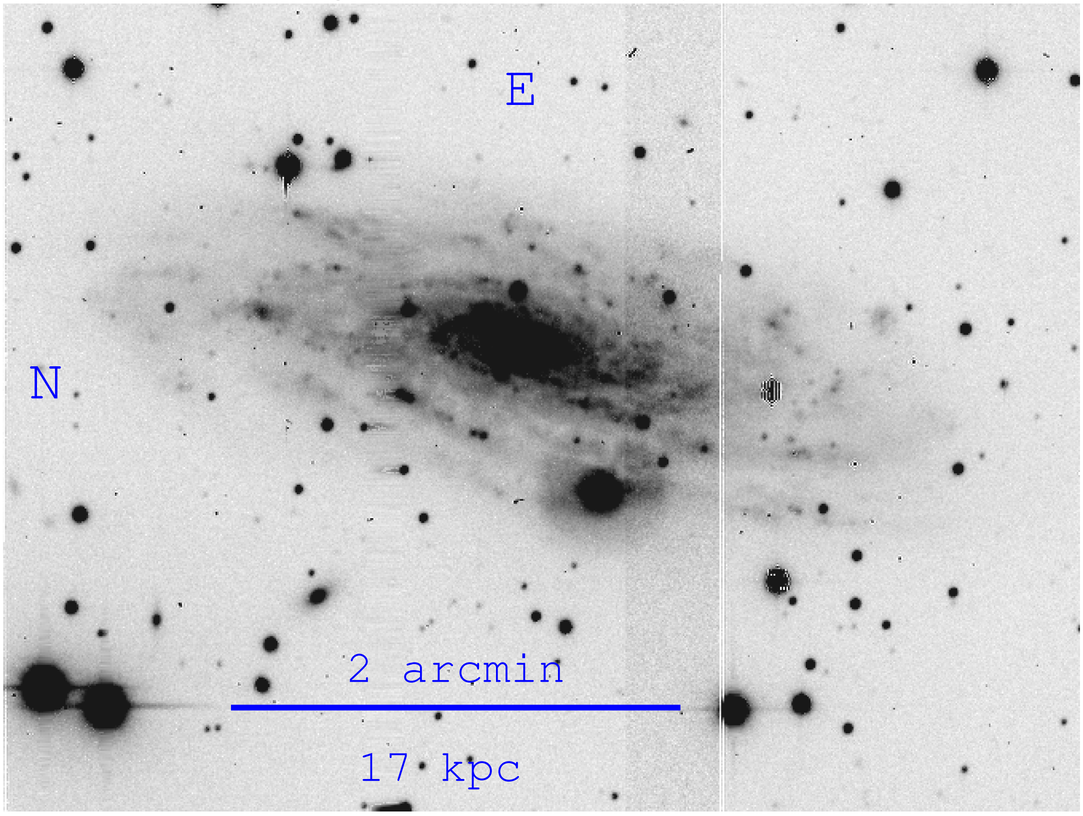

9.3 SELECTED COLOR IMAGES OF THE STUDIED GALAXIES

Figure 9.16: IC 4721

Figure 9.17: IC 4889

Figure 9.18: NGC 134

Figure 9.19: NGC 150

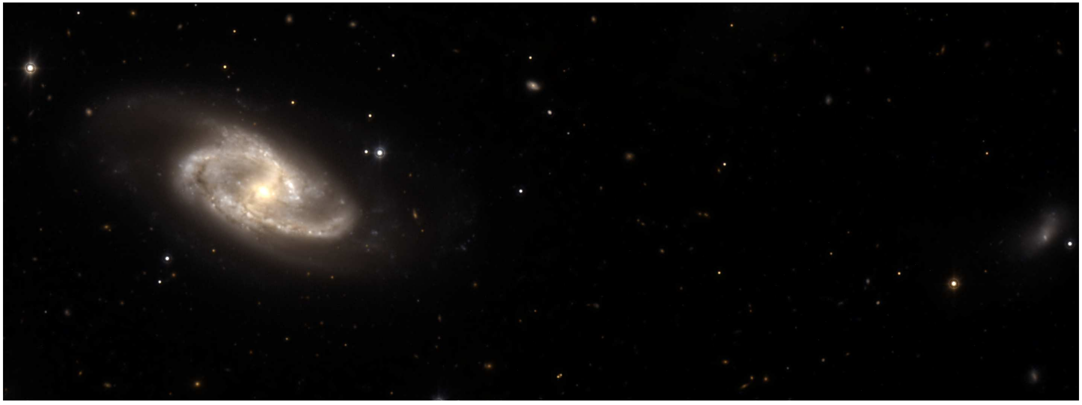

Figure 9.20: NGC 578

Figure 9.21: NGC 134

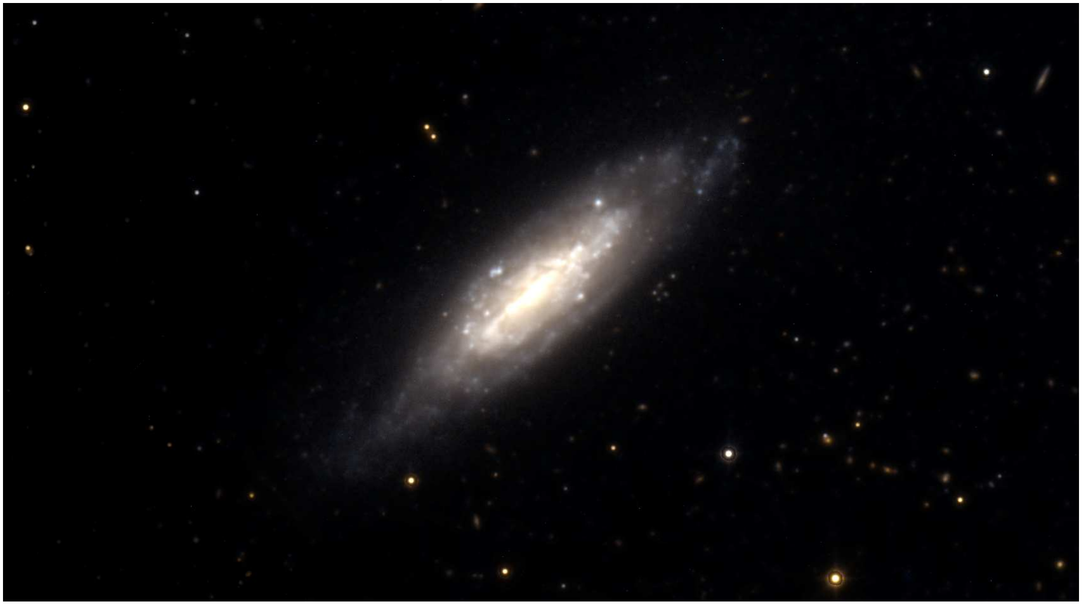

Figure 9.22: NGC 908

Figure 9.23: NGC 1365

Figure 9.24: NGC 1421

Figure 9.25: NGC 1425

Figure 9.26: NGC 1532

Figure 9.27: NGC 1964

Figure 9.28: NGC 2310

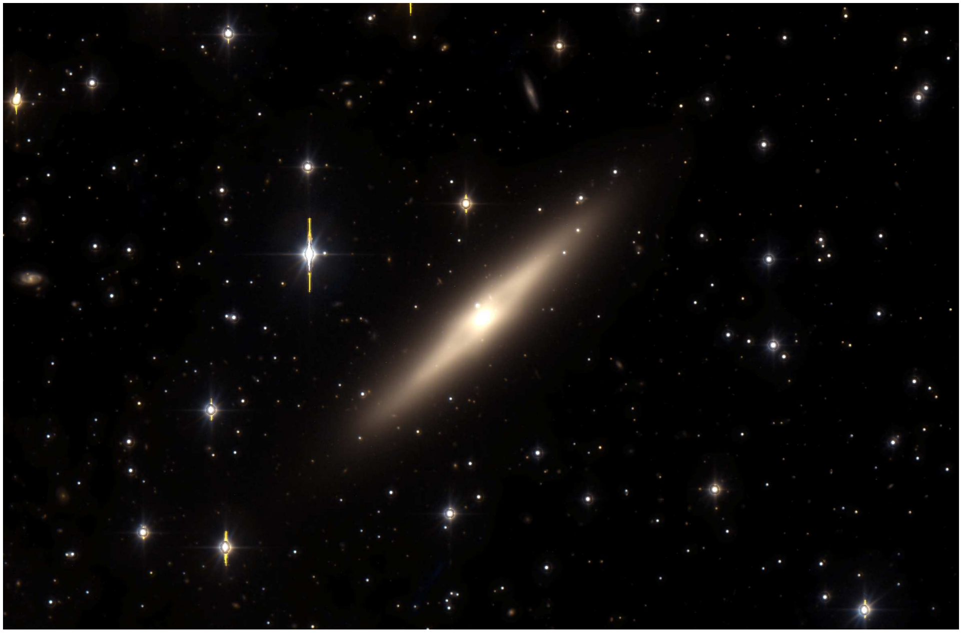

Figure 9.29: NGC 1964

Figure 9.30: NGC 2460

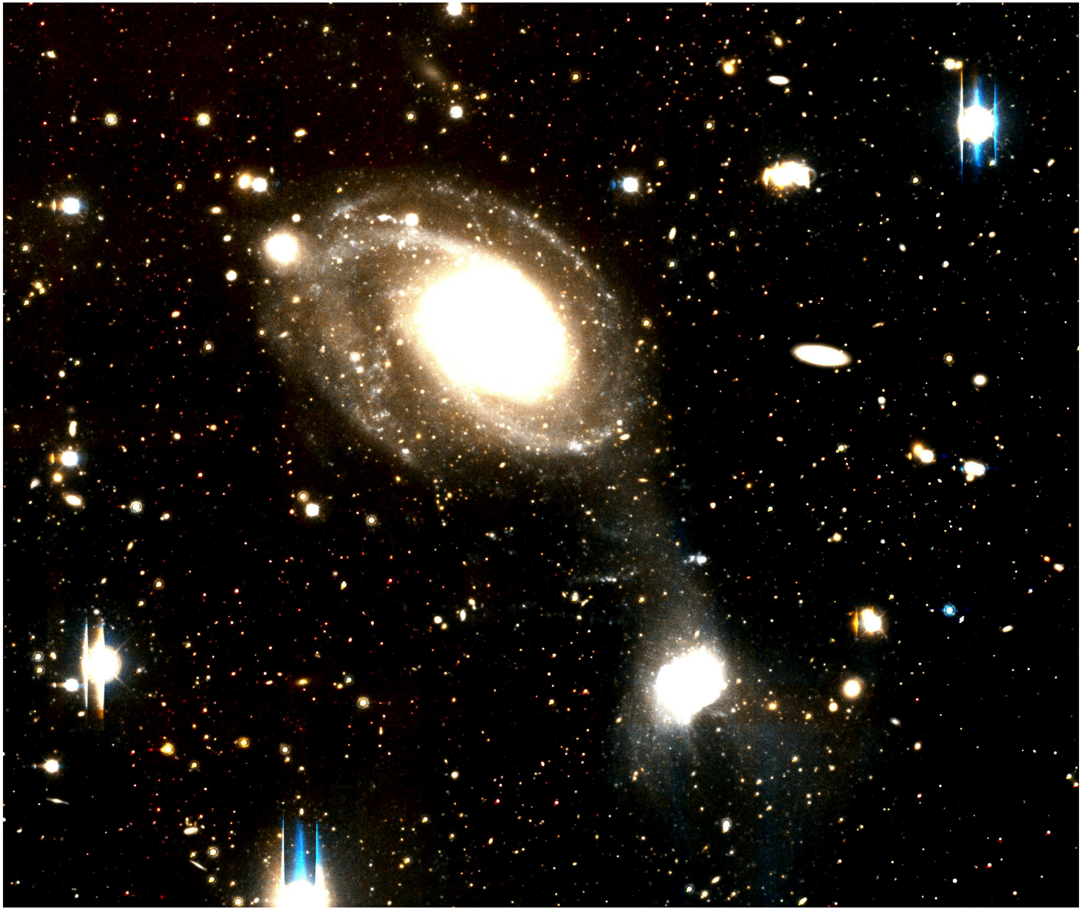

Figure 9.31: NGC 3227

Figure 9.32: NGC 3521

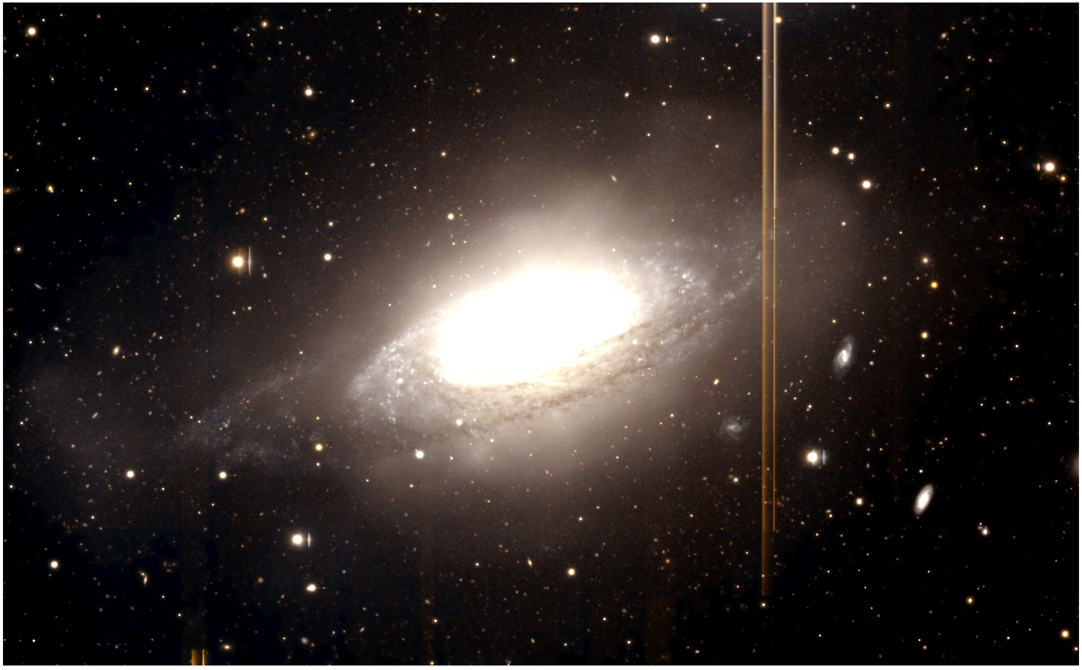

Figure 9.33: NGC 3628

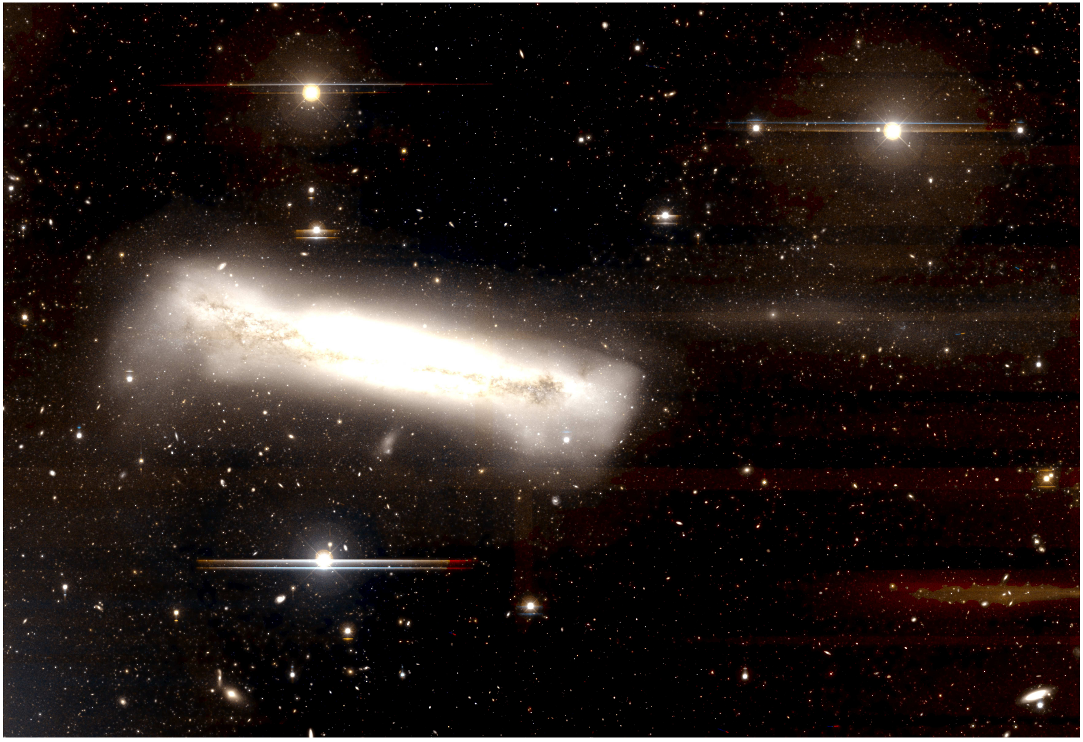

Figure 9.34: NGC 3717

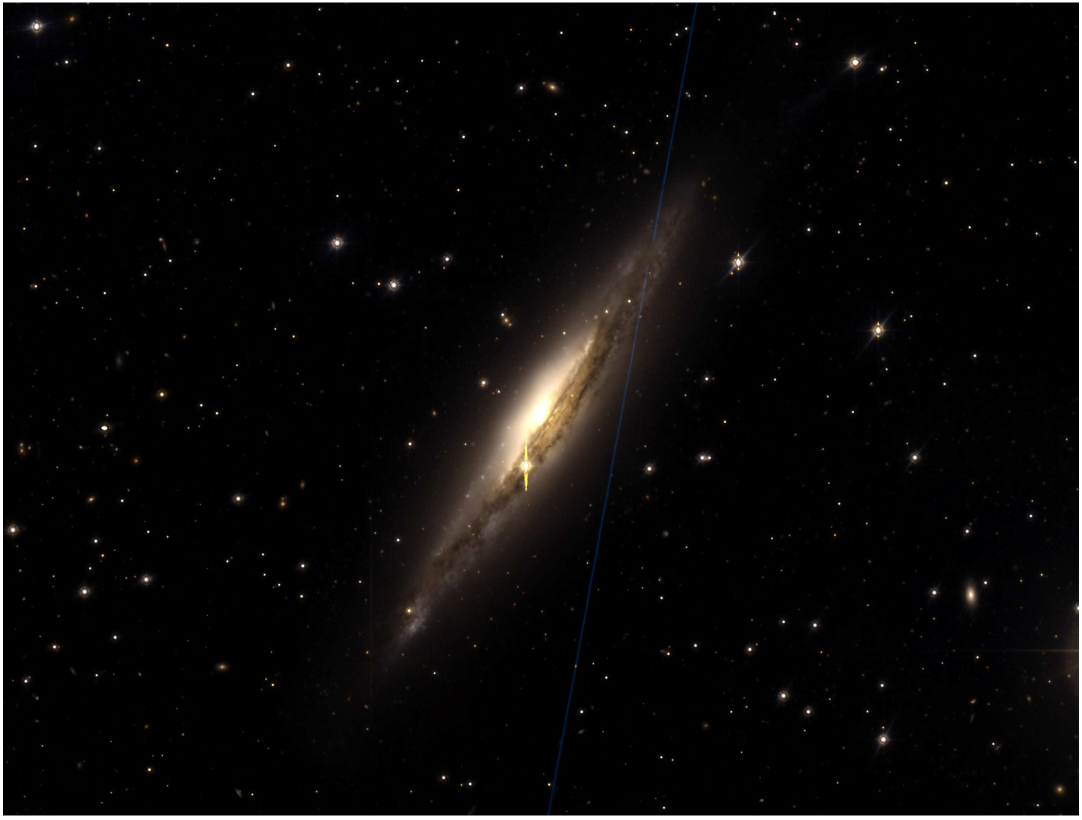

Figure 9.35: NGC 3936

Figure 9.36: NGC 3956

Figure 9.37: NGC 3981

Figure 9.38: NGC 4219

Figure 9.39: NGC 4835

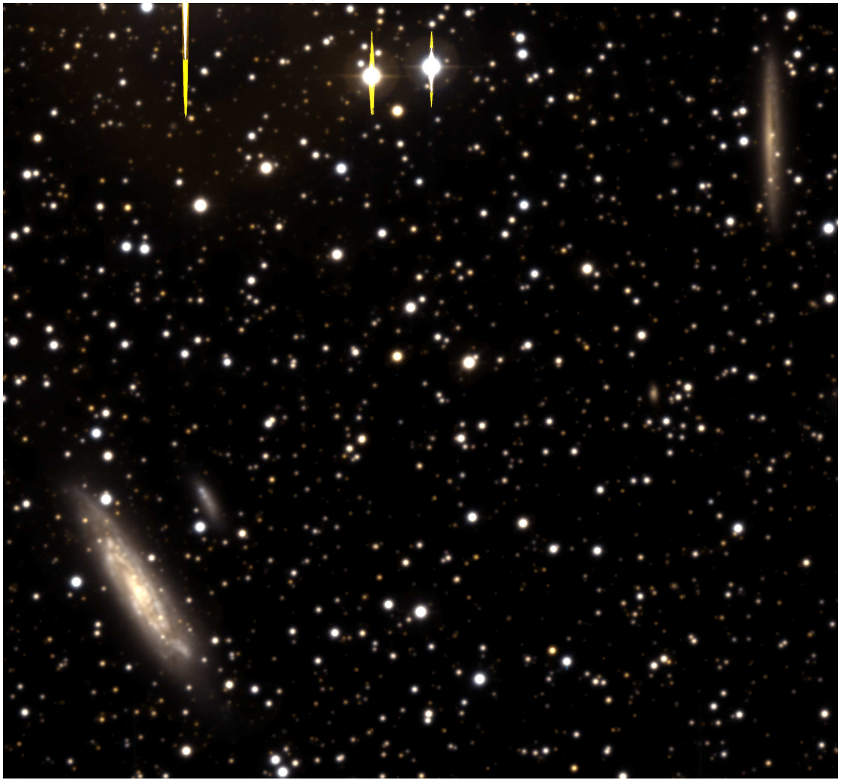

Figure 9.40: NGC 6810

Figure 9.41: NGC 7314

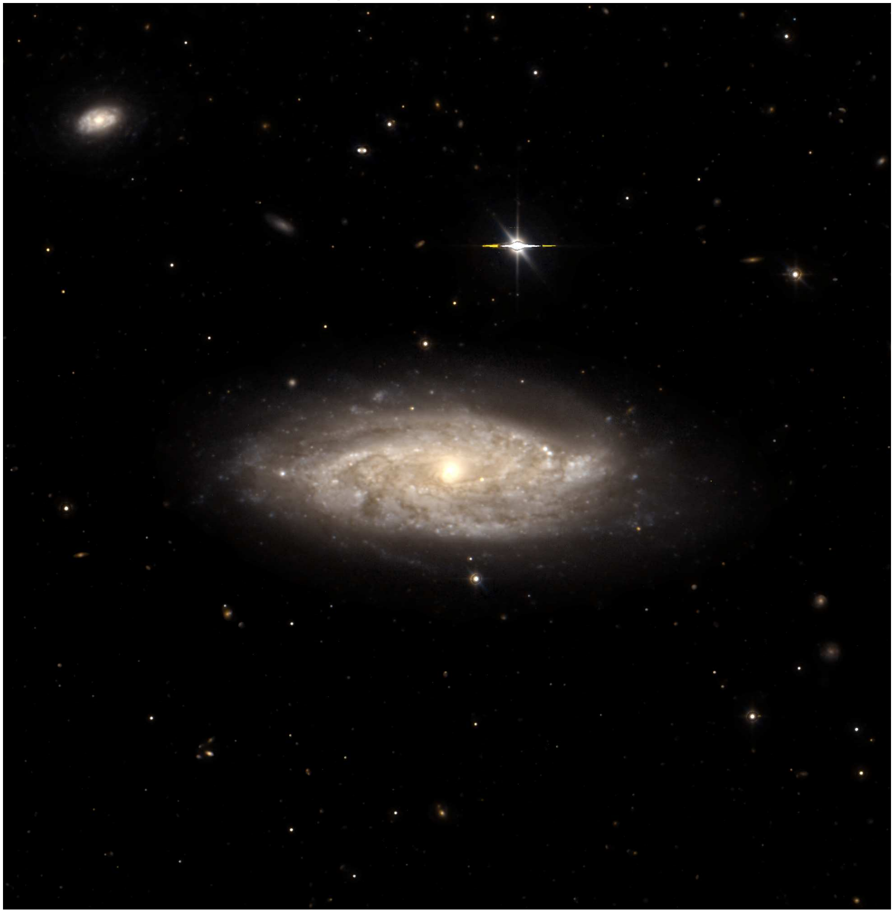

Figure 9.42: NGC 7599

Figure 9.43: NGC 7721

Figure 9.44: NGC 7727

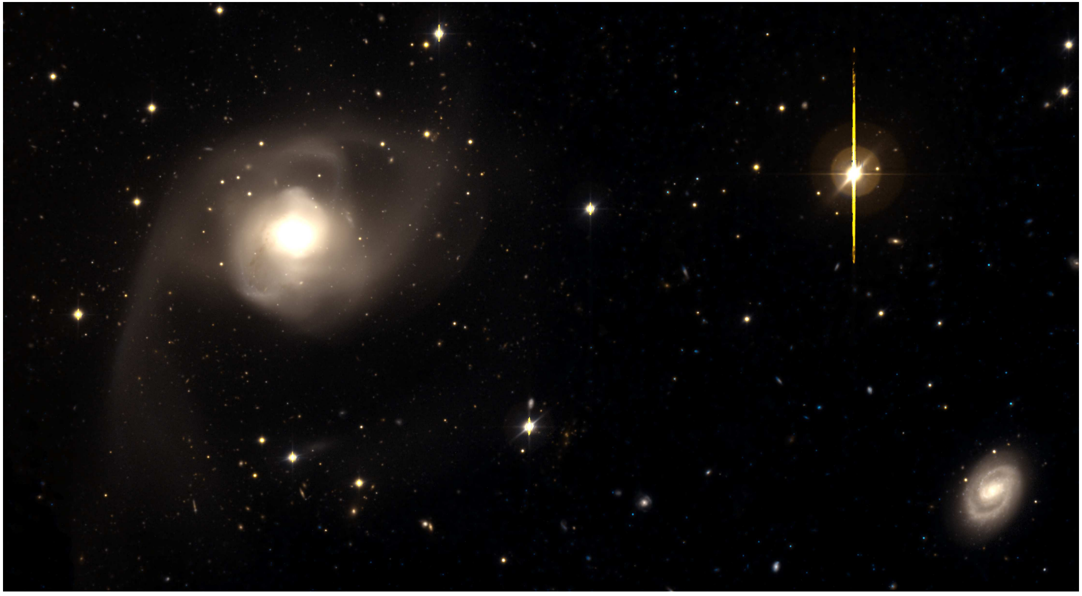

Figure 9.45: UGCA 071

Bibliography

Aaronson, M. 1977, PhD thesis, Harvard University, Cambridge, MA.

Abazajian, K. N., et al. 2009, ApJS, 182, 543

Arp, H., & Madore, B. F. 1977, QJRAS, 18, 234

Atkinson, A. M., Abraham, R. G., & Ferguson, A. M. N. 2013, ApJ, 765, 28

Beaton, R. L., et al. 2013, ArXiv e-prints: 1312.0585

Bekki, K. 2009, MNRAS, 399, 2221

Belokurov, V., et al. 2006, ApJ, 647, L111

Bertin, E., & Arnouts, S. 1996, A&AS, 117, 393

Binggeli, B., Sandage, A., & Tammann, G. A. 1988, ARAA, 26, 509

Bosma, A. 1981, AJ, 86, 1791

Bottema, R. 1999, A&A, 348, 77

Bottinelli, L., Gouguenheim, L., & Paturel, G. 1982, A&AS, 47, 171

Boylan-Kolchin, M., Ma, C.-P., & Quataert, E. 2008, MNRAS, 383, 93

Brassington, N. J., Ponman, T. J., & Read, A. M. 2007, MNRAS, 377, 1439

Busha, M. T., Wechsler, R. H., Behroozi, P. S., Gerke, B. F., Klypin, A. A., & Primack, J. R. 2011, ApJ, 743, 117

Butler, D. J., & Martínez-Delgado, D. 2005, AJ, 129, 2217

Caldwell, N., Armandroff, T. E., Seitzer, P., & Da Costa, G. S. 1992, AJ, 103, 840

Cappellari, M., Bertola, F., Burstein, D., Buson, L. M., Greggio, L., & Renzini, A. 1999, ApJ, 515, L17

Cardelli, J. A., Clayton, G. C., & Mathis, J. S. 1989, ApJ, 345, 245

Cellone, S. A. 1999, A&A, 345, 403

Chaboyer, B. 1994, in European Southern Observatory Conference and Workshop Proceedings, Vol. 49, European Southern Observatory Conference and Workshop Proceedings, ed. G. Meylan & P. Prugniel, 485

Chiboucas, K., Karachentsev, I. D., & Tully, R. B. 2009, AJ, 137, 3009

Chiboucas, K., Tully, R. B., Marzke, R. O., Trentham, N., Ferguson, H. C., Hammer, D., Carter, D., & Khosroshahi, H. 2010, ApJ, 723, 251

Chonis, T. S., Martínez-Delgado, D., Gabany, R. J., Majewski, S. R., Hill, G. J., Gralak, R., & Trujillo, I. 2011, AJ, 142, 166

Chromey, F. R. 2010, To Measure the Sky (Cambridge University Press)

Cole, S., Lacey, C. G., Baugh, C. M., & Frenk, C. S. 2000, MNRAS, 319, 168

Colpi, M., Mayer, L., & Governato, F. 1999, ApJ, 525, 720

Cooper, A. P., et al. 2010, MNRAS, 406, 744

Crabtree, D. R., & Smecker-Hane, T. 1994, in Bulletin of the American Astronomical Society, Vol. 26, American Astronomical Society Meeting Abstracts, 107.14

de Mello, D. F., Smith, L. J., Sabbi, E., Gallagher, J. S., Mountain, M., & Harbeck, D. R. 2008, AJ, 135, 548

de Vaucouleurs, G., de Vaucouleurs, A., & Corwin, Jr., H. G. 1976, Second reference catalogue of bright galaxies. Containing information on 4,364 galaxies with references to papers published between 1964 and 1975. (University of Texas Press)

de Vaucouleurs, G., de Vaucouleurs, A., Corwin, Jr., H. G., Buta, R. J., Paturel, G., & Fouque, P. 1991, Third Reference Catalogue of Bright Galaxies (New York: Springer)

Drinkwater, M. J., Gregg, M. D., Couch, W. J., Ferguson, H. C., Hilker, M., Jones, J. B., Karick, A., & Phillipps, S. 2004, PASA, 21, 375

Duc, P.-A., Brinks, E., Springel, V., Pichardo, B., Weilbacher, P., & Mirabel, I. F. 2000, AJ, 120, 1238

Eke, V. R., Baugh, C. M., Cole, S., Frenk, C. S., King, H. M., & Peacock, J. A. 2005, MNRAS, 362, 1233

Elahi, P. J., et al. 2013, MNRAS, 433, 1537

Eskridge, P. B., et al. 2002, ApJS, 143, 73

Evans, I. N., Koratkar, A. P., Storchi-Bergmann, T., Kirkpatrick, H., Heckman, T. M., & Wilson, A. S. 1996, ApJS, 105, 93

Ferguson, A. M. N., Irwin, M. J., Ibata, R. A., Lewis, G. F., & Tanvir, N. R. 2002, AJ, 124, 1452

Ferguson, H. C., & Sandage, A. 1991, AJ, 101, 765

Fukugita, M., Shimasaku, K., & Ichikawa, T. 1995, PASP, 107, 945

Geehan, J. J., Fardal, M. A., Babul, A., & Guhathakurta, P. 2006, MNRAS, 366, 996

Gil de Paz, A., Madore, B. F., & Pevunova, O. 2003, ApJS, 147, 29

Grebel, E. K. 2001, Astrophysics and Space Science Supplement, 277, 231

Grebel, E. K. 2005, in American Institute of Physics Conference Series, Vol. 752, Stellar Astrophysics with the World's Largest Telescopes, ed. J. Mikolajewska & A. Olech, 161–174

Grebel, E. K., Gallagher, III, J. S., & Harbeck, D. 2003, AJ, 125, 1926

Grebel, E. K., & Stetson, P. B. 1999, in IAU Symposium, Vol. 192, The Stellar Content of Local Group Galaxies, ed. P. Whitelock & R. Cannon, 165

Guhathakurta, P., & Cutri, R. M. 1994, in The First Symposium on the Infrared Cirrus and Diffuse Interstellar Clouds, ed. R. M. Cutri & W. B. Latter, ASP Conf. Ser., 58 (San Francisco, CA: ASP), 34

Guo, Q., Cole, S., Eke, V., & Frenk, C. 2011, MNRAS, 417, 370

Harbeck, D., et al. 2001, AJ, 122, 3092

Harris, W. E. 1996, AJ, 112, 1487

Hayes, D. S., & Latham, D. W. 1975, ApJ, 197, 593

Haynes, M. P. 1981, AJ, 86, 1126

Haynes, M. P., van Zee, L., Hogg, D. E., Roberts, M. S., & Maddalena, R. J. 1998, AJ, 115, 62

Heraudeau, P., Simien, F., & Mamon, G. A. 1996, A&AS, 117, 417

Hibbard, J. E., van der Hulst, J. M., Barnes, J. E., & Rich, R. M. 2001, AJ, 122, 2969

Hodge, P. W. 1963, AJ, 68, 691

Howell, S. B. 2006, Handbook of CCD Astronomy, ed. R. Ellis, J. Huchra, S. Kahn, G. Rieke, & P. B. Stetson (Cambridge University Press)

Jerjen, H., Binggeli, B., & Freeman, K. C. 2000, AJ, 119, 593

Jerjen, H., Freeman, K. C., & Binggeli, B. 1998, AJ, 116, 2873

Johnston, K. V., Bullock, J. S., Sharma, S., Font, A., Robertson, B. E., & Leitner, S. N. 2008, ApJ, 689, 936

Johnston, K. V., Sackett, P. D., & Bullock, J. S. 2001, ApJ, 557, 137

Jordi, K., Grebel, E. K., & Ammon, K. 2006, A&A, 460, 339

Karachentsev, I. D. 2005, AJ, 129, 178

Karachentsev, I. D., et al. 2003a, A&A, 404, 93

—. 2003b, A&A, 398, 467

Kniazev, A. Y., Grebel, E. K., Pustilnik, S. A., Pramskij, A. G., Kniazeva, T. F., Prada, F., & Harbeck, D. 2004, AJ, 127, 704

Knierman, K. A., Scowen, P., Veach, T., Groppi, C., Mullan, B., Konstantopoulos, I., Knezek, P. M., & Charlton, J. 2013, ApJ, 774, 125

Kormendy, J., & Djorgovski, S. 1989, ARAA, 27, 235

Kravtsov, A. 2010, Advances in Astronomy, 2010

Lambas, D. G., Alonso, S., Mesa, V., & O'Mill, A. L. 2012, A&A, 539, A45

Landolt, A. U. 1983, AJ, 88, 439

Lisker, T., Grebel, E. K., & Binggeli, B. 2006, AJ, 132, 497

—. 2008, AJ, 135, 380

Lisker, T., Grebel, E. K., Binggeli, B., & Glatt, K. 2007, ApJ, 660, 1186

Lo, K. Y., & Sargent, W. L. W. 1979, ApJ, 227, 756

Lotz, J. M., Jonsson, P., Cox, T. J., Croton, D., Primack, J. R., Somerville, R. S., & Stewart, K. 2011, ApJ, 742, 103

Ludwig, J., Pasquali, A., Grebel, E. K., & Gallagher, III, J. S. 2012, AJ, 144, 190

Madau, P., Diemand, J., & Kuhlen, M. 2008, ApJ, 679, 1260

Makarova, L., Karachentsev, I., Rizzi, L., Tully, R. B., & Korotkova, G. 2009, MNRAS, 397, 1672

Makarova, L. N., Karachentsev, I. D., Grebel, E. K., Harbeck, D., Korotkova, G. G., & Geisler, D. 2005, A&A, 433, 751

Makarova, L. N., et al. 2002, A&A, 396, 473

Malin, D., & Hadley, B. 1999, in Galaxy Dynamics - A Rutgers Symposium, ed. D. R. Merritt, M. Valluri, & J. A. Sellwood, ASP Conf. Ser., 182 (San Francisco, CA: ASP), 445

Martinez, P., & Klotz, A. 1998, A practical guide to CCD astronomy (Cambridge University Press)

Martínez-Delgado, D., Peñarrubia, J., Gabany, R. J., Trujillo, I., Majewski, S. R., & Pohlen, M. 2008, ApJ, 689, 184

Martínez-Delgado, D., Pohlen, M., Gabany, R. J., Majewski, S. R., Peñarrubia, J., & Palma, C. 2009, ApJ, 692, 955

Martínez-Delgado, D., et al. 2010, AJ, 140, 962

Mateo, M. L. 1998, ARAA, 36, 435

Materne, J., & Tammann, G. A. 1974, A&A, 35, 441

McCarthy, I. G., Frenk, C. S., Font, A. S., Lacey, C. G., Bower, R. G., Mitchell, N. L., Balogh, M. L., & Theuns, T. 2008, MNRAS, 383, 593

McLean, I. S. 2008, Electronic Imaging in Astronomy: Detectors and Instrumentation (Second Edition) (Praxis Publishing)

Meurer, G. R., et al. 2006, ApJS, 165, 307

Mihos, J. C., Harding, P., Feldmeier, J., & Morrison, H. 2005, ApJ, 631, L41

Miskolczi, A., Bomans, D. J., & Dettmar, R.-J. 2011, A&A, 536, A66

Monaco, L., Saviane, I., Perina, S., Bellazzini, M., Buzzoni, A., Federici, L., Fusi Pecci, F., & Galleti, S. 2009, A&A, 502, L9

Monet, D. G., et al. 2003, AJ, 125, 984

Monet D., et al. 1998, VizieR Online Data Catalog, 1252, 0

Moore, B., Ghigna, S., Governato, F., Lake, G., Quinn, T., Stadel, J., & Tozzi, P. 1999, ApJ, 524, L19

Mouhcine, M., & Ibata, R. 2009, MNRAS, 399, 737

Mouhcine, M., Ibata, R., & Rejkuba, M. 2010, ApJ, 714, L12

—. 2011, MNRAS, 415, 993

Mould, J. R., et al. 2000, ApJ, 528, 655

Mundell, C. G., Pedlar, A., Axon, D. J., Meaburn, J., & Unger, S. W. 1995, MNRAS, 277, 641

Papaderos, P., Loose, H.-H., Thuan, T. X., & Fricke, K. J. 1996, A&AS, 120, 207

Peng, E. W., Ford, H. C., Freeman, K. C., & White, R. L. 2002, AJ, 124, 3144

Regan, M. W., et al. 2004, ApJS, 154, 204

Richardson, J. C., et al. 2011, ApJ, 732, 76

Rothberg, B., & Joseph, R. D. 2004, AJ, 128, 2098

Sancisi, R., Fraternali, F., Oosterloo, T., & van der Hulst, T. 2008, A&A Rev., 15, 189

Sandage, A. 1976, AJ, 81, 954

Sandage, A., & Bedke, J. 1994, The Carnegie Atlas of Galaxies. Volumes I, II. (Carnegie Institution of Washington Publ.)

Sandage, A., & Binggeli, B. 1984, AJ, 89, 919

Saviane, I., Held, E. V., & Bertelli, G. 2000, A&A, 355, 56

Schlegel, D. J., Finkbeiner, D. P., & Davis, M. 1998, ApJ, 500, 525

Schweizer, F., & Seitzer, P. 1988, ApJ, 328, 88

Sersic, J. L. 1968, Atlas de galaxias australes (Observatorio Astronomico)

Sharina, M. E., et al. 2008, MNRAS, 384, 1544

Siegel, M. H., et al. 2007, ApJ, 667, L57

Simien, F., & Prugniel, P. 2002, A&A, 384, 371

Sparke, L. S., & Gallagher, III, J. S. 2007, Galaxies in the Universe: An Introduction (Cambridge University Press)

Steinmetz, M., & Navarro, J. F. 2002, New Astronomy, 7, 155

Stetson, P. B. 2000, PASP, 112, 925

Szomoru, A., & Guhathakurta, P. 1998, ApJ, 494, L93

Tal, T., van Dokkum, P. G., Nelan, J., & Bezanson, R. 2009, AJ, 138, 1417

Tolstoy, E. 2000, Dwarf Irregular Galaxies, ed. P. Murdin (Institute of Physics Publishing)

Toomre, A. 1977, in Evolution of Galaxies and Stellar Populations, ed. B. M. Tinsley & R. B. G. Larson, D. Campbell (Yale University Observatory), 401

Trentham, N., & Tully, R. B. 2002, MNRAS, 335, 712

Tully, R. B. 1987, ApJ, 321, 280

Tully, R. B., & Fisher, J. R. 1988, Catalog of Nearby Galaxies (Cambridge: Cambridge Univ. Press)

Tully, R. B., et al. 2006, AJ, 132, 729

van den Bergh, S. 1977, in Evolution of Galaxies and Stellar Populations, ed. B. M. Tinsley & R. B. G. Larson, D. Campbell (Yale University Observatory), 19–21

van der Marel, R. P. 1994, MNRAS, 270, 271

van Zee, L., Skillman, E. D., & Haynes, M. P. 2004, AJ, 128, 121

Walter, F., Brinks, E., de Blok, W. J. G., Bigiel, F., Kennicutt, Jr., R. C., Thornley, M. D., & Leroy, A. 2008, AJ, 136, 2563

Wang, J., Hammer, F., Athanassoula, E., Puech, M., Yang, Y., & Flores, H. 2012, A&A, 538, A121

Wehner, E. H., Gallagher, J. S., Papaderos, P., Fritze-von Alvensleben, U., & Westfall, K. B. 2006, MNRAS, 371, 1047

Weilbacher, P. M., Duc, P.-A., Fritze v. Alvensleben, U., Martin, P., & Fricke, K. J. 2000, A&A, 358, 819

Werk, J. K., Putman, M. E., Meurer, G. R., Oey, M. S., Ryan-Weber, E. V., Kennicutt, Jr., R. C., & Freeman, K. C. 2008, ApJ, 678, 888

Wetzstein, M., Naab, T., & Burkert, A. 2007, MNRAS, 375, 805

White, S. D. M., & Frenk, C. S. 1991, ApJ, 379, 52

Xu, C. K., Sun, Y. C., & He, X. T. 2004, ApJ, 603, L73

Yun, M. S., Ho, P. T. P., & Lo, K. Y. 1994, Nature, 372, 530

Zibetti, S. 2009, ArXiv e-prints: 0911.4956

Zucker, D. B., et al. 2006, ApJ, 650, L41

LIST OF ABBREVIATIONS

ADU	Analog-to-Digital Unit
BCD	blue compact dwarf galaxies
BG	background
BPM	bad-pixel masks
CDG	candidate dwarf galaxy
CSB	central surface brightness
dE	dwarf elliptical galaxies
dE(bc)	blue-core dwarf ellipticals
DEC	declination
DECam	camera of the dark energy survey
dIrr	dwarf irregular galaxies
dSph	dwarf spheroidal galaxies
ESO	European Southern Observatory
FWHM	full width at half maximum
GGADDS	giant galaxies, dwarfs and debris survey
KPNO	Kitt Peak National Observatory
LG	Local Group
MEF	multi image file
N_{pix}	number of pixels
NED	NASA Extragalactic Database
NGB	Nearby Galaxies Catalog
NOAO	National Optical Astronomy Observatory
ODI	One Degree Imager
PA	position angle
PSF	point-spread function
RA	right ascension
RDNOISE	the read-out-noise
S/N	signal-to-noise
SB	surface brightness
SBP	surface brightness profile
SDSS	Sloan Digital Sky Survey
SMA	semi major axis
TDG	tidal dwarf galaxies
TDGC	tidal dwarf galaxy candidate
UCD	Ultra compact dwarf galaxies
WCS	world coordinate system
WFI	Wide Field Imager
WFIC	wide-field image cameras
WIYN	WIYN consortium consists of the University of Wisconsin, Indiana University, Yale University, and the National Optical Astronomy Observatory

ACKNOWLEDGEMENTS

The acknowledgements are the place where I want to leave a personal note to all the people who helped me throughout my PhD. I hope that I did not forget anyone, if so I am very sorry and I can assure that this happened not on purpose. I thank hereby also all the people I am not aware of that they supported me.

First of all I would like to thank Eva Grebel for her fantastic support during my PhD. It was a great pleasure to discuss scientific questions with you and I enjoyed your ability of making the atmosphere more relaxed. I am very thankful for everything I learned from you and for sharing your great knowledge about dwarf galaxies, your comments and your exceptional conception of causal relation, these improved this thesis substantially. Also your support and sympathy during my parental leave was very helpful and important for our family life and is noteworthy in the research field. I very much appreciated that you always have a sympathetic ear!

A big thank you goes to Anna Pasquali, you helped me throughout all the issues in the jungle of image reduction with IRAF and without you it would have not been possible to reduce such an amount of data. Thanks for all the hours you invested in my PhD and for the time you patiently sit next to me and explained me everything one should know about data reduction, your outstanding expertise in this technique helped to improve my thesis appreciably.

A special thank goes to Jay Gallagher, your nearly infinite knowledge about the universe and all astronomical topics was very helpful during my PhD. I enjoyed our fruitful morning coffee discussions during your visits in Heidelberg and I tried to catch as many things as possible you explained to me. Also your support during the observations at KPNO and your collaboration improved this thesis, without that it would not have been possible to observe so many galaxies. I also appreciated your hospitality during my research visit at the University of Wisconsin.

I am also very grateful to Jochen Heidt, who agreed to be second referee of this thesis and accepted that I had to move the deadline of this thesis several times. Your straightforward communication was very helpful in order to fulfill all forms for finishing my PhD.

A thank you goes to all members of my disputation committee, namely Eva Grebel, Jochen Heidt, Joachim Wambsganß and Michael Hausmann. Important questions always improve the understanding of the studied topics, and discussions are the basis of scientific work. I am very excited to look forward to my PhD exam.

All past and current members of the ARI made this institute to an enjoyable environment. Special thanks go to Raoul Haschke, who shared not only an office with me but also the favorite football club, you left more than a substantial gap after you joined your new job. I appreciated all the scientific discussion with you, especially when using our blackboard. A warm thank you goes to Sonia Duffau, especially your communication skills made our group to an enjoyable working group. Also your great ideas for hats and farewell presents helped to fill our free time and to expand our creativity. I am thankful to Anthony Pavkovic and Xiaoying Pang for assisting me during observations with the WIYN 0.9m telescope and fighting through all the problems during observational nights. Special thanks go to Peter Zeidler, who is always open for scientific discussions and helped to give our small office an enjoyable atmosphere. Great thanks go to Stefan Schmeja, who not only shared scientific discussions with me but also experiences of having a child. I thank the past ARI members Denija Crnojevic, Katharina Glatt, Katrin Jordi, Raoul

Haschke, Shoko Jin, Sonia Duffau and Stefano Pasetto for sharing great moments together during our time at ARI.

Great thanks for proof reading of applications, proposals, papers and the PhD thesis go to Eva Grebel, Anna Pasquali, and Jay Gallagher, you helped me a lot in order to finish this thesis. I also thank Avon Huxor, Jan Rybizki, Peter Zeidler and especially Stefan Schmeja for proof reading, your comments were always very helpful. I thank all the members of the research group of Eva Grebel for great discussions and thus improving my thesis and extending the knowledge of astrophysical topics.

The Heidelberg Graduate School of Fundamental Physics is acknowledged for the great support during my PhD thesis. In particular thanks go to Sandra Klevansky, you provided great support for having a child during a PhD and it was a pleasure to work with you on the Homepage and other matters of the HGSFP. All the offers of the HGSFP help significantly during the phase of my PhD. I also thank IMPRS for all the support, namely Christian Fendt who helped unconventionally at any concerns which arose from time to time.

I am very thankful to my whole family, which supported me throughout all my studies. I would have never managed all of this without you. I especially thank my parents Christine and Alfons Ludwig, you helped with everything in all circumstances and always believed in me! I appreciated that you took it always relaxed when you had to struggle with my experiments and other matters. Without your encouragement I would not be where I am now. I thank my sisters Theresia and Maria and my brother Kilian for the great time we had together and for taking care of my son Linus, so that I could concentrate on working on my thesis. I also thank my grandparents for their constant support throughout all parts of my life. I am also grateful to my father-in-law for his engagement of managing our bureaucratic matters and for fulfilling his duties as grandfather.

My greatest thanks go to my wife Nicola, without you it would not have been possible to finish all this. Your limitless support and permanent encouragement rescued me when I got lost in the world of PhD students. Also your great help in the last days and hours of finishing my thesis was unbelievable. You are the most important person in my life! Special thanks go to my son Linus, who is always remembering me to look at the world from a different point of view and brings a smile into my life after an exhausting scientific work day.